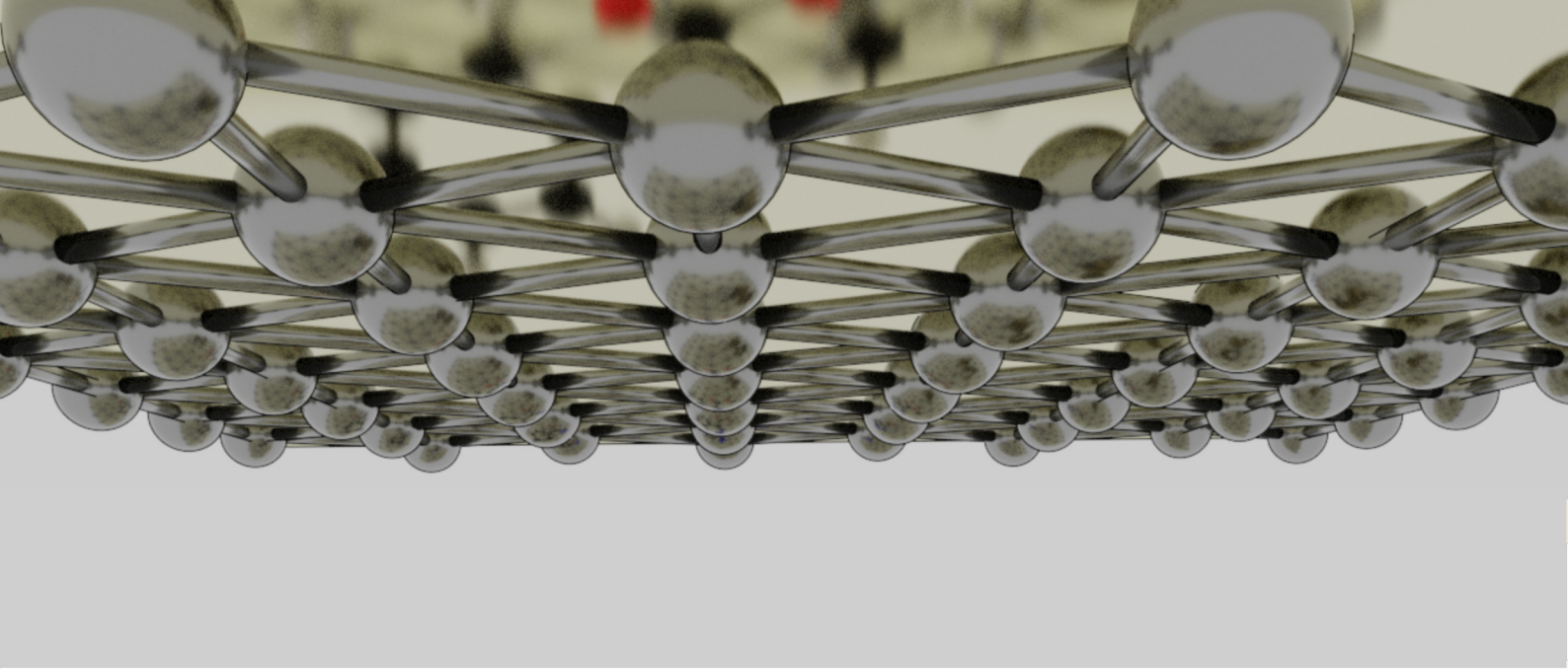

北海道大学
HOKKAIDO UNIVERSITY

GRADUATE SCHOOL OF
CHEMICAL SCIENCES AND ENGINEERING
HOKKAIDO UNIVERSITY

Theoretical Study on Mechanically Stressed Chemical Systems

機械的応力下における化学反応系に関する理論的研究

Danjo De Chavez

2021

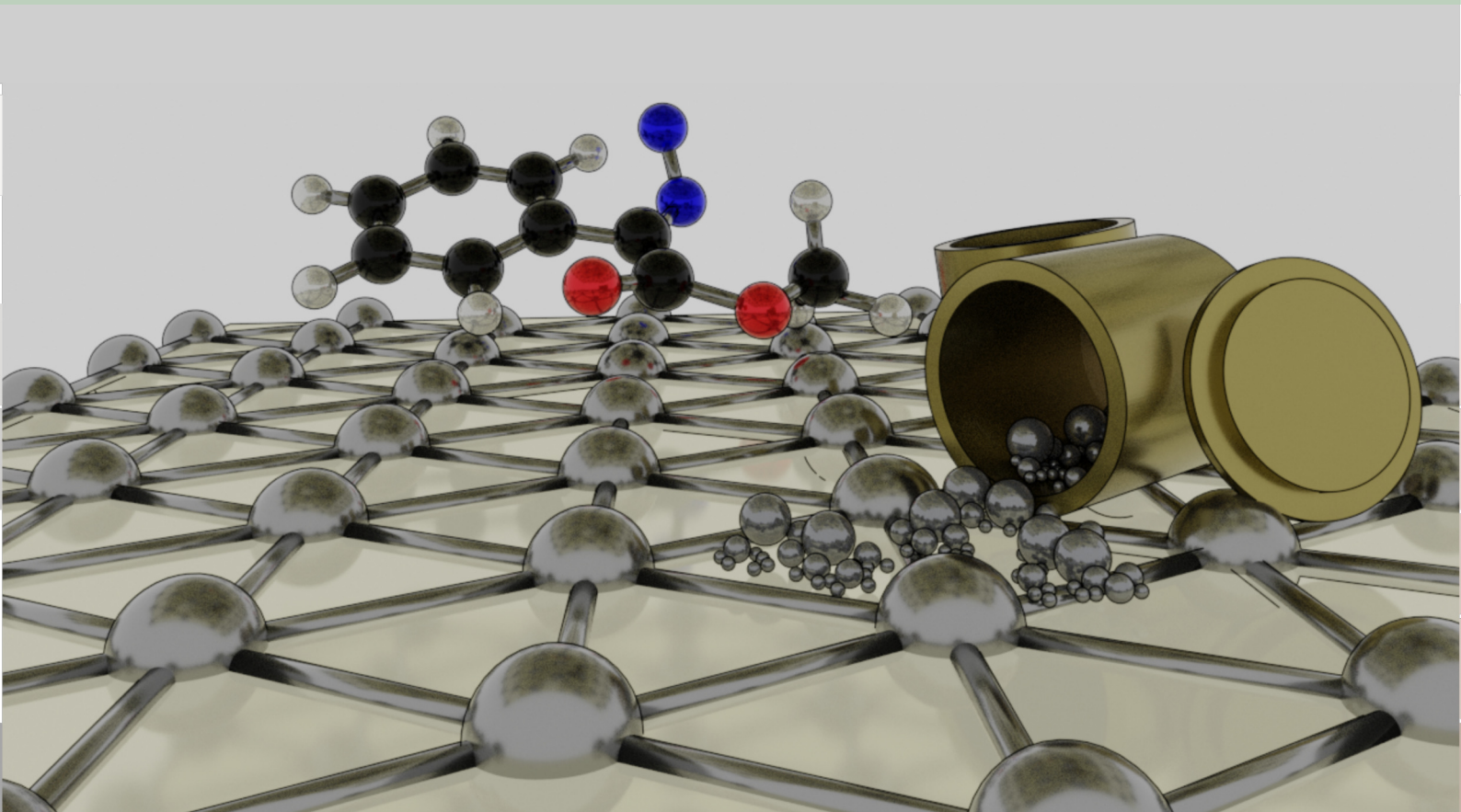

GRADUATE SCHOOL OF CHEMICAL SCIENCES AND ENGINEERING,
HOKKAIDO UNIVERSITY
DECHAVEZDANJO@GMAIL.COM
September 2021

Contents

General Introductions

1.1 Mechanochemistry: Old tool for new chemistry

Mechanochemistry is the branch of chemistry that deals with the interaction of external mechanical forces with any chemical system [10, 12]. Figure 1.2 shows a theoretical diatomic molecule along with its Morse potential curve (blue). Upon the addition of external applied force (orange) along the bond coordinate, the one dimensional potential energy surface (grey) changes. This results in the lowering of bond dissociation energy from D to D' [5].

Mechanochemistry can be considered alongside other chemical systematics such thermochemistry and photochemistry. In thermochemical activation, thermal energy is used to increase the average energy of the chemical ensemble to overcome the activation barrier of a chemical phenomena such as reaction or surface diffusion. On the other hand, the photochemical process includes excitation of an electron of a molecule. In this case, two or more overlapping potential energy surfaces are considered. One of which allows the reaction to proceed with a lowered activation barrier in comparison to the others. The resulting elementary step product may then relax to its ground state multiplicity. Mechanochemistry

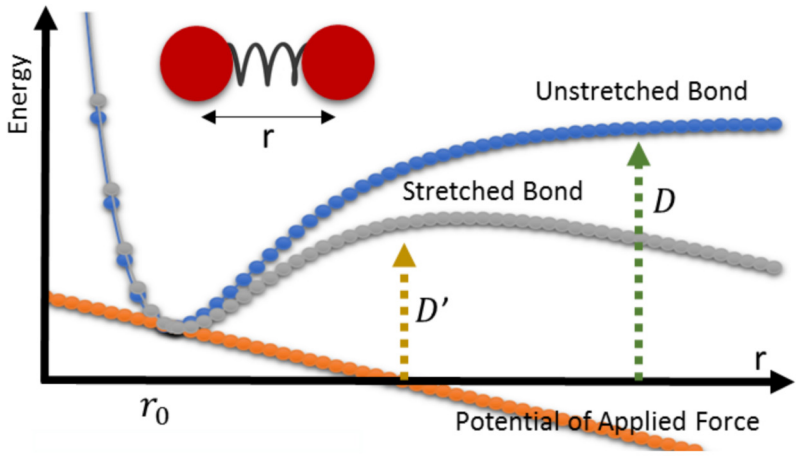

Figure 1.1: Force modification of potential energy landscape. Adapted with permission from Ref. [5]. Copyright 1940 American Chemical Society.

affords unique chemical activation in comparison to the previous. In mechanical activation, the mode of activation is via a force vector, and hence the effective activation is dependent on both the magnitude and direction of applied external force.

The potential energy surface given in Figure 1.2 shows the simplest possible scenario in which there is a singular molecular coordinate. However, molecules of interest normally contain tens to hundreds of redundant internal molecular coordinates. In general, the potential energy surface of any molecule with N atoms is a 3N-6 dimensional hypersurface in which the effect of the external force varies with magnitude and direction along which the force is applied.

Considering explicit addition of forces, the effective nuclear force acting on atom i of a molecule is given by

$$F^i_{total} = F^i_{abinitio} + F^i_{ext} = \frac{\partial V_{abinitio}}{\partial R} + F^i_{ext} \tag{1.1}$$

where the first term accounts for the effective ab initio nuclear forces and the second term is the external applied force. This shifts the positions of the stable manifolds, such as reactants and transition states, based on the external forces which translates to a unique control on chemical reaction and dynamics.

With the recent increasing popularity of mechanochemical research, it would seem

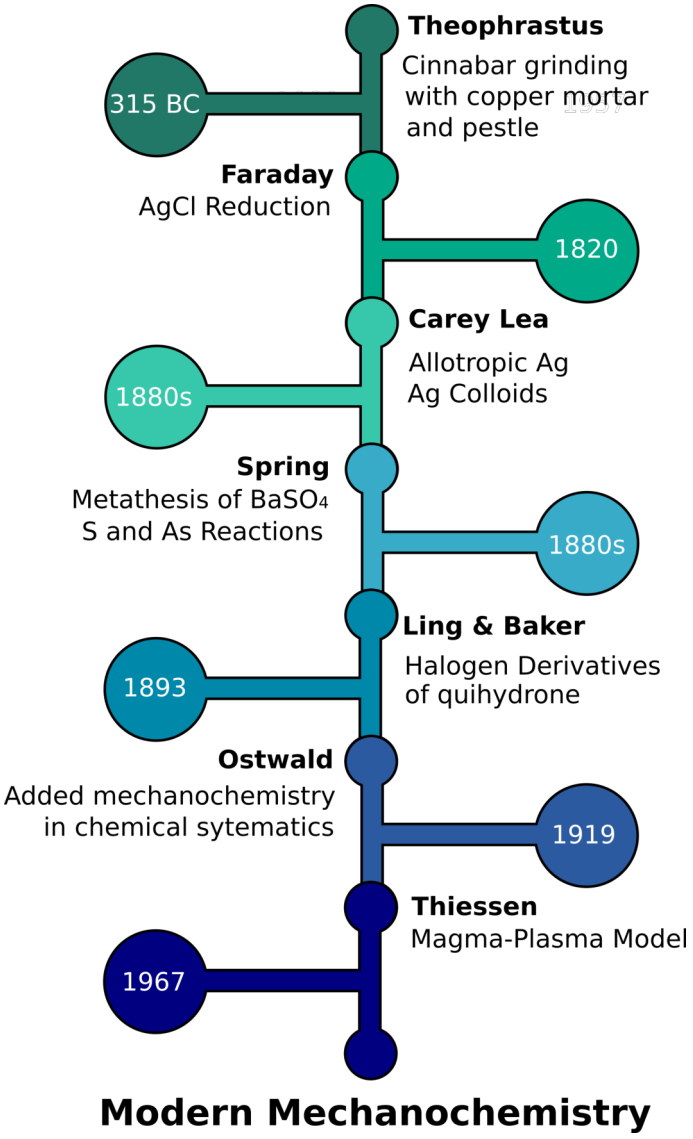

Figure 1.2: Historical development of modern mechanochemistry.

that mechanochemical phenomena have only been recently discovered. This is actually not the case, as mechanochemistry existed as early as 315 B.C.[13]. The earliest recorded mechanochemical reaction is the reduction of mercury. Theophrastus of Eresus produced quick silver or mercury from cinnabar by grinding with copper mortar and pestle.

$$HgS + Cu \longrightarrow Hg + CuS$$

In 1820, Michael Faraday used metallic mortar and pestle with silver salts for silver reduction reaction. He used the term "dry method" rather than mechanochemistry which would only be coined in a later year.

Perhaps, the most lasting contribution to the development of mechanochemistry was done by Carey Lea in the 1880s. Carey Lea studied allotropic silver and sliver colloids [13]. Specifically, Lea studied the following reactions

$$2AgCl \longrightarrow 2Ag + Cl_2$$

$$HgCl_2 \longrightarrow Hg + Cl_2$$

An important contemporary of Carey Lea is Spring. Spring studied various sulfur and arsenic reactions. He is best known for the metathesis reaction of BaSO4.

$$BaSO_4 + Na_2CO_3 \longrightarrow BaCO_3 + Na_2SO_4$$

Though mechanochemistry has existed from the early days of chemistry. Mechanochemistry has only been recognized as a separate subfield in a chemistry textbook in 1893 by Ostwald. He also made significant contributions to the chemistry of viscous fluids under the mechanochemical paradigm [13].

In the advent of chemical understanding, the first unified theory of mechanochemistry was devised by Peter Thiessen in the early 20th century. Thiessen's magma-plasma model discusses mechanical activation. According to this theory, the collision of reacting particles releases a high amount of energy at contact. This energy produces plasma-like state at the contact point, as well as excited solid fragments, electrons and phonons at an infinitesimal time scale. Though the magma-plasma model failed to create an integrated concept on how to understand mechanochemical phenomena, it served as a basis on which theories like hierarchical model and spherical model have been built upon [13].

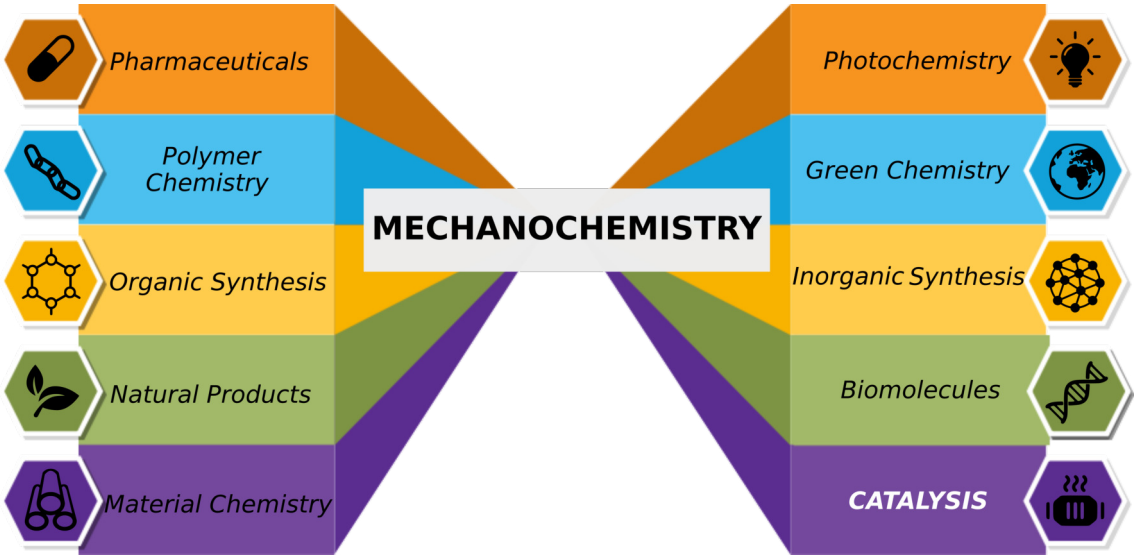

Figure 1.3: Current applications of mechanochemistry

1.2 Catalysis and Mechanical forces

The utility of mechanochemistry in modern day chemistry have been vastly growing due to the current booming interest in the field. Modern day applications includes pharmaceutical, polymer chemistry, photochemistry, organic chemistry, among others [2].

Catalysis is one of the fields in which mechanochemistry has been applied. A catalyst is any substance that allows the reaction to proceed faster without being consumed in the course of the reaction [14]. Catalyst does this by providing an alternate reaction pathway characterized by lower activation barriers. Take for example the case given in Figure 1.4 where the uncatalyzed and catalyzed reactions are given in red and green, respectively [4].

Figure 1.4 shows the typical action of heterogeneous catalysts [3]. A single uncatalyzed step changes to a 3-step route with overall lower activation energy E_a' and same reaction energy E_R. In this case, the initial step and energy barrier would correspond to adsorption and the last one to the desorption process. Intermediate to these steps is the same reaction corresponding to the uncatalyzed reaction happening in the catalytic surface of the heterogeneous catalyst [15]. Catalysts are of particular importance in biological systems and also in industry [1, 4]. An important example of biological catalysts are enzymes which catalyze biological reactions in the mild physiological environment. Industrial catalysts

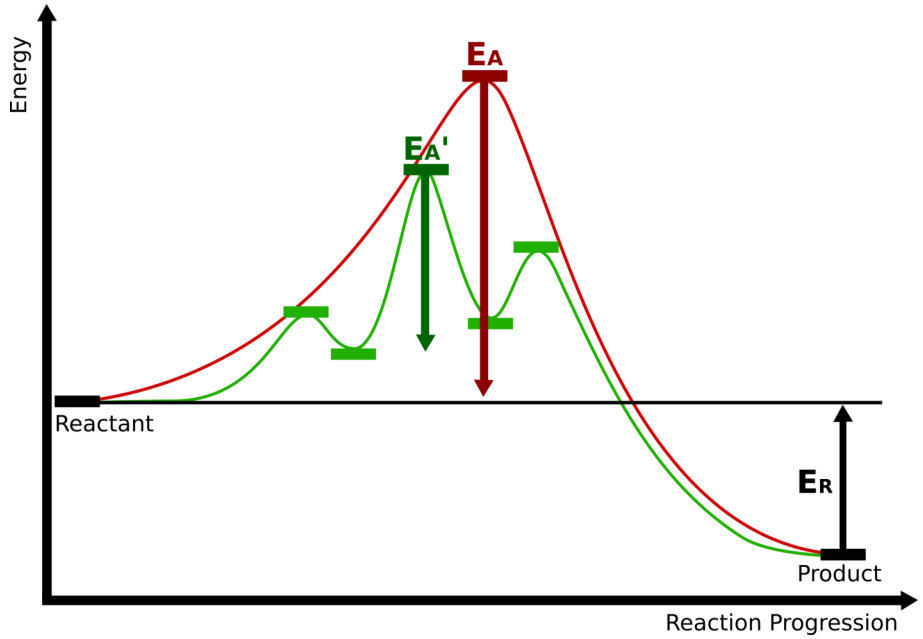

Figure 1.4: Effect of catalyst in a reaction energy diagram

are important in lowering the production cost of chemical synthesis thereby allowing more economic prices. Catalysis also allows lower reaction temperatures which further lowers the costs.

As earlier discussed, external force can decrease the dissociation energy barrier for diatomic molecules, effectively catalyzing decomposition reaction [5, 12]. In the example given, it is rather straightforward to predict the effect of external force since it is applied directly to the reaction coordinate and the molecular internal coordinate has only one degree of freedom. The dimensionality of the potential energy surface increases dramatically with the chemical structure. In cases of complex chemical structures, predicting the effect of external force becomes non-trivial. Linear models predict that the movement of minima is along the stressed internal coordinate. Such models more often fail than not in revealing the relevant chemistry and physics lying within. But nevertheless, such models show predictive power with, presumably, cancellation of errors. For example, bond strengthening due to the existence of catch bonds have been found both experimentally and theoretically. This phenomenon is not covered by simple linear models [9]. Possible movements of chemically relevant extrema are summarized as Figure 1.5 where χ is the compliance of

pulling coordinate to force that is

$$\chi_\alpha = \frac{\partial x_\alpha}{\partial F} \tag{1.2}$$

where F is the applied force along the pulling coordinate x of the chemical state α. When the pulling coordinate increases with the application of force, the compliance of such a system is considered to be positive.

Figure 1.5(a) shows the general assumption in a linear model of mechanical pulling where the compliance of reactant state is positive while that of the transition state is negative. Effectively, reactant and transition state move closer together and the energy barrier diminishes until it becomes zero [6, 11, 16]. However, this is not the only possibility. Stable structures in the potential energy surface is characterized by

$$\sum_i^N F_i = 0 \tag{1.3}$$

and as given in Eq. 1.1, the applied external forces are added to the atomic forces derived from electronic energy. Hence, the solution to condition Eq. 1.3 is

$$\sum_i^N F_{abinitio} = \sum_i \nabla V^i_{abinitio} = -\sum F^i_{ext} \tag{1.4}$$

Eq. 1.4 may be satisfied by numerous solutions, each corresponding to different displacement along the potential energy surface. And hence, prediction of the movement of an extremum in the potential energy surface is non-trivial. Examples of such events are given as Figures 1.5(b) and 1.5(c). In Figure 1.5(b), the transition state initially has a positive compliance with respect to the pulling direction. After which, the compliance of the transition state changes and proceeds to meet the reactant state effectively lowering energy difference between states. Figure 1.5(c) is similar to Figure 1.5(b) but the transition state at $F = 0$ lies on the left of the graph. This means that the relaxed structure of the transition state has a shorter x coordinate than the reactant. In terms of reaction energetics, this type of reaction would experience an initial increase in activation energy and would effectively hinder the reaction.

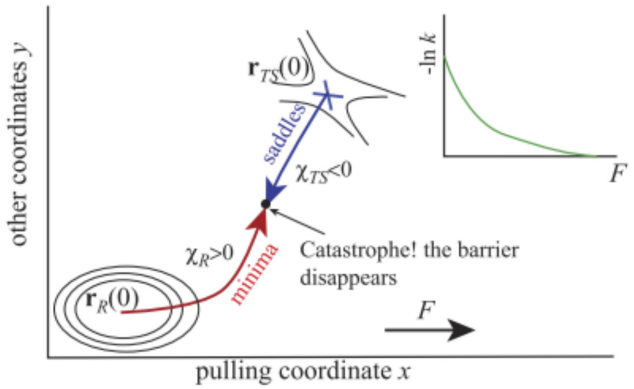

(a)

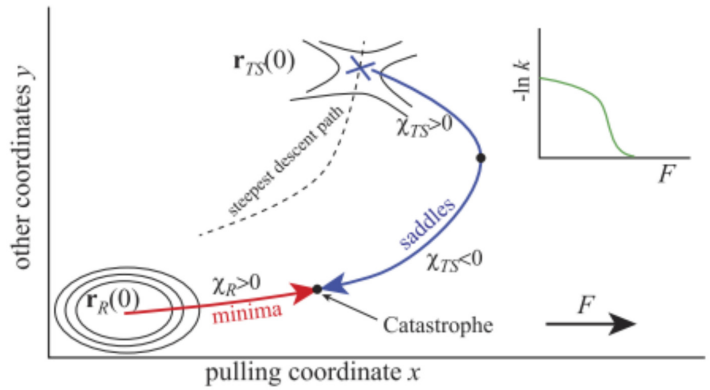

(b)

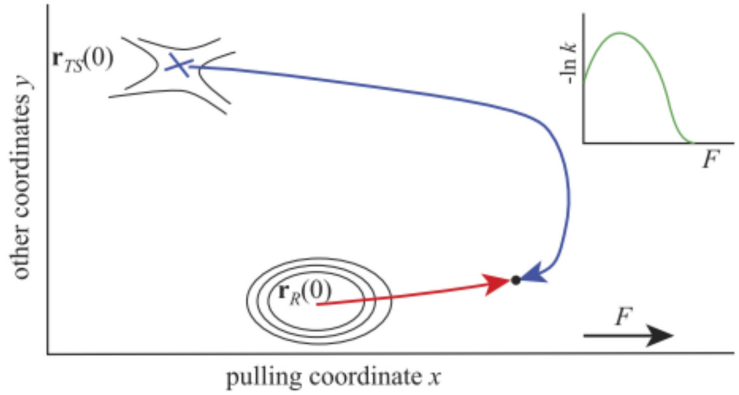

(c)

Figure 1.5: Force induced displacements in a theoretical reactant (R) and transition states (TS). Reprinted from Ref. [9], with the permission of AIP Publishing.

$$k(F) = k(0)e^{\frac{F}{k_B T}} \tag{1.5}$$

The Bell model, given as Eq. 1.5, is a popular model used to model and predict the kinetic changes in a mechanochemical reaction [7]. However, it should be noted that the underlying assumption of such a model is that δx during the reaction is conserved. Such a premise is often unmet due to different compliances at the reactant and transition states as debated above. In this regard, a simple linear model such as Bell model and related work does not describe the underlying complexity in a mechanochemical reaction [8]. Additional considerations such as thermal fluctuations due to the components of the applied force which are not converted to work also increases this chemical problem.

1.3 Research Scope

This dissertation aims to gain fundamental chemical understanding of mechanochemical phenomena relating to catalytic reaction systems through quantum chemical simulations as well as to develop simulation and analysis tools for the emerging field of computational mechanochemistry.

Prior to mechanochemical simulations and tools, a review of density functional theory is written. This aims to provide the reader with a sufficient background in understanding DFT simulations in the context of molecular simulations and catalytic reactions. Additionally, a review of linear scaling quantum chemical software packages utilized in this work are also presented in Chapter 2.

Chapter 3 of this dissertation is dedicated to the development of mechanochemical simulation tools and analysis. This covers a python module dedicated to mechanochemistry which can be used in tandem with several quantum chemical softwares.

In Chapter 4, the mechanochemically induced selectivity in acid catalyzed hydrolysis in the chitin system was investigated using mechanical pulling developed in the previous

chapter.

Following pulling simulations, the pushing regime is studied in the context of mixed catalysis. The stereoselective cyclopropanation in Ag(111) surface was done to probe the effect of spatial constraints in the reaction path and product selectivity.

In Chapter 6, the effect of mechanically strained catalytic surfaces is investigated. In this chapter, carbon monoxide dissociation in relaxed and isotropically, and anisotropically strained ruthenium surfaces is studied.

All of the research included in this dissertation did not include molecular dynamics as one of the methods and hence pulling rate and other time related variables are excluded from the study. Furthermore, finite thermal effects that are expected from a physical standpoint are not included in the simulations.

Lastly, in Chapter 7, a brief summary is provided. Mechanochemical research outlook has also been given as a guide to future studies.

References

"Biocatalysis" (2008). In: *Catalysis*. John Wiley Sons, Ltd. Chapter 5, pages 189–229. ISBN: 9783527621866 (cited on page 15).

Do, Jean-Louis and Tomislav Friščić (2017). "Mechanochemistry: A Force of Synthesis". In: *ACS Central Science* 3.1. PMID: 28149948, pages 13–19 (cited on page 15).

"Heterogeneous Catalysis" (2008). In: *Catalysis*. John Wiley Sons, Ltd. Chapter 4, pages 127–187. ISBN: 9783527621866 (cited on page 15).

"Heterogeneous Catalysis and a Sustainable Future" (2014). In: *Fundamental Concepts in Heterogeneous Catalysis*. John Wiley Sons, Ltd. Chapter 1, pages 1–5. ISBN: 9781118892114 (cited on page 15).

Kauzmann, Walter and Henry Eyring (1940). "The Viscous Flow of Large Molecules". In: *Journal of the American Chemical Society* 62.11, pages 3113–3125 (cited on pages 11, 12, 16).

Konda, Sai Sriharsha M, Stanislav M Avdoshenko, and Dmitrii E Makarov (2014). "Exploring the topography of the stress-modified energy landscapes of mechanosensitive molecules". In: *J. Chem. Phys.* 140.10 (cited on page 17).

Konda, Sai Sriharsha M et al. (2011). "Chemical reactions modulated by mechanical stress: Extended Bell theory". In: *J. Chem. Phys.* 135.16 (cited on page 19).

Krupicka, Martin and Dominik Marx (2015). "Disfavoring mechanochemical reactions by stress-induced steric hindrance". In: *J. Chem. Theory Comput.* 11.3, pages 841–846 (cited on page 19).

Makarov, Dmitrii E (2016). "Perspective: Mechanochemistry of biological and synthetic molecules". In: *J. Chem. Phys.* 144.3 (cited on pages 16, 18).

Ribas-Arino, Jordi and Dominik Marx (2012). "Covalent mechanochemistry: Theoretical concepts and computational tools with applications to molecular nanomechanics". In: *Chem. Rev.* 112.10, pages 5412–5487 (cited on page 11).

Ribas-Arino, Jordi, Motoyuki Shiga, and Dominik Marx (2009). "Understanding covalent mechanochemistry". In: *Angew. Chem., Int. Ed.* 48.23, pages 4190–4193 (cited on page 17).

Stauch, Tim and Andreas Dreuw (2016). "Advances in quantum mechanochemistry: electronic structure methods and force analysis". In: *Chem. Rev.* 116.22, pages 14137–14180 (cited on pages 11, 16).

Takacs, Laszlo (2013). "The historical development of mechanochemistry". In: *Chem. Soc. Rev.* 42 (18), pages 7649–7659 (cited on page 14).

"The Basics of Catalysis" (2008). In: *Catalysis*. John Wiley Sons, Ltd. Chapter 2, pages 39–75. ISBN: 9783527621866 (cited on page 15).

"The Potential Energy Diagram" (2014). In: *Fundamental Concepts in Heterogeneous Catalysis*. John Wiley Sons, Ltd. Chapter 2, pages 6–25. ISBN: 9781118892114 (cited on page 15).

Wollenhaupt, Miriam et al. (2018). "Force-Induced Catastrophes on Energy Landscapes: Mechanochemical Manipulation of Downhill and Uphill Bifurcations Explains the

Ring-Opening Selectivity of Cyclopropanes". In: *ChemPhysChem* 19.7, pages 837–847 (cited on page 17).

II Chemistry and Computations

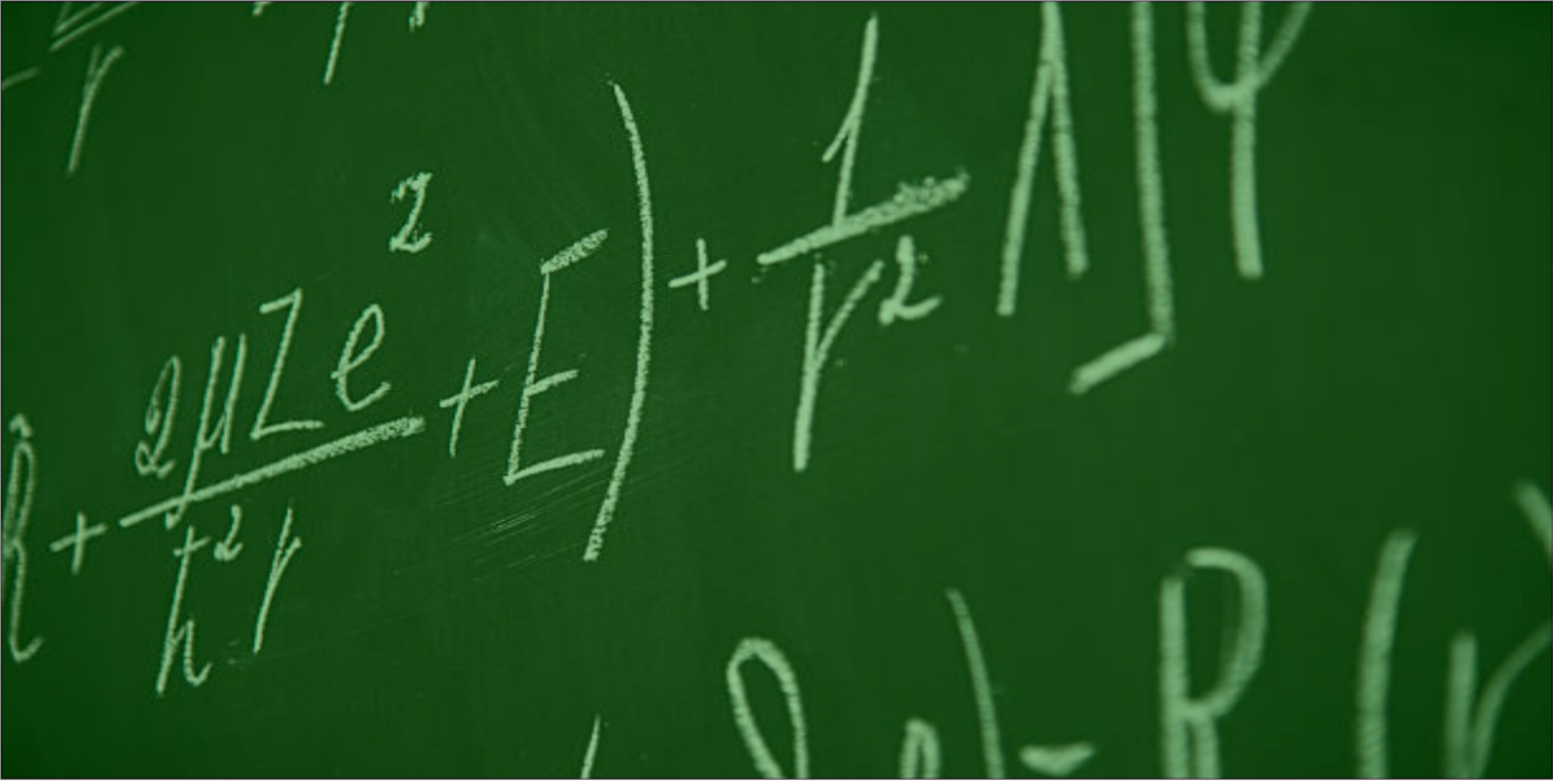

2.1 Density Functional Theory

The density functional theory can be treated as a parallel paradigm to the wave function theory. On this basis, observable properties of matter are described by its corresponding electronic structure. The electronic structure in wave function theory is the solution to the Schrodinger equation. Neglecting the time dependency of a wave, the Schrodinger equation is an eigenvalue problem that can be written as

$$\hat{H}\Psi = E\Psi \tag{2.1}$$

where the E is the electronic energy [12]. The Ψ is the electronic wavefunction of a molecule which is a function of the set of atomic coordinates, $\{x_A\}$.

$$\Psi = \Psi(x_1, x_2, \cdots, x_N) \tag{2.2}$$

Under the Born-Oppenheimer approximation , the electronic Hamiltonian operator has the following simplified form

$$\hat{H} = \hat{T} + \hat{V}_{ne} + \hat{V}_{ee} \tag{2.3}$$

where

$$\hat{T} = \sum_{i=1}^{N} (-\frac{1}{2}\nabla_i^2) \tag{2.4}$$

is the kinetic energy operator,

$$\hat{V}_{ne} = -\sum_{i=1}^{N} \frac{Z_\alpha}{r_{i\alpha}} \tag{2.5}$$

is the nucleus-electron potential energy operator. The negative sign of the operator translates to the attractive nature of this interaction. The last term of Eq 2.3

$$\hat{V}_{ee} = \sum_{i<j}^{N} \frac{1}{r_{ij}} \tag{2.6}$$

is the electron-electron potential energy operator. In parallel to the second term, the positive sign in Eq. 2.6 denotes repulsion of electrons. Substituting Eqs. 2.4, 2.5, and 2.6 to Eq. 2.3, the Hamiltonian operator can be rewritten in long form as

$$\hat{H} = \sum_{i=1}^{N} (-\frac{1}{2}\nabla_i^2) - \sum_{i=1}^{N} \frac{Z_\alpha}{r_{i\alpha}} + \sum_{i<j}^{N} \frac{1}{r_{ij}} \tag{2.7}$$

In solving the Schrodinger Equation , two general class of methods can be used; (1) *ab initio* calculations, and (2) semi-empirical methods [1]. Semi-empirical methods solve for the electronic structure with the help of pre-optimized parameters and simplified effective Hamiltonian. This allows one to calculate larger systems. However, chemically accurate calculations are hard to achieve. Semi-empirical methods are beyond the scope of this chapter but for the interested reader, the method review is recommended. On the other hand, *ab initio* methods calculate the electron density by variationally solving the Slater determinant following the Hartree-Fock formalism. In DFT, the wavefunction is substituted

with the simpler electron density, $\rho(r)$, and an associated electronic Hamiltonian.

Today, DFT calculations are based on self-consistently solving the Kohn-Sham equations. However, the original idea of simplifying the N electron wavefunction to a statistically predicted electron density function is attributed to Thomas and Fermi. It was Hohenberg and Kohn who formalized the idea through their well known theorems which we will introduce and prove [8, 10].

The postulates of quantum chemistry states that the number of electrons and potential energy function can determine the electronic wave function and consequently the electron density and potential energy of an electronic matter. In relation to this, the first theorem states that

Theorem 2.1.1 — Hohenberg-Kohn Theorem 1. The external potential $V_{ext}(r)$ can be determined within a constant by the ground state particle density, $\rho_o(r)$, as its unique functional.

Contrastingly, in the wavefunction theory in which the basic requirement is the molecular wavefunction, the theorem states that electron density can act as a replacement to the original wavefunction. Consider an electron density which gives two unique potential functions, v and v', for the same electron density $\rho(r)$. This then gives two different Hamiltonians, $\hat{H}$ and $\hat{H}'$, and consequently two distinct ground state wavefunctions, Ψ and Ψ'. Using Ψ' as a trial wavefunction for the $\hat{H}$ operator then

$$\begin{aligned} E_0 < \left\langle \Psi' \middle| \hat{H} \middle| \Psi' \right\rangle &= \left\langle \Psi' \middle| \hat{H}' \middle| \Psi' \right\rangle + \left\langle \Psi' \middle| \hat{H} - \hat{H}' \middle| \Psi' \right\rangle \\ &= E_0' + \int \rho(r)[v(r) - v'(r)]dr \end{aligned} \tag{2.8}$$

In the reverse case, using Ψ with $\hat{H}'$ gives a solution greater than E_0'

$$\begin{aligned} E_0' < \langle \Psi | \hat{H}' | \Psi \rangle &= \langle \Psi | \hat{H} | \Psi \rangle + \left\langle \Psi' \middle| \hat{H}' - \hat{H} \middle| \Psi' \right\rangle \\ &= E_0 - \int \rho(r)[v(r) - v'(r)]dr \end{aligned} \tag{2.9}$$

Adding Eqs. 2.8 and 2.9 gives

$$E_0 + E_0' < E_0' + E_0 \tag{2.10}$$

It should be noted that Eq. 2.10 is a fallacy by contradiction. Hence, a unique v gives a distinct $\rho(r)$ as a solution. In extension, $\rho(r)$ determines all the ground state properties with a certain functional form. This follows that the kinetic energy, T, and potential energies, V_{ee} and V_{ne}, can be written as

$$\begin{aligned} E_v[\rho] &= T[\rho] + V_{ne}[\rho] + V_{ee}[\rho] \\ &= \int \rho(r) v(r) dr + F_{HK}[\rho] \end{aligned} \tag{2.11}$$

where F_{HK} is parallel to the F_{TF} term of the Thomas-Fermi model. F_{HK} has the form

$$F_{HK}[\rho] = T[\rho] + V_{ee}[\rho] \tag{2.12}$$

where the electronic repulsion potential, V_{ee}, can be written as

$$V_{ee}[\rho] = J[\rho] + nonclassical \tag{2.13}$$

In Eq. 2.13, the first term, $J[\rho]$, accounts for the classical electron repulsion, and the second term accounts for the nonclassical contribution and mainly accounts for electron correlation, and exchange.

Theorem 1 gives an existence proof that a unique potential corresponds to a unique electron density. Following this, the second theorem of Hohenberg and Kohn states that

Theorem 2.1.2 — Hohenberg-Kohn Theorem 2. There exist a functional in terms of $\rho(r)$ that is valid for any external potential $-V(r)$ and the global minimum of this functional is the ground state energy of the system and the density corresponding is the electronic ground state density

This statement asserts that density functional theory follows variational principle and the ground state energy is the energy functional $E_v[\rho]$ which is an upper bound solution to the

Schrodinger equation.

$$E_0 \leq E_v[\tilde{\rho}] \tag{2.14}$$

In the proof of the first theorem, it shows that the ground state energy corresponds to unique set of $\rho(r)$, v, and $\hat{H}$, and hence

$$\begin{aligned} \langle \tilde{\Psi} | \hat{H} | \tilde{\Psi} \rangle &= \int \tilde{\rho}(r) v(r) d(r) + F_{HK}[\tilde{\rho}] \\ &= E_v[\tilde{\rho}] \geq E_v[\rho] \end{aligned} \tag{2.15}$$

Following variational principle, the derivative of the ground state energy with the constraint that the number of electrons is conserved, renders the ground state electron density $\rho(r)$ to be an extremum.

$$\delta \left\{ E_v[\rho] - \mu \left[\int \rho(r) dr - N \right] \right\} = 0 \tag{2.16}$$

where μ is the chemical potential and the Euler-Lagrange expression for chemical potential is given by

$$\mu = \frac{\delta E_v[\rho]}{\delta \rho(r)} = v(r) + \frac{\delta F_{HK}[\rho]}{\delta \rho(r)} \tag{2.17}$$

The chemical potential, electron density, and their corresponding derivatives are essential components in the conceptual density functional theory [2]. This branch of DFT describes molecular reactivity such as nucleophilicity, electrophilicity, hardness, and softness in terms of the electron density of the molecule. Conceptual density functional theory has been useful not only in predicting global molecular reactivity indices but also local site reactivity through indices such as local softness and Fukui functions.

The realization of Thomas and Fermi, together with the Hohenbergy-Kohn theorems allowed the development of modern DFT [1]. A further step in the development of an accurate method to solve the electronic structure problem is proposed by Kohn and Sham [10]. Rather than imposing approximations which was the direction of the Thomas-Fermi models, Kohn and Sham proposed the introduction of orbital based calculation to

systematically solve the variational problem. The energy functional can be written as the equation below.

$$\begin{aligned} E[\rho] &= T_s[\rho] + [\rho] + [\rho] + \int v(r)\rho(r)dr \\ &= \sum_i^N \sum_s \int \psi_i^*(r)(-\frac{1}{2}\nabla^2)\psi_i(r)dr + J[\rho] + E_{xc}[\rho] + \int v(r)\rho(r)dr \end{aligned} \tag{2.18}$$

and the electron density can be written as

$$\rho(r) = \sum_i^N \sum_s |\psi_i(r)|^2 \tag{2.19}$$

From the Eq 2.19, the DFT problem can now be expressed as a determinantal problem such that the molecular wavefunction can be expressed as

$$\Psi_s = \frac{1}{\sqrt{N}} \det[\psi_1 \psi_2 \cdots \psi_N] \tag{2.20}$$

It should be noted that these one-electron wavefunctions, $\{\psi\}$, are normalized and orthogonal with each other.

$$\int \psi_i^*(x)\psi_j(x)dx = \delta_{ij} \tag{2.21}$$

At this point, we define the functional $\Omega[\{\psi_i\}]$ as

$$\Omega[\{\psi_i\}] = E[\rho] - \sum_i^N \sum_j^N \varepsilon_{ij} \int \psi_i^*(x)\psi_j(x)dx \tag{2.22}$$

where $E[\rho]$ is the energy functional given as Eq 2.18, ψ is a one-electron wavefunction and ε is the Lagrange multiplier to impose orthogonality within the elements of the set $\{\psi\}$. For $E[\rho]$ to be a minimum, the functional derivative should be zero.

$$\delta\Omega[\{\psi_i\}] = 0 \tag{2.23}$$

This then leads to the Kohn-Sham equations which should be solved iteratively.

$$\hat{h}_{eff}\psi_i = [-\frac{1}{2}\nabla^2 + v_{eff}]\psi_i = \sum_j^N \varepsilon_{ij}\psi_i \tag{2.24}$$

where $\hat{h}_{eff}$ is the one-electron Hamiltonian operator and v_{eff} is the effective potential. The canonical Kohn-Sham equations can be written as Eqs. 2.25, 2.26, and 2.27.

$$[-\frac{1}{2}\nabla^2 + v_{eff}]\psi_i = \varepsilon_i \psi_i \tag{2.25}$$

$$v_{eff}(r) = \int \frac{\rho(r')}{|r-r'|} dr' + v_{xc}(r) \tag{2.26}$$

$$\rho(r) = \sum_{i}^{N} \sum_{s} |\psi_i(r)|^2 \tag{2.27}$$

The total energy can be determined by substituting the electron density to Eq. 2.18 or through the equation below.

$$E = \sum_{i}^{N} \varepsilon_i - \frac{1}{2} \int \frac{\rho(r)\rho(r')}{r-r'} dr dr' + E_{xc}[\rho] - \int v_{xc}(r)\rho(r')dr \tag{2.28}$$

In concept, the density functional theory is an exact theory but the exact form of the exchange correlation functional is unknown. However, in practice, several approximations are called such as Local Density Approximation (LDA) and Generalized Gradient Approximation (GGA) is called to determine the v_{xc} term [7, 10].

Local density approximation existed since the early developmental stages of DFT by Thomas and Fermi. The exchange correlation energy under LDA assumes the form

$$E_{XC}^{LDA}(\rho) = \rho(r)\varepsilon_{xc}(\rho) \tag{2.29}$$

where $\varepsilon_{xc}(\rho)$ is the exchange correlation energy of a uniform electron gas with density ρ. Noticed that Eq. 2.29 is a functional dependent only with electron density at a given radial distance. In comparison, the Generalized Gradient Approximation (GGA) included the topological effect of electron density with explicit dependence on density gradients, that is

$$E_{XC}^{GGA}(\rho, s) = \varepsilon_{XC}^{LDA}(\rho) F_{XC}(s) \tag{2.30}$$

where ε_{XC}^{LDA} is the LDA-based electronic energy. The different variations in GGA-based functionals lie in the form of F_{XC}. It should be noticed that F_{XC} is a function of s which is the reduced gradient of electron density. This takes the form of

$$s = \frac{|\nabla\rho(r)|}{2(3\pi^2)^{\frac{1}{3}}\rho(r)^{\frac{4}{3}}} \tag{2.31}$$

Perhaps, the most widely used GGA functional is the PBE functional which has an F_{XC} given as Eq. 2.32.

$$F_{XC}^{PBE}(x) = 1 + \kappa\left(1 - \frac{1}{1+\frac{x}{\kappa}}\right) \tag{2.32}$$

From the given equation, $x = \mu s^2$, κ and μ are determined to be 0.804, and 0.2195 respectively. These constants are zeroes of the F_{XC} factor as $s \to 0$.

In this section, the fundamentals of DFT are given. Corresponding concepts in wave function theory and DFT are discussed. In this dissertation, three quantum chemical software were utilized; (1) Gaussian09 (Chapter 4), (2) SIESTA 4.0 (Chapter 5), and (3) GPAW 10.0 (Chapter 6). For the purposes of completeness, software used in this study will be briefly discussed. The DFT implementation in Gaussian follows standard computational algorithms. As seen above, DFT calculations can be treated as a special case of Hartree-Fock calculations with which an additional term, E_{XC} is added [5]. In Gaussian, the E_{XC} is solved numerically, that is, the integration is done in a grid space. In the following sections, linear scaling $O(N)$ quantum chemical software packages, SIESTA and GPAW, will be introduced.

2.2 SIESTA: A Highly Localized Atomic Orbital Approach

In Chapter 5, a selective cyclopropanation reaction done under mechanochemical regime is simulated using SIESTA 4.0. SIESTA (Spanish Initiative for Electronic Simulations with Thousands of Atoms) is a linear scaling electronic structure software developed in Spain [6, 11]. Similar to other implementations, Born-Oppenhaimer approximation is employed. This is augmented with a pseudopotential approximation. Under such treatment, the core

electrons are neglected. This assumption is valid as core electrons are chemically inert and do not participate in chemical bond breaking and formation. When a bond breaks during a chemical reaction, the associated electron pair remains in the valence shell and does not affect the core shell electrons. Similarly, electrons associated with a bond formation are those in the outer shell of an atom. This assumption is congruent with the Lewis picture of chemical reactions.

However, core electrons are not without physical function. The main role of core electrons relating to chemical reactivity is nuclear potential screening. As described in the previous section, the DFT Hamiltonian (see Eq 2.3) contains a $\hat{V}_{ne}$ term. For the convenience of the reader, the equation is reiterated here.

$$\hat{H} = \hat{T} + \hat{V}_{ne} + \hat{V}_{ee} = \sum_{i=1}^{N}(-\frac{1}{2}\nabla_i^2) - \sum_{i=1}^{N}\frac{Z_\alpha}{r_{i\alpha}} + \sum_{i<j}^{N}\frac{1}{r_{ij}} \tag{2.33}$$

The core electrons effectively screen the external attractive potential due to the positive charge of the nucleus. Under the pseudopotential approximation, this is alleviated with an effective potential along the core region. Using pseudopotentials in simulations affords less expensive electronic structure calculations since the relevant matrices become exponentially smaller with lesser electrons.

Perhaps, the key feature of SIESTA is the utilization of the localized atomic basis set [6, 11]. In solving the Kohn-Sham equations, the molecular wavefunction is expanded in terms of numerical functions.

As discussed in the previous section, DFT calculations rely on solving the Kohn-Sham equations. The one-particle Kohn-Sham equation can be written as

$$[-\frac{1}{2}\nabla^2 + V_{eff}^{\sigma}(r)]\psi_i^{\sigma}(r) = \varepsilon_i^{\sigma}\psi_i^{\sigma}(r) \tag{2.34}$$

To solve this eigenvalue problem, the eigenvectors are expanded in terms of basis functions that is

$$\psi_i(r) = \sum_{\sigma} c_{i\sigma} f_\alpha(r) \tag{2.35}$$

In Eq 2.35, $f_\alpha(r)$ is the basis function. Traditionally, basis functions can be based on atomic spheres, plane waves, or localized basis sets. SIESTA method utilizes localized atomic spheres as basis functions. The choice of strictly localized atomic basis also affords efficient calculations which effectively reduces CPU time and memory. Aside from numerical efficiency, the choice of localized atomic basis aids in chemical and physical interpretations.

Atomic orbital follows the form

$$\phi_{Ilmn}(r) = R_{Iln}(|\ r_I|)Y_{lm}(\hat{r}_I) \tag{2.36}$$

where $R_{Iln}(|\ r_I|)$ is a radial function contributing to the atomic orbital size, and $Y_{lm}(\hat{r}_I)$ is the spherical harmonics which gives the shape of the orbitals. This takes the form of the equation below

$$Y_{lm}(\theta,\varphi) = \begin{cases} C_{lm}P_l^m(cos\theta)sin(m\varphi) & m \leq 0 \\ C_{lm}P_l^m(cos\theta)cos(m\varphi) & m \geq 0 \end{cases} \tag{2.37}$$

The locality condition in the basis set of SIESTA contributes to the computational efficiency by having smaller matrices. Physically, this translates to a neglect in the interaction beyond a given cutoff. Beyond a certain chosen cut-off, the overlap matrix, and Hamiltonian matrix elements becomes

$$S_{v\mu} = \langle \phi_v | \phi_\mu \rangle = \int dr \phi_v^*(r)\phi_v(r) = 0 \tag{2.38}$$

$$H_{v\mu} = \langle \phi_v | \hat{H} | \phi_\mu \rangle = \int dr \phi_v^*(r)\hat{H}\phi_v(r) = 0 \tag{2.39}$$

In calculations, the cut-off radius can be systematically controlled using PAO.EnergyShift parameter [6, 11]. In SIESTA, the Hamiltonian is a combination of two-center, and three-center matrix elements.

$$\hat{H} = \hat{T} + \hat{V}_{NL} + V_{NA}(r) + \delta V_H(r) + V_{XC}(r) \tag{2.40}$$

The first two terms in Eq. 2.40 corresponds to two-center integrals, while the last three terms correspond to three-center integrals. The two center integrals have the form

$$S_{12}(R) = \langle \psi_1 | \psi_2 \rangle = \int dr \psi_1^*(r) \psi_2(r-R) \tag{2.41}$$

which can be seen as convolution of the two atomic orbitals, ψ_1 and ψ_2, that is

$$f * g = \frac{1}{\sqrt{2\pi}} g(y) f(x-y) dy \tag{2.42}$$

Taking the Fourier transform of one eigenvector ψ in the Eq. 2.41,

$$\psi(k) = \frac{1}{(2\pi)^{\frac{3}{2}}} \int \psi(r) e^{-ik\cdot r} dr \tag{2.43}$$

then the corresponding Fourier transform of Eq. 2.41 is

$$S_{12}(R) = \int dk \psi_1^*(k) \psi_2(k) e^{-ik\cdot R} \tag{2.44}$$

For calculation efficiency, pairs of basis functions are calculated and stored in a radial grid. This then serves as a look-up table for further calculations. Another key component of any DFT calculation is the density matrix. The molecular eigenvector, ψ_i, is expanded using the localized atomic orbitals.

$$\psi_i(r) = \sum_\mu \phi_\mu(r) c_{\mu i} \tag{2.45}$$

where $\phi_\mu(r)$ are the orthogonal basis functions, and $c_{\mu i}$ is the corresponding coefficient.

$$\left\langle \tilde{\phi}_\mu \middle| \phi_v \right\rangle = \delta_{\mu v} \tag{2.46}$$

$$c_{\mu i} = \left\langle \phi_\mu \middle| \psi_i \right\rangle \tag{2.47}$$

The electron density in real space can be written as

$$\rho(r) = \sum_i n_i |\psi_i(r)|^2 \tag{2.48}$$

where n is the occupation of the molecular eigenvector, ψ_i. Expressing this in terms of the basis function, Eq. 2.48 can be rewritten as Eq. 2.49

$$\rho(r) = \sum_{\mu\nu} \rho_{\mu\nu} \phi_\nu^*(r) \phi_\mu^*(r) \tag{2.49}$$

The corresponding matrix elements have the form,

$$\rho_{\mu\nu} = \sum_i c_{\mu i} n_i c_{i\nu} \tag{2.50}$$

This density matrix can then be used to restart calculations. Note that the behavior of this matrix dictates the convergence of a single SCF iteration. After which, neutral atom potential, Eq. 2.51, and exchange correlation potential, Eq. 2.52, are calculated.

$$\delta\rho(r) = \rho(r) - \rho_{atoms}(r) \tag{2.51}$$

$$\rho(r) \rightarrow V_{XC}(r) \tag{2.52}$$

The Hartree potential $V^H(r)$ is calculated via the Poisson equation in real space using fast fourier transform.

$$\delta\rho(r) \xrightarrow{\text{FFT}} \delta V_H(r) \tag{2.53}$$

After determining the required potentials in the KS equation, these grid contributions are combined and integrated in the real space by finite addition which gives Eqs. 2.54 and 2.55, respectively.

$$V(r) = V_{NA}(r) + \delta V_H(r) + V_{XC}(r) \tag{2.54}$$

$$\int \phi_\nu^*(r) V(r) \phi_\nu(r) \approx \sum_i \phi_\nu^*(r) V(r) \phi_\nu(r) \Delta r \tag{2.55}$$

This combination of pseudopotential and pseudoatomic orbital basis, together with real space numerical evaluation of matrix elements, affords SIESTA an O(N) scaling for

electronic calculations. Interestingly, this method is also coined SIESTA [6, 11].

2.3 GPAW: Grid-based Projector Augmented Wave Method

In Chapter 6, the effect of strain on heterogeneous catalysis is explored with another linear scaling software, GPAW. GPAW is the first real space implementation of Projector Augmented Wave (PAW) formalism [3, 4, 9]. In the advent of programming efficiency for the development of new algorithms and workflows, GPAW is implemented mainly using Python. However, it is known that interpreted languages such as Python perform slower in comparison to compiled languages such as FORTRAN and C. To increase calculation efficiency, GPAW utilized the Python package NumPy. NumPy is a C-based extension of Python which allows efficient numerical operations similar to that of compiled languages. C-based extensions for Python are also written in other parts of GPAW code such as the reiterative refinement of the wavefunction in the SCF cycle. Parallelization of GPAW relies in general with MPI, but a hybrid parallelization OpenMP/MPI scheme is also implemented.

The PAW formalism is effectively an all-electron formalism employing a frozen core approximation together with pseudopotentials. The all-electron molecular wavefunction, $\Psi_n(r)$, is obtained as

$$\psi_n(r) = \tilde{T}\,\tilde{\psi}_n(r) \tag{2.56}$$

where the $\tilde{\psi}_n(r)$ is the corresponding smooth pseudomolecular wavefunction, and the $\hat{T}$ is the transformation operator. The transformation operator effectively maps the corresponding pseudomolecular wavefunction to the all-electron molecular wavefunction, and has the following form

$$\tilde{T} = 1 + \sum_a \sum_i \left(|\phi_i^a\rangle - |\tilde{\phi}_i^a\rangle\right)\langle \tilde{p}_i^a| \tag{2.57}$$

Note that beyond a certain cut-off, r_c^a, the partial all-electron wavefunction and the partial smooth pseudowavefunction becomes equivalent that is

$$\phi_i^a(r) = \tilde{\phi}_i^a(r), \qquad |r - R^a| > r_c^a \tag{2.58}$$

and their corresponding contributions to $\hat{T}$ vanishes. In addition to this, the projector functions, $\{\tilde{p}\}$, and the partial smooth pseudowavefunctions, $\{\tilde{\phi}\}$, are orthogonal to each other. Hence, they follow the relation

$$\left\langle \tilde{p}_{i_1}^a \middle| \tilde{\phi}_{i_2}^a \right\rangle = \delta_{i_1 i_2} \tag{2.59}$$

Theoretically, an infinite set of partial pseudowavefunction is needed to completely map the complex all-electron wavefunction. However, in practice, a few basis for each angular momentum is able to accurately describe the all-electron wavefunction.

$$\psi_n = \tilde{\psi}_n + \sum_a (\psi_n^a - \tilde{\psi}_n) \tag{2.60}$$

Under the PAW formalism, the electron density can be expressed as

$$\tilde{n}(r) = \sum_n f_n |\tilde{\psi}_n(r)|^2 + \sum_a \tilde{n}_c^a(|r - R^a|) \tag{2.61}$$

where f_n is the occupation number of the $\tilde{\Psi}_n(r)$. In Eq. 2.61, the first term accounts for the electron density outside the radial cut-off while the second term accounts for the core electron density. In GPAW, electron density is determined in a grid-based two step . A grid-based representation of the previous equation is written as

$$\tilde{n}_G = \sum_n f_n |\tilde{\psi}_{nG}|^2 + \sum_a \tilde{n}_{cG}^a \tag{2.62}$$

The Eq. 2.62 is evaluated in the grid space with h as the grid spacing. In GPAW calculations, h is determined via user input, and should be converged during benchmarking calculations. The definition of h relative to the real space grid points is

$$h_\alpha = \frac{a_\alpha}{N_\alpha} \tag{2.63}$$

where a is the lattice constant along $\alpha \in \{1,2,3\}$ direction, and N is the number of grid points along that direction. The electron density at the coarse grid spacing, $\tilde{n}_G$, is interpolated to a fine grid with twice the number of grid points at each direction using the following equation

$$\tilde{n}_g = \sum_G I_{gG} \tilde{n}_G \tag{2.64}$$

where I_{gG} is the cubic spline fitting coefficients. Finally, the total electron density is given as

$$n_g = \tilde{n}_g + \sum_a \left[n_a(r - R^a) - \tilde{n}_a(r - R^a) \right] \tag{2.65}$$

Following the form of the wavefunction in Eq. 2.60, the electron density can be seen as the combination of the smooth pseudoelectron density as the first term and the correction to the all-electron density as the latter.

To obtain the neutral atom electron density, the compensating nuclear charge should be added to Eq. 2.62, that is

$$\tilde{\rho}(r) = \tilde{n}(r) + \sum_a \tilde{Z}^a(r - R^a) \tag{2.66}$$

Analogously, the grid-based neutral atom electron density expression is

$$\tilde{\rho}_g = \tilde{n}_g + \sum_a \tilde{Z}^a_g \tag{2.67}$$

Using the electron density, potential energy terms of the one-electron Kohn-Sham equation can be evaluated. The Hartree potential, v_H, can be evaluated using the Poisson equation below.

$$\nabla^2 v_H(r) = -4\pi\, \rho(r) \tag{2.68}$$

As the form of electron density resides in the real space grid, the Laplace operator, ∇, is rendered in grid space as well.

$$\nabla^2 f(x) = \sum_{\alpha=1}^{D} \sum^{N} b_\alpha c_n^N f(r + n h_\alpha) + O(h^{2N}) \tag{2.69}$$

The original Poisson equation Eq. 2.68 can be evaluated in grid space using

$$\sum_{g'} C_{gg'} \tilde{v}_{g'}^H = -4\pi \tilde{\rho}_g \tag{2.70}$$

After determining the solution to the one-electron KS equation, electronic energy can easily be determined by addition. The total electronic energy can be calculated as

$$E = \tilde{E} + \sum_a (\tilde{E}^a - \tilde{E}^a) \tag{2.71}$$

As a recurring theme in the PAW formalism, and by extension in GPAW, the electronic energy can be evaluated simply by adding the contribution from the smooth pseudopotential based energy and the corresponding correction for the core shell energy.

$$\begin{aligned} \tilde{E} = & \sum_n f_n \int dr \tilde{\psi}_n^*(r)(-\frac{1}{2}\nabla)\ \tilde{\psi}_n(r) + \frac{1}{2}\int dr \tilde{v}^H(r)\tilde{\rho}(r) \\ & + E_{xc}[\tilde{n}(r)] + \int dr \tilde{n}(r) \sum_a \tilde{v}^a(|r - R^a|) \end{aligned} \tag{2.72}$$

$$\begin{aligned} \tilde{E} = & \sum_n f_n V_c \sum_G \tilde{\psi}_{nG} \sum_{G'} (-\frac{1}{2}\nabla)\ \tilde{\psi}_{nG'} + \frac{1}{2} V_f \sum_f \tilde{v}^H(r)\tilde{\rho}_g \\ & + E_{xc}(\{\tilde{n}_g\}, V_f) + V_g \sum_g \tilde{n}_g \sum_a \tilde{v}_g^a \end{aligned} \tag{2.73}$$

Equations 2.72 and 2.73 correspond to the PS energy in analytical and grid-based discretized forms, respectively.

In GPAW, the finite difference, restriction, and interpolation schemes are done in C extension. Subspace diagonalization is also done in C to avoid large memory required for transient matrices in Python. Using a grid-space formalism , GPAW is able to achieve linear scaling O(N). However, grid-space algorithms require high memory to store intermediate values during calculations.

References

Atkins, P. W. (Peter William) and R. S Friedman (1996). *Molecular quantum mechanics / P.W. Atkins and R.S. Friedman.* eng. 3rd ed. New York: Oxford University Press. ISBN: 0198559488 (cited on pages 28, 31).

Cedillo, Andrés (2007). "Chapter 2 Density functional theory models of reactivity based on an energetic criterion". In: *Theoretical Aspects of Chemical Reactivity*. Edited by Alejandro Toro-Labbé. Volume 19. Theoretical and Computational Chemistry. Elsevier, pages 19–30 (cited on page 31).

Enkovaara, J et al. (June 2010). "Electronic structure calculations with GPAW: a real-space implementation of the projector augmented-wave method". In: *Journal of Physics: Condensed Matter* 22.25, page 253202 (cited on page 39).

Enkovaara, Jussi et al. (2011). "GPAW - massively parallel electronic structure calculations with Python-based software". In: *Procedia Computer Science* 4. Proceedings of the International Conference on Computational Science, ICCS 2011, pages 17–25 (cited on page 39).

Frisch, M. J. et al. (no date). *Gaussian09 Revision E.01*. Gaussian Inc.: Wallingford, CT, 2009 (cited on page 34).

García, Alberto et al. (2020). "Siesta: Recent developments and applications". In: *The Journal of Chemical Physics* 152.20, page 204108 (cited on pages 34–36, 39).

Jensen, Frank (2006). *Introduction to Computational Chemistry*. Hoboken, NJ, USA: John Wiley amp; Sons, Inc. ISBN: 0470011874 (cited on page 33).

Martin, Richard M. (2004). *Electronic Structure: Basic Theory and Practical Methods*. Cambridge University Press (cited on page 29).

Mortensen, J. J., L. B. Hansen, and K. W. Jacobsen (Jan. 2005). "Real-space grid implementation of the projector augmented wave method". In: *Phys. Rev. B* 71 (3), page 035109 (cited on page 39).

Parr, Robert G. and Weitao Yang (1994). *Density-Functional Theory of Atoms and Molecules (International Series of Monographs on Chemistry)*. Oxford University Press, USA. ISBN: 0195092767 (cited on pages 29, 31, 33).

Soler, José M et al. (Mar. 2002). "The SIESTA method forab initioorder-Nmaterials simulation". In: *Journal of Physics: Condensed Matter* 14.11, pages 2745–2779 (cited on pages 34–36, 39).

Szabo, Attila and Neil S. Ostlund (1996). *Modern Quantum Chemistry: Introduction to Advanced Electronic Structure Theory*. First. Mineola: Dover Publications, Inc. (cited on page 27).

III

Mechanochemical Simulation and Tools

3.1 Simulating Molecular Pulling

Atomic Force Microscopy have been used to probe several mechanical behavior of polymers. This technique allowed experimentalists to probe force sensitivity of several mechanophores via pulling experiments. Simulations of such systems can easily be accomplished using several procedures. In general, current calculation techniques can be categorized in two paradigms: (1) geometry constraints based methods and (2) force inclusion based methods.

In this group of methods, the pulling coordinate is selected and a distance constraint is implemented to mimic the pulling.

1S-COGEF

Although geometric constraints have been around for a long time, the method of using geometry constraints to simulate mechanical pulling was initiated by Beyer in 2000 [1]. Under the COGEF (Constrained geometries simulate external force) formalism, a distance coordinate, r, is chosen. The atoms a and b which form the bond r are subjected to distance constraint and then allowed to relax. The force, f, is approximated afterwards, hence the

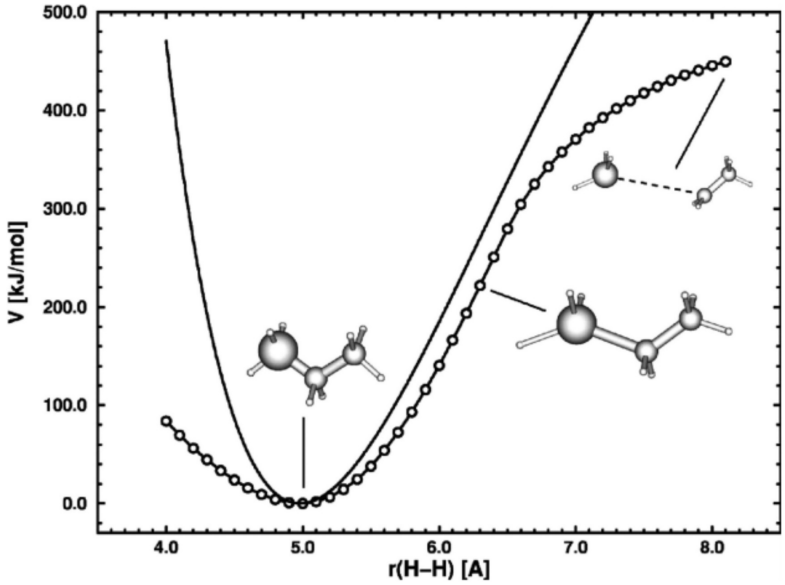

Figure 3.1: COGEF Potential Energy Surface. Reprinted with permission from Ref. [2]. Copyright 2005 American Chemical Society.

effective force applied to the system is determined *a posteriori* to the simulations. Using a different distance r for the bond allows one to simulate the pulling and produce the COGEF potential.

As an application Beyer and colleagues simulated pulling of SiH3CH2H3 using the terminal hydrogen atoms [2]. Figure 3.1 shows the COGEF potential energy surface. The critical r(H-H) distance is the point at which bond breaking happens and corresponds to the inflection point of the PES. It should be pointed out that the abrupt change in force is due to the systemic relaxation of the molecule upon bond breaking.

In such simulation, rupture forces are taken to be the average with respect to elongated bonds. This then translates to an averaging of chemical bonds types as well as local bond environments. Such a physical parameter has an important chemical meaning in which chemical reactions, that is bond breaking and forming, lay upon. As a result, COGEF simulations tend to overestimate bond rupture forces. This is also attributed to the exclusion of finite thermal effects which is a consequence of static simulations.

The main advantage of this formalism lies in the fact that geometry constrained optimization algorithms are readily available to a variety of quantum chemical softwares.

Hence, by extension, renders COGEF formalism available to simulate pulling phenomena.

3S-COGEF

In the advent to improve fidelity to chemistry, the original COGEF has been improved by Krugner and Walter. As discussed above, the original COGEF formalism renders the molecule to be pulled to be a single continuous string stretched along the edges, which leads to the overestimation of rupture forces. In 3S-COGEF, the reaction of concern is studied with standard computational techniques such that reactant, transition state, and product structures are optimized. These constitute the three components of 3S-COGEF which are connected by previously converged minimum energy paths [3]. Furthermore, aside from the total linearized length of the model, the potential energy surface is also expressed in a second molecular parameter corresponding to the bond length of concern. Doing so, the 3S-COGEF shows a dramatic decrease in the predicted bond rupture force requirements. In their original paper, they reported a comparable prediction to explicit force models. Though this improvement is remarkable, underlying assumptions should be understood. The additional parameter b is the bond to be broken which limits the utility of the 3S-COGEF formalism to reactions known to happen due to mechanical pulling experiments. Following this limitation, it is also known that mechanical perturbations do not only move the location of stable manifolds but also the characteristic path. This characteristic path may lead to different reaction mechanisms which the 3S-COGEF does not consider.

In this group of methods, pulling simulations are done by altering the nuclear forces during optimizations. Compared with the previous group of methods, applied forces are defined prior to simulations while changes in the molecular internal coordinates are determined after optimizations.

Force Modified Potential Energy Surface (FMPES)

This formalism is the first explicit treatment of force for mechanochemical application. The Force Modified Potential Energy Surface defines a set of points coined as pulling

points which defines the direction of pulling. The net force on an atom can be calculated as the sum of electronic force and applied force. Consequently, potential as function of force can be written as

$$V_{FMPES}(r,F) = V_{abinitio}(r) + \sum_{i}^{N} F_0(||r_i^{fix} - r_i|| - ||r_i^{fix} - r_i^0||) \tag{3.1}$$

The first term of Eq. 3.1 is the total electronic energy which is the solution to the Schrodinger equation. As dictated by quantum mechanics, this term shows dependence on the atomic coordinates **r**. Under this regime, a constant force, F_0, is applied to selected atoms of the molecule towards a set of fixed points, r_i^{fix}, in the Cartesian space. The second term accounts for the classical work, $w = Fd$, done by the external force to the system. Effectively, this is a multidirectional extension of the Kauzmann-Eyyring model shown in Chapter 1.

Ong and co-workers studied the ring opening of cyclobutene through sonication which is one of the most popular mechanochemically driven reactions [8]. It was previously shown that cyclobutene breaks the Woodward-Hoffman rules under mechanochemical conditions. This shows that mechanochemical activation is different from thermochemical activation and can lead to new and interesting pathways.

Using FMPES formalism, Ong and colleagues showed that force dependence of both the conrotatory and disrotatory ring opening of cyclobutene. The force modified potential energy surface of cyclobutene ring opening is shown as Figure 3.2.

Subramanian and co-workers further developed the previous formalism to account non-constant force functions [12]. As given in Eq. 3.1, the external force acting in the molecule is constant which translates as a linear potential along the applied direction. The Generalized FMPES equation can be written as

$$V_{G-FMPES}(r,s) = V_{abinitio}(r) + \int_{s_i}^{s_f} F_{ext}(s)ds \tag{3.2}$$

It can be noticed that the difference of the two equations is their second term which corrects or modifies the potential energy surface. In the G-FMPES formalism, the external

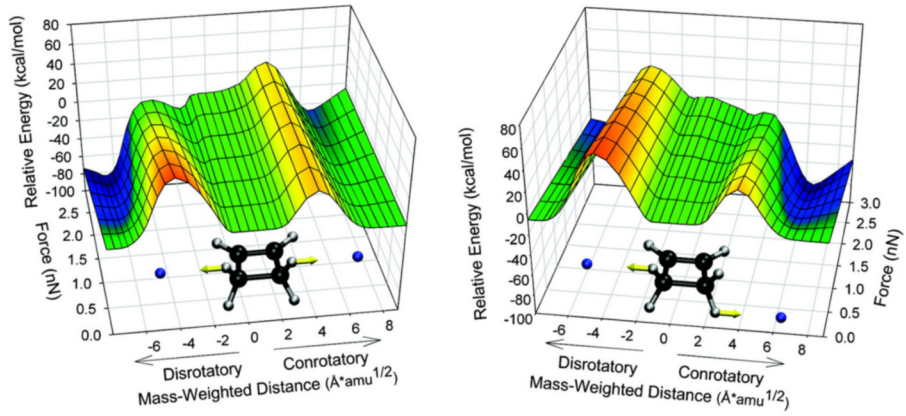

Figure 3.2: Force Modified Potential Energy Surface of cyclobutene ring opening. Reprinted with permission from Ref. [8]. Copyright 2009 American Chemical Society.

force is a function of the distance coordinates. The effect of such a force function can be described by Figure 3.3.

At the condition that the $F_{ext}(s)$ assumes a constant value independent of the distance coordinates, it can be shown that the G-FMPES equation becomes the FMPES equation. Therefore, the G-FMPES is indeed a generalized revision of the same physical treatment for the interaction of chemical systems and applied external force.

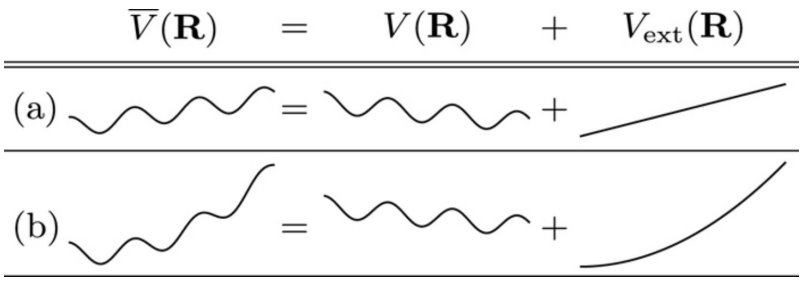

Figure 3.3: Generalized Force Modified Potential Energy Surface Schematic. Reprinted from Ref. [12], with the permission of AIP Publishing.

The versatility of G-FMPES is best demonstrated not by distance dependent force function but rather by the applicability of such formalism to simulate pressure in molecular simulations. Traditional modelling of pressure and its consequent calculation lies on the average forces that a molecule experiences due to the intermolecular interactions and constricted periodic simulation box. G-FMPES treats pressure as an external pushing force

directed toward a point, usually the molecular center, in the molecule.

External Force Explicitly Included (EFEI)

A related treatment of external force during optimizations and dynamics is developed by Ribas-Arino and Marx in 2009 [10]. The EFEI potential function assumes the following form

$$V_{EFEI}(r,F_0) = V_{abinitio}(r) - F_0 q(r) \tag{3.3}$$

It can be seen that FMPES and EFEI potential energy function share the same first term, and a similar second term. The second term of the EFEI depends on the q(r), which is the molecular internal coordinate. Perhaps, one of the advantages of EFEI lies in this internal coordinate dependence. Molecular geometry optimizations are normally done along the internal coordinate space and direct dependence is expected to lessen the numerical instability during the inversion of force matrices. In contrast to FMPES (G-FMPES), the EFEI method is readily available in the Q-Chem package.

Enforced Geometry Optimization (EGO)

Enforced Geometry Optimization (EGO) may be considered as a multiforce-multipoint extension of FMPES. In comparison to the previous formalism, the discussion of Wolinski and Baker is initiated by discussing the separability of the effective Hamiltonian [13].

$$H = H_0 + H_1 = H_0 - \sum_a R_a \cdot F_a \tag{3.4}$$

It should be noted that the solution to the above equation regresses to the potential function similar to that of FMPES. That is the FMPES associated with F_0 is replaced with F_a along a distance coordinate R_a. This translates to a physical model in which variable forces can be manually distributed to the atoms. Upon relaxation or geometry optimizations, these initial forces redistribute throughout the molecule following the Hessian of the potential energy surface.

An extension of EGO(n) was developed by the same group in 2010 [13]. In comparison

to the original EGO(n), EGO(ne) assumes the external forces also affect the electron density of an atom which makes the H_0 and H_1 inseparable. It should be noted that in the previous formalism, electron clouds are not subjected to the external applied force. The distortion of electron clouds can be explained by external force driven displacements in the nucleus and invoking Born-Oppenheimer approximation.

In general the methods discussed in this section simulates only molecular pulling which is only realized using single atom force microscopy. As discussed in previous chapters, mechanochemical methods are not only limited to pulling. In preparative mechanochemical synthesis, the ball milling is the tool of choice on the basis of popularity. The forces in ball-milling are complex and non-trivial in comparison to the single molecule pulling.

Another limitation of these methods is the fact that finite temperature effects which could lead to early rupture events are also not considered in these formalisms. Temperature correction under such formalism can be achieved using condensed phase calculation with sufficient sampling of the chemical ensemble. This is traditionally done using molecular dynamics. Force modification to mimic artificial pulling such as those surveyed above can be combined to a MD engine to have appropriate statistical description of bond breaking phenomena.

For the interested reader, the reviews of Ribas-Arino and Marx and of Stauch and Dreuw are recommended [9, 11].

3.2 ASE and the OpenMechanochem Module

As mentioned earlier, explicit addition of external mechanical forces during geometry optimization procedure is generally not available to common quantum chemical packages such as Gaussian, GPAW, Quantum Espresso, Siesta, etc. With the exemption of the Q-Chem package (v4.3 or higher), previously discussed methods can only be done by in-house versions of their choice of QM packages which incorporate the additional forces in the atom center. In the advent of paving the road for further mechanochemical simulations, an original python based package, OpenMechanochem, is developed. This module is

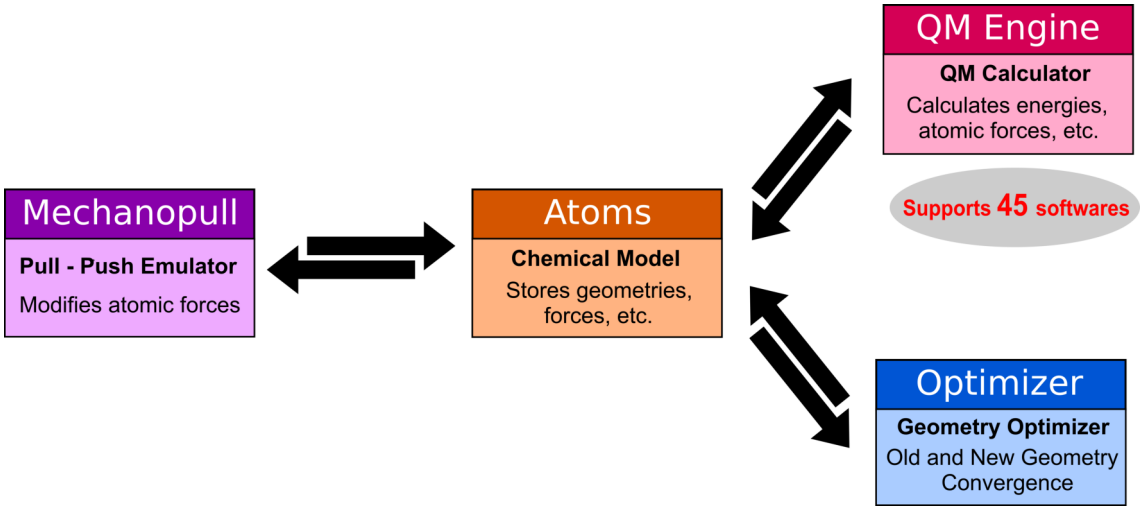

Figure 3.4: Data Exchange Flowchart in ASE

designed to work with the Atomic Simulation Environment (ASE) which can be easily connected to various quantum chemical software packages [6]. Since ASE is a Python based simulation environment, it follows an object-oriented programming paradigm. The data exchange between several ASE objects is summarized as a flowchart and is given as Figure 3.4.

As seen in the figure above, central to any simulations using ASE is the Atoms object. Atoms object contains details of the chemical model. That is, it summarizes Cartesian geometry, energy, atomic forces in a JSON format. This also contains periodic boundary conditions, cell size, stress tensor and higher derivatives such as polarizability. Additionally, user defined tags can be used to subset a complex model structure which can be utilized for QM/MM calculations, automation and/or visualization purposes.

Another important object in simulating using ASE is the Calculator object. The Calculator object contains the type of quantum chemical software or molecular mechanics software to be used in the simulations. It also determines the calculation parameters unique to the software of choice.

An example of such calculation parameters is given for GPAW in the figure below

```
calc = GPAW(xc='PBE',
            mode=PW(700),
            h=0.2,
            kpts=(4, 4, 4),
            txt='GPAW.txt')
```

From the given example above, a GPAW calculator object is set to a variable named calc [4, 5, 7]. In this case, GPAW parameterization sets the exchange correlation functional to the popular GGA based PBE functional. Augmentation of wave functions will be based on plane waves with a cut of 700 Ry. The real space grid parameter h is set to 0.2. Monkhorst-Pack k sampling is 4x4x4 in the simulation cell. Note that details of the simulation cell are not stored in the calculator object. Scratch output file is named GPAW.txt. Other parameters which are not explicitly defined during instantiation are taken to be the default value. This is not only the case for GPAW but also for other quantum chemistry calculators available to ASE suite.

At this point, a single point energy calculation can readily be done and parameters such as energy and its derivatives can be determined. However, such calculations offer minimal chemical meaning. It is imperative that the structure is optimized either to a minima or maxima, corresponding to equilibrium and transition state structures, respectively. To do so, separate ASE objects are available. An optimizer object is dedicated to optimized structures to a minimum using common algorithms such as BFGS, GPMin, MDMin and FIRE are readily available. To determine the transition state geometries, three unique modules are available. Dimer, NEB, and String modules implement the dimer method, nudged elastic band and its variations, and the string method, respectively. Python objects derived from these modules communicate with the atoms object to obtain previous geometry and derivatives. Additionally, these objects also provide the new geometry to be calculated by the calculator object.

The OpenMechanochem module can produce two types of python objects, LinearPull and WallPot. Both of which inherit from the original ASE atoms object. Hence, it contains both geometric coordinates and atomic forces of the current molecular geometry. Common to both objects is that these objects calculate the external forces to be added to the atomic forces derived from the quantum chemical calculator.

The LinearPull object mimics a single atom pulling. Currently, three formalisms are implemented under this; (1) FMPES, (2) EFEI, and (3) EGO. This naming is followed

as the method argument in the LinearPull object. As these theories have been discussed previously, only the object implementations will be discussed. Note that all formalism needs to be provided with an explicit applied force using the pullforce key.

Under FMPES mode, the object instance further requires two lists of length equal to 2, corresponding to pulling points (pp) and applied points (ap). The ap set is defined using the atomic index of the original atoms object. While the pp set is defined using a list of three elements corresponding to the Cartesian coordinates of the pulling points.

In EFEI mode, the pulling coordinate is a bond coordinate of the chemical system which can be defined as any set of two atoms. This is provided for the LinearPull object using the ap keyword. Similar to the FMPES, the ap set is defined by an atomic index list with respect to the atoms object.

The EGO formalism can be thought of as a multidirectional extension of the EFEI formalism. That said, the implementation calls for a list of lists with inner lists being the same as an app set. The total force indicated in the pullforce key is divided by the total number of bond coordinates to be pulled, which is the length of the 2D list required by the EGO mode.

On the other hand, the WallPot object provides an imaginary constraining wall that interacts with the chemical system via a specified potential function. The wall is an imaginary plane calculated using the three point formula. The WallPot object determines the equation of the plane using the Cartesian coordinates of three atoms provided by the user with the plane keyword. The calculated plane can then be displaced by a certain distance along the z direction using the height keyword.

Current implementations include four different types of potential functions, (1) linear, (2) inverse, (3) lennard-jones, and (4) $1/r^6$ potentials. Similar to the OpenMechanochem object, WallPot object adds forces on atoms to mimic the constraints. Hence, the energy is corrected afterwards using a classical work function.

The forces to be added are evaluated using the derivative of the potential function selected by the user. The magnitude of the force can be scaled using the force key, which

is done by multiplying the constant with the derivative. For the Lennard-Jones potential, additional parameters are needed which can be provided by the user using the params key. The params key call for a list of length 2 which is the epsilon and sigma, respectively.

In this tutorial, we will use FMPES and EFEI formalism to pull hydrogen molecules along the bond coordinate.

The OpenMechanochem classes LinearPull, and WallPot inherit from the ASE atoms object and hence an Atoms instance is required. As discussed previously, the OpenMechanochem module is designed to work with ASE objects. To start the simulations, we load necessary python and ASE modules.

```
from ase import Atoms
from ase.io import read
from ase.optimize import BFGS
from ase.calculators.emt import EMT
```

In the code block above, Atoms, read, BFGS, and EMT classes are loaded. An Atoms instance produces the molecule. Read function allows the user to read several types of molecule objects such as xyz, csf, cube files, among others. In this sample code, the geometry will be optimized to minimum using Broyden–Fletcher–Goldfarb–Shanno(BFGS) algorithm and hence the corresponding Optimizer class is preloaded. In ASE, Effective Medium Theory (EMT) based quantum chemical calculator is available. EMT calculator is a simple and efficient calculator which has atom specific parameterization. In ASE, EMT calculator is included for demonstration and code testing, which makes it an appropriate calculator engine for our case.

```
import numpy as np
import OpenMechanochem as mc
```

At this point, numpy and OpenMechanochem modules are loaded and aliased as np and mc, respectively. Following this, an Atoms object named mol wherein details from the hydrogen.xyz were loaded.

```
mol = read('hydrogen.xyz')
```

```
2
Hydrogen
 H                          0.000   0.000   0.000
 H                          0.000   0.000   1.000
```

Users should provide specific keyword arguments for the LinearPull object which would depend on the method key. As stated earlier the OpenMechanochem classes inherits from Atoms object and accepts similar parameters such as calculator, pbc, etc. Using FMPES, the required parameters are pulling points, applied points and applied forces . This can be done by using the keywords pp, ap, and pullforce, respectively. In FMPES, the relative Cartesian coordinates of pulling points and applied points are of utmost importance. For example, a system described below where H0 and H1 are hydrogen atoms pulled towards points A and B, respectively.

```
          A <---   H0   ------- H1    --->     B
```

would have the following pp and ap arguments

```
PullPoints = [[0.000,  0.000, -2.000],    #  Point  A
              [0.000,  0.000,  3.000]]    #  Point  B

AppPoints   = [0,1]
```

Care should be given that the positions in pp and ap lists correspond with each other. That is, the first list in the pp list is the direction where the atom with index as the first element of the ap list is pulled to. The code below submits the object mol as an argument of the LinearPull object named pull.

```
pull = mc.LinearPull(mol)
```

At this point, we will prepare a series of mechanopulling runs with increasing applied force along the hydrogen bond coordinate inside a for loop.

```
for i in np.linspace(0,10,21):
    force = i
    pull.set_params(method='FMPES',
                            pp=PullPoint,
                            ap=AppPoints,
                            pullforce = force)
    pull.set_calculator(EMT())
    dyn = BFGS(pull,
                       trajectory  ='Hydrogen_{}nN.traj'.format(force))
    dyn.run(fmax=0.05)
```

The magnitude of the applied force can be controlled using the pullforce key which was naturally chosen as the iterator of the loop. Note that the force provided should be in atomic units and the pullforce is divided in the two force vectors equally.

In comparison to FMPES, the EFEI pulls along the internal molecular coordinates. Using this method, the pulling coordinate can be defined using only the applied points and pullforce.

```
pull.set_params(method='EFEI', ap=AppPoints, pullforce = force)
```

which pulls away the hydrogen molecule as

```
      H0 <--------> H1
```

The ap list is same as the FMPES case above, which is

```
AppPoints    = [0,1]
```

Similar to FMPES mode, the pull force is divided equally to the two atoms given by the ap list.

After parameterization of the LinearPull class, geometry optimization or molecular dynamics can be done. An example is given below for a BFGS optimization to a minima with a force tolerance of 0.05 $eV/bohr$.

```
pull.set_calculator(EMT())
dyn = BFGS(pull, trajectory='optimization.traj')
dyn.run(fmax=0.05)
```

Molecular dynamics can be done similarly. Users are suggested to visit ASE documentations for descriptions of parameters needed for MD and optimizations.

Similar to the LinearPull class, the WallPot inherits from the atoms class. Hence, a prior instance of atoms should be provided.

```
wall = mc.WallPotential(slab)
```

The WallPot class takes the parameters method, plane, height, and wallforce.

```
wall.set_params(method='linear', plane=atomplane , height=10,
    wallforce=force)
```

Method defines the type of interacting potential with the wall. The plane is a list of len(3) corresponding to atom indices which defines the equation of the plane. The imaginary plane can then be displaced along the z direction with a height key. Similar to the LinearPull class, the magnitude of force can be controlled by the wallforce key.

```
wall.set_calculator(EMT())
dyn = BFGS(wall, trajectory='optimization.traj')
dyn.run(fmax=0.05)
```

Optimization and dynamics are also supported using the WallPotential class.

References

Beyer, Martin K (2000). “The mechanical strength of a covalent bond calculated by density functional theory”. In: *J. Chem. Phys.* 112.17, pages 7307–7312 (cited on page 49).

Beyer, Martin K. and Hauke Clausen-Schaumann (2005). “Mechanochemistry: The mechanical activation of covalent bonds”. In: *Chem. Rev.* 105.8, pages 2921–2948 (cited on page 50).

Brügner, Oliver and Michael Walter (Nov. 2018). “Temperature and loading rate dependent rupture forces from universal paths in mechanochemistry”. In: *Phys. Rev. Materials* 2 (11), page 113603 (cited on page 51).

Enkovaara, J et al. (June 2010). “Electronic structure calculations with GPAW: a real-space implementation of the projector augmented-wave method”. In: *Journal of Physics: Condensed Matter* 22.25, page 253202 (cited on page 57).

Enkovaara, Jussi et al. (2011). “GPAW - massively parallel electronic structure calculations with Python-based software”. In: *Procedia Computer Science* 4. Proceedings of the International Conference on Computational Science, ICCS 2011, pages 17–25 (cited on page 57).

Larsen, Ask Hjorth et al. (June 2017). “The atomic simulation environment—a Python library for working with atoms”. In: *Journal of Physics: Condensed Matter* 29.27, page 273002 (cited on page 56).

Mortensen, J. J., L. B. Hansen, and K. W. Jacobsen (Jan. 2005). “Real-space grid implementation of the projector augmented wave method”. In: *Phys. Rev. B* 71 (3), page 035109 (cited on page 57).

Ong, Mitchell T. et al. (2009). “First principles dynamics and minimum energy pathways for mechanochemical ring opening of cyclobutene”. In: *J. Am. Chem. Soc.* 131.18, pages 6377–6379 (cited on pages 52, 53).

Ribas-Arino, Jordi and Dominik Marx (2012). “Covalent mechanochemistry: Theoretical concepts and computational tools with applications to molecular nanomechanics”. In: *Chem. Rev.* 112.10, pages 5412–5487 (cited on page 55).

Ribas-Arino, Jordi, Motoyuki Shiga, and Dominik Marx (2009). “Understanding covalent mechanochemistry”. In: *Angew. Chem., Int. Ed.* 48.23, pages 4190–4193 (cited on page 54).

Stauch, Tim and Andreas Dreuw (2016). “Advances in quantum mechanochemistry: electronic structure methods and force analysis”. In: *Chem. Rev.* 116.22, pages 14137–14180 (cited on page 55).

Subramanian, Gopinath, Nithin Mathew, and Jeff Leiding (2015). “A generalized force-modified potential energy surface for mechanochemical simulations”. In: *J. Chem. Phys.* 143.13, page 134109 (cited on pages 52, 53).

Wolinski, Krzysztof and Jon Baker (2009). “Theoretical predictions of enforced structural changes in molecules”. In: *Mol. Phys.* 107.22, pages 2403–2417 (cited on page 54).

IV Changing Reactivity with Molecular Pulling

On the Electronic Structure Origin of Mechanochemically Induced Selectivity in Acid Catalyzed Chitin Hydrolysis

On the Electronic Structure Origin of Mechanochemical Induced Selectivity in Acid Catalyzed Chtin Hydrolysis

Abstract

Recently, mechanical ball milling was applied to chitin depolymerization. The mechanical activation afforded higher selectivity toward glycosidic bond cleavage over amide bond breakage. Hence, the bioactive *N*-acetylglucosamine (GlcNAc) monomer was preferentially produced over glucosamine. In this regard, the force-dependent mechanochemical activation–deactivation process in the relaxed and pulled GlcNAc dimer undergoing deacetylation and depolymerization reactions was studied. For the relaxed case, the activation energies of the rate-determining steps (RDS) proved that the two reactions could occur simultaneously. Mechanical forces associated with ball-milling was approximated with linear pulling and was introduced explicitly in the RDS of both reactions through force modified potential energy surfaces (FMPES) formalism. In general, as the applied pulling force increases, the activation energy of the RDS of deacetylation shows no meaningful change, while that of depolymerization decreases. This result is consistent with the selectivity exhibited in the experiment. Energy and structural analyses for the depolymerization showed that the activation can be attributed to a significant change in the glycosidic dihedral at the eactant state. A lone pair of the neighboring pyranose ring O adopts a *syn*-periplanar conformation relative to the glycosidic bond. This promotes electron donation to the σ^*-orbital of the glycosidic bond, leading to activation. Consequently, the Brønsted–Lowry basicity of the glycosidic oxygen also increases, which can facilitate acid catalysis.

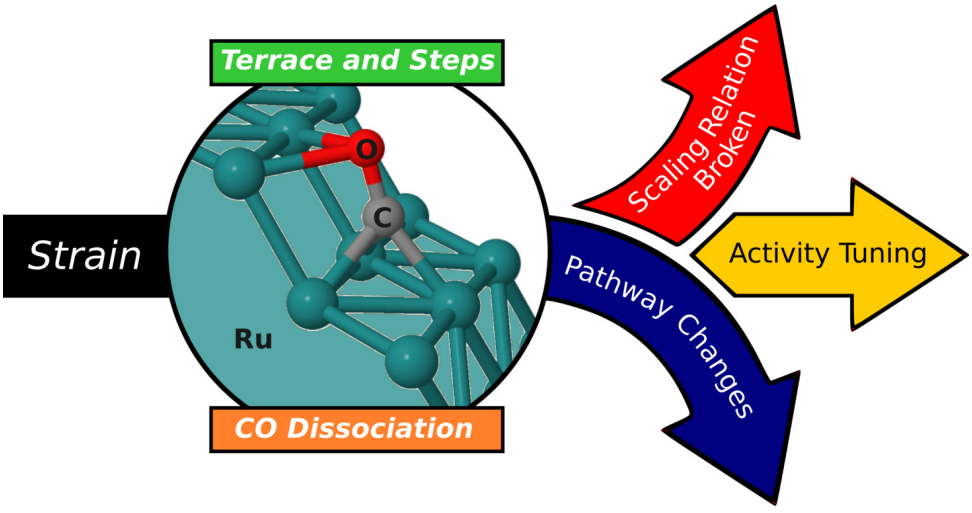

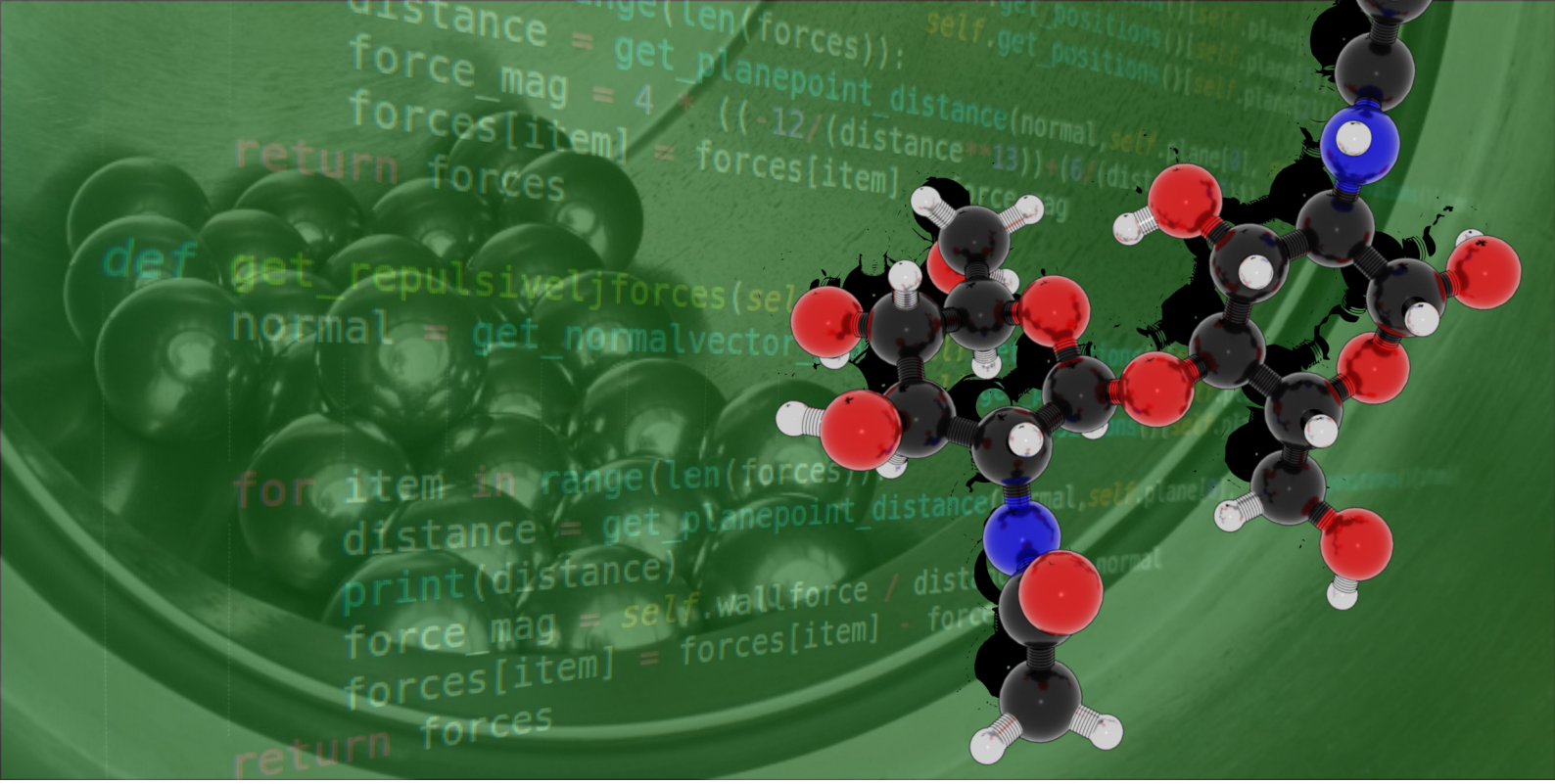

4.1 Introduction

Chitin , one of the abundant naturally available carbohydrates, is a polymer of *N*-acetylglucos -amine linked by β-glycosidic linkages. The said biopolymer is conventionally derived from the base digestion of the exoskeleton of arthropods, such as crabs and shrimps [18, 30], followed by deproteination using alkaline proteases and proteolytic bacteria [1, 16, 45].

The chitin monomer, *N*-acetylglucosamine, is typically obtained via acid hydrolysis of the polymer. Unfortunately, the acid-catalyzed hydrolysis of chitin produces two major products: *N*-acetylglucosamine and glucosamine [11]. Glucosamine results from *N*-deacetylation during the depolymerization.

The structures of chitin, *N*-acetylglucosamine and glucosamine are shown in Figure 4.1. Of the two possible products, *N*-acetylglucosamine is of higher value in comparison to glucosamine. The value of *N*-acetylglucosamine lies to its diverse utility. It has been used as a starting material in the synthesis of N-containing compounds [8]. Furthermore, *N*-acetylglucosamine is a bioactive molecule that plays a role in cell signaling [20]. The

pharmacological activities of this molecule have also been proven, including inflammation inhibition activity and a potential anti-cancer activity [36, 41]. Hence, selective depolymerization is desired for industrial purposes. In conventional processes, a high concentration of acid catalyst is employed to achieve a significant selectivity toward the desired *N*-acetylglucosamine product which produces high acid wastes.

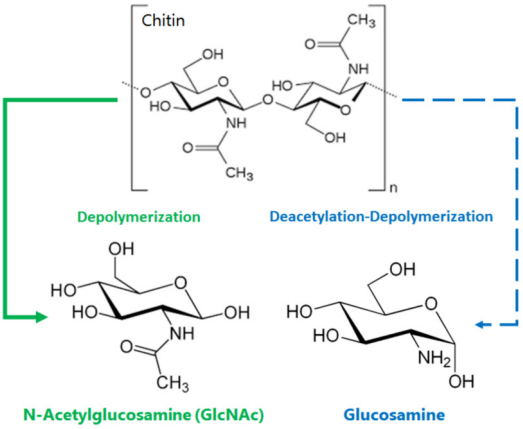

Figure 4.1: Possible chitin hydrolysis products. Glucosamine is derived from the hydrolysis of the acetyl group. *N*-acetylglucosamine is obtained by the hydrolysis of the glycosidic bond.

Recently, ball milling was employed to acid-impregnated chitin to increase the selectivity toward depolymerization [43]. This process afforded the desired selectivity with significantly low acid catalyst requirement. A theoretical study on mechanochemical activation of lignin was investigated by East and colleagues. [29] Ball milling is a preparative grinding technique which falls under the mechanochemical paradigm. Mechanochemistry can be defined as the interaction of external mechanical forces with a chemical system. An in-depth review on the theoretical aspects of mechanochemistry was written by Marx and Ribas-Arino [34], and more recently, by Stauch and Dreuw [37]. In comparison to the different modes of activation, such as the thermochemical activation and photochemical activation, mechanochemistry activates chemical reactions using a force vector. A typical example is single-molecule force-mediated activation in atomic force microscopy (AFM) experiments [5, 9, 37]. As this technique allows a specific part of the atom to be pulled in a specific direction, the translation in the computational approach is direct and intuitive. In

comparison, techniques such as ball milling, apply forces in a random fashion. Friction, compression, and shearing are also associated with ball milling. In addition to these, the impact of the ball is expected to increase temperature for minute instance. Therefore, an exact quantum chemical simulation has not been conducted.

Several fundamental methods have been developed to calculate the potential energy surface under an external force, such as COGEF (constrained geometries simulate external force) [4], FMPES (force-modified potential energy surface) [28, 39], EFEI (external force explicitly included) [35], and EGO (enforced geometry optimization) [42]. However, the complexity of simulating ball milling experiments hindered mechanistic calculations for related phenomena. A fundamental chemical understanding of this phenomenon is necessary to guide the further development of related processes. In this regard, the effect of ball milling on chitin hydrolysis reactions has been studied via theoretical simulations. This work is focused on the electronic structure understanding of the mechanochemical causality of selectivity in acid-catalyzed chitin hydrolysis under an external force. Furthermore, this work offers a simplified approach to treating forces for ball milling simulations.

4.2 Computational Methodology

Density functional theory (DFT) calculations were conducted to investigate the depolymerization selectivity afforded by ball milling in competing chitin hydrolysis reactions. B3LYP was selected as the exchange-correlation functional [3]. All calculations were carried using 6-311G(d,p) basis sets [44]. The chitin dimer was modeled using a *N*-acetylglucosamine (GlcNAc) dimer. The solvation model used in this study is a mix of implicit and explicit water environments. This mixed model was successfully applied to calculate the potential energy surface of the acid-catalyzed hydrolysis of cellobiose [10]. A total of 15 water molecules was introduced around the GlcNAc dimer. In addition, a polarizable continuum model (PCM) [6, 26, 27] with the dielectric constant of water (78.3553) was used. To simulate the acidic environment in the experiments, a singly protonated system (+1) was adopted.

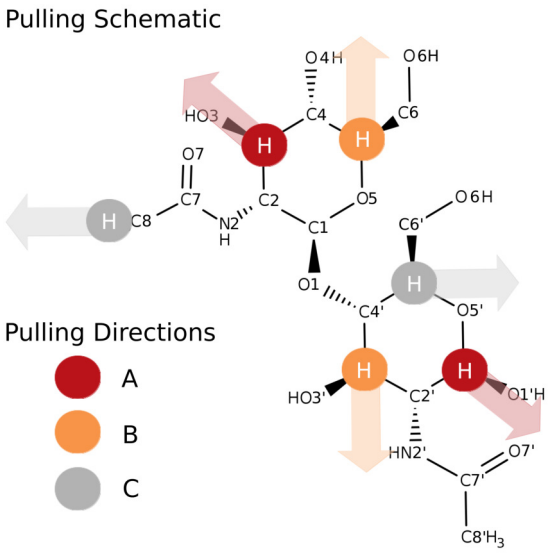

Figure 4.2: Three sets (A,B, and C) of the pulling directions (arrows) and pulling points (circles) in the model structure

The depolymerization and deacetylation reaction mechanisms were examined stepwise. Potential energy profiles were calculated with the computational setting described above. Transition states were verified using frequency and intrinsic reaction coordinate calculations [14]. Natural population analysis was utilized for partial charge determinations. Donor–acceptor orbital interactions were analyzed using second-order perturbation theory analysis of the Fock matrix in the natural bonding orbital (NBO) basis [7, 12, 15, 31, 32, 33].

The mechanical forces applied by ball milling were simulated using explicit addition of pulling forces to selected atoms in the dimer through the force modified potential energy surface (FMPES) formalism [28]. The multi-directional forces associated with the impact of the ball were simplified to linear pulling. That is, a single effective resultant vector can be derived from the variety of mechanical forces experienced by molecules due to ball milling. The forces given by the ball with respect to the molecular plane can be considered as coplanar or non-coplanar. The non-coplanar forces can be attributed to mainly break and reform interchain hydrogen bonding which can result to amorphization in experiments [25]. Coplanar forces would exist as a set of radially outward vector from point of impact as shown in Figure S1. Since these vectors are additive, there exist a resultant linear vector

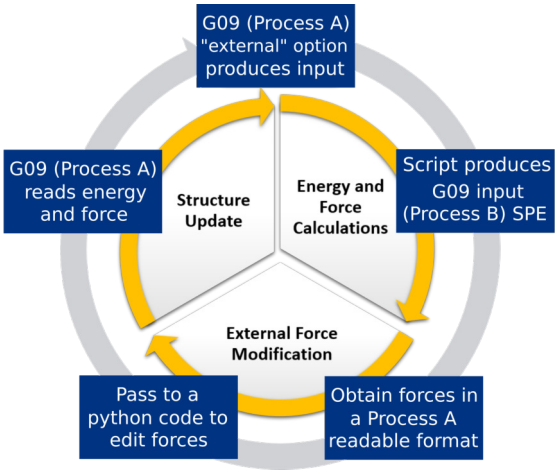

Figure 4.3: Force modification algorithm. SPE means single point energy calculation

passing through the molecular model. Hence, linear pulling can approximate ball milling. In this study, three pulling coordinates were sampled in the rate-determining steps (RDS) of the competing hydrolysis reactions. The pulling scheme is illustrated in Figure 4.2. Pulling direction A is along the glycosidic linkage of the polymer chain, Pulling Direction B samples with a direction force vector which is non-parallel to both hydrolyzable groups, while Pulling Direction C includes the hydrolyzable acetyl group, which captures the effect of other pulling coordinates concerning the elongation of C-N bond in the RDS of the deacetylation reaction. In all cases, hydrogen atoms were pulled because of the stability of C-H bond against pulling. It was observed that in the limits of the sampled force magnitude and directions, the pulled hydrogen atoms remained intact and were not broken in a purely mechanical manner; hence, the application of forces in C-H bonds to study depolymerization and deacetylation is a justifiable approach.

To introduce the pulling forces during geometry optimizations, the Gaussian 09 [13] optimization cycle was modified. This in-house version executes the algorithm given in Figure 4.3 using the External function of G09. Process A is the parent G09 process and determines the progression of the geometry optimizations. Process B is the daughter G09 process and serves as an external quantum chemical calculator for atomic forces and energies. Before process B passes atomic coordinates, energy, and forces to process A, an external force is added to the force of the pulling points by a python code. The addition

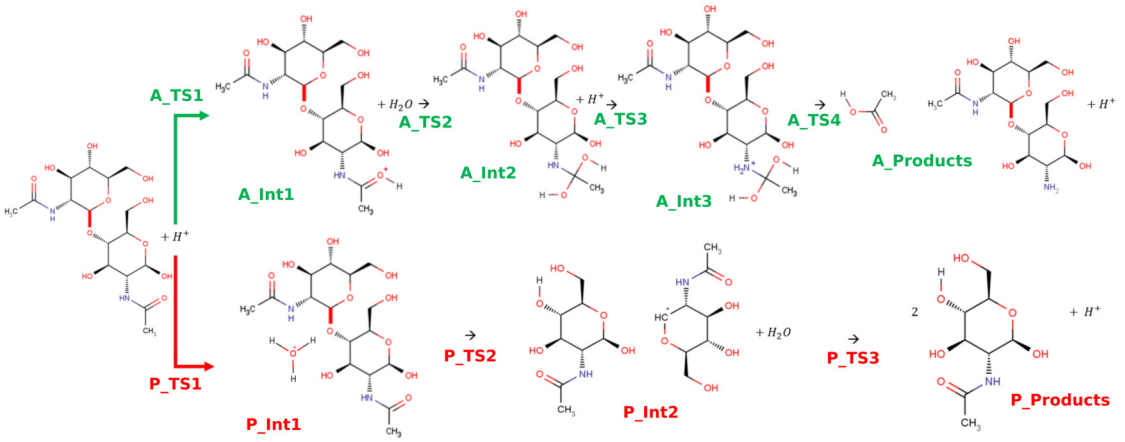

Figure 4.4: Acid-catalyzed deacetylation (green) and depolymerization (red) reaction mechanisms. (A - deacetylation, P - depolymerization, Int - intermediate and TS - transition state)

of an external force vector to the calculated nuclear atomic force components effectively includes the effect of pulling along the selected directions. A more detailed description of the FMPES implementation is included in .

4.3 Results and Discussion

There are two possible hydrolysis reactions of chitin, both of which can be catalyzed by an acid: (1) deacetylation and (2) depolymerization. The mechanisms of these two reactions are illustrated in Figure 4.4.

Deacetylation starts with the protonation of the carbonyl oxygen, which increases the positive charge of the carbonyl carbon (A_Int1). This is followed by a nucleophilic attack of water (A_Int2). It was found that the incoming water molecule simultaneously loses a proton, which was also determined by Zahn and co-workers in another theoretical study [46, 47]. Proton transfer to the amide nitrogen follows (A_Int3), after which acetic acid is dissociated (A_Products).

Depolymerization is led by the hydrolysis of the glycosidic bond. This is initiated by the protonation of the glycosidic oxygen, which simultaneously breaks the glycosidic bond producing a carbocation (P_Int2) [22]. To complete the reaction, a solvent water molecule

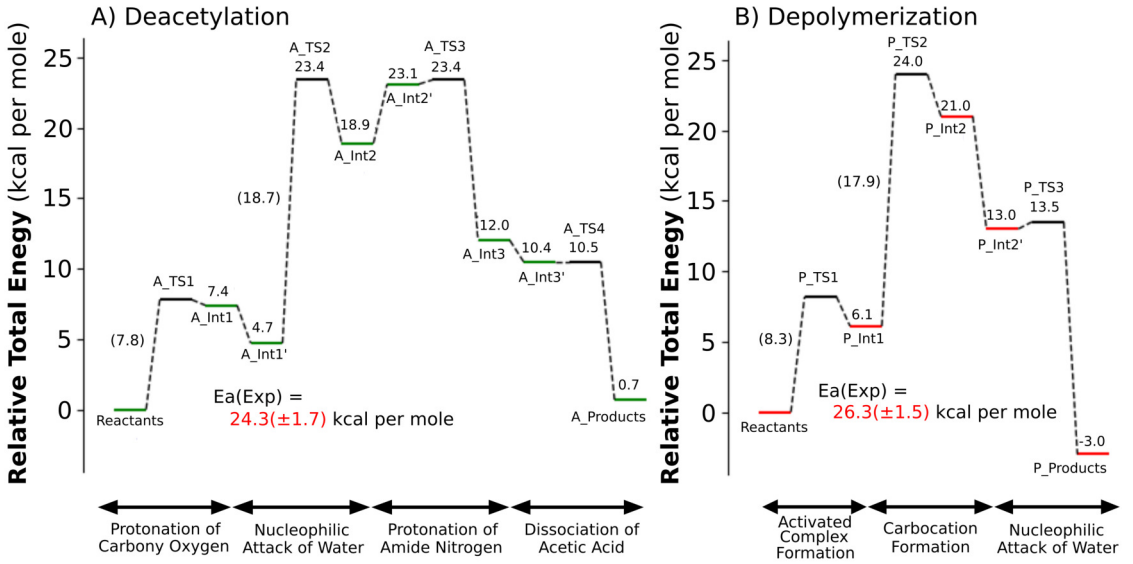

Figure 4.5: Reaction mechanism energy diagrams of (A) deacetylation and (B) depolymerization. Activation energies are shown in parentheses.

attacks the carbocation to form two GlcNAc products (P_Products).

The energy diagrams for the deacetylation and depolymerization are shown in Figure 4.5. The RDSs were determined as the elementary reaction step with the highest energy requirement. For the deacetylation reaction, the nucleophilic attack of water was determined to be the RDS with an activation energy (E_a) of 18.7 kcal·mol^{-1}. Conversely, the formation of the carbocation was considered as the RDS of the depolymerization reaction with an E_a of 17.9 kcal·mol^{-1}. In the experiments, these steps were also determined as the RDSs of the respective reactions. The calculated values are comparable to the experimental activation energies which were 24.3($\pm$1.7) kcal·mol^{-1}, and 26.3($\pm$1.5) kcal·mol^{-1}, respectively [11]. The relative energies of A_TS2 (23.4 kcal·mol^{-1}) and P_TS2 (24.0 kcal·mol^{-1}) could be regarded as apparent activation energies. These values are close to the experimental ones. As revealed by the calculated E_as of the corresponding RDSs, the two reactions could occur simultaneously due to the similar barrier heights. The results also correspond to the experimental results, indicating the loss of the high value product which is *N*-acetylglucosamine. The optimized structures for the RDS of the depolymerization and deacetylation are included in Appendix A.

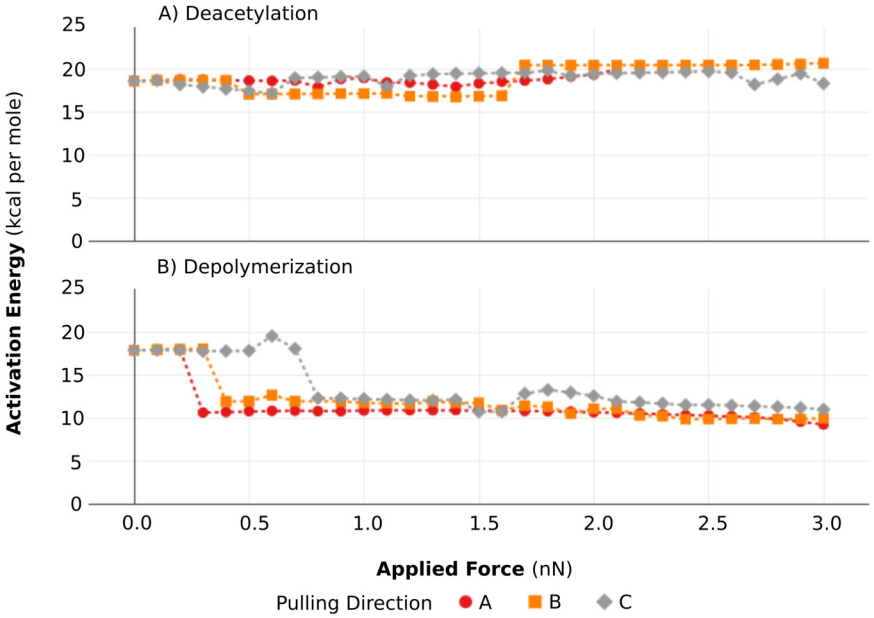

Figure 4.6: E_a progression of GlcNAc (A) deacetylation and (B) depolymerization as a function of the applied force

The force modification algorithm was used to determine the optimized structures of the reactants and transition states in the RDSs of the deacetylation and depolymerization reactions. From the calculated $E_a s$ in FMPES, a sudden drop in E_a by 8 kcal·mol^{-1} was observed in the depolymerization, as shown in Figure 4.6, which suggests that the mechanochemical perturbation activated the depolymerization reaction. The effect of the pulling directions was manifested with the difference in the required force to induce the activation. The direction dependence of mechanochemical activation has been studied and proven in several experimental and theoretical studies [2, 23, 38]. In addition to activation, it was also proven that it is possible to deactivate a reaction coordinate by controlling the direction of the force vector [21]. The importance of the direction in this case is minor as the three directions all resulted in the activation of the reaction. In contrast, no characteristic change was observed in the $E_a s$ of the deacetylation RDS with the introduction of pulling forces. Hence, the deacetylation was found to be unsusceptible to the effect of mechanical pulling in these directions within the range of the applied pulling force. The selected force modified structures are appended in Appendix A.

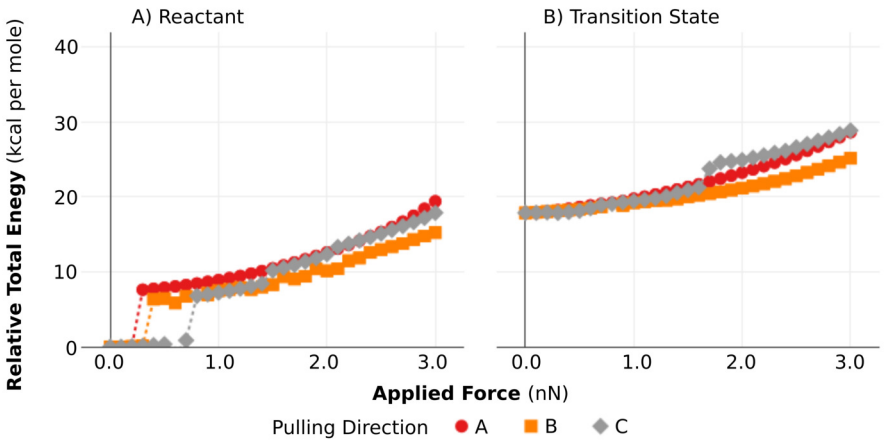

Figure 4.7: Relative energies of the depolymerization (A) reactant and (B) transition state as a function of the applied force

Notably, the induced difference in E_as also follows the experimentally observed results, that mechanical activation leads to depolymerization selective hydrolysis [43]. To determine the origin of the sudden decrease in the activation energy of depolymerization, the energy changes of the reactant and transition states were compared. From Figure 4.7, it is evident that the depolymerization activation can be attributed to the reactant state destabilization. At the applied force of 0.3–0.8 nN, the energy of the reactant state became unstable discontinuously by approximately 6–8 kcal·mol^{-1}, while no such change was found in the transition state.

As the molecular geometric configuration dictates the energy, it is necessary to investigate the structural changes with respect to the relative energy along with the applied forces. To study the effect of the force in the location of the global minima in the hypersurfaces, root mean square displacements (RMSD) was chosen to quantitatively depict the structural progressions. The RMSD calculations were performed to compare two structures, X and Y, with different applied forces, x and y, respectively. X and Y can denote the reactant and transition states. The RMSD is defined as

$$RMSD = \sqrt{\frac{1}{N_{atom}} \sum^{N} |\Delta|^2} \tag{4.1}$$

where $\Delta = \mathbf{R}_{X,x} - \mathbf{R}_{Y,y}$. $\mathbf{R}_{X,x}$ and $\mathbf{R}_{Y,y}$ are the atomic coordinates and N_{atom} is the number of atoms included in the system. The RMSD is minimized by maximizing the overlap of the X and Y structures. This analysis visualizes the structure changes between the reactant states, transition states, and reactant-transition states with different applied forces, which is useful for determining the divergence or convergence of the two states as the applied force increases.

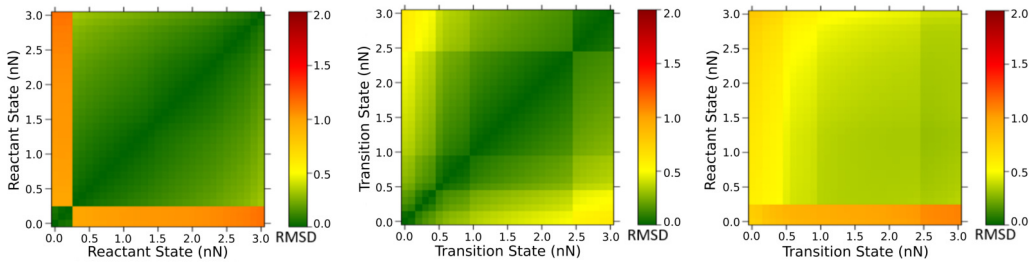

(a) (b) (c)

Figure 4.8: Depolymerization RMSD matrices for pulling direction A for (a) reactant–reactant (b) transition state–transition state and (c) reactant–transition state comparisons

The RMSD matrix in Figure 4.8(a) shows the structural deviation among the reactant states with different external forces. A striking color change was observed at an applied force of 0.3 nN, which indicates the abrupt change in the structure of the reactant state at an applied force of 0.3 nN. In contrast, Figure 4.8(b) shows the gradual change in the transition state structure with an increase in the applied force. These matrices reflected the energy changes in pulling direction A (Figure 4.7). Figure 4.8(c) summarizes the similarity between the reactant and transition state at different applied forces. It can be seen that the reactant structure approaches the transition state structure. The horizontal rectangular orange region below 0.3 nN shows that the structures of the reactant states are less similar to those of the transition states at any applied force. In contrast, over 0.3 nN, the RMSD of the corresponding reactant and transition state structures start exhibiting structural similarity. As stated earlier, the reactant structure changes at this applied force. This follows the Hammond postulate, which states that the activation barrier for the reaction decreases when the similarity between the reactant and transition state structures increases

[17, 19]. Similar trends were observed for pulling directions B and C, which are appended as Figures S4 and S5 in Appendix A.

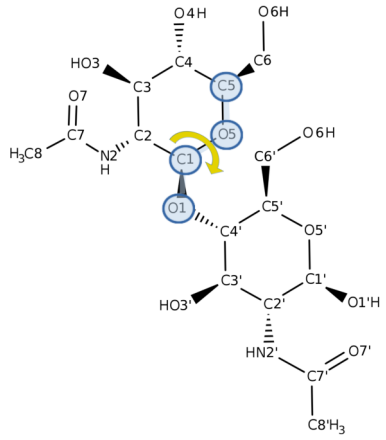

Figure 4.9: Mechanical force susceptible internal coordinate in the GlcNAc dimer

The changes in the RMSD and energy are associated with the glycosidic dihedral angle, C5-O5-C1-O1 (Figure 4.9). The change in the dihedral angle was greater than 30^o for all the pulling directions (Table 4.1). To confirm that the glycosidic dihedral angle is indeed the associated internal coordinate needed for the activation, constrained geometry optimizations with the C5-O5-C1-O1 angle fixed to -94.3^o without external applied force were performed for the reactant and transition state. The calculated activation energy in this case was determined as 11.0 kcal·mol^{-1}, similar to those of the external force activated cases ($\sim$10 kcal·mol^{-1}).

It is also noted that the transition state structure was preserved during the introduction of the external forces. This is evidenced by the lower values of calculated RMSD values shown in Figure 4.8(b). Furthermore, the imaginary frequency varied minimally within computational accuracy. Thus, it can then be interpreted that the original intrinsic reaction coordinate was also preserved around the transition state.

Similar RMSD matrices for the deacetylation were also prepared, analyzed, and are shown in Figure S6 of Appendix A. It should be noted that the diagonal elements of the RMSD matrix for the reactant–transition state remained similar, as shown in in Figure S6(c). This indicates that the structural differences of the reactant and transition state

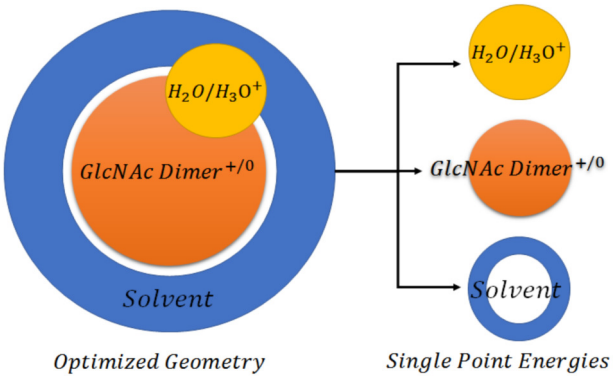

Figure 4.10: Energy decomposition scheme

remain similar upon the application of a pulling force.

Energy decomposition analysis (EDA) was performed to account for the role of each fragment in the model. This also allows the determination of the behavior of stressed GlcNAc dimer with increasing force. The decomposition scheme is illustrated in Figure 4.10. The decomposition was conducted by separating different fragments in the chemical model. Specifically, this corresponds to 1) the GlcNAc dimer, 2) the attacking hydronium molecule, and 3) the solvent molecules.

Aside from the single point energies (SPE), the two-body interaction energy (IE) was calculated as

$$IE_{AB}(F) = E_{AB}(F) - E_A(F) - E_B(F) \tag{4.2}$$

where E is the total electronic energy, F is the applied external force, and $A, B \in \{H_2O, H_3O^+, GlcNAc\ dimer, Solvent\}$

Analyzing the two-body interaction energies in the depolymerization reactant state, it was found that the trend in the total electronic energy follows that of the GlcNAc-solvent interaction (Figure S7). This change can be attributed to the conformational change in the GlcNAc dimer which disrupted the orientation of the water cluster, effectively changing the solvent interaction.

As the change in the depolymerization activation energy is dictated by the reactant destabilization due to the change in the GlcNAc-solvent interaction, the calculated change

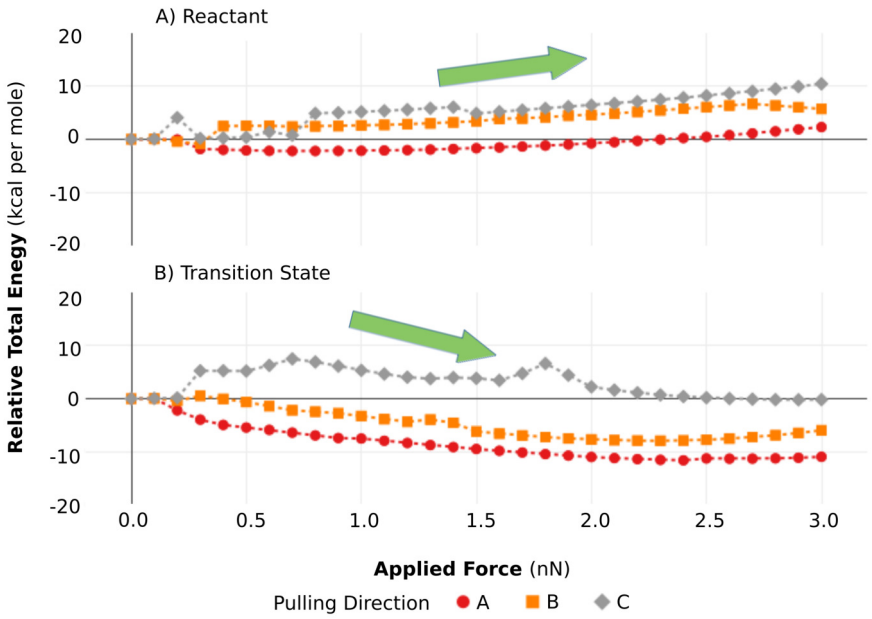

Figure 4.11: Selected energies in the decomposition analysis. Single point energy of the GlcNAc dimer in the (A) reactants and (B) transition states of the depolymerization as a function of the external force

in E_a could be affected by the solvent model used in the study. However, the EDA result for the GlcNAc dimer fragment (Figure 4.11) shows that the energy of the reactant state increases with the applied force, while that of the transition state decreases. Hence, the activation of the depolymerization also originates from the energy change in the GlcNAc dimer fragment. Considering only the GlcNAc fragment, the activation energies as function of applied forces (F) were recalculated as

$$E_a(F) = E(F)^{TS}_{GlcNAcDimer} - E(F)^{Reactant}_{GlcNAcDimer} \tag{4.3}$$

Figure 4.12 shows that the GlcNAc fragment is intrinsically activated upon pulling along all the sampled directions.

In the case of the deacetylation, the result of EDA revealed that the energy contribution of the GlcNAc dimer increases with the magnitude of the applied force, as shown in Figure S8. The amount of increase in the reactant state is close to that in the transition state. The structural analysis in Figure S6 also shows that the structural difference between the reactant and the transition state remains the same. This verifies that the deacetylation

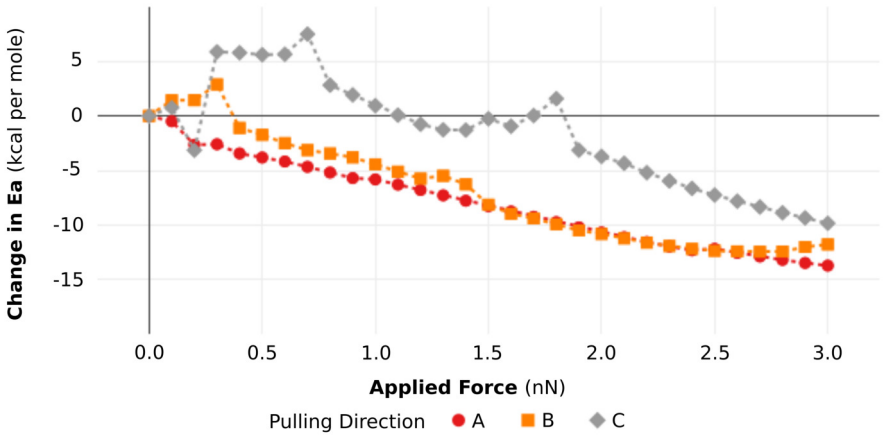

Figure 4.12: Changes in the activation energy with an applied force in the GlcNAc fragment.

reaction, within the limits of the sampled forces in this research, is insusceptible to either mechanical activation or deactivation.

The electronic structure of the active sites were then analyzed via NBO calculations [15]. As previously mentioned, in the RDS of the deacetylation reaction, the active site is the carbonyl carbon of the *N*-acetyl arm of the GlcNAc dimer, while that of the depolymerization reaction is the glycosidic oxygen of the same molecule. Using the second order perturbation theory analysis, the stabilization due to the electron delocalization among the NBOs was calculated. In this paradigm, E(2) is the associated stabilization energy when an electron is donated from an occupied NBO to an empty NBO. We note that E(2) is a measure of the orbital interaction and does not directly interpret the destabilization of the reactant state under the applied force.

In the case of the deacetylation, there was no significant change in the electron delocalization in the NBO basis. The selected donor–acceptor, orbital occupancy, and partial charges for the deacetylation are summarized in Tables S1 and S2 in Appendix A. This was expected, as the local geometry in the model was maintained under the applied force. Consequently, the orbital occupancy and partial charges remained similar to the relaxed reactant state which corresponds to the unsusceptibility of the deacetylation to mechanical activation–deactivation in the range of the sampled applied forces.

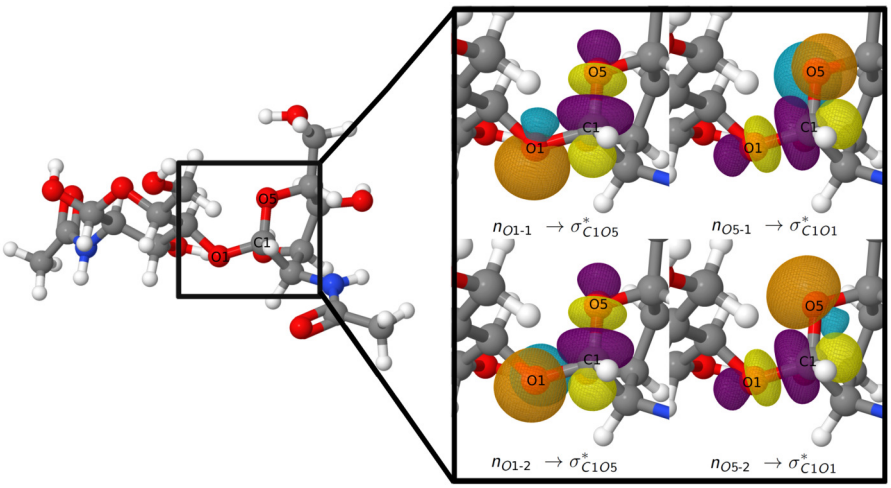

Figure 4.13: Selected donor–acceptor natural bonding orbitals of the GlcNAc dimer in the relaxed reactant state of the depolymerization

In contrast, the depolymerization case, which is activated upon the application of an external force, showed a significant change in the electron donor–acceptor interaction on the onset of activation. In Table 4.1, the interactions concerning the glycosidic bond and the depolymerization active site are tabulated with orbital naming following that in Figure 4.13 [24].

On the onset of activation, which is also marked by the change in the dihedral angle highlighted in blue in Figure 4.9, there is a corresponding significant change in the stabilizing E(2) energy. Table 4.1 shows that the conformational change due to the mechanical force accompanies electron donation from the non-bonding lone pair n_{O5-2} orbital to the glycosidic anti-bonding σ^*_{C1O1} orbital (See Figure 4.13). For example, in pulling direction A, the E(2) for $n_{O5-2} - \sigma^*_{C1O1}$ shows a discontinuous increase from 3.47 kcal·mol^{-1} to 18.39 kcal·mol^{-1} when the applied force changes from 0.0 nN to 0.5 nN. The same trend is followed for the other pulling directions. Hence, the activation can be attributed to this donor–acceptor interaction.

To further probe the changes in the electronic structure, the orbital occupancies along the glycosidic bond are summarized in Table 8.3. For the depolymerization reaction in which an abrupt change was observed in the stabilizing energy E(2), an expected increase in the occupancy of the σ^*_{C1O1} orbital was also observed. In the case of pulling direction A,

Table 4.1: Stabilizing interaction E(2) (kcal·mol^{-1}) for the depolymerization reactant state at different directions and forces

Pulling	Interaction		Applied Force (nN)						
Direction	Donor	Acceptor	0.00	0.50	1.00	1.50	2.00	2.50	3.00
A	n_{O1-1}	σ^*_{C1O5}	3.19	2.34	2.37	2.57	2.69	2.69	2.75
	n_{O1-2}	σ^*_{C1O5}	2.22	4.88	5.00	5.07	5.01	5.22	5.52
	n_{O5-1}	σ^*_{C1O1}	2.96	< 0.50	< 0.50	< 0.50	< 0.50	< 0.50	< 0.50
	n_{O5-2}	σ^*_{C1O1}	3.47	18.39	18.27	18.03	17.76	17.36	16.55
	Dihedral angle[a]		-155.9	-94.3	-96.2	-98.4	-100.6	-103.2	-107.3
B	n_{O1-1}	σ^*_{C1O5}	3.19	1.06	0.81	1.76	1.53	< 0.50	4.44
	n_{O1-2}	σ^*_{C1O5}	2.22	4.19	4.78	5.01	5.65	6.16	0.62
	n_{O5-1}	σ^*_{C1O1}	2.96	< 0.50	< 0.50	< 0.50	< 0.50	< 0.50	< 0.50
	n_{O5-2}	σ^*_{C1O1}	3.47	14.63	14.74	14.40	14.15	15.20	17.59
	Dihedral angle[a]		-155.9	-120.6	-120.3	-118.6	-119.5	-119.01	-93.9
C	n_{O1-1}	σ^*_{C1O5}	3.19	2.70	1.22	0.85	0.73	0.61	0.53
	n_{O1-2}	σ^*_{C1O5}	2.22	2.82	3.34	3.65	3.64	3.76	3.70
	n_{O5-1}	σ^*_{C1O1}	2.96	2.72	0.64	< 0.50	< 0.50	< 0.50	< 0.50
	n_{O5-2}	σ^*_{C1O1}	3.47	4.21	13.64	18.47	18.99	19.72	19.96
	Dihedral angle[a]		-155.9	-153.3	-125.3	-107.2	-105.9	-102.0	-102.2

[a] Dihedral angle, C5-O5-C1-O1, in degrees. See Figure 4.9 for atomic labels.

Table 4.2: Selected orbital occupancy for the depolymerization reactant state at different pulling directions and forces

Pulling	Orbital	AppliedForce (nN)						
Direction		0.00	0.50	1.00	1.50	2.00	2.50	3.00
A	σ^*_{C1O1}	0.048	0.085	0.085	0.085	0.084	0.083	0.081
	σ^*_{C1O5}	0.036	0.037	0.041	0.048	0.042	0.042	0.043
B	σ^*_{C1O1}	0.048	0.077	0.078	0.075	0.075	0.082	0.079
	σ^*_{C1O5}	0.036	0.036	0.036	0.039	0.040	0.038	0.041
C	σ^*_{C1O1}	0.048	0.050	0.075	0.089	0.092	0.095	0.096
	σ^*_{C1O5}	0.036	0.036	0.035	0.034	0.033	0.033	0.033

the occupancy of σ^*_{C1O1} increases at the applied force of 0.5 nN, while no such change was found in that of σ^*_{C1O5}. The same trend was observed in other pulling directions. The main contributing donor–acceptor interaction can then be inferred to be $n_{O5-2} \rightarrow \sigma^*_{C1O1}$ (See Table 4.1).

Upon the application of a limiting force in a pulling manner, the reactant structure was destabilized, and the σ^*_{C1O1} occupancy was increased. In our result, the occupancy of σ^*_{C1O1} increased by a factor of > 1.5 in all pulling directions. Since there is an increase in the occupancy of the said anti-bonding orbital, the corresponding glycosidic bond decreases its bond order, rendering this bond weaker. As these suggest that the electron density in the active site is increased, an increase in the Brønsted–Lowry basicity of the glycosidic oxygen is expected as a consequence.

To assess the change in the Brønsted–Lowry basicity, the relative electrostatic interaction energy (ΔE) of the glycosidic oxygen with a point charge (q = +1) at the typical hydrogen bonding distance of 2 Å was calculated as

$$\Delta E = \frac{(+1)\Delta Q}{r} \tag{4.4}$$

where $r = 2$ Å and ΔQ is the NBO partial charge difference of the stressed and relaxed ($F = 0$) structures in the reactant state. This is a reasonable measure because hydrogen bonding originates from electrostatic interactions [40].

Figure 4.14 summarizes the electrostatic interaction calculated according to Eq. 4.4. A significant increase in the electrostatic interaction up to -3 kcal·mol^{-1} was found with the application of external force, which is consistent with the changes in the second order energy in Table 4.1 and the orbital occupancy in Table 8.3. Thus, it can be concluded that the basicity of the active site was increased; consequently, the proton affinity and, therefore, the reactivity were also increased. As the partial negativity of the glycosidic oxygen increases, the protonation should be relatively easier due to the electronic structural change caused by the applied force. It is also known that the other hydroxyl oxygen sites of the GlcNAc dimer are more basic than the glycosidic oxygen; hence, these sites compete

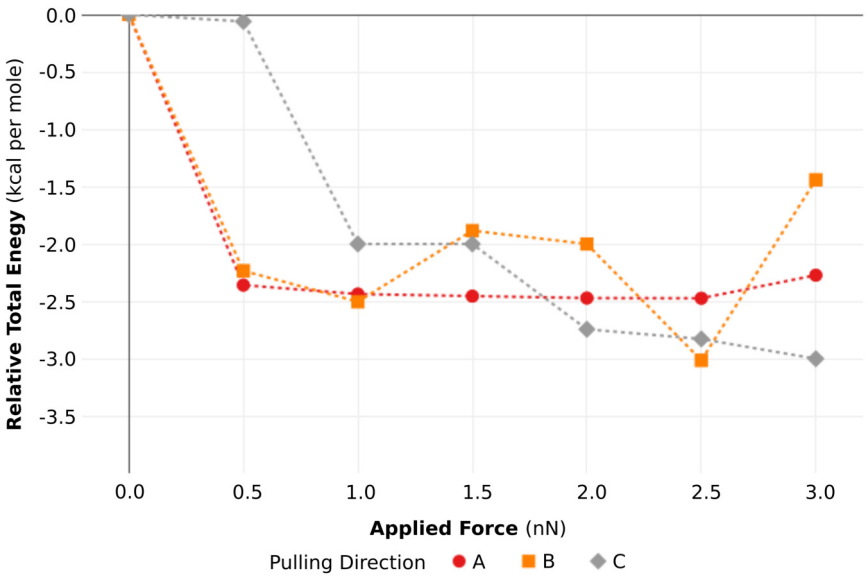

Figure 4.14: Relative energy associated with the electrostatic interaction with increasing applied force. See Eq. 4.4 for the definition.

for the proton at low acid concentrations [11]. This increase in basicity is important for the acid catalysis to occur.

4.4 Summary and Conclusions

The electronic structural effect of mechanochemical pulling, on the competing chitin hydrolysis reactions was investigated by DFT calculations with an externally applied force. In the calculations without force, the RDSs of deacetylation and depolymerization have similar activation energies, which reflect the non-selective acid hydrolysis observed experimentally [18].

The mechanical pulling exerted different effects on the competing reactions. In the deacetylation reactions, the energies of the reactant and transition state increased monotonically, resulting in an almost constant deacetylation activation energy with increasing applied force up to 3 nN. In the mechanistic studies, the RDS of deacetylation is the nucleophilic attack of H2O, not the C-N bond cleavage. This is one of the reasons why the deacetylation is insusceptible to the external pulling. Contrastingly, the depolymerization activation energy significantly decreased with the application of sufficient pulling force

with respect to the sampled directions.

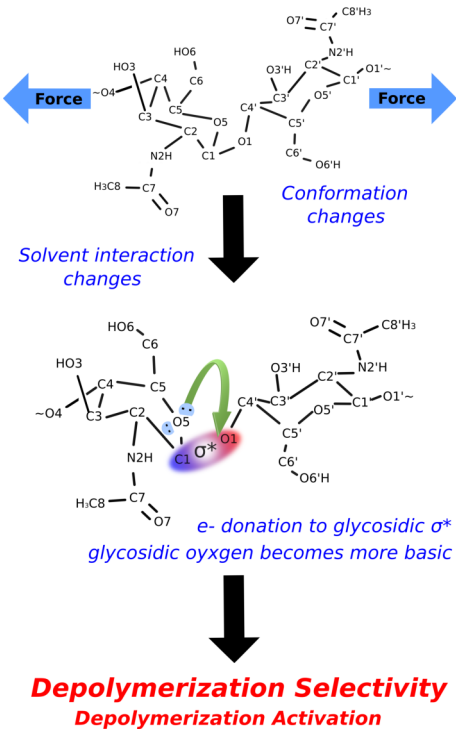

Figure 4.15: Scheme of mechanochemical activation toward chitin depolymerization

The activation of depolymerization can be mainly attributed to the destabilization of the reactant state upon the introduction of sufficient pulling force. A graphical representation of the activation of depolymerization is shown in Figure 4.15. The mechanical stress changes the GlcNAc dimer conformation. In the depolymerization active site, the glycosidic dihedral angle, C5-O5-C1-O1, rotates by more than 30^o degrees which induces a *syn*-periplanar conformation of an O5 lone pair to the C1-O1 bond pair. This results in a significant increase in the charge transfer interaction from the O5 lone pair (n_{O5-2}) to the glycosidic bond anti-bonding orbital (σ^*_{C1O1}), $n_{O5-2} \rightarrow \sigma^*_{C1O1}$, leading to a higher occupancy of the σ^*_{C1O1} orbital. Partial negative charges were found to increase at the glycosidic oxygen increasing its Brønsted–Lowry basicity, which facilitates the acid catalysis.

The results of this study showed that a mechanochemical pulling simulation, which represents a part of complex mechanical forces, can successfully interpret the selectivity

enhancement of depolymerization. It should be noted, however, that the complexity addressed in this work revolves in the geometric deformation due to the mechanical pulling forces while neglecting the other components of mechanical force and instantaneous finite temperature effects associated with ball milling.

References

Arbia, W et al. (2013). "Chitin extraction from crustacean shells using biological methods -A review". In: *Food Technol. Biotechnol.* 51.1, pages 12–25 (cited on page 69).

Barbee, Meredith H. et al. (2018). "Substituent effects and mechanism in a mechanochemical reaction". In: *J. Am. Chem. Soc.* 140.40, pages 12746–12750 (cited on page 76).

Becke, Axel D. (1993). "Density-functional thermochemistry. III. The role of exact exchange". In: *J. Chem. Phys.* 98.7, pages 5648–5652 (cited on page 71).

Beyer, Martin K (2000). "The mechanical strength of a covalent bond calculated by density functional theory". In: *J. Chem. Phys.* 112.17, pages 7307–7312 (cited on page 71).

Binnig, G., C. F. Quate, and Ch. Gerber (Mar. 1986). "Atomic force microscope". In: *Phys. Rev. Lett.* 56 (9), pages 930–933 (cited on page 70).

Cammi, Roberto, Benedetta Mennucci, and Jacopo Tomasi (2000). "Fast evaluation of geometries and properties of excited molecules in solution: a Tamm-Dancoff model with application to 4-dimethylaminobenzonitrile". In: *J. Phys. Chem. A* 104.23, pages 5631–5637 (cited on page 71).

Carpenter, J.E. and F. Weinhold (1988). "Analysis of the geometry of the hydroxymethyl radical by the "different hybrids for different spins" natural bond orbital procedure". In: *J. Mol. Struct.: THEOCHEM* 169, pages 41–62 (cited on page 72).

Chen, Xi and Ning Yan (2014). "Novel catalytic systems to convert chitin and lignin into valuable chemicals". In: *Catal. Surv. Asia* 18.4, pages 164–176 (cited on page 69).

De Bo, Guillaume (2018). "Mechanochemistry of the mechanical bond". In: *Chem. Sci.* 9 (1), pages 15–21 (cited on page 70).

De Chavez, Danjo P. et al. (2019). “Adsorption mediated tandem acid catalyzed cellulose hydrolysis by ortho-substituted benzoic acids”. In: *Mol. Catal.* 475, page 110459 (cited on page 71).

Einbu, Aslak and Kjell M. Vrum (2007). “Depolymerization and de-N-acetylation of chitin oligomers in hydrochloric acid”. In: *Biomacromolecules* 8.1, pages 309–314 (cited on pages 69, 75, 86).

Foster, J. P. and F. Weinhold (1980). “Natural hybrid orbitals”. In: *J. Am. Chem. Soc.* 102.24, pages 7211–7218 (cited on page 72).

Frisch, M. J. et al. (no date). *Gaussian09 Revision E.01*. Gaussian Inc.: Wallingford, CT, 2009 (cited on page 73).

Fukui, Kenichi (1981). “The path of chemical reactions - the IRC approach”. In: *Acc. Chem. Res.* 14.12, pages 363–368 (cited on page 72).

Glendening, E. D. et al. (2011). *NBO Version 3.1* (cited on pages 72, 82).

Hamdi, Marwa et al. (2017). “Chitin extraction from blue crab (Portunus segnis) and shrimp (Penaeus kerathurus) shells using digestive alkaline proteases from P. segnis viscera”. In: *Int. J. Biol. Macromol.* 101, pages 455–463 (cited on page 69).

Hammond, George S. (1955). “A correlation of reaction rates”. In: *J. Am. Chem. Soc.* 77.2, pages 334–338 (cited on page 79).

Kaya, Murat, Talat Baran, and Muhsin Karaarslan (2015). “A new method for fast chitin extraction from shells of crab, crayfish and shrimp”. In: *Nat. Prod. Res.* 29.15, pages 1477–1480 (cited on pages 69, 86).

Konda, Sai Sriharsha M et al. (2013). “Molecular catch bonds and the anti-hammond effect in polymer mechanochemistry”. In: *J. Am. Chem. Soc.* 135.34, pages 12722–12729 (cited on page 79).

Konopka, James B (2012). “N-acetylglucosamine (GlcNAc) functions in cell signaling.” In: *Scientifica* 2012, pages 489208–48922 (cited on page 69).

Krupicka, Martin and Dominik Marx (2015). "Disfavoring mechanochemical reactions by stress-induced steric hindrance". In: *J. Chem. Theory Comput.* 11.3, pages 841–846 (cited on page 76).

Liang, Xiao, Alejandro Montoya, and Brian S. Haynes (2011). "Local site selectivity and conformational structures in the glycosidic bond scission of cellobiose". In: *J. Phys. Chem. B* 115.36, pages 10682–10691 (cited on page 74).

Lin, Yangju et al. (2018). "Regiochemical effects on mechanophore activation in bulk materials". In: *J. Am. Chem. Soc.* 140.46, pages 15969–15975 (cited on page 76).

Loerbroks, Claudia, Roberto Rinaldi, and Walter Thiel (2013). "The electronic nature of the 1,4-B-glycosidic bond and its chemical environment: DFT insights into cellulose chemistry". In: *Chem. - Eur. J.* 19.48, pages 16282–16294 (cited on page 83).

Margoutidis, George et al. (2018). "Mechanochemical amorphization of α-chitin and conversion into oligomers of N-acetyl-d-glucosamine". In: *ACS Sustainable Chem. Eng.* 6.2, pages 1662–1669 (cited on page 72).

Mennucci, Benedetta and Jacopo Tomasi (1997). "Continuum solvation models: A new approach to the problem of solute's charge distribution and cavity boundaries". In: *J. Chem. Phys.* 106.12, pages 5151–5158 (cited on page 71).

Miertuš, S., E. Scrocco, and J. Tomasi (1981). "Electrostatic interaction of a solute with a continuum. A direct utilizaion of AB initio molecular potentials for the prevision of solvent effects". In: *Chem. Phy.* 55.1, pages 117–129 (cited on page 71).

Ong, Mitchell T. et al. (2009). "First principles dynamics and minimum energy pathways for mechanochemical ring opening of cyclobutene". In: *J. Am. Chem. Soc.* 131.18, pages 6377–6379 (cited on pages 71, 72).

Patel, Darpan, Dominik Marx, and Allan East (2020). "Improving yield and rate of acid-catalyzed deconstruction of lignin by mechanochemical activation". In: *ChemPhysChem* 21.n/a (cited on page 70).

Percot, Aline, Christophe Viton, and Alain Domard (2003). "Optimization of chitin extraction from shrimp shells". In: *Biomacromolecules* 4.1, pages 12–18 (cited on page 69).

Reed, Alan E., Larry A. Curtiss, and Frank Weinhold (1988). “Intermolecular interactions from a natural bond orbital, donor-acceptor viewpoint”. In: *Chem. Rev.* 88.6, pages 899–926 (cited on page 72).

Reed, Alan E. and Frank Weinhold (1983). “Natural bond orbital analysis of near-Hartree–Fock water dimer”. In: *J. Chem. Phys.* 78.6, pages 4066–4073 (cited on page 72).

Reed, Alan E., Robert B. Weinstock, and Frank Weinhold (1985). “Natural population analysis”. In: *J. Chem. Phys.* 83.2, pages 735–746 (cited on page 72).

Ribas-Arino, Jordi and Dominik Marx (2012). “Covalent mechanochemistry: Theoretical concepts and computational tools with applications to molecular nanomechanics”. In: *Chem. Rev.* 112.10, pages 5412–5487 (cited on page 70).

Ribas-Arino, Jordi, Motoyuki Shiga, and Dominik Marx (2009). “Understanding covalent mechanochemistry”. In: *Angew. Chem., Int. Ed.* 48.23, pages 4190–4193 (cited on page 71).

Shikhman, Alexander R et al. (2018). “N-acetylglucosamine prevents IL-1B-mediated activation of human chondrocytes”. In: *J. Immunol.*, pages 1–15 (cited on page 70).

Stauch, Tim and Andreas Dreuw (2016). “Advances in quantum mechanochemistry: electronic structure methods and force analysis”. In: *Chem. Rev.* 116.22, pages 14137–14180 (cited on page 70).

— (2017). “Force-induced retro-click reaction of triazoles competes with adjacent single-bond rupture”. In: *Chem. Sci.* 8 (8), pages 5567–5575 (cited on page 76).

Subramanian, Gopinath, Nithin Mathew, and Jeff Leiding (2015). “A generalized force-modified potential energy surface for mechanochemical simulations”. In: *J. Chem. Phys.* 143.13, page 134109 (cited on page 71).

Umeyama, Hideaki and Keiji Morokuma (1977). “The origin of hydrogen bonding. An energy decomposition study”. In: *J. Am. Chem. Soc.* 99.5, pages 1316–1332 (cited on page 85).

Wasonga, Gilbert et al. (2013). "Synthesis of N -acetyl glucosamine analogs as inhibitors for hyaluronan biosynthesis". In: *J. Carbohydr. Chem.* 32.5-6, pages 392–409 (cited on page 70).

Wolinski, Krzysztof and Jon Baker (2009). "Theoretical predictions of enforced structural changes in molecules". In: *Mol. Phys.* 107.22, pages 2403–2417 (cited on page 71).

Yabushita, Mizuho et al. (Nov. 2015). "Catalytic depolymerization of chitin with retention of N-acetyl group". In: *ChemSusChem* 8.22, pages 3760–3763 (cited on pages 70, 77).

Yamabe, Shinichi, Wei Guan, and Shigeyoshi Sakaki (2013). "Three competitive transition states at the glycosidic bond of sucrose in its acid-catalyzed hydrolysis". In: *J. Org. Chem.* 78.6, pages 2527–2533 (cited on page 71).

Younes, Islem et al. (2014). "Chitin extraction from shrimp shell using enzymatic treatment. Antitumor, antioxidant and antimicrobial activities of chitosan". In: *Int. J. Biol. Macromol.* 69, pages 489–498 (cited on page 69).

Zahn, Dirk (2003). "Theoretical study of the mechanisms of acid-catalyzed amide hydrolysis in aqueous solution". In: *J. Phys. Chem. B* 107.44, pages 12303–12306 (cited on page 74).

Zahn, Dirk et al. (2002). "Quantum/classical investigation of amide protonation in aqueous solution". In: *J. Phys. Chem. A* 106.34, pages 7807–7812 (cited on page 74).

V Conformer Stabilization and Destablilization

Mechanical Pushing Induced Selective Cyclopropanation Reaction in Ag(111) Surface

Mechanical Pushing Induced Selective Cyclopropanation Reaction in Ag(111) Surface

Abstract

The application of mechanochemistry to chemical synthesis has opened new chemistry by allowing novel reaction pathways that are otherwise inaccessible to thermal or photochemical activation. Recent trends in mechanochemical synthesis employ transition metals to augment the catalytic activity offered by mechanical forces. Transition metal catalysts have long provided a variety of applications in the field of chemical synthesis. In this work, a silver foil assisted mechanochemical stereoselective cyclopropanation reaction has been studied using Density Function Theory (DFT) calculations. Computational results show that using a single slab-corresponding to a system with no external force-did not replicate the experimentally observed selectivity. This shows that mechanical constraint is needed to drive the stereoselectivity. To do so, a slab sandwich model was designed. Ball milling action was simulated using varying slab distances which provided different chemical environment strains for the cyclopropanation step. Results show a lower activation energy for the E isomer which agrees with the experimentally observed major product. Additionally, a distance dependent pathway was observed. A one step mechanism is preferred at greater slab distances while two step mechanism is favoured at lesser slab distances. This work emphasizes the capability of mechanical constraints to change the reaction mechanism as well as to dictate selectivity.

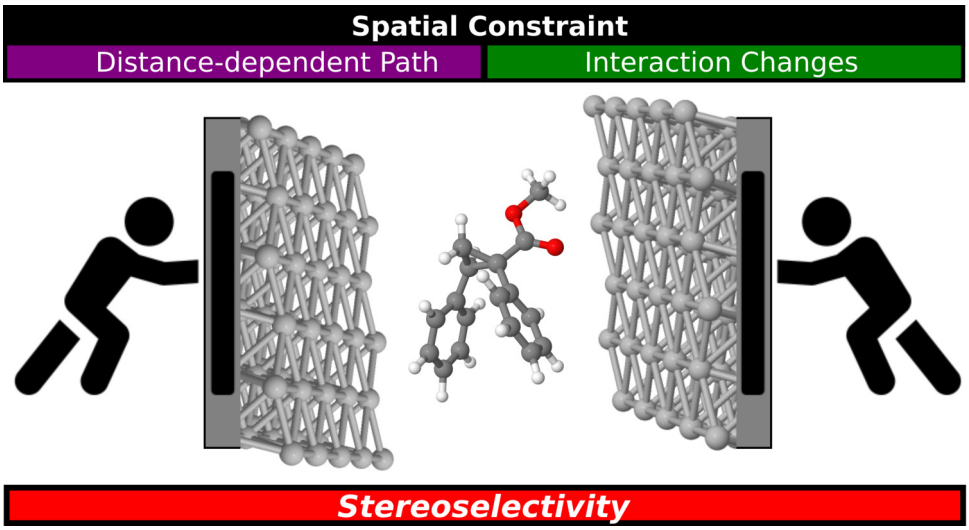

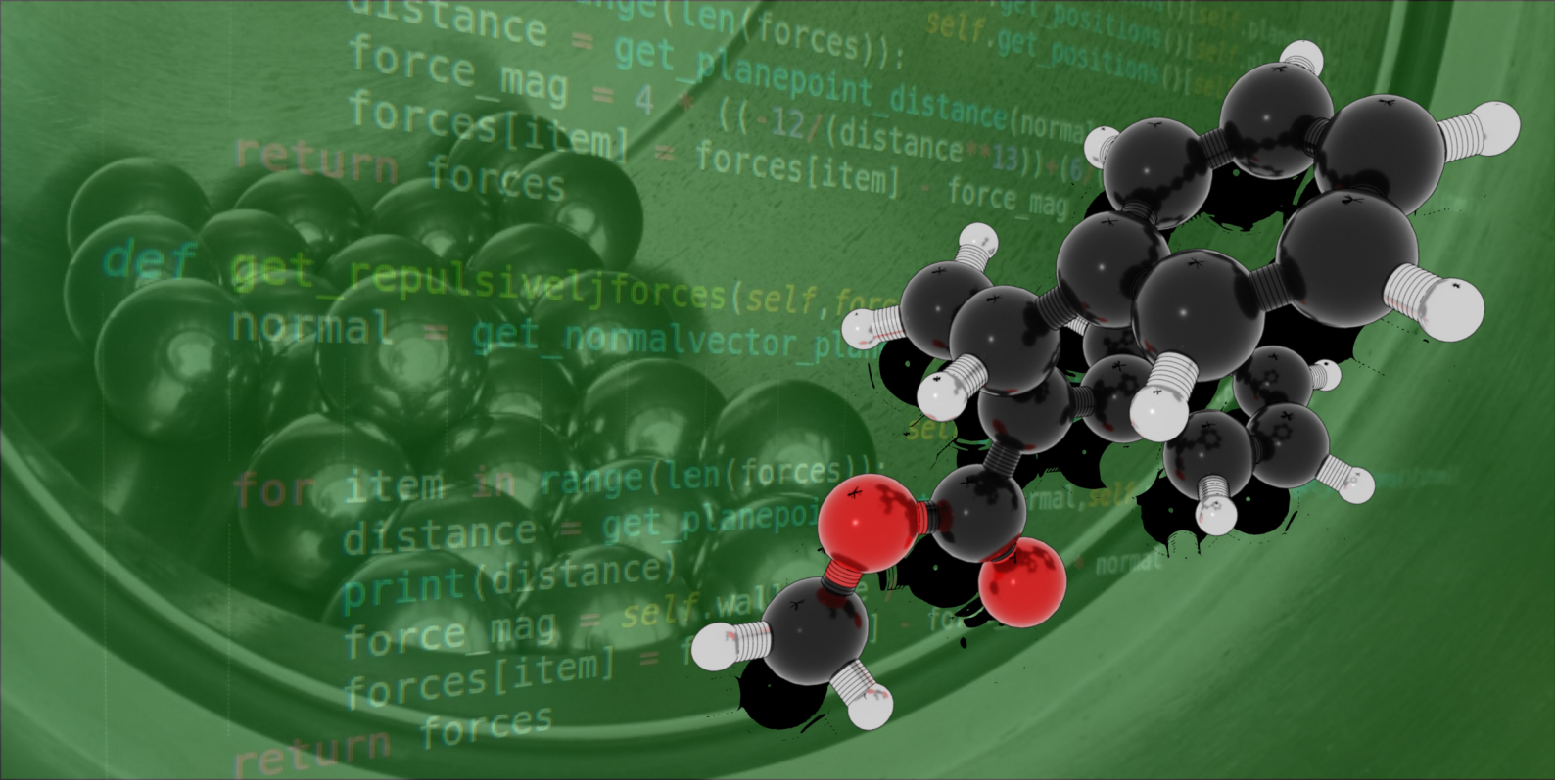

5.1 Introduction

Mechanochemical activation has been applied to numerous chemical reactions which spans from organic chemistry to inorganic chemistry [7]. Single molecule mechanochemistry often relies on atomic force microscopy (AFM) and molecular force probes. These experimental procedures allow detailed mechanistic description of the pulling effect to selected molecules. However, single molecule experiments are difficult to translate on large scales and thus, real world applications are scarce.

Perhaps, the most popular tool for preparative mechanochemistry is ball milling. Ball milling has been historically used for pulverization of minerals and related materials. In the current mechanochemistry trend, ball milling has also been utilized for biomass degradation such as cellulose and chitin [6, 15, 25]. Ball milling has also been applied in both organic and inorganic synthesis. Suzuki reactions under mechanochemical conditions have also been reported [21]. Metal-organic framework (MOF) syntheses are also realized [1].

Current protocols in ball-milling can be categorized in two: (1) neat grinding and (2) liquid-assisted grinding (LAG) [3, 13, 14]. In liquid assisted grinding, a small amount of liquid reactant or solvent is added. This is normally applied to biomass where water is part of the net reaction. In other cases, the additional liquid either acts as co-catalyst or solvent.

Contrastingly, neat grinding is a solid state process where no liquid is added to the reactor. Traditionally, only the reactants are added in the ball mill. However, recent methods in synthetic chemistry utilizes solid additives in the ball mill to presumably act as a catalyst. In addition to this, ball and vial made with reactive metals are now available. Such ball milling apparatus have also been reported to produce different reactions than the conventional stainless steel analogues.

A recent study reported a diastereoselective cyclopropanation reaction using silver foil additive [4]. Interestingly, Chen and colleagues reported that this reaction does not occur in both stainless steel and Teflon vial and ball. This shows that the force-based mechanical activation alone is insufficient to drive the reaction. In this regard, the combined effect of silver and mechanochemical activation in a stereoselective cyclopropanation reaction is studied. This study aims to elucidate the role of silver foil in such a reaction system. In addition to this, the present research aims to provide a simulation approach in studying a similar system which combines mechanochemistry and solid state catalysis.

5.2 Computational Methodology

In this study, density functional theory calculations were done using SIESTA 4.0 package [8, 23]. Calculations were carried using AM05, a Generalized Gradient Approximation (GGA) functional, with double zeta with polarization (DZP) basis set. [19]. The chosen functional afforded the Ag lattice constants closest to that of the experimentally determined values at the converged calculation parameters within GGA-based functionals available in SIESTA.

SIESTA GGA pseudopotentials for all elements were obtained from the GGA pseudopotential database. Mesh cut-off and pseudoatomic orbital filter which is used to

minimize egg box effect were set to 250 Ry and 100 Ry, respectively. To sample the Brillouin zone, off-gamma Monkhorst-Pack k-point sampling of 4x4x1 is used [20]. Pulay mixing of the density matrix with N = 10 was used during the Self-Consistent Field (SCF) cycle. Spin polarization was turned off and hence all calculations are treated to be spin paired calculations. Slab dipole correction was used to account for the induced dipole due to the asymmetry originating from the adsorption of molecules.

It is expected that Van der Waals dispersion interaction is significant due to the existence of benzene ring moieties. To correct for dispersion, Grimme-type DFT-D2 dispersion correction was used for all atomic species combinations[9].

Table 5.1: Grimme DFT-D2 dispersion correction parameters for selected elements.

Element	**C6**	**D**
C	1.75	1.452
H	0.14	1.001
O	0.70	1.397
N	1.23	1.342
Ag	24.67	1.639

To calculate for the minimum energy pathways, nudged elastic band calculations were done by interfacing Atomic Simulation Environment (ASE) with SIESTA 4.0 as the quantum chemical calculator with the converged parameters described above[16]. To decrease computational cost, the slab geometry was fixed and only Γ point was sampled during Nudge Elastic Band (NEB) calculations. Dynamic optimization and force scaling was used to hasten convergence of CI-NEB calculations [2, 11, 17, 22]. NEB path optimization was considered converged when the maximum atomic force is less than 0.05 eV/bohr.

Silver foil was modeled using the Ag(111) surface. Ag(111) is the most thermodynamically stable facet and is expected to be most abundant in a foil type material. Slab surface area was set to 14.4 Å by 15.0 Å. Slab dimension was chosen to have a diagonal longer than the linearized product to limit the interaction to the neighboring periodic image. To remove slab interaction with the periodic image along the z direction, simulation height

was set to 30 Åwhich affords a 20 Å vacuum region along the z direction. Change in surface energy converged to < 0.01 meV/Å using 3 layers and hence, was used throughout the study [10].

The mechanical forces associated in ball milling are simulated here using a slab sandwich model given as Figure 5.1. The chemical environment of ball bombardment is carried by decreasing the slab distance. Here, we limited the simulation to 3 slab distances specifically, 7.0 Å, 8.5 Å, and 10.0 Å. Although this model is expected to mimic the chemical environment changes during milling, dynamics and finite temperature effects are not incorporated in these calculations.

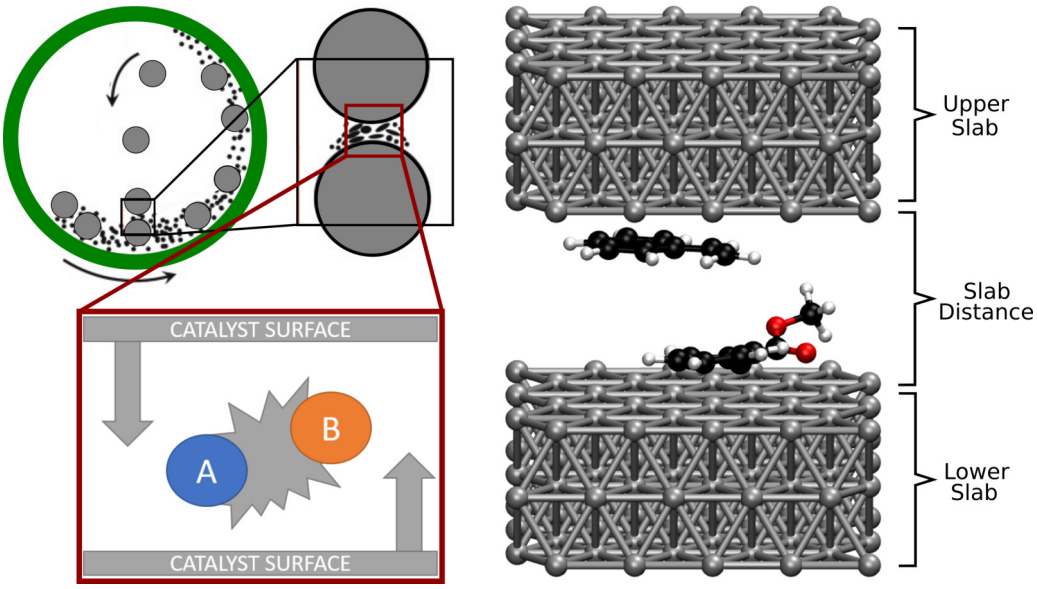

(a) (b)

Figure 5.1: Possible scenarios in the interplay of silver foil and ball milling.

5.3 Results and Discussion

Metal catalyzed cyclopropanation reaction generally follows the general mechanism given in Figure 5.2[18]. Initially, diazo moiety decomposes and a metal carbene intermediate is formed (Figure 5.2(a)). This is followed by the cyclopropanation step where the olefin attacks the carbocation forming the cyclopropane ring (Figure 5.2(b)).

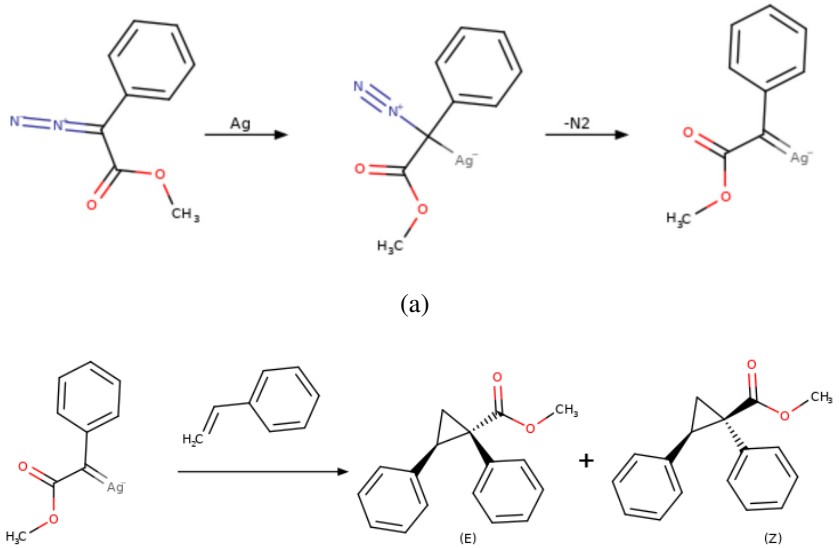

Figure 5.2: Elementary steps in a metal catalyzed cyclopropanation reaction. (a) phenyldiazoacetate decomposition, and (b) cyclopropanation step

In this work, the previous reaction mechanism given in in Figure 5.2 is assumed to be followed [18]. As the object of this research is the mechanochemical ball milling effect in selectivity, the second step of the above mechanism was the focus of mechanistic studies. However, to decide on the rational initial position of the silver-carbene, the adsorption and dissociation were also calculated.

In the Ag(111) surface, there are four unique adsorption sites, specifically, (1) *ontop*, (2) *bridge*, (3) face-centered cubic (*fcc*), and (4) hexagonal closed pack *hcp* sites. As a point of reference, the pro-carbene carbon was chosen and was placed accordingly and the molecule was allowed to relax. Corresponding optimized adsorption structures are included in the Appendix B. Adsorption energies were then calculated as

$$E_{ads} = E_{complex} - E_{diazo} - E_{slab} \tag{5.1}$$

Table 5.2: Phenyldiazoacetate adsorption energy on different sites of Ag(111) surface.

Site	Ads Energy eV	Rel Energy $kcal\ mol^{-1}$
Ontop	-2.05	-2.31
Bridge	-2.09	-3.32
FCC	-1.94	0.00
HCP	-2.09	-3.28

where $E_{complex}$, E_{diazo}, and E_{slab} are the energy of optimized diazo-slab complex, phenyldiazoacetate, and Ag slab, respectively. It can be seen in Table 5.2 that adsorption at the bridge site afforded the most stable conformation. However, adsorption at the other available sites is also stable, and with comparable adsorption energies. The minimum energy pathway of phenyldiazoacetate decomposition reaction was then studied using NEB calculations.

Table 5.3: Phenyldiazoacetate decomposition on different sites of Ag(111) surface.

Site	Activation Energy eV	Reaction Energy eV
Ontop	0.53	-0.03
Bridge	0.63	-0.04
FCC	0.55	-0.28
HCP	0.72	-0.06

Activation energies and reaction energies are summarized in Table 5.3. From the activation energies of the calculated pathways, it can be seen that phenyldiazoacetate decomposition favors an *ontop* orientation prior to dissociation. However, the most stable carbene product is associated with the dissociation pathway starting with an *fcc* absorbed phenyldiazoacetate. As the activation barrier of the *ontop* pathway is only 0.02 eV lower than the *fcc* pathway, the carbene adsorbed on *fcc* site is chosen as the starting configuration to study the cyclopropanation step.

The reacting olefin in our system is styrene. With respect to the rationally chosen configuration of carbene intermediate, there are four possible orientations of the styrene molecule. Such orientations are illustrated as Figure 5.3. These corresponds to two

pathways, **Z1** and **Z2**, leading to *Z* stereoisomeric product and two pathways, **E1** and **E2**, producing *E* isomeric product.

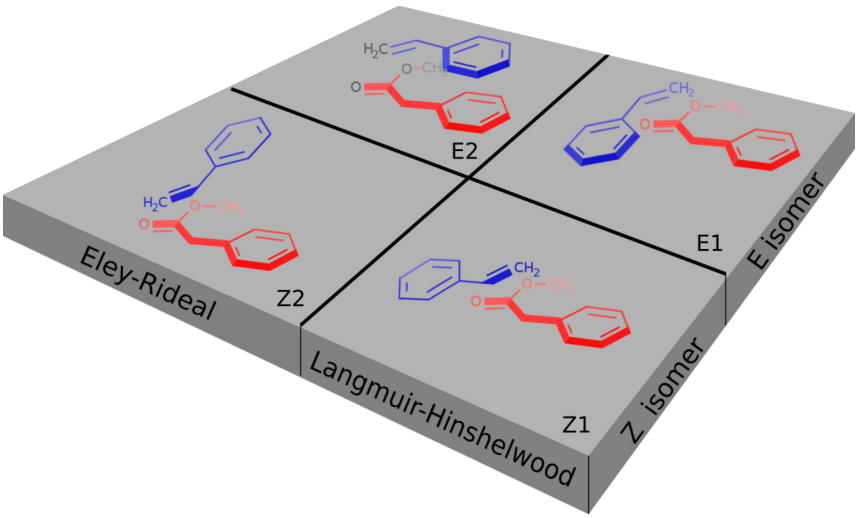

Figure 5.3: Possible styrene orientations with respect to carbene.

The four possible pathways can also be described by traditional surface reaction mechanisms. At the pro-attacking complex, **E1** and **Z1** reactants are both absorbed on the surface and hence can be described by Langmuir-Hinshelwood mechanism. On the other hand, the styrene in **E2** path does not absorbed in the surface, but rather in a complex state with carbene. This can then be considered as Eley-Rideal mechanism. We loosely associate **Z2** path to an Eley-Rideal mechanism because at the optimized reactant state of the **Z2** path, styrene is interacting to the surface via a CH bond of the alkene moiety.

From the converged CI-NEB calculation, key differences were found in the sampled mechanisms. **E2** pathway undergoes a single step cyclopropanation. In contrast to this, the remaining pathways, **E1**, **Z1**, and **Z2**, all undergone a two-step cyclopropanation. The intermediate of these pathways formed an initial carbon-carbon bond. This is reminiscent of a metallocycle. However, instead of a single metal, the carbons are interacting with different silver atoms of the surface. The second step of such mechanism forms the cyclopropane ring, weakening the interaction with the metal surface.

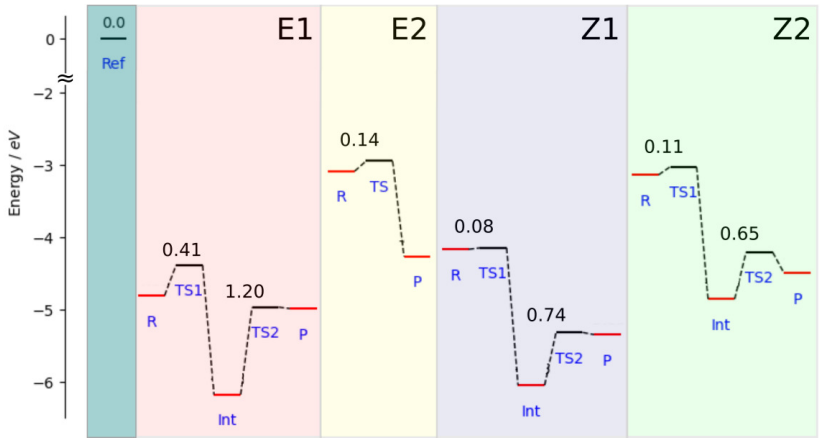

Figure 5.4: Energy diagrams of cyclopropanation pathways in single Ag(111) surface.

The reaction energetics of the four pathways are summarized as Figure 5.4 where the reference energy is that of carbene absorbed to Ag(111) and styrene. From these pathways, it can be seen that the reactant states of Eley-Rideal related pathways are less stable than those of Langmuir-Hinshelwood pathways. The energy difference is justified by the amount of Ag(111) surface interaction of both **E2** and **Z2** reactants. At reaction completion, the product stability is also determined by the relative amount of Van der Waals surface contacts of the cyclopropane product to the surface.

As discussed above, the reactant energies are functions of the interaction with Ag(111) surface and hence it is beneficial to compare related pathways. Comparing **E2** and **Z2**, it can be seen that the apparent activation energy of **Z2** path is less steep than that of **E2** pathway. In addition to this, **Z2** reaction energy is also more exothermic than **E2**. This shows that **Z2** is preferred over **E2**. The contrasting difference in **E1** and **Z1** pathways is the second step of the reaction where the apparent activation energy of **E1** is 1.2 eV while that of **Z2** is 0.74 eV. In comparing reaction energies, E1 path is also more exothermic than **Z1**. The same can be said in terms of the reaction product: **Z1** product is more stable than the **E1** product. Optimized reactant, transition state, and product state of the simulations described above are appended in the Appendix B.

This leads us to conclude that the preferred product is *Z* isomer which is not the stereoisomer produced in experiments. This is translated that mechanical forces indeed

contribute to the diastereoselectivity of the reaction developed by the Mack group [4].

As described in computational methods, the action of ball milling is simulated using a slab sandwich model with varying slab separation. In such system, carbene and styrene can be absorbed either on a single slab or on opposite slabs. The former case is expected to behave similar to the single slab treatment of the reaction and hence focused on the case where carbene and styrene are absorbed on opposite slabs. The position of the carbene is maintained to be the same as the single slab calculations while the reacting styrene is oriented according to Figure 5.5.

The styrene orientation would determine the stereoisomerism exhibited by the product. It should also be noted that the studied pathways in the slab sandwich model are direct analogues of those in the single slab calculations. However, these mechanisms can not be considered as Langmuir-Hinshelwood nor Eley-Rideal mechanisms which describes the previous single slab pathways. In addition to the possible orientation of styrene, we studied two mechanisms for the cyclopropanation step as depicted in Figure 5.6: one step and two step pathways.

To compare one another, activation energies of both pathways are given in Table 5.4. In general, the single step mechanism is preferred which afforded overall lower activation energies. It should be noted, however, that our calculations were restricted to be spin paired systems. In literature, preference for multi-step cyclopropanation was observed at a triplet state system.

Distance dependence of reaction energetics differs in step 1 and 2. Step 1 of the two step mechanism follows the same slab separation distance relation as one step mechanism. This follow chemical intuition as step 1 and the one step mechanism can be characterized by the decomplexation of carbene from the metal slab. The step 2 on the other hand follows no clear relationship with the separation distance.

On the context of reaction selectivity and with activation energy as basis, it can be seen that E pathways have generally lower reaction barrier in comparison to the Z pathway which

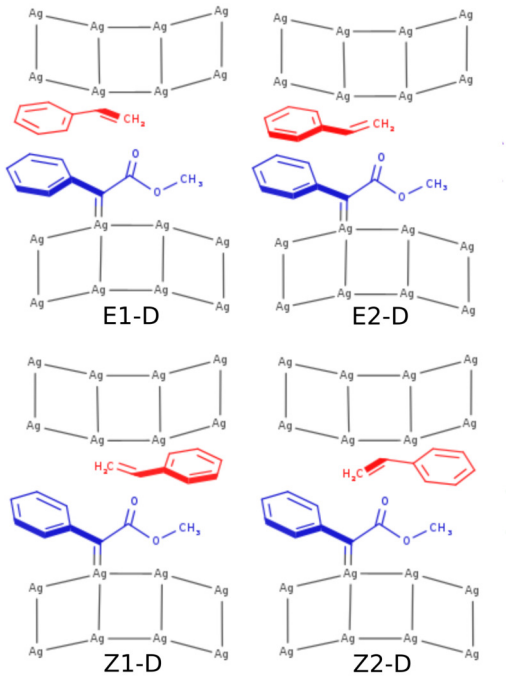

Figure 5.5: Possible orientations of styrene with respect to Ag-carbene group.

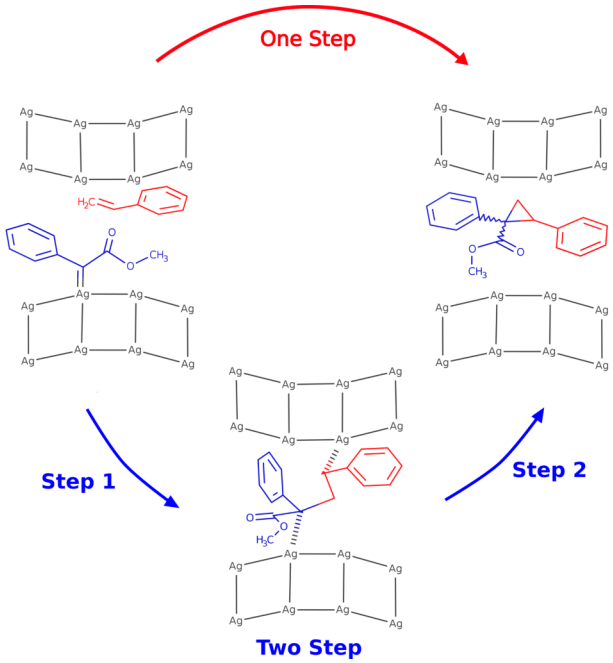

Figure 5.6: Reaction mechanism schematic of cyclopropanation reaction.

Table 5.4: Activation energies in $kcal\ mol^{-1}$ for the cyclopropanation step at different slab separation distances.

Slab Distance	Path	One Step	Two Step	
			Step 1	Step 2
7 Å	E1-D	0.46	0.56	3.71
	E2-D	5.73	6.54	9.43
	Z1-D	8.97	2.34	17.77
	Z2-D	18.93	17.13	39.01
8.5 Å	E1-D	22.30	28.36	1.06
	E2-D	31.83	28.15	3.18
	Z1-D	34.54	23.83	10.62
	Z2-D	28.44	23.66	5.36
10 Å	E1-D	50.08	52.55	5.12
	E2-D	13.53	26.16	1.37
	Z1-D	53.17	47.17	0.68
	Z2-D	40.17	39.44	0.32

lead us to conclude that E isomer is preferred. This agrees well with the experimentally determined product. At 7 Å, slab separation, lower activation barriers than those of single slab analogues were achieve. This shows the effect of chemical environment in mechanochemical regime was captured in our simulations.

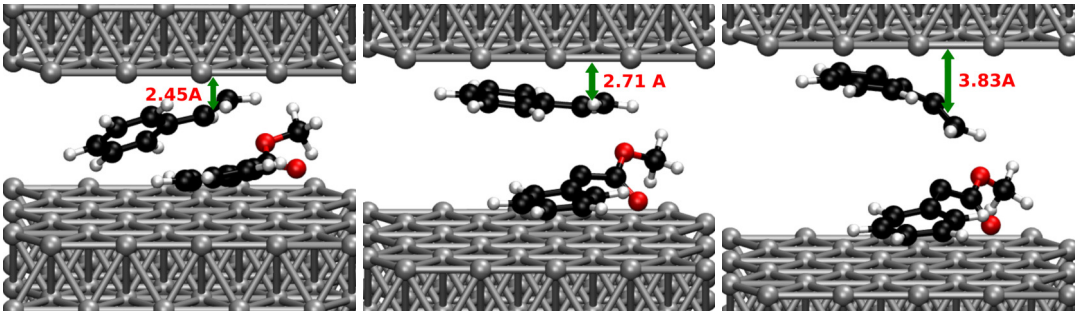

(a) (b) (c)

Figure 5.7: Optimized transition state structures for one step cyclopropanation along E1 pathway at (a) 7.0 Å, (b) 8.5 Å, and (c) 10.0 Å slab distance separation.

At this point, we focus on the effect of the slab separation distance in the cyclopropanation reaction in the context of the single step mechanism. Activation barrier of the minimum energy pathways for one step mechanism was found to be higher with increasing distance. During the course of reaction, it is observed that both molecules approach each

other to form the cyclopropane moiety. As the slab separation increase, it follows that the molecules have to initially desorb from the Ag(111) surface. Such desorption phenomenon is captured at the corresponding transition state. In Figure 5.7, it can be seen that there is a proportional increase in the distance between alkene moiety of styrene and the upper slab. On the other hand, the carbene roughly maintains its association with lower slab.

To understand the importance of the slab in stabilization of the reaction minima, interaction energy is chosen to be the descriptor. Interaction energy, IE, is calculated as

$$IE = E_{total}^{complex} - (E_{slab}^{complex} + E_{reactants}^{complex}) \tag{5.2}$$

where $E_{total}^{complex}$ is the energy of optimized diazo-slab complex. $E_{reactants}^{complex}$ and $E_{slab}^{complex}$ are the energies of the reactants and slab at the complex geometry, respectively. Calculated interaction energies are summarized in Figure 5.8.

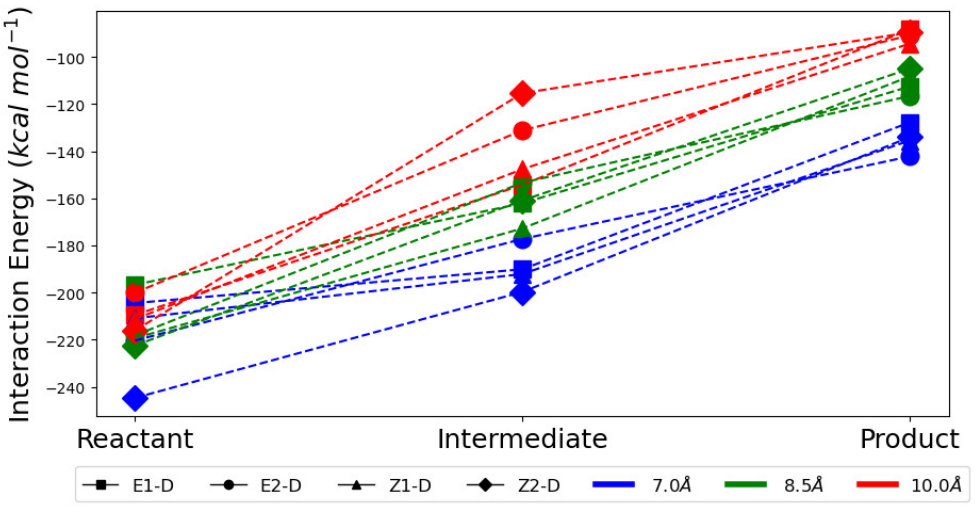

Figure 5.8: Calculated interaction energy in reaction minima

Interestingly, the interaction energy increases from the reactant to the intermediate and from intermediate to the product. This shows that the product states has the least amount of interaction with the slab. Distance relation is also clear from Figure 5.8. This physically translates to the amount of contacts with slab. Naturally, at higher slab separation, relaxation of chemical bonds of the intermediate and product state decreases

the contacts to the Ag(111) slabs. It should also be noticed that such distance dependence is not found in the reactant state, signifying the separated state of carbene and styrene.

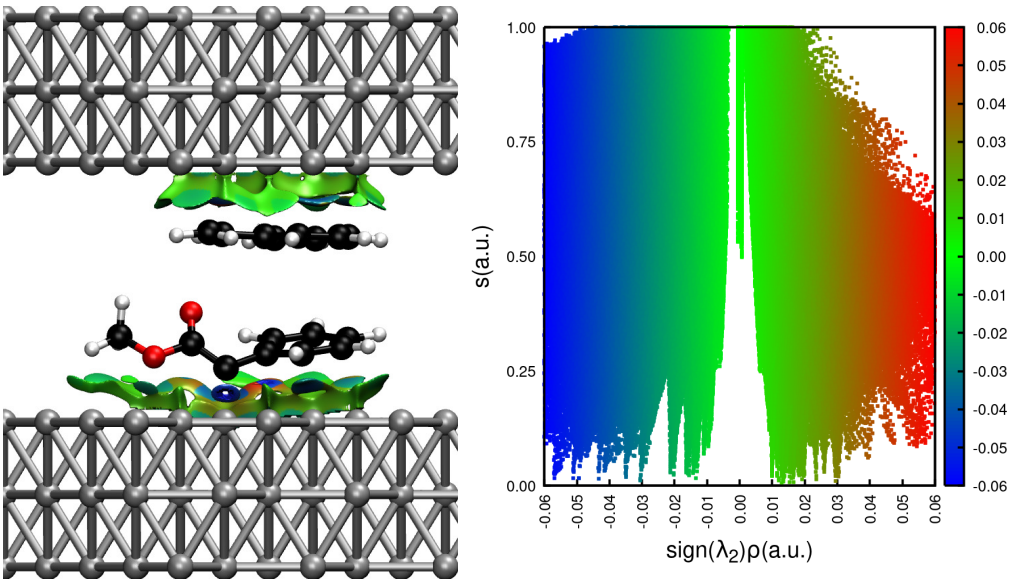

(a) (b)

Figure 5.9: Representative non-covalent interaction plot for surface - reactant complex.

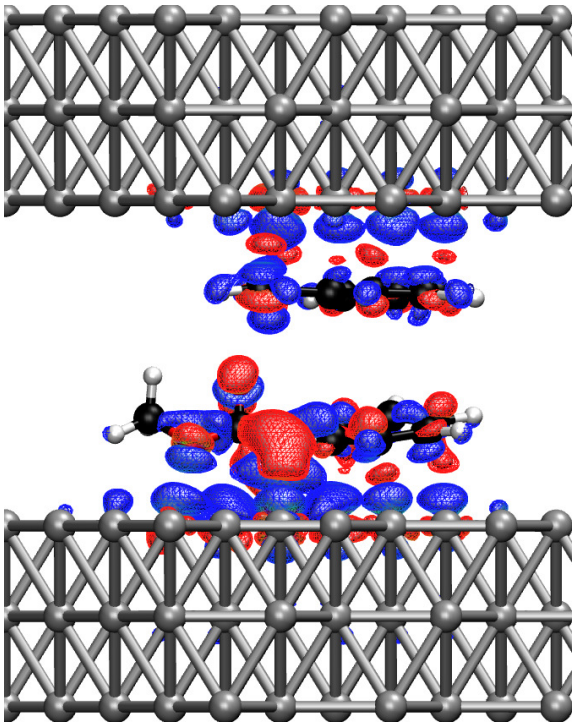

Figure 5.10: Representative charge density difference plots for surface - reactant complex (red - decrease in density, blue - increase density).

To characterize the nature of interaction, non-covalent interactions and charge density difference maps are given as Figures 5.9 and 5.10, respectively. Non-covalent interaction (NCI) plots shows non-bonded interactions while charge density difference (CDD) maps shows the electrostatic interactions in the complex [5, 24].

In Figure 5.9, the attractive non-covalent interactions which lie in the left side of the plot with a $-\lambda_2$ dominated the repulsive interactions which lie in the left side of the plot with a $+\lambda_2$. It can be seen that the carbene shows a high attraction (blue) to the Ag(111) slab. This reveals the importance of the carbene silver interaction. This is also seconded by the electrostatic picture through the charge density difference map. In Figure 5.10, it can be seen that there is a decrease in electron density in the carbene while an increase in electron density along the slab contact point. Similar observations can be made for other molecular states and are are given in the Appendix B.

To complete the interaction analysis, Hirshfeld charges were calculated for the reactant, transition state, and product of the single step mechanism [12]. In Figure 5.3, it can be seen that the magnitude of charge in the slab decrease after the reaction. The partially negative carbene also became less negative. Hence, the Coulombic interaction during the course of the reaction decreases which effectively decreased the slab interactions. Hirshfeld changes of other states are also given in the Appendix B.

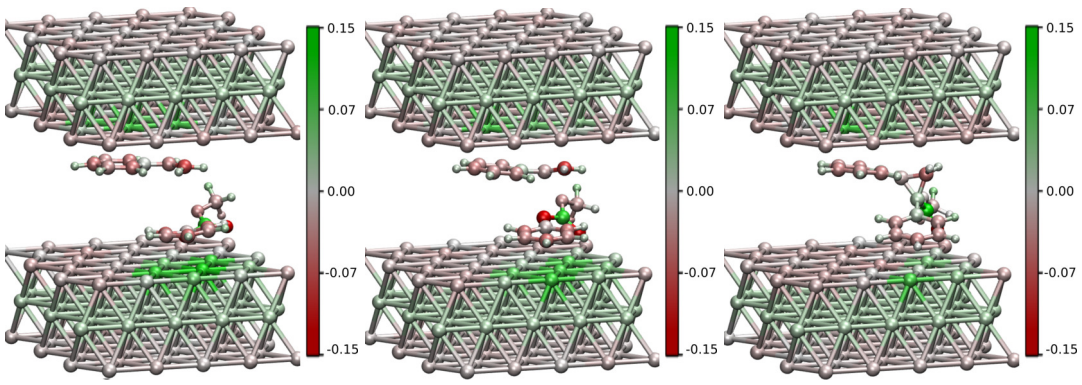

(a) (b) (c)

From the chemical information gathered, we defined reaction fingerprints to capture the most important features of the reaction and the role of the slab sandwich. In the reaction

center, the carbene, C_0, is initially sited in a hollow site of the lower slab. Thus, slab effect was chosen to be summarized by the C_0 complexation with 3 silver atoms. During the reaction, the alkene group approaches the carbene, which corresponds to a carbene-π interaction. Such interactions are given in Figure 5.11.

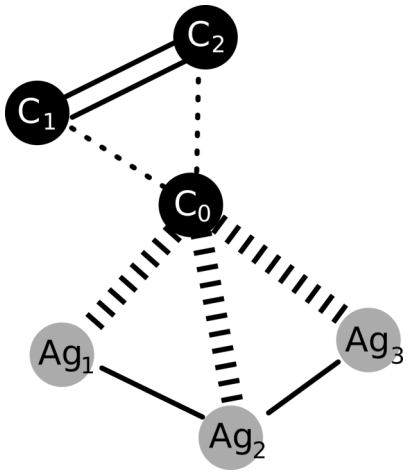

Figure 5.11: Schematic of the reaction center.

To account for the styrene-carbene interaction, cabene-π Index (I_C) is defined as

$$I_C = \sum^{N_C} \frac{r_{C_i} - r_{C_0}}{N_C} \tag{5.3}$$

where r_{C_0} and r_{C_i} are the Cartesian coordinates of the carbene and alkene carbon, respectively. Carbene-π index (I_C) is basically the average bond distance of carbene to the alkene carbons. On the other hand, metal complexation index (I_M) is defined as

$$I_M = \sum_i^{N_{Ag}} \frac{r_{Ag_i} - r_{C_0}}{N_{Ag}} \tag{5.4}$$

where r_{C_0} and r_{Ag_i} are the Cartesian coordinates of the carbene and silver, respectively. Note that summation only runs on the complexation site.

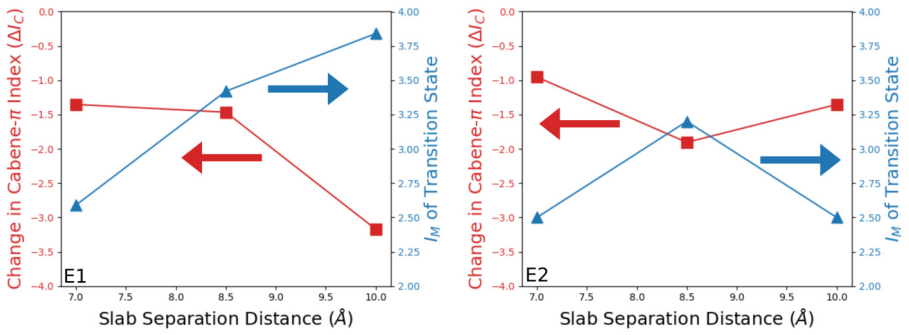

(a) E1-D (b) E2-D

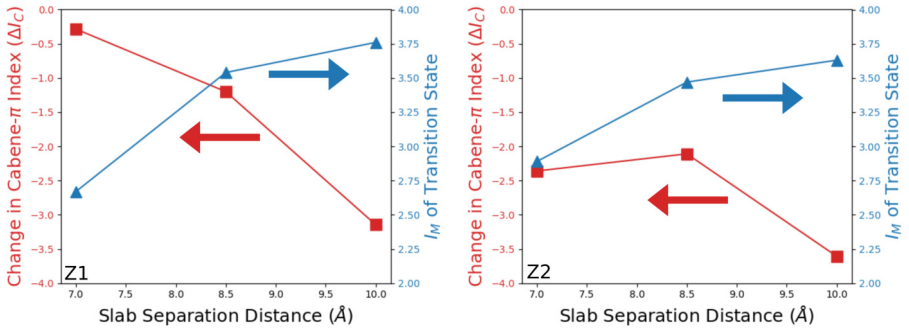

(c) Z1-D (d) Z2-D

Figure 5.12: Calculated reaction indices in the (a) E1-D, (b) E2-D, (c) Z1-D, and (d) Z2-D pathways at different slab separation.

Similar to the carbene-π index, metal complexation index is the average carbene-silver bond. To demonstrate the potential of our defined indices, we applied it in the single step mechanism in all sampled slab separation distances. Calculated I_M for the transition state of the one step mechanism are given as Figure 5.12. The change in I_C corresponds to the difference of transition state I_C and reactants I_C. It can be seen that trends in reaction fingerprints follows the reaction activation energies in Table 5.4, which means that the developed reaction fingerprints effectively captures the important chemical interactions, carbene-π and metal complexation.

5.4 Summary and Conclusions

In the present work, the silver metal-aided mechanical activation of a stereoselective cyclopropanation reaction was investigated using DFT calculations. Silver foil was modeled

using the Ag(111) surface which is the most thermodynamically stable silver surface. Mechanical ball milling conditions are mimicked with a non-standard slab sandwich model. The pummelling action inside the ball mill is translated as the slab separation distance.

The generally accepted cyclopropanation reaction mechanism of phenyldiazoacetate and styrene using a metal-based catalyst initially starts with the decomposition of the diazo group of the phenyldiazoacetate followed by the cyclopropane ring formation. Diazo decomposition and cyclopropane ring formation is the rate determining step and stereodetermining step, respectively.

To serve as a relaxed environment equivalent, conventional surface calculations were initially done. Four mechanisms were studied corresponding to different orientations of styrene with respect to the metal carbene. Using such model and on the basis of activation energies, it was found that the reaction favors Z isomer, contrary to the experimental findings. This shows that mechanochemical effect is important to describe stereoselectivity.

Similar to the single slab calculation, four mechanisms were studied. Under mechanochemical conditions, the calculated activation energies are found to scale with the slab separation. In general, this trend is dominated by the desorption barrier associated during the reaction which is revealed by the slab-complex interaction energy. This is also proven by NCIplot showing minimal interaction of the reactants with each other and slab-complex interaction is highly predominant.

NEB calculations show related mechanisms where the ethene group of styrene approaches the carbene as it is formed by breaking metal carbon bonds. To describe these chemical concepts during the reaction, the carbon-π index (I_c) and metal complexation index (I_m) are defined. The carbon-π and metal complexation indices follow the reaction energetics which shows the importance of carbene complexation to the hollow site of the Ag(111) surface.

Calculated activation energies revealed lower activation barriers for E isomer producing pathways. This corresponds with the results observed in experiments. The chemical environment during a metal-aided ball milling, as modeled in these simulations, is impor-

tant to induce the mechanical force associated with geometric changes. This then leads to a change in reaction energetics resulting in stereoselectivity. Other than the physical constraints given by such models, the chemical character of the metal is also explicitly handled during our simulations. Though the geometric restriction during ball milling is indeed captured by the slab sandwich model by providing a similar chemical environment, grinding-associated thermal effects are not considered in such calculations.

References

Beamish-Cook, Jethro et al. (2021). "Insights into the Mechanochemical Synthesis of MOF-74". In: *Crystal Growth & Design* 21.5, pages 3047–3055 (cited on page 97).

Berne, Bruce J, Giovanni Ciccotti, and David F Coker (1998). *Classical and Quantum Dynamics in Condensed Phase Simulations*. WORLD SCIENTIFIC (cited on page 99).

Bonnamour, Julien et al. (2013). "Environmentally benign peptide synthesis using liquid-assisted ball-milling: application to the synthesis of Leu-enkephalin". In: *Green Chem.* 15 (5), pages 1116–1120 (cited on page 98).

Chen, Longrui et al. (2015). "An Inexpensive and Recyclable Silver-Foil Catalyst for the Cyclopropanation of Alkenes with Diazoacetates under Mechanochemical Conditions". In: *Angewandte Chemie International Edition* 54.38, pages 11084–11087 (cited on pages 98, 105).

Contreras-García, Julia et al. (2011). "NCIPLOT: A Program for Plotting Noncovalent Interaction Regions". In: *Journal of Chemical Theory and Computation* 7.3. PMID: 21516178, pages 625–632 (cited on page 110).

De Chavez, Danjo et al. (2021). "On the Electronic Structure Origin of Mechanochemically Induced Selectivity in Acid-Catalyzed Chitin Hydrolysis". In: *The Journal of Physical Chemistry A* 125.1. PMID: 33382273, pages 187–197 (cited on page 97).

Do, Jean-Louis and Tomislav Friščić (2017). "Mechanochemistry: A Force of Synthesis". In: *ACS Central Science* 3.1. PMID: 28149948, pages 13–19 (cited on page 97).

García, Alberto et al. (2020). “Siesta: Recent developments and applications”. In: *The Journal of Chemical Physics* 152.20, page 204108 (cited on page 98).

Grimme, Stefan (2006). “Semiempirical GGA-type density functional constructed with a long-range dispersion correction”. In: *Journal of Computational Chemistry* 27.15, pages 1787–1799 (cited on page 99).

Gross, A. (2002). “Theoretical Surface Science: A Microscopic Perspective”. In: (cited on page 100).

Henkelman, Graeme, Blas P. Uberuaga, and Hannes Jónsson (2000). “A climbing image nudged elastic band method for finding saddle points and minimum energy paths”. In: *The Journal of Chemical Physics* 113.22, pages 9901–9904 (cited on page 99).

Hirshfeld, F. L. (1977). “Bonded-atom fragments for describing molecular charge densities”. In: *Theoretical Chemistry Accounts* 44.2, pages 129–138 (cited on page 110).

Howard, Joseph L. et al. (2017). “Controlling reactivity through liquid assisted grinding: the curious case of mechanochemical fluorination”. In: *Green Chem.* 19 (12), pages 2798–2802 (cited on page 98).

Jiang, Zhi-Jiang et al. (2016). “Liquid-Assisted Grinding Accelerating: Suzuki–Miyaura Reaction of Aryl Chlorides under High-Speed Ball-Milling Conditions”. In: *The Journal of Organic Chemistry* 81.20. PMID: 27690440, pages 10049–10055 (cited on page 98).

Kuga, Shigenori and Min Wu (2019). “Mechanochemistry of Cellulose”. In: *Cellulose* 26.215 (cited on page 97).

Larsen, Ask Hjorth et al. (June 2017). “The atomic simulation environment—a Python library for working with atoms”. In: *Journal of Physics: Condensed Matter* 29.27, page 273002 (cited on page 99).

Lindgren, Per, Georg Kastlunger, and Andrew A. Peterson (2019). “Scaled and Dynamic Optimizations of Nudged Elastic Bands”. In: *Journal of Chemical Theory and Computation* 15.11. PMID: 31600078, pages 5787–5793 (cited on page 99).

Maas, Gerhard (2004). "Ruthenium-catalysed carbenoid cyclopropanation reactions with diazo compounds". In: *Chem. Soc. Rev.* 33 (3), pages 183–190 (cited on pages 100, 101).

Mattsson, Ann E. et al. (2008). "The AM05 density functional applied to solids". In: *The Journal of Chemical Physics* 128.8, page 084714 (cited on page 98).

Monkhorst, Hendrik J. and James D. Pack (June 1976). "Special points for Brillouin-zone integrations". In: *Phys. Rev. B* 13 (12), pages 5188–5192 (cited on page 99).

Seo, Tamae et al. (2019). "Solid-state Suzuki–Miyaura cross-coupling reactions: olefin-accelerated C–C coupling using mechanochemistry". In: *Chem. Sci.* 10 (35), pages 8202–8210 (cited on page 97).

Smidstrup, Søren et al. (2014). "Improved initial guess for minimum energy path calculations". In: *The Journal of Chemical Physics* 140.21, page 214106 (cited on page 99).

Soler, José M et al. (Mar. 2002). "The SIESTA method forab initioorder-Nmaterials simulation". In: *Journal of Physics: Condensed Matter* 14.11, pages 2745–2779 (cited on page 98).

Wang, Linfeng et al. (2019). "The electronic behaviors and charge transfer mechanism at the interface of metals: A first-principles perspective". In: *Journal of Applied Physics* 126.20, page 205301 (cited on page 110).

Yabushita, Mizuho et al. (Nov. 2015). "Catalytic depolymerization of chitin with retention of N-acetyl group". In: *ChemSusChem* 8.22, pages 3760–3763 (cited on page 97).

VI Catalytic Activity Tuning Using Lattice Strains

Potential Strain Effects in the Catalytic Activity of Ru in CO Decomposition

Potential of Compressive Strain in Increasing Catalytic Activity of Ru in CO Decomposition

Abstract

The potential control of strain in the catalytic activity of heterogeneous catalysts has previously been generalized according to the d-band model and conventional understanding of the scaling relations. Recently, it was reported that the strain may influence the reaction system incongruently, that is, a different strain effect can be seen in the reactant state in comparison to the transition state. This offers a novel route to break the Bronsted-Evans-Polyani (BEP) relation in catalysis. In this work, the effect of isotropic and anisotropic strain in the catalytic activity of terrace Ru(0001) and stepped Ru(1015) surface have been studied for the initial step of Fischer-Tropsch (FT) reaction. Adsorption-strain relations have been investigated using the d-band model and the novel eigenstress model. In general, adsorption relation in the reactant state follows that of the d-band. The eigenstress model also predicts similar qualitative changes in the adsorption energies without the need to calculate for the d-band center of the slab. Activation energies were found to scale according to BEP relation with some exemptions. These cases include new minimum energy pathways according to the CI-NEB calculations which do not break the scaling relations but reinforces the mechanochemical effect of producing new chemical pathways with the strain. In addition, it was found that in the case of a compressed Ru(1015) surface, reactant adsorption energy does not scale with dissociation activation energy. This is explained by the heightened difference in the reactant interaction energy.

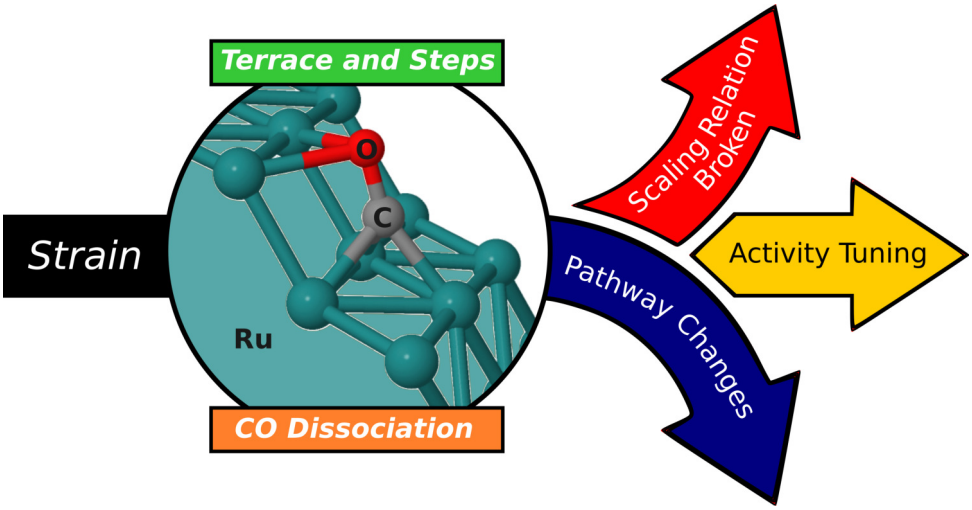

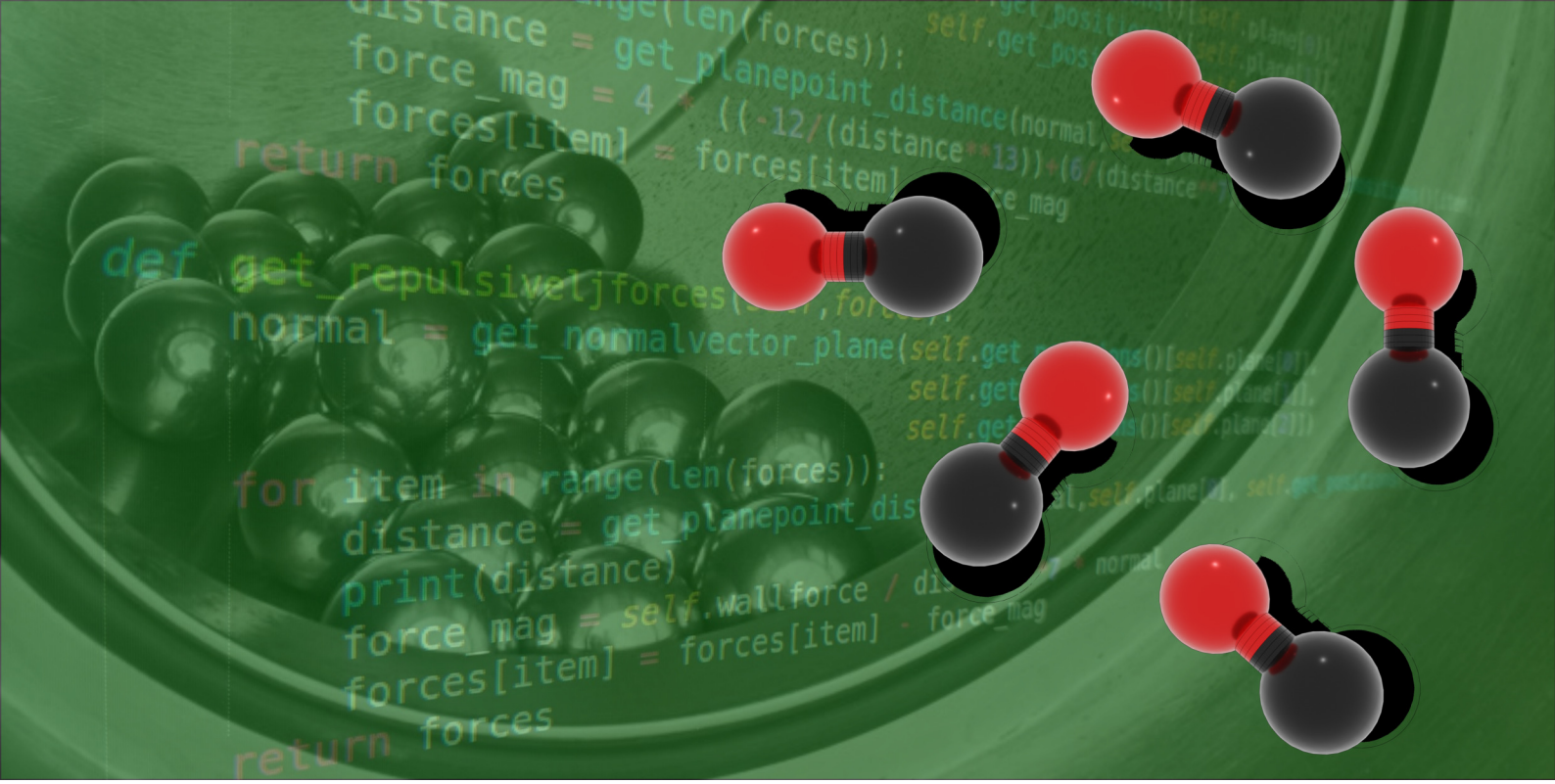

6.1 Introduction

Fischer-Tropsch (FT) reaction is an industrially relevant reaction route used to produce long chain saturated and unsaturated hydrocarbons which utilizes carbon monoxide as the primary carbon source [4]. FT reaction starts with adsorption of carbon monoxide (CO) to a metal slab. This is followed by CO dissociation as the initial bond breaking process. Reaction schema is given as Figure 6.1. Conventional catalysts used in such applications are ruthenium (Ru), iron (Fe), and cobalt (Co).

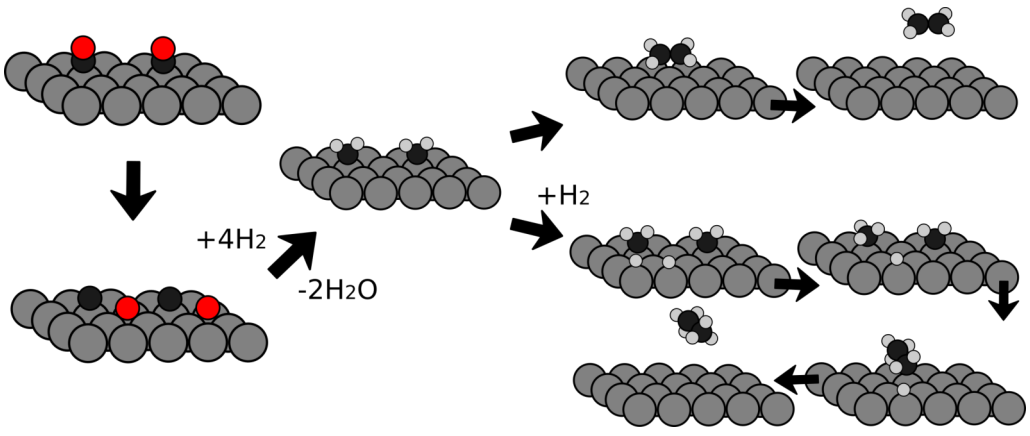

Figure 6.1: Reaction scheme of Fischer-Tropsch process.

Strain engineering has been utilized to control the activity of several catalytic and functional materials [20]. It has been predicted based on the d-band model that compression leads to lesser binding energy to adsorbate, while expansion contributes to greater binding energy. Because of adsorption scaling relations, activation and reaction energies are also affected accordingly. Bronsted-Evans-Polyani (BEP) relation describes the linear relation which exists between activation energy and reaction energy [8]. While the analogue for transition state energy and reactant/product energy scaling is referred as Transition State Scaling (TSS) relation. BEP and TSS relations are given in their equation form as Eqs. 6.1 and 6.2 [25].

$$E_a = \alpha_{BEP}\Delta H_R + \beta_{BEP} \tag{6.1}$$

$$E_{TS} = \alpha_{TSS}\Delta E + \beta_{TSS} \tag{6.2}$$

Catalytic activity tuning via lattice strain is not a novel concept and has been used in CO oxidation, oxygen reduction reaction, to give a few examples [1, 15, 22]. Recently, it was shown that the paradigm offered by the conventional BEP relation can also be circumvented by strain [13]. The potential of strain to break the scaling relation stems from the difference in adsorbate-surface interaction during the reaction progression. During the relaxation to the optimum adsorption conformation, the adsorbate exerts either an attractive or repulsive force to the surface. The force exerted by the adsorbate to the surface results in a lattice strain on the adsorption site. Consequently, the surface exerts force to adsorbate inducing molecular geometry changes.

These adsorbate-surface interactions can be amplified or reduced by an externally induced lattice strain. The interplay of the adsorption-attributed strain as well as the external material scale strain can result in the tuning of reaction energetics. As the reaction progresses, the geometric transition from the reactant to the product is accompanied by a change in surface interaction. A schematic of the concept is given as Fig. 6.2. An incongruent change in the interaction from reactant to product via the corresponding transition state can lead to the non-linear relations in reaction energetics. However, computational

catalysts screening normally assumes scaling relationship with respect to strain effects.

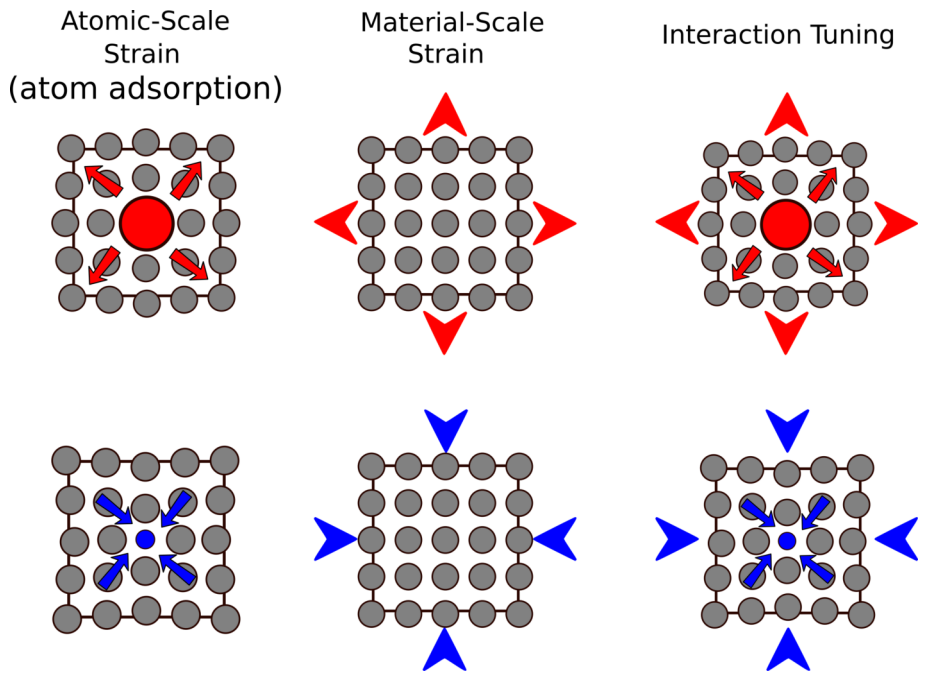

Figure 6.2: Potential of strain to tune reactivity and break scaling relations.

The surface adsorption energy is conventionally discussed by the d-band model which requires the calculation of d-band center of the metal surface [23]. An alternative model to assess the effect of compressive and tensile strain have recently been formulated by Khorshidi and colleagues which was coined as eigenstress model. Eigenstress model requires only the nuclear forces on the optimized adsorption complex in relaxed surfaces. Details of which will be further discussed later on this paper.

The objective of this work is to explore the effect of isotropic and anisotropic strain in the CO dissociation catalytic activity of Ru by sampling the relevant minimum energy pathways in Ru(0001) and Ru(1015) surfaces and its implications to the BEP relationship. Furthermore, adsorption energies are analyzed using both the conventional d-band model and the novel eigenstress model.

6.2 Computational Methodology

In this work, density functional theory (DFT) calculations are carried out using the GPAW package accompanied by the Atomic Simulation Environment (ASE) [6, 7, 14, 17]. Us-

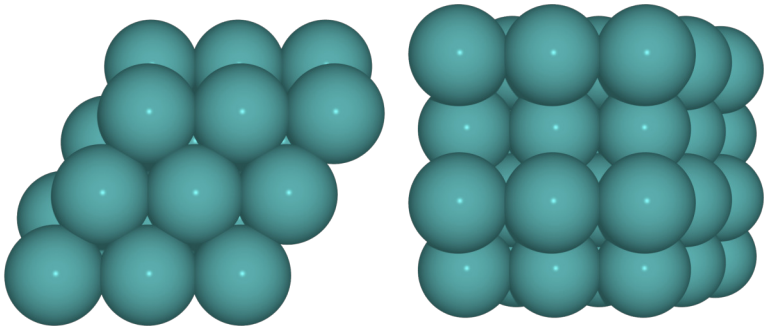

(a) (b)

Figure 6.3: Terrace Ru(0001) surface model in the (a) normal and (b) lateral views.

ing the available generalized gradient approximation (GGA) DFT functionals, it was determined that the revised Perdew–Burke–Ernzerhof (RPBE) functional, coupled with converged calculation parameters, afforded the closest crystal lattice parameters in comparison to the experimental values, and hence RPBE was chosen to account for the exchange-correlation [10]. The RPBE performance is expected as previous studies have also determined experimentally comparable lattice constants and energetics using this functional.

GPAW calculations were done in the plane-wave mode with an energy cutoff of 700 eV and real space grid spacing parameter h of 0.2, corresponding to 5 grid points per 1 Å. Self-consistent energies and its derivatives were achieved with Pulay density mixing using beta constant of 0.2 and 10 percent weight from 10 previous SCF iterations. Brillouin zone sampling for ruthenium unit cells converged with a Monkhorst-Pack 12x12x12 k-point grid [16]. These parameters are determined from bench-marking calculations.

To model ruthenium terrace sites, a 3x3 slab Ru(0001) surface was used. The Monkhorst-Pack k-point grid for the unit cell was scaled according to the surface model size, and hence we employed a 4x4x1 k-point grid [16]. Other calculation parameters are retained. Change in surface energy converged to < 0.01 meV/A using 4 layers and hence, was used throughout the study [8, 9]. Optimized Ru(0001) surface structures are illustrated in Figure 6.3.

The step sites were modeled using the Ru(1015) surface as illustrated in Figure 6.4.

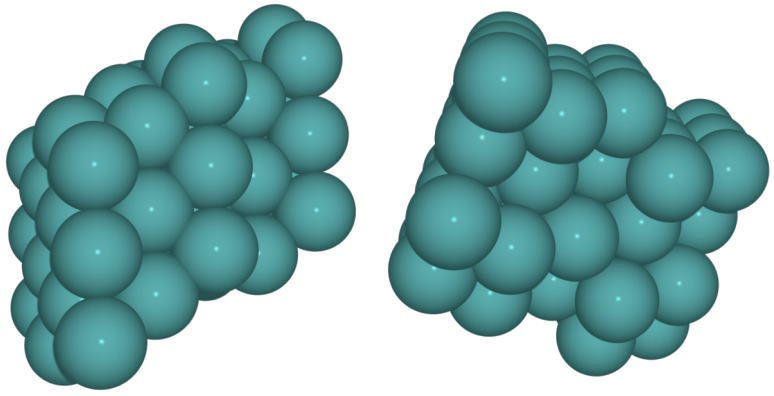

(a) (b)

Figure 6.4: Stepped Ru(1015) surface model in the (a) normal and (b) lateral views.

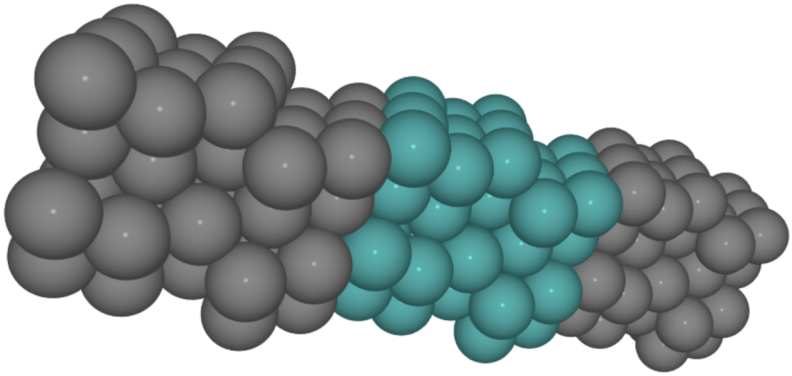

Figure 6.5: Stepped Ru(1015) surface model repeated along the x axis.

This model can be physically described as a Ru(0001) surface having step sites without kink sites. Similar to the terrace model, converged k-point sampling was scaled; hence, 2x4x1 k-point grid was used for all calculations for this surface. Number of layers was chosen to be similar to the terrace model along the Ru(0001) area of stepped Ru(1015) surface model.

To demonstrate the stepped structure of the Ru(1015) surface, the unit cell is repeated along the x axis and illustrated on Figure 6.5.

In this study, both isotropic and anisotropic strain were considered. Prior to the introduction of strain, Poisson ratio was determined. Poisson ratio is the quotient of the relative contraction strain to the relative extension strain which can be calculated as

$$\mu = -\frac{\varepsilon_{transverse}}{\varepsilon_{lateral}} \tag{6.3}$$

where strain is defined as

$$\varepsilon = \frac{\Delta L}{L_o} \tag{6.4}$$

At 3% expansion or compression, the calculated Poisson ratio is 0.31, which is comparable to the experimental value of 0.30 [18]. This can be interpreted that the physical changes due to the isotropic and anisotropic strain can be modeled using the calculation parameters described above. Additionally, the compressibility of the model material was also calculated using the Murnaghan equation of state and is determined to be 292 GPa. This value is closer to the experimental value of 220 GPa than the reported value of 330 GPa in the Materials Project. Materials Project is a consolidation of different theoretical calculations. This shows that the energetics of the strained cells are better described using our current calculation methods compared to the method described in the Materials Project. [12].

To achieve strained surface models, the previously optimized lattice constants were adjusted and geometry optimizations were done. Isotropic mode employed lattice constraints in both a and b cell parameters. Anisotropic mode employed lattice constraints only in a single lattice constant. For the terrace Ru(0001) slab model which has the same a and b constant, constraints were imposed along the a direction only, producing 5 unique slabs. On the other hand, the stepped Ru(1015) slab does not share the same symmetry and hence constraints were done along a and b separately, resulting in 7 unique slabs.

To calculate for the minimum energy pathways, climbing image nudged elastic band (CI-NEB) calculations were done by interfacing to Atomic Simulation Environment (ASE) with GPAW as the quantum chemical calculator while using the converged parameters described above [14]. Dynamic optimization and force scaling were used to hasten convergence of CI-NEB calculations [2, 11, 21]. CI-NEB path optimization was considered converged when the maximum atomic force is less than 0.05 eV/bohr.

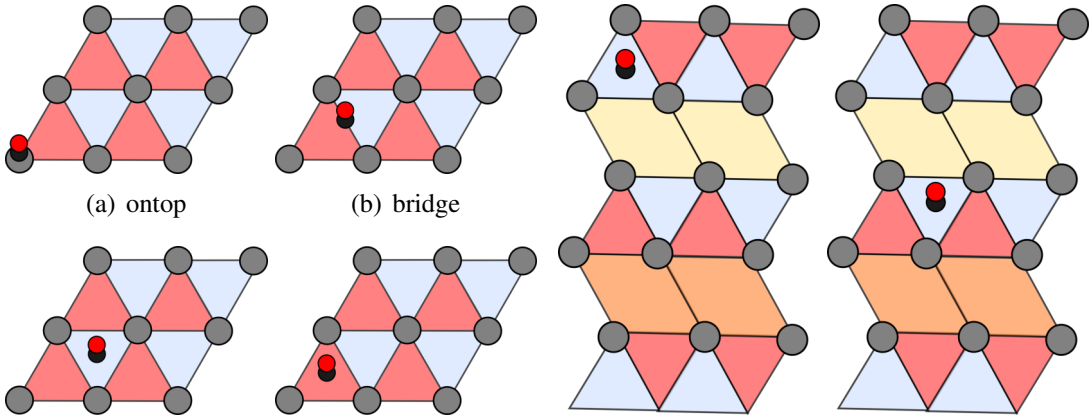

Figure 6.6: Adsorption Sites in (a-d) Terrace Ru(0001) and (e-f) Stepped Ru(1015)

6.3 Results and Discussion

To initiate this study, we investigated the carbon monoxide adsorption energetics in the terrace Ru(0001) slab model. In this slab, there are four unique adsorption sites: (1) on-top, (2) hexagonal-close pack (hcp), (3) face-centered cubic, (fcc) and (4) bridge sites. These sites are illustrated in a diagram in Figure 6.6. The adsorption energy calculations were done using a single CO molecule for both slabs.

Adsorption energy was calculated as

$$E_{ads} = E_{complex} - E_{CO} - E_{slab} \tag{6.5}$$

where $E_{complex}$, E_{CO} and E_{slab} are the energy of optimized CO-slab complex, CO and Ru slab, respectively.

Our calculation results showed a preferential adsorption on the *ontop* site with -37.9 kcal mol^{-1} which corresponds to the experimental at low coverage. This is followed by *hcp* with -32.9 kcal mol^{-1}, *bridge* with -31.33 kcal mol^{-1} and *fcc* with -31.0 kcal mol^{-1}. As these values are similar with each other, it can be considered that the CO molecule is mobile along the terrace sites. Similar discussion was done by other computational studies [19].

Adsorption energies were also calculated for the stepped Ru(1015) surface. As seen

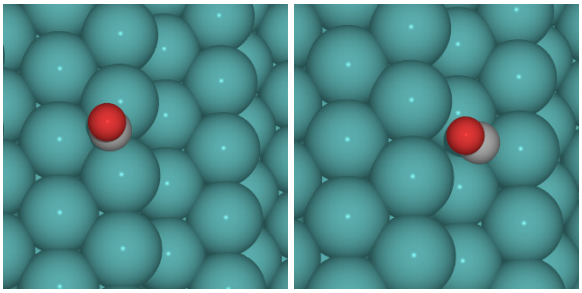

(a) (b)

Figure 6.7: CO adsorption geometries at (a) hcp-1 (b) hcp-2 sites in relaxed Ru(0015) surface.

in Figure 6.5, there are many unique adsorption sites in the model. Adsorption sites were limited to 2 unique *hcp* sites as illustrated in Figure 6.6. The difference in these sites is their chemical environments. Figure 6.7(a) corresponds to a step-edge site, while Figure 6.7(b) directly interacts with the stepped surface.

From the calculated adsorption energies, the uniqueness of these sites is demonstrated. It shows that the step-edge site has higher binding energies in comparison to the other. Corresponding adsorption geometries are given in Figure 6.7. Note that the CO at the *hcp-2* site is oriented laterally to the step site. This induces a decrease in the effective overlap of CO molecular orbital to the metal d-orbitals during adsorption. The calculated adsorption energies in the *hcp-1* and *hcp-2* sites are -35.29 kcal mol^{-1} and -30.58 kcal mol^{-1}, respectively. Adsorption energies are summarized in Tables 6.1 and 6.2 for Ru(0001) and Ru(1015), respectively.

Table 6.1: CO adsorption energies (kcal·mol^{-1}) at different adsorption sites in relaxed and strained Ru(0001).

Slab	On top	Bridge	HCP	FCC
Relaxed	-37.95	-31.32	-32.87	-31.00
Isotropic Expansion	-40.27	-39.04	-35.84	-33.31
Isotropic Compression	-36.56	-29.14	-30.12	-28.49
Anisotropic Expansion	-38.84	-31.84	-33.80	-33.80
Anisotropic Compression	-37.08	-29.92	-31.98	-30.13

Table 6.2: CO adsorption energies (kcal·mol^{-1}) at different adsorption sites in relaxed and strained Ru(1015).

Slab	HCP-1	HCP-2
Relaxed	-35.29	-30.58
Isotropic Expansion	-36.48	-33.27
Isotropic Compression	-33.89	-25.74
Anisotropic Expansion in a	-35.67	-31.86
Anisotropic Compression in a	-35.02	-29.14
Anisotropic Expansion in b	-35.73	-31.04
Anisotropic Compression in b	-35.21	-30.03

Prior to studying the CO dissociation reaction on both models, the effect of strain to adsorption energies was investigated. It is notable that adsorption geometries are generally maintained with the exemption of step-edge sites where relaxed and expanded cells have an upright CO orientation with respect to the normal vector of the step site, while the compressed cells have CO tilted towards the edge of the step. This can be seen in Figure 6.8 where the CO orientation in Figure 6.8(c) differs with Figures 6.8(a) and 6.8(b). This trend is also seen in anistorpically compressed lattices.

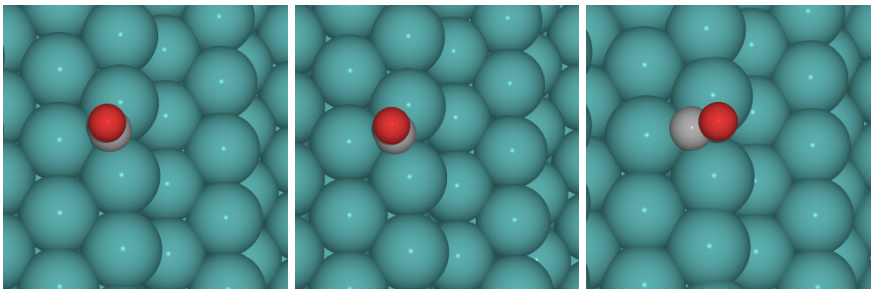

(a) (b) (c)

Figure 6.8: CO adsorption geometries at step-edgesite of (a) relaxed, (b) isotropically expanded, and (c) isotropically compressed Ru(0015) surface.

It is generally accepted that the adsorption energy of a molecule to a metal surface scales with the d-band center of the associated metal [23]. This is known as the d-band model given as Figure 6.9(a). The said model summarizes the contribution of metal orbitals to the adsorption in a single parameter which is the d-band center. According to the d-band model, the d-band center of the metal surface should lie at higher energies to achieve a

stronger adsorption. In contrast, adsorbents with a low-lying d-band center would have weaker adsorption. This can be rationalized in an orbital picture. If the metal d orbitals lie low, it would produce a stable bonding orbital upon hybridization with the molecular orbitals of the adsorbate. However, in consequence, it would also produce relatively low-lying antibonding orbitals. When electron fills up to the Fermi level, this would result in higher occupancy of these antibonding orbitals leading to a lower bond order.

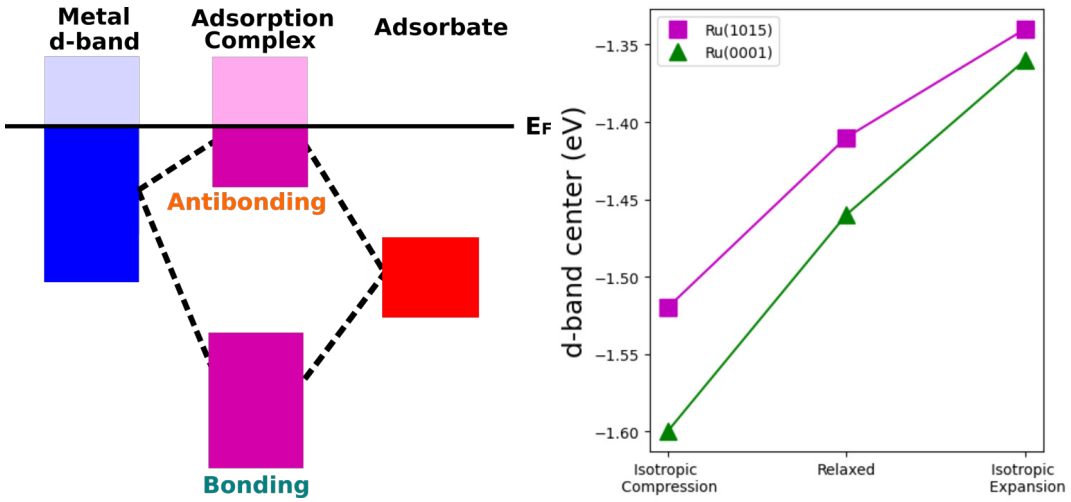

(a) (b)

Figure 6.9: (a) d-band model of adsorption and (b) calculated d-band center of Ru(0001) and Ru(1015) surfaces.

To study the adsorption phenomena according to this paradigm, the d-band centers of relaxed, isotropically compressed and expanded Ru(0001) and Ru(1015) surfaces were calculated and summarized as Figure 6.9(b). This shows that expansion pushes the d-band center to higher energy level while compression leads the d-band to lower energy level. The d-band centers of anisotropically stressed systems were also calculated and found to be intermediate to their isotropically stressed analogues and for simplicity was not reported.

CO adsorption energies at different sites of relaxed, and isotropically stressed systems are reported in Figure 6.10. It can be said that compression leads to weaker binding and expansion leads to stronger binding. As discussed above, the compression and expansion leads to a lower and higher d-band center, respectively. This shows that the d-band model of adsorption can qualitatively predict the effect of strain to adsorption.

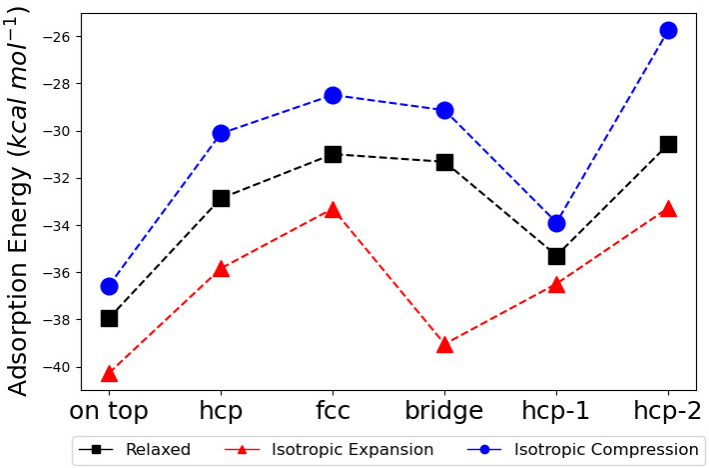

Figure 6.10: Adsorption energies in different sites of Ru(0001) and Ru(1015) Surface. Dashed lines are added for visualization.

A recent paper demonstrated a new model called eigenstress model to (semi)quantitatively predict changes in binding energies [13]. According to this formalism, binding energy changes due to strain can be summarized as

$$E_B(\varepsilon^0) = E_B(0) + E_{int}(\varepsilon^0, \sigma^*) \tag{6.6}$$

where

$$E_{int}(\varepsilon^0, \sigma^*) = -\int_V \sum_{i,j} [\varepsilon^0_{ij}(r)\sigma^*_{ij}(r)]dr \tag{6.7}$$

with ε and σ as the applied strain and adsorption eigenstress, respectively. The eigenstress is a tensor that accounts for the atomic level stress during adsorption, while the applied strain is the material level strain that can be introduced externally.

As Eq. 6.7 is non-trivial to determine, a qualitative description can be generalized as

$$E_B(\varepsilon^0) \begin{cases} > E_B(0) & \text{if } -\sum_{i,j} \varepsilon^0_{ij}\sigma^*_{ij} > 0 \\ < E_B(0) & \text{if } -\sum_{i,j} \varepsilon^0_{ij}\sigma^*_{ij} < 0 \end{cases} \tag{6.8}$$

The above equation can be physically interpreted that if the applied strain to the system relieves the stress due to adsorption of the molecule, this would lead to stronger binding.

Inversely, if the externally applied strain aggravates the adsorption induced stress, this would lead to a weaker binding. To further simplify the discussion, take for example, Figure 6.11. In Figure 6.11(a), which upon adsorption pushes the surface atoms producing positive eigenstress at the surface. In order to relieve such stress, lattice expansion can be applied so that the system can relax. While in a system with a negative eigenstress such as the case in Figure 6.11(b), the adatom pulls the surface atoms. This type of stress can be relieved if a compressive strain is applied to the surface.

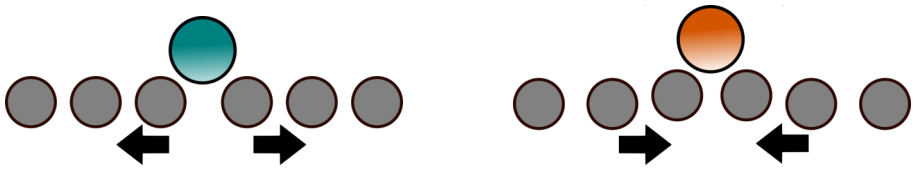

(a) (b)

Figure 6.11: Schema of (a) positive eigenstress, and (b) negative eigenstress due to adsorbate. Adapted by permission from Nature Catalysis. Ref. Alireza2018, COPYRIGHT (2018).

To verify its effectiveness in predicting changes in adsorption energy, this model is applied in our system. In Figure 6.12(a), the CO induces a positive eigenstress to the Ru surface. According to the above discussion, lattice expansion would relieve the stress resulting in a more stable binding. This was observed in our calculations and is given as Figure 6.12(b).

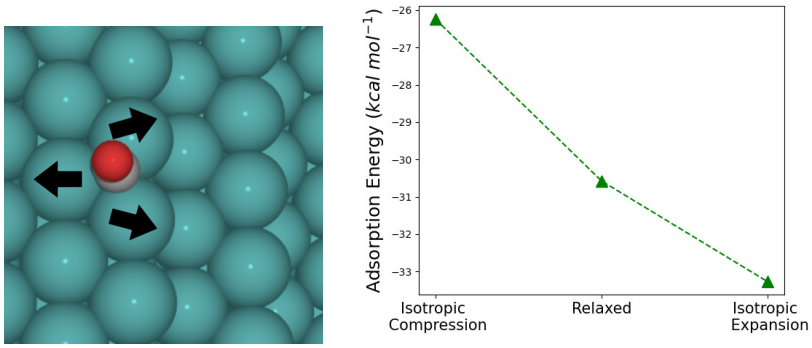

(a) (b)

Figure 6.12: Eigenstress Analysis. (a) Eigenstress, and (b) adsorption energy vs strain plot of CO adsorption in hcp-S1 site.

In this case, both d-band model and eigenstress model were able to qualitatively predict the changes in the adsorption energies due to strain. Therefore, it can be said that eigenstress can be an alternative to d-band model. Furthermore, force calculation in eigenstress model is already part of the routine calculation while d-band center calculation requires a density of states calculation and a subsequent d-orbital projections. That is to say, eigenstress model is an inexpensive alternative to the d-band model.

To study CO decomposition in our models, we calculated six unique pathways given as Figures 6.13 and 6.14. These pathways are a subset from a previous study which focused on relaxed Ru surface [3, 19]. In Path T1, CO sits on top of a Ru atom. At the converged minimum energy pathway, it was found that CO diffuses to the neighboring *hcp* site prior to dissociation. This observation was also found by Ciobica and Van Santen [3]. To offer a discussion on this diffusion, we calculated the projected density of states (PDOS) of this system. The DOS projected on CO molecular orbitals shows that the 2π orbital which is the lowest unfilled molecular orbital (LUMO) of the carbon monoxide increased in occupancy from 31.6% to 40.3% when moving from the *ontop* site to the *hcp* site. This prepares the CO molecule for the subsequent decomposition. The PDOS and integrated PDOS of CO on *ontop* and *hcp* of Ru(0001) surface are given in Figure 6.15. Path T2 is the preferred pathway in a terrace Ru(0001) surface with an E_a of 216.96 kcal mol^{-1} where the CO is initially located at the hcp site. In the corresponding transition state, the O sits asymmetrically in a *bridge* and *fcc* site. Path T3 and T4 have activation energies of 250.81 kcal mol^{-1}, and 209.27 kcal mol^{-1}, respectively. This is rationalized by the lesser stability of C and O in the fcc site relative to hcp site.

Activation energies from converged CI-NEB calculations are given as Table 6.3. This shows that the preferred pathway for CO dissociation in the Ru surface is Path S2 with calculated activation energy of 91 kcal mol^{-1}. This agrees with the known importance of the step sites in FT reactions as well as the accepted CO dissociation pathway [3]. The stability of this pathway can be associated with the transition state. As illustrated in Figure 6.16(e), the dissociating O is coordinated to two step-edge metal atoms. These atoms have

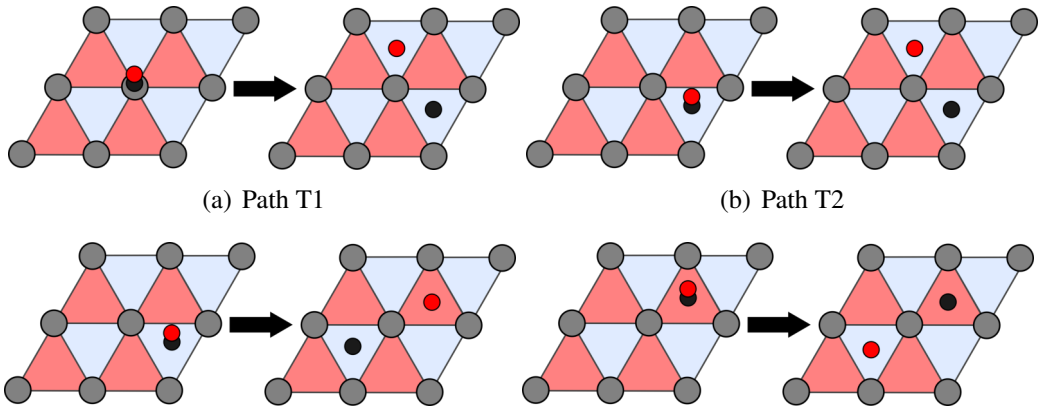

(a) Path T1 (b) Path T2

(c) Path T3 (d) Path T4

Figure 6.13: CO dissociation pathways sampled in Ru(0001) surface. ontop (gray), hcp (red), and fcc (blue).

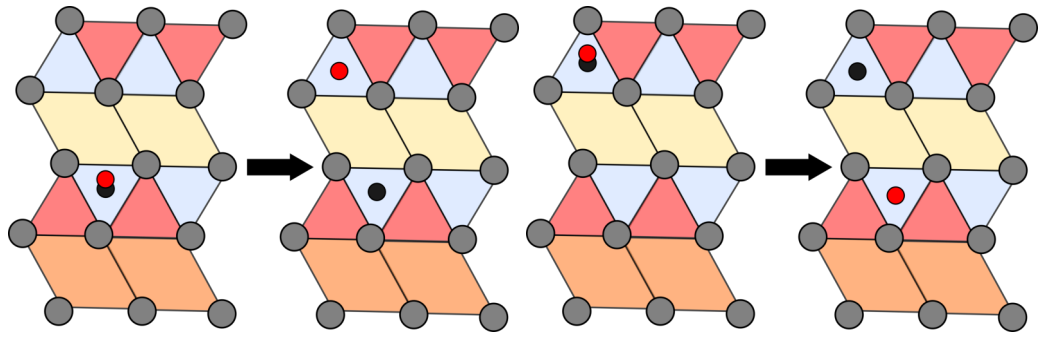

(a) Path S1 (b) Path S2

Figure 6.14: CO dissociation pathways sampled in Ru(1015) surface. ontop (gray), hcp (red), fcc (blue), yellow and orange(step layer).

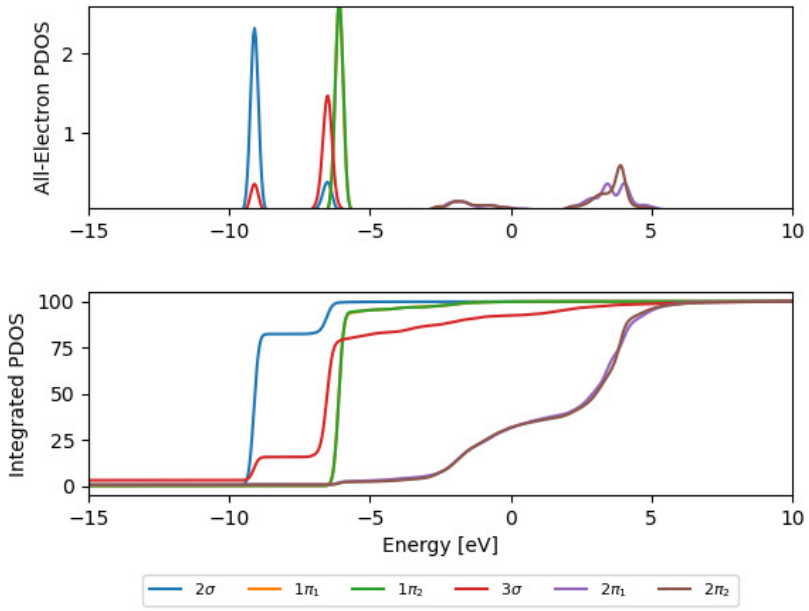

(a) ontop

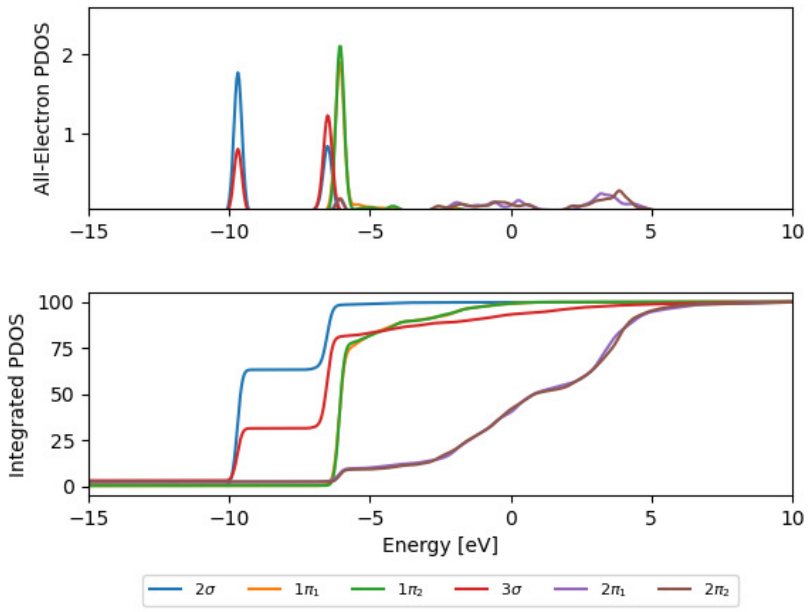

(b) hcp

Figure 6.15: PDOS and Integrated PDOS of CO at (a) ontop and (b) hcp sites on Ru(0001) surface.

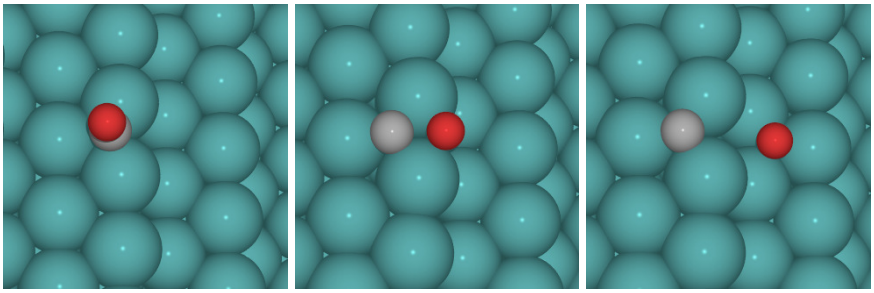

(a) R (b) TS (c) P

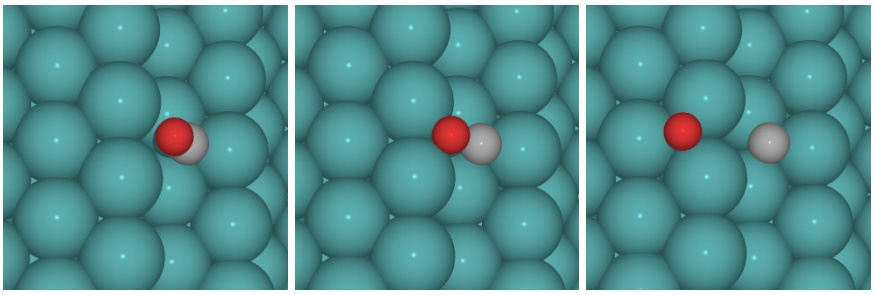

(d) R (e) TS (f) P

Figure 6.16: Optimized structures of reactants (R), transition states (TS), and products (P) in (a-c) Path S1 and (d-f) Path S2 in a relaxed Ru(1015) cell.

a higher number of dangling bonds, and hence metal associated stabilization is expected. In contrast, such stabilization is not seen in Figure 6.16(b) since the C atom is located in the nearby *hcp* site and is also coordinated to the step-edge Ru atoms.

Table 6.3: Calculated activation and reaction energies from different reaction pathways in the relaxed Ru(0001) and Ru(1015) surfaces.

Surface	Path	E_a		E_R	
		eV	kcal·mol $^{-1}$	eV	kcal· mol^{-1}
Ru(0001)	T1	2.47	238.23	0.64	61.97
	T2	2.25	216.96	0.42	40.71
	T3	2.60	250.81	0.42	40.41
	T4	2.17	209.27	0.62	59.74
Ru(1015)	S1	2.25	217.48	0.77	74.34
	S2	0.94	91.17	0.29	28.22

After determining dissociation reaction mechanism in the relaxed Ru(0001) and Ru(1015) surface. Corresponding reaction mechanisms in isotropically and anisotropically strained surfaces were calculated. To characterize the binding, charge density difference (CDD) maps were calculated for adsorption complexes [24]. Representative CDD maps

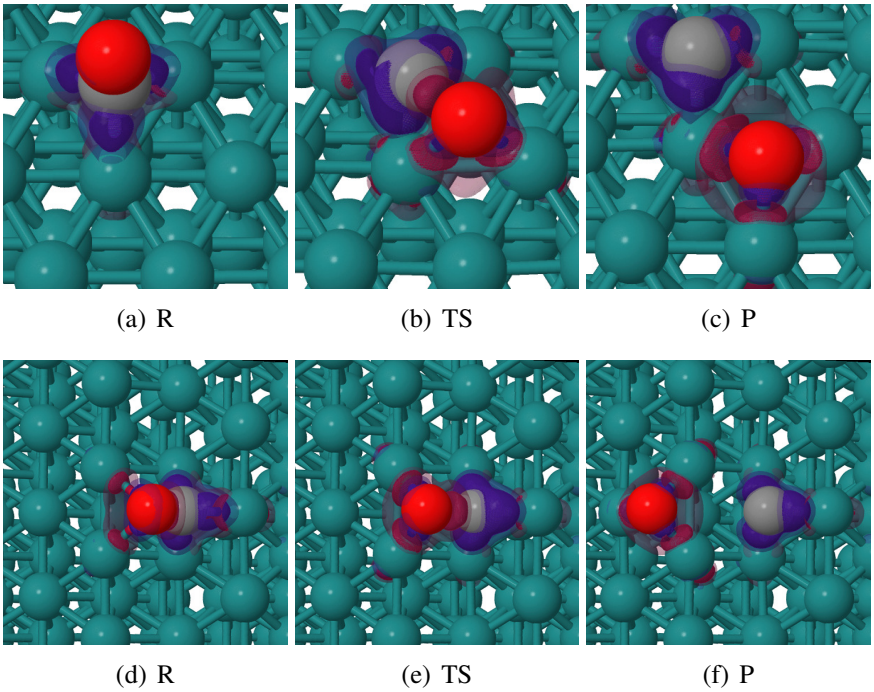

(a) R (b) TS (c) P

(d) R (e) TS (f) P

Figure 6.17: Charge Density Difference plots of reactants (R), transition states (TS), and products (P) in (a-c) terrace Ru(0001), and (d-f) stepped Ru(1015).

are given in Figure 6.17.

The electron flow is qualitatively maintained in all cases as depicted in the CDD maps attached on the Appendix C. This is expected as external force induced geometry changes do not change the electronic characteristic of an atom.

Bader charges also show a similar trend for all cases as seen in Figure 6.18. However, as electron distribution changes due to conformation, the magnitude of Bader charge differs with each case showing dependence on dissociation path and slab.

The effect of strain in Path T3 is given as Figure 6.19 where it can be easily seen that it follows scaling relation —that is the reaction energies and activation energies scale with each other [5]. Interestingly, expansion shows higher stabilization leading to a lower activation energy and reaction energy. Similar observations are seen in other paths and corresponding CI-NEB profiles are appended in Appendix C.

However, this is not the case in Path T4. A notable change in the minimum energy pathway is shown in Figure 6.20. At a relaxed state, the dissociation path starts with the diffusion of CO to a neighboring *hcp* site. CO then tilts until the CO bond is broken.

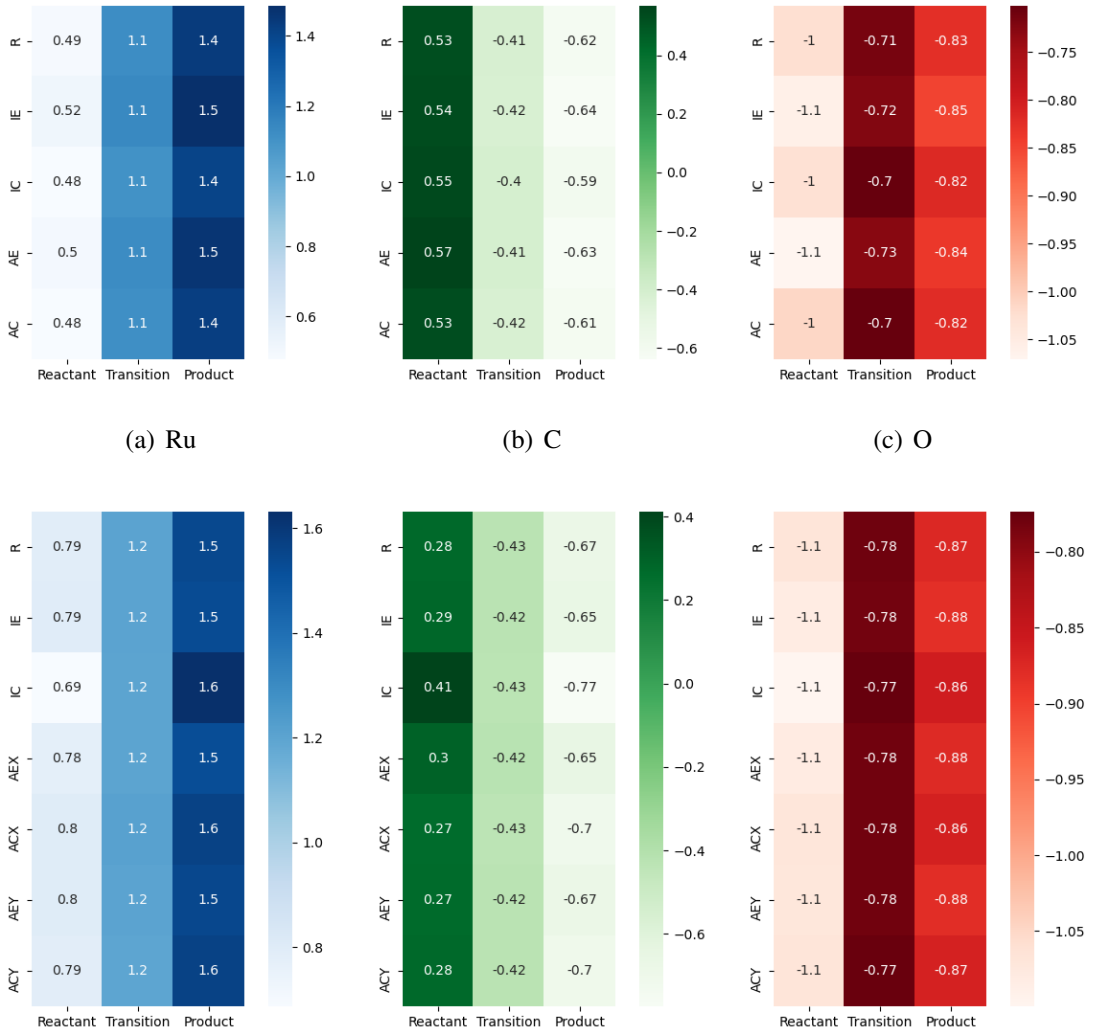

(a) Ru (b) C (c) O

(d) Ru (e) C (f) O

Figure 6.18: Bader charge analysis in (a-c) terrace Ru(0001) and (d-f) stepped Ru(1015). R-Relaxed, IE-Isotropic Expansion, IC-Isotropic Compression, AE(X/Y)-Anisotropic Expansion, AC(X/Y)-Anisotropic Compression.

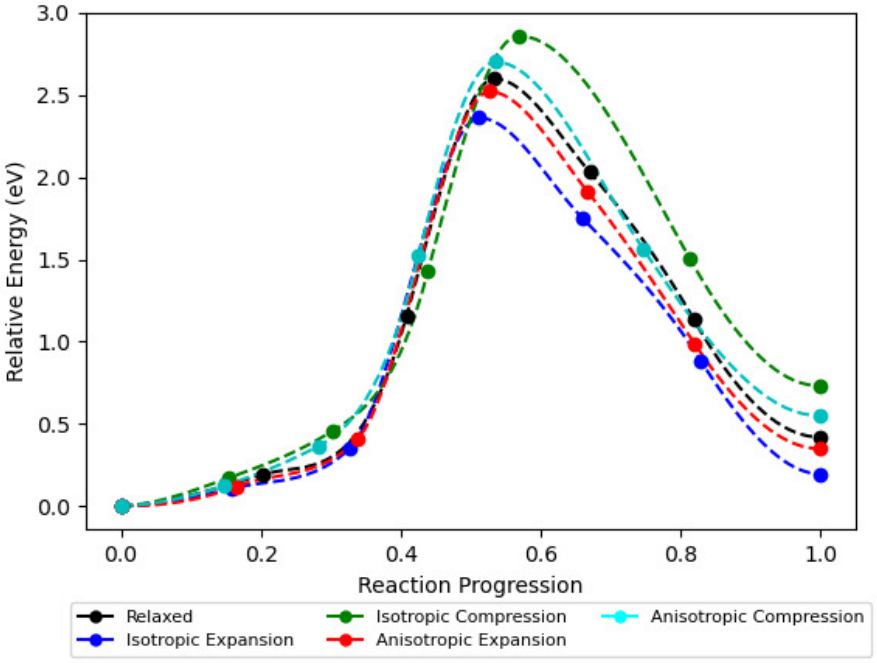

Figure 6.19: CI-NEB pathways for path T3 in terrace Ru(0001) surfaces.

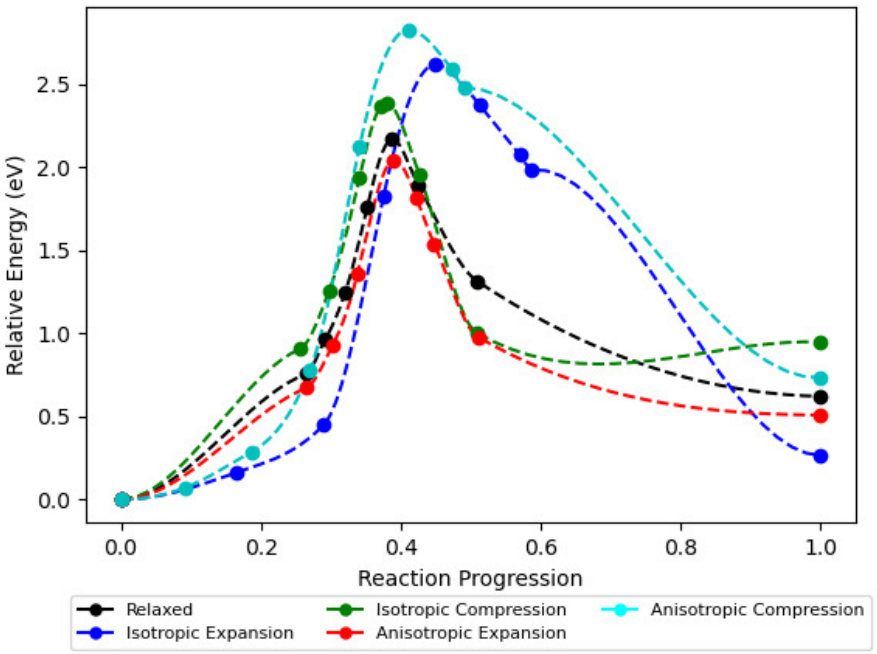

Figure 6.20: CI-NEB pathways for path T4 in terrace Ru(0001) surfaces.

In comparison, at an isotropically expanded Ru(0001) surface, the reaction proceeds directly from the *fcc* site through an *"over the hill"* transition state structure. The optimized structure of chemical reaction relevant extrema is shown in Figure 6.21. This shows that the strain—as a mechanochemical concept—changes the minimum energy pathway. Naturally, a change in the minimum path is an exemption to BEP and TSS scaling relations. Hence, reaction energy and activation energy of this pathway do not show a linear relation.

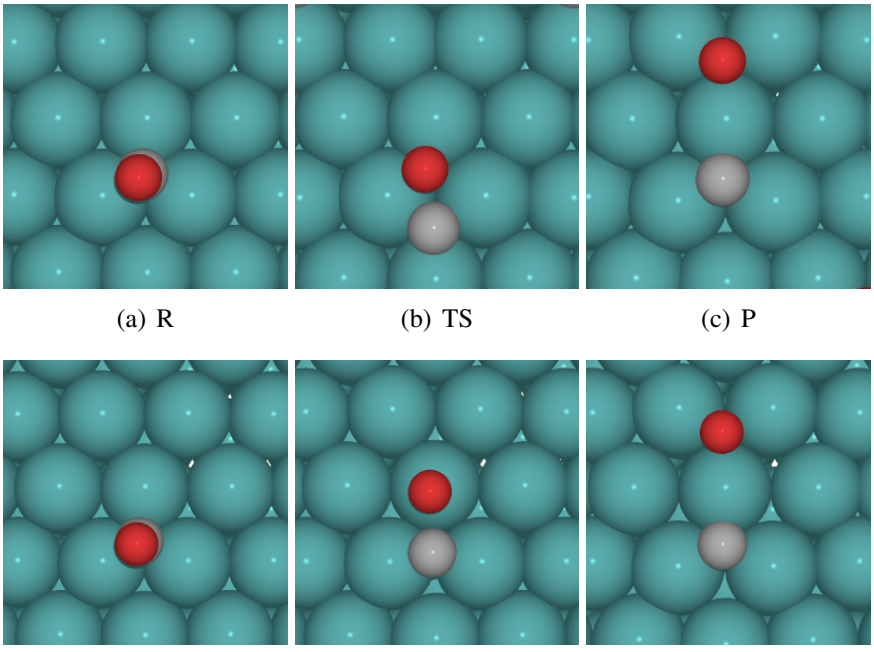

(a) R (b) TS (c) P

(d) R (e) TS (f) P

Figure 6.21: Optimized structures of reactants (R), transition states (TS), and products (P) in path 4 in (a-c) relaxed and (d-f) isotropically expanded Ru(0001) cell.

Another important concept in heterogeneous catalysis and a consequence of scaling relation is the Sabatier principle which is illustrated as Figure 6.22. This principle asserts that there is an optimum amount of slab interaction to attain optimum turn-over frequency. The kinetics of the reaction would be hindered by strong binding via a lowered product desorption. On the other hand, weak interaction to the surface would lead to inefficient activation of reaction.

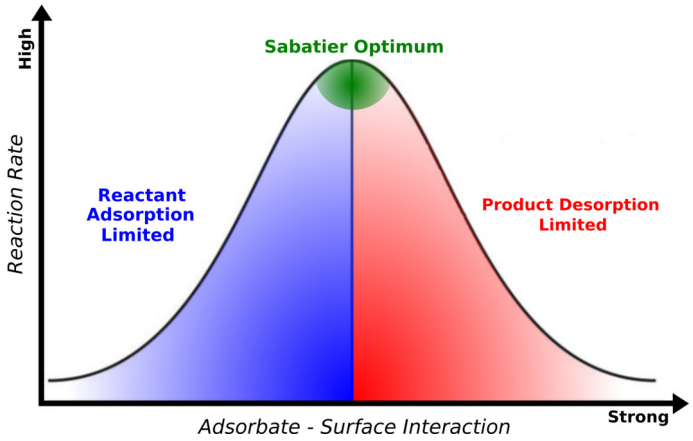

Figure 6.22: Schematic of Sabatier principle.

The premise of the Sabatier principle is that the adsorption energy of the reactant to the surface is directly proportional to the activation energy of the reaction. However, this was not followed in one of our simulations. In Path S2, 3% compression leads to a lower activation energy with a weaker adsorption as seen in Figure 6.23.

This curious result can be rationalized by the interaction energy with respect to the slab. Interaction energy is calculated as

$$E_{int} = E_{complex} - E_{CO}^{complex} - E_{slab}^{complex} \tag{6.9}$$

where $E_{complex}$ is the total energy of the system, $E_{CO}^{complex}$ and $E_{slab}^{complex}$ is the total energy of CO and slab at the complex geometry, respectively.

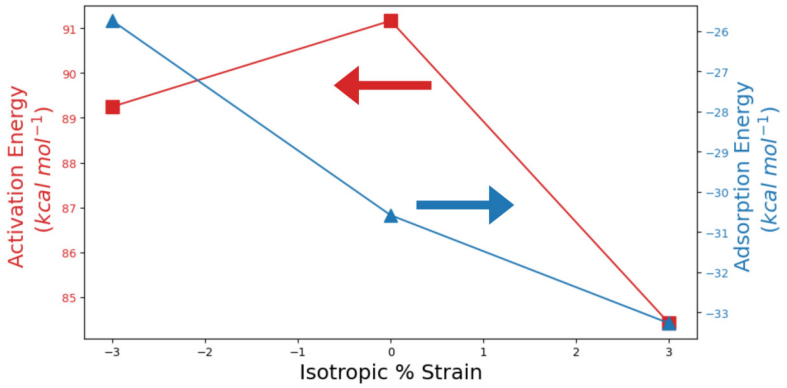

Figure 6.23: Adsorption energy (Red) in hcp-2 site and activation energy of Path S2 (Blue) of Ru(1015) surface as function of strain.

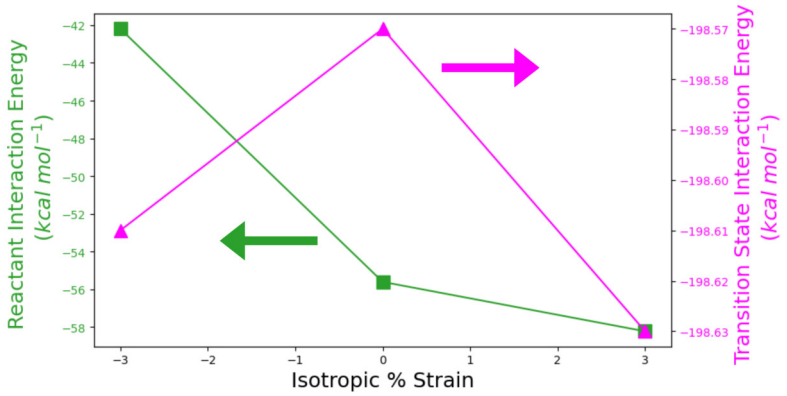

Figure 6.24: Interaction energy of reactant (green) and transition state (magenta) in hcp-2 site of Ru(1015) surface as function of strain.

Figure 6.24 shows that the trend in activation energy follows the trend in transition state interaction energy. It should also be noted that the reactant interaction energy follows that of adsorption. This shows that the slab contribution in stabilizing the transition state is different to that of the reactant which is seen as the different trend in adsorption and activation energies. In such cases, the Sabatier principle is not followed.

To discuss the physical relevance of Figure 6.24, we will take the isotropically expanded case as reference where we define the ratio of adsorbed CO and dissociating CO to be equal. In comparison to the reference, the relaxed slab would have more molecular CO absorbed to the surface than those proceeding to the dissociation reaction. The compressed Ru(1015) would correspond to a system with a higher ratio of dissociated CO than the currently absorbed CO. This break in relation may potentially lead to a more efficient catalyst for CO decomposition using Ru and other Fischer-Tropsch related metal systems such as copper, iron, and corresponding alloys.

6.4 Summary and Conclusions

In this work, the potential of isotropic and anisotropic strain in the heterogenous catalysis was explored. Specifically, the strain effects on the activity of terrace Ru(0001), and stepped Ru(1015) surfaces towards CO dissociation reaction was put in focus. Initially, the CO adsorption energies were calculated and found that on top site was preffered. Using

the stepped surface, the step-edge site was preferred which follows classical understanding of unsaturated dangling bonds.

The effect of the applied strain on the adsorption energy is well predicted by the d-band center model. The lowering of the d-band center during compression resulted to lower adsorption energy. Tensile strain has the exact opposite effect following the d-band model. In addition to this, the novel eigenstress model also provided the same prediction regarding the effect of external strain to CO adsorption.

In general, the electron flow remains qualitatively the same during adsorption and dissociation. This was supported by the similar Charge Density Difference plots in each slab. Trends in Bader charges are also the same. Compression afforded higher bader charges which signifies higher electron donation due to compressive strain.

There are several notable effects of surface strain to the calculated minimum energy pathway. Some pathways remained the same and its corresponding energies scales according to BEP and TSS relationships. On the other hand, some pathways proceeded through a different transition state. This effectively changes the NEB path and its energetics.

Furthermore, the adsorption scaling relation was also broken in the case of S2 path in an isotropicaly compressed Ru(1015) model. Activation energy was found to decrease rather than increase as expected by the BEP relation. This decrease is associated with the change in the interaction energy in the reactant and transition state complexes. This is another instance that the scaling relation in heterogenous catalysis can be broken due to applied strain.

The findings of this reseach exemplified the utility of mechanical stress to open up reaction pathways. This also opens up an escape from the adsorption scaling relation in heterogenous catalysis. Though compression allowed lower CO dissocation activation energy with respect to adsorption energy, the expected speed up for the Fisher-Tropsch reaction need to be validated by kinetic simulations or by experiments.

References

Asano, Masato et al. (2016). "Oxygen Reduction Reaction Activity for Strain-Controlled Pt-Based Model Alloy Catalysts: Surface Strains and Direct Electronic Effects Induced by Alloying Elements". In: *ACS Catalysis* 6.8, pages 5285–5289 (cited on page 122).

Berne, Bruce J, Giovanni Ciccotti, and David F Coker (1998). *Classical and Quantum Dynamics in Condensed Phase Simulations*. WORLD SCIENTIFIC (cited on page 126).

Ciobica, I. M. and R. A. van Santen (2003). "Carbon Monoxide Dissociation on Planar and Stepped Ru(0001) Surfaces". In: *The Journal of Physical Chemistry B* 107.16, pages 3808–3812 (cited on page 133).

Coulson, E. A. (1950). "The Fischer–Tropsch Process". In: *Nature* 533.166 (cited on page 121).

"Energy Trends in Catalysis" (2014). In: *Fundamental Concepts in Heterogeneous Catalysis*. John Wiley Sons, Ltd. Chapter 6, pages 85–96. ISBN: 9781118892114 (cited on page 137).

Enkovaara, J et al. (June 2010). "Electronic structure calculations with GPAW: a real-space implementation of the projector augmented-wave method". In: *Journal of Physics: Condensed Matter* 22.25, page 253202 (cited on page 123).

Enkovaara, Jussi et al. (2011). "GPAW - massively parallel electronic structure calculations with Python-based software". In: *Procedia Computer Science* 4. Proceedings of the International Conference on Computational Science, ICCS 2011, pages 17–25 (cited on page 123).

Greeley, Jeffrey (2016). "Theoretical Heterogeneous Catalysis: Scaling Relationships and Computational Catalyst Design". In: *Annual Review of Chemical and Biomolecular Engineering* 7.1. PMID: 27088666, pages 605–635 (cited on pages 122, 124).

Gross, A. (2002). "Theoretical Surface Science: A Microscopic Perspective". In: (cited on page 124).

Hammer, B., L. B. Hansen, and J. K. Nørskov (Mar. 1999). “Improved adsorption energetics within density-functional theory using revised Perdew-Burke-Ernzerhof functionals”. In: *Phys. Rev. B* 59 (11), pages 7413–7421 (cited on page 124).

Henkelman, Graeme, Blas P. Uberuaga, and Hannes Jónsson (2000). “A climbing image nudged elastic band method for finding saddle points and minimum energy paths”. In: *The Journal of Chemical Physics* 113.22, pages 9901–9904 (cited on page 126).

Jain, Anubhav et al. (2013). “The Materials Project: A materials genome approach to accelerating materials innovation”. In: *APL Materials* 1.1, page 011002 (cited on page 126).

Khorshidi, Alireza et al. (2018). “How strain can break the scaling relations of catalysis”. In: *Nature Catalysis* 263 (268), pages 2520–1158 (cited on pages 122, 131).

Larsen, Ask Hjorth et al. (June 2017). “The atomic simulation environment—a Python library for working with atoms”. In: *Journal of Physics: Condensed Matter* 29.27, page 273002 (cited on pages 123, 126).

Liu, Fuzhu et al. (2015). “CO Oxidation over Strained Pt(100) Surface: A DFT Study”. In: *The Journal of Physical Chemistry C* 119.27, pages 15500–15505 (cited on page 122).

Monkhorst, Hendrik J. and James D. Pack (June 1976). “Special points for Brillouin-zone integrations”. In: *Phys. Rev. B* 13 (12), pages 5188–5192 (cited on page 124).

Mortensen, J. J., L. B. Hansen, and K. W. Jacobsen (Jan. 2005). “Real-space grid implementation of the projector augmented wave method”. In: *Phys. Rev. B* 71 (3), page 035109 (cited on page 123).

Research, Wolfram (2014). *ElementData*. `https://reference.wolfram.com/language/ref/ElementData.html` (cited on page 126).

Shetty, Sharan and Rutger A. van Santen (2011). “CO dissociation on Ru and Co surfaces: The initial step in the Fischer–Tropsch synthesis”. In: *Catalysis Today* 171.1, pages 168–173 (cited on pages 127, 133).

Shi, Jian and Long-Qing Chen (2019). “Strain Engineering in Functional Materials”. In: *Journal of Applied Physics* 125.8, page 082201 (cited on page 122).

Smidstrup, Søren et al. (2014). "Improved initial guess for minimum energy path calculations". In: *The Journal of Chemical Physics* 140.21, page 214106 (cited on page 126).

Temmel, Sandra E. et al. (2016). "Investigating the Role of Strain toward the Oxygen Reduction Activity on Model Thin Film Pt Catalysts". In: *ACS Catalysis* 6.11, pages 7566–7576 (cited on page 122).

"The Electronic Factor in Heterogeneous Catalysis" (2014). In: *Fundamental Concepts in Heterogeneous Catalysis*. John Wiley Sons, Ltd. Chapter 8, pages 114–137. ISBN: 9781118892114 (cited on pages 123, 129).

Wang, Linfeng et al. (2019). "The electronic behaviors and charge transfer mechanism at the interface of metals: A first-principles perspective". In: *Journal of Applied Physics* 126.20, page 205301 (cited on page 136).

Wang, Shengguang et al. (2014). "Brønsted–Evans–Polanyi and Transition State Scaling Relations of Furan Derivatives on Pd(111) and Their Relation to Those of Small Molecules". In: *ACS Catalysis* 4.2, pages 604–612 (cited on page 122).

VII Generalizations and Outlook

The growing application of mechanochemistry to various fields of chemistry has been rapidly increasing. However, elucidation of the reaction mechanism in situ remains very limited. This present dissertation aimed to bridge chemical understanding of mechanochemical reaction. The first part of the dissertation introduces the rudiments of mechanochemistry in the context of catalysis. As the interplay of mechanical force in chemical systems provides a variety of associated effects. One of which is the modification of the potential energy surface as a function of magnitude and direction of applied external force. This then initiates relocations of minima and maxima in such PES, and consequently, affects reaction thermodynamics and kinetics. In addition to this, mechanochemical techniques such as ball milling also induces thermal heating due to friction.

In Chapter 2, fundamentals of computational chemistry, specifically density functional theory is presented. The development of DFT has been discussed starting from the original idea of Thomas and Fermi, to the Hohenberg-Kohn theorems which formalized and mathematically proved the existence of such functional, and finally to the inclusion of orbital basis in the Kohn-Sham equations. This provides the reader with a working knowledge of DFT computations. In the latter part of the chapter, the reader is provided

with the introduction of quantum chemical software packages used in this work. SIESTA and GPAW are modern quantum chemical software packages which scale linearly $O(N)$ with the number of atomic orbitals. SIESTA achieves linear scaling using pseudopotential formalism in combination with strictly localized basis functions. Numerical grid-based integration is also done for three-center integrals. On the other hand, GPAW is the first real space grid-based implementation of the projector augmented wave (PAW) formalism. Using a transformation matrix, the ultrasoft psuedowavefunction is mapped to an all-electron wavefunction. This renders GPAW, effectively, an all-electron quantum chemical software.

Chapter 3 provides a review of mechanochemical pulling formalism that have been developed throughout the years. Though these formalisms do not directly translate to other mechanochemical techniques other than single molecule pulling in AFM experiments, the utility of such methods have been extended to different mechanochemical techniques such as ball milling and sonication. Additionally, with the advent of a Generalized Force Modified Potential Energy Surface formalism, high pressure chemistry can be simulated without the use of periodic boundary conditions. This chapter also discussed the developed python module, mechanochem, which provides classes and functions that permits inclusion of external force according to several pulling formalisms during geometry optimization and molecular dynamics. Additionally, a constricting wall potential is implemented. The mechanochem module works in tandem with Atomic Simulation Environment (ASE) which is an open source code that can patch 45 different quantum chemistry and molecular mechanics software as a quantum chemical calculator. This includes popular software packages such as Gaussian, ORCA, and Amber among others.

A collection of theoretical studies on mechanochemical catalysis is given in Chapters 4, 5 and 6. This included the effect of mechanical forces such as push and pull to the reaction center. In addition to this, the effect of stain in the catalyst to its catalytic activity is also studied.

In Chapter 4, the effect of ball milling to the acid catalyzed selective hydrolysis of

chitin is studied. External mechanical forces are expected to affect the polymer along the chain and pulling simulations were done according to the Force Modified Potential Energy Surface (FMPES) formalism. Pulling simulations showed a decrease in the activation energy for the depolymerization. This can be explained by the increase in basicity of the glycosidic oxygen driven by force-induced conformational change.

The effect of pushing is introduced in Chapter 5. A recent trend in mechanochemical synthesis is the use of reactive additives, presumably to act as catalytic surface, during ball milling. A recent experiment found that silver foil induces a selective cyclopropanation under mechanochemical conditions. Using a single surface slab, trends in activation energy do not follow that of the experiment which proves that external force associated effect is needed to drive the stereoselectivity. To mimic the experimental condition, an unconventional sandwich slab model is used in this study and found that the constricted reaction environment drives the reaction to the E isomer as seen in the experiment.

In contrast to the previous chapters where mechanical effects were directed toward the reaction center, Chapter 6 presented a study in which the catalytic surface is subjected to mechanical strain. Specifically, Ru(0001) and Ru(1015) surface models were subjected to isotropic and anisotropic compressive and tensile strain. Here, CO decomposition, the initial reaction in Fischer-Tropsch reaction, is studied. In general, the effect of strain on adsorption energies follows the long accepted d-band model. Interestingly, the novel eigenstress model arrives with similar predictions. It is curious but not surprising to find that some converged NEB pathways differ with application of stress. This exemplifies that stress and strain can open new chemical reaction routes. Furthermore, a break in scaling relations was also found. Typical heterogeneous catalyst screening relies on such scaling relation for activity prediction. This study proves that applied strain can cause unexpected effects in reaction energetics. The interplay of the original intricacy of any chemical system and force vector activation dramatically increases the computational complexity of studying mechanochemical reactions. This is the consequence of the force being a vector which can affect the potential energy surface with its magnitude and applied direction. In

addition to this, the rate of applying the forces is also expected to affect the kinetics and mechanism of reaction. With these given points, a general effect and a unified model is difficult, if not impossible, to be drawn. However, fundamental points of considerations in understanding mechanochemistry can be drawn from the several topics presented. The presented work can also serve as general simulation protocols to mimic the effect of forces in a variety of mechanochemical reaction systems.

Appendices

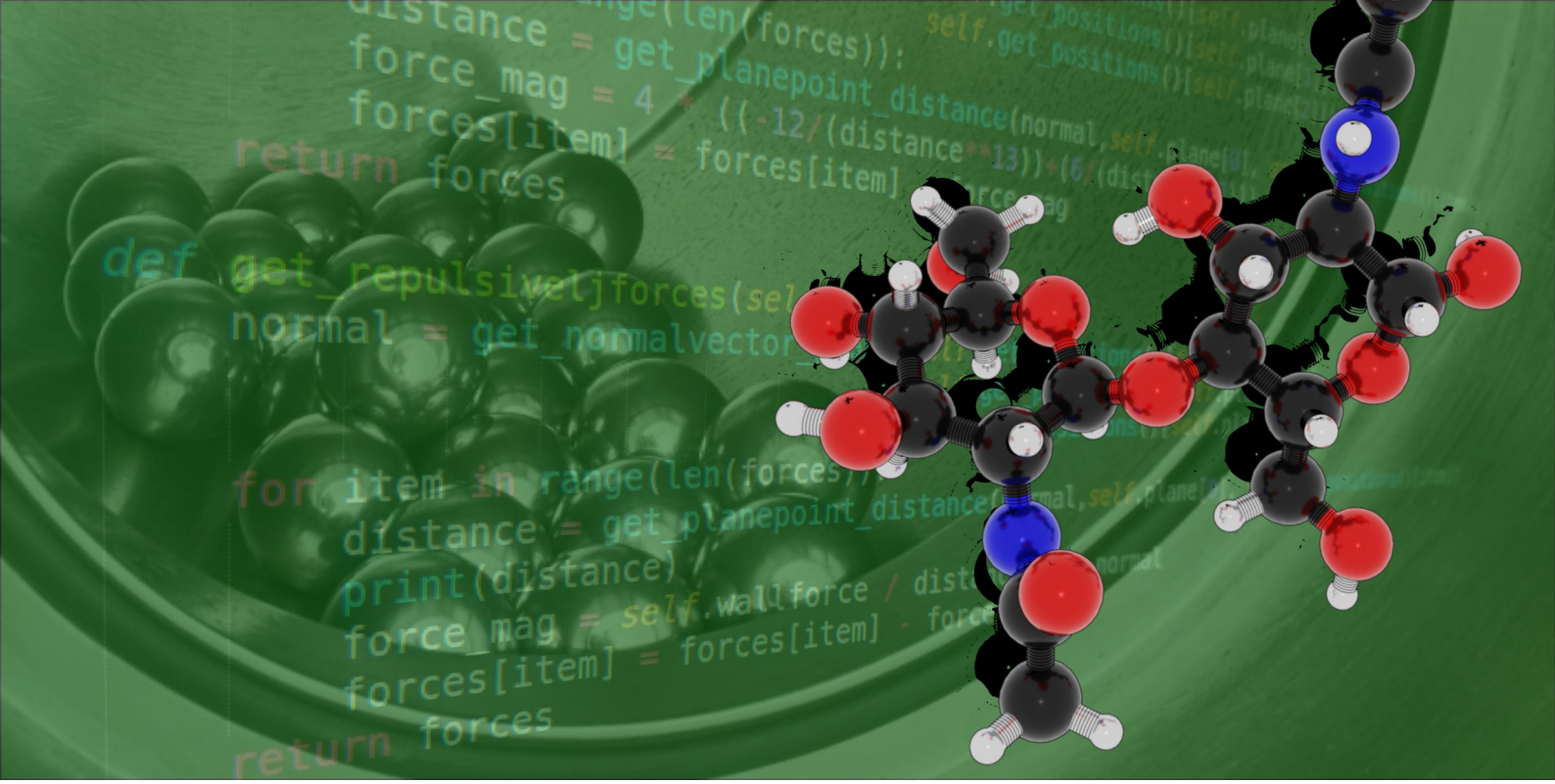

Force diagram of a ball bombarding to a molecular plane

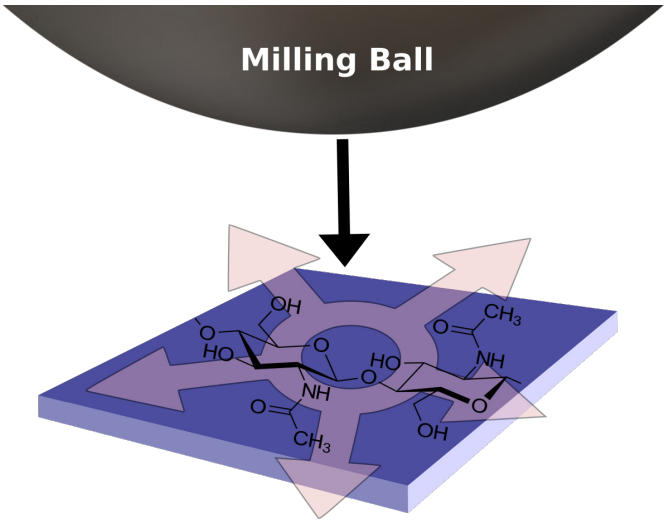

Figure 8.1: Force Diagram in a Ball Bombarding to Plane

In ball milling, a ball pounds the sample inside an inert metallic cell. As the size of ball is much greater than any molecular size, the bombardment would introduce external forces both coplanar and noncoplanar to the molecular plane of chitin oligomer. The force diagram of the coplanar forces can be illustrated as above. As described in the Chapter 4, these forces can be added and hence a resultant linear vector can be expected.

Optimized Structures at the RDS of the Deacetylation

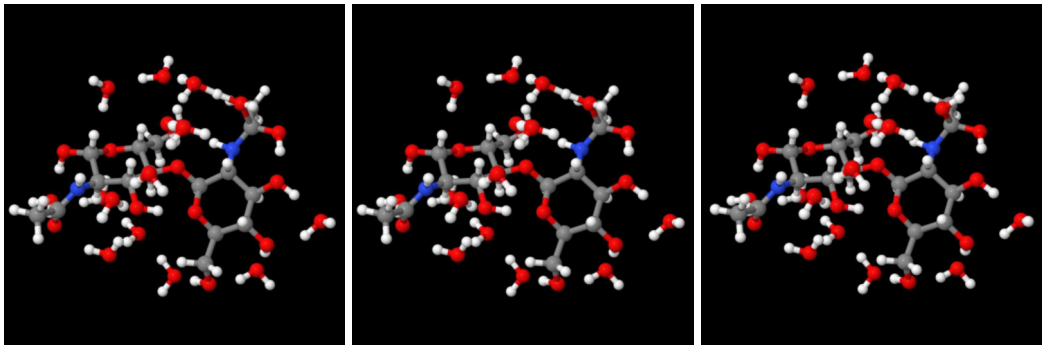

(a) (b) (c)

Figure 8.2: Deacetylation RDS (Nucleophilic Attack of Water). Optimized structures of (a) A_Int1' (b) A_TS2 and (c) A_Int2. See Figure 1 for labels

This step starts with a protonated carboxyl oxygen (Fig. S8.2(a)) which has an increased reactivity towards the nucleophilic attack of water. In Fig. S8.2(c), it can be seen that the attacking water lost a proton and resulted to a protonated neighboring water molecule. This is captured in the imaginary frequency of the corresponding transition state, Fig. S8.2(b), which is charaterized by C_{GlcNAc}-O_{water} bond formation and O_{water}-H_{water} bond breaking.

Optimized Structures at the RDS of the Depolymerization

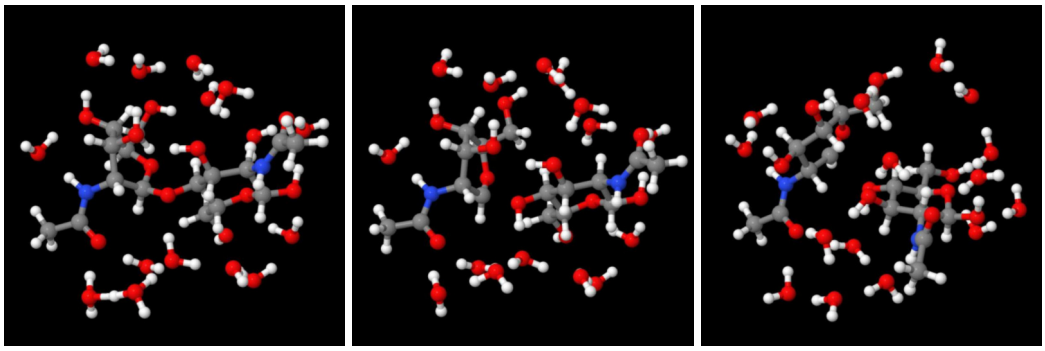

(a) (b) (c)

Figure 8.3: Depolymerization RDS (Carbocation Formation). Optimized structures of (a) P_Int1 (b) P_TS2 and (c) P_Int2. See Figure 1 for labels

Depolymerization RDS is the formation of carbocation specie. In Fig. S8.3(a), the solvated proton is within the reaction center. The imginary frequency of the transition state (Fig. S8.3(b)) shows protonation of the glycosidic oxygen and cleavage of the glycosidic bond. This occurs with a proton relay thru the nearest water molecule from the glycodic oxygen.

Structure Progression RMSD Matrices

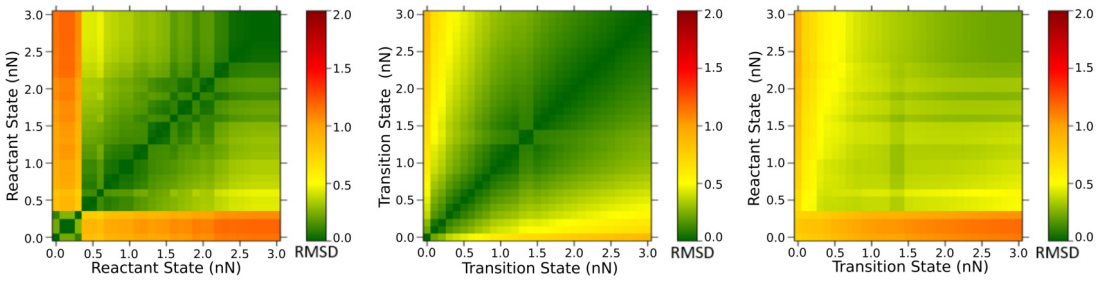

(a) (b) (c)

Figure 8.4: Depolymerization RMSD Matrices for Pulling Direction B for (a)Reactant-Reactant (b)Transition State-Transition State and (c)Reactant-Transition State Comparisons

Structure progression in Pulling Direction B is similar to Pulling Direction A. It can be seen that the diagonal of the reactant - transition state matrix decreases in value. This shows that the reactant and transition state structures converges together. It can be seen in Figures 8.4(a) and 8.4(b), that the reactant structure is more susceptible to the applied force. Same conclusion can be drawn that the reactant structure approaches that of the transition state.

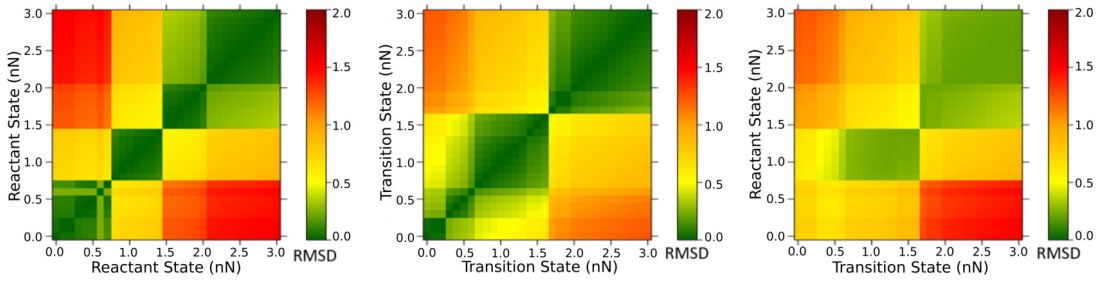

(a) (b) (c)

Figure 8.5: Depolymerization RMSD Matrices for Pulling Direction C for (a)Reactant-Reactant (b)Transition State-Transition State and (c)Reactant-Transition State Comparisons

In the Pulling Direction C, multiple sections can be seen that does not correlate tochanges in total energy. These can be attributed to the changes in water environment which drives the changes calculated RMSD. At the 0.7 nN boundary, it can clearly be seen that reactant and transition state structure converges as well. Similar to the other directions, it can be attributed to the reactant structure approaching that of the transition state structure.

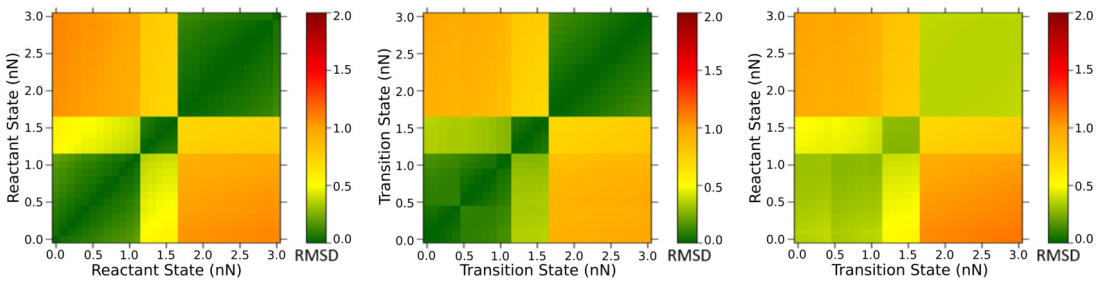

(a) (b) (c)

Figure 8.6: Deacetylation RMSD Matrices for Pulling Direction B for (a)Reactant-Reactant (b)Transition State-Transition State and (c)Reactant-Transition State Comparisons

In this representative RMSD matrices for the deacetylation, it can be seen that though the reactant and transition state structure changes with the application of force, the structural difference of the reactant and transition state remains the same. This can be seen in the diagonal of the Figure 8.6(c). This conserved structural difference was expected to the energy trend previously calculated.

Energy Decomposition Analysis

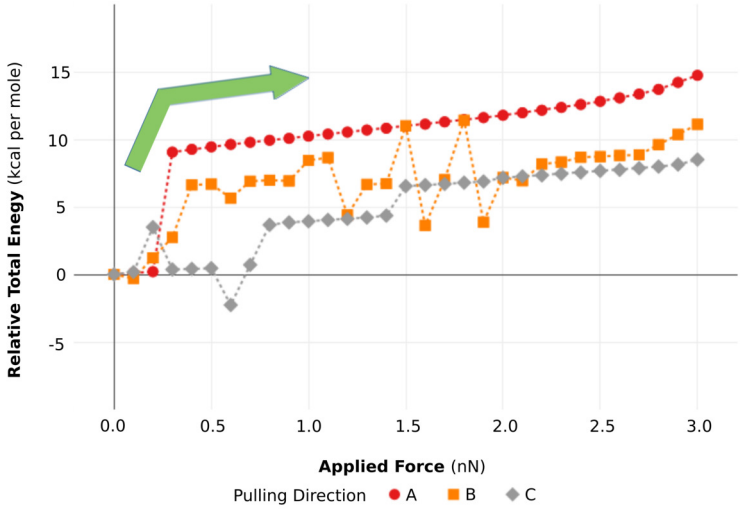

Figure 8.7: Calculated GlcNAc dimer - solvent interaction energy of the depolymerization reactant state as a function of external force

As discussed in the main text, the activation of the depolymerization is mainly attributed to the change in the conformation of the reactant. In Figure 8.7, it can be seen that the destabilization in the reactant state can be anchored to GlcNAc Dimer - Solvent Interaction.

This was concluded since the force required to increase the energy of the reactant is also the same energy in which the GlcNAc Dimer - Solvent interaction decreased.

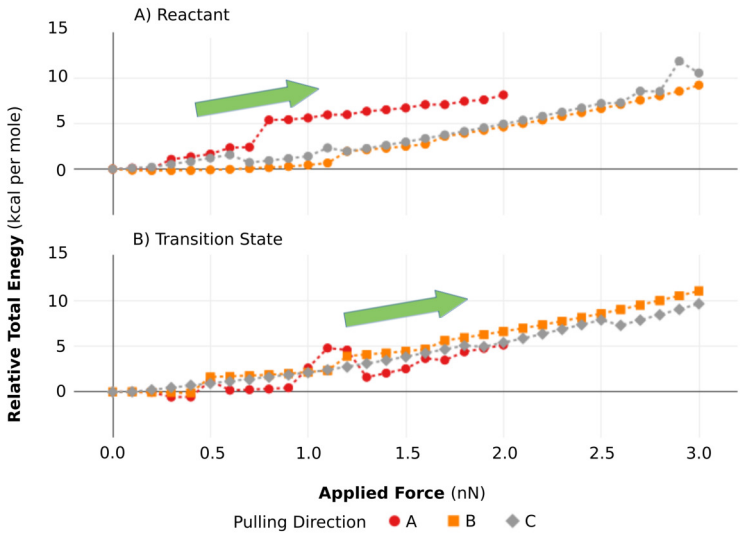

Figure 8.8: Selected energies in the decomposition analysis. GlcNAc dimer of (a)reactant and (b)transition state single point energy of the deacetylation reactant as a function of external force

GlcNAc dimer contribution to total energies both follow a monotonic increase as function of the applied force. It can be seen that the destabilization brought by force to reactant state is very similar in magnitude to its effect in the transition state. This trend corresponded to calculated activation energy in FMPES using the chemical model described in main text (See Figure 5).

Second Order Perturbation Theory Analysis of Deacetylation

Table 8.1: Stabilizing interaction E(2) (kcal mol^{-1}) for deacetylation reactant state at different directions and forces

Pulling	Interaction		Applied Force (nN)						
Direction	Donor	Acceptor	0.00	0.50	1.00	1.50	2.00	2.50	3.00
A	n_{O3-1}	σ^*_{O7H}	1.97	1.99	2.07	2.13	2.15		
	n_{O3-2}	σ^*_{O7H}	49.73	51.68	55.17	55.93	56.08		
B	n_{O3-1}	σ^*_{O7H}	1.97	1.96	1.97	2.06	2.19	2.21	2.23
	n_{O3-2}	σ^*_{O7H}	49.73	51.40	51.96	54.89	59.91	60.62	61.27
C	n_{O3-1}	σ^*_{O7H}	1.97	1.96	1.99	2.00	2.03	2.03	2.06
	n_{O3-2}	σ^*_{O7H}	49.73	51.06	53.41	54.26	54.54	55.00	57.99

Selected Natural Bonding Orbital Occupancies

Table 8.2: Selected orbital occupancies for deacetylation reactant state at different directions and forces

Pulling Direction	Orbital	Applied Force (nN)						
		0.00	0.50	1.00	1.50	2.00	2.50	3.00
A	σ^*_{N2C7-1}	0.043	0.043	0.043	0.044	0.043		
	σ^*_{N2C7-2}	0.330	0.334	0.333	0.334	0.332		
	σ^*_{O7C7}	0.027	0.027	0.027	0.028	0.027		
	σ^*_{C7C8}	0.021	0.021	0.022	0.022	0.022		
	σ^*_{C7H}	0.111	0.114	0.119	0.119	0.120		
B	σ^*_{N2C7-1}	0.043	0.043	0.044	0.046	0.044	0.044	0.044
	σ^*_{N2C7-2}	0.330	0.331	0.332	0.335	0.335	0.335	0.336
	σ^*_{O7C7}	0.027	0.031	0.042	0.052	0.036	0.038	0.041
	σ^*_{C7C8}	0.021	0.021	0.021	0.021	0.022	0.022	0.022
	σ^*_{C7H}	0.111	0.113	0.114	0.118	0.125	0.126	0.126
C	σ^*_{N2C7-1}	0.043	0.041	0.043	0.043	0.044	0.044	0.044
	σ^*_{N2C7-2}	0.330	0.338	0.333	0.334	0.335	0.335	0.343
	σ^*_{O7C7}	0.027	0.027	0.026	0.026	0.039	0.029	0.082
	σ^*_{C7C8}	0.021	0.021	0.021	0.021	0.021	0.021	0.021
	σ^*_{C7H}	0.111	0.113	0.116	0.118	0.118	0.119	0.124

Table 8.3: Selected orbital occupancy for depolymerization reactant state at different directions and forces

Pulling Direction	Orbital	AppliedForce (nN)						
		0.00	0.50	1.00	1.50	2.00	2.50	3.00
A	σ^*_{C1O1}	0.048	0.085	0.085	0.085	0.084	0.083	0.081
	σ^*_{C1O5}	0.036	0.037	0.041	0.048	0.042	0.042	0.043
B	σ^*_{C1O1}	0.048	0.077	0.078	0.075	0.075	0.082	0.079
	σ^*_{C1O5}	0.036	0.036	0.036	0.039	0.040	0.038	0.041
C	σ^*_{C1O1}	0.048	0.050	0.075	0.089	0.092	0.095	0.096
	σ^*_{C1O5}	0.036	0.036	0.035	0.034	0.033	0.033	0.033

Optimized Structures Phenyldiazoaceteate Decomposition

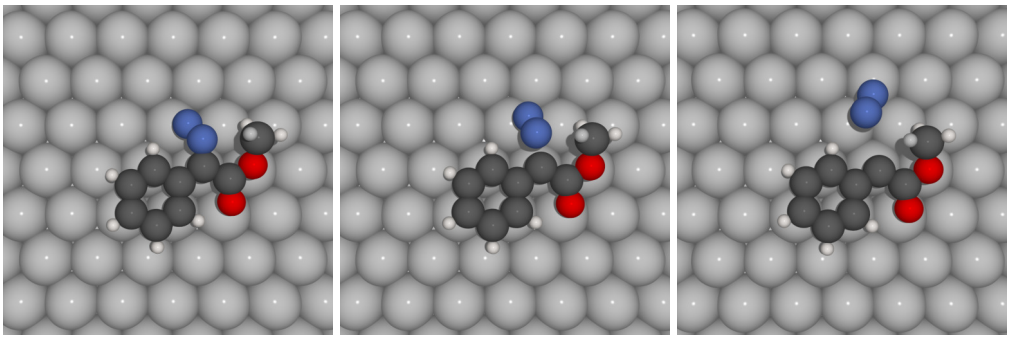

(a) (b) (c)

Figure 9.1: Optimized structures of (a) reactant, (b) transition state, and (c) product for phenyldiazoaceteate decomposition starting from ontop-sitting procarbene carbon

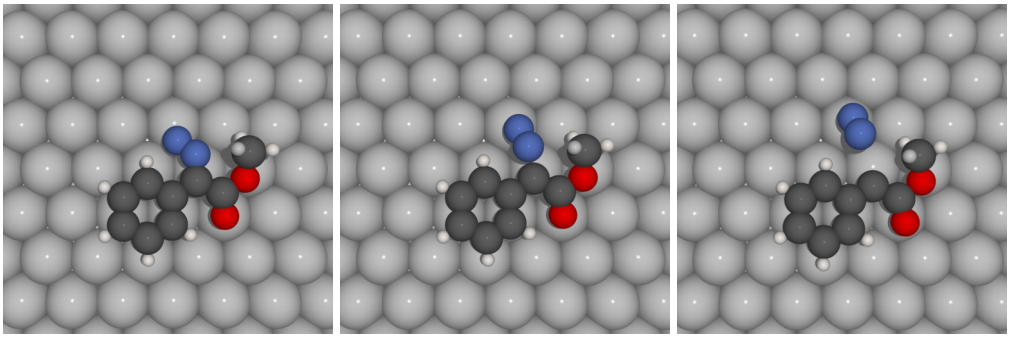

(a) (b) (c)

Figure 9.2: Optimized structures of (a) reactant, (b) transition state, and (c) product for phenyldiazoaceteate decomposition starting from bridge-sitting procarbene carbon

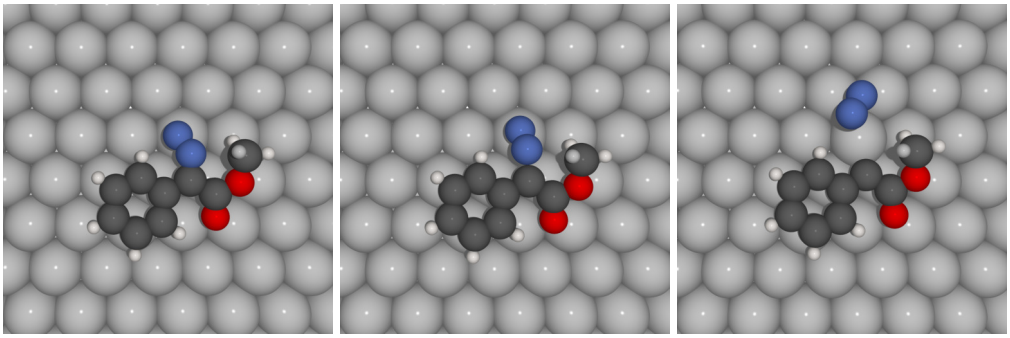

(a) (b) (c)

Figure 9.3: Optimized structures of (a) reactant, (b) transition state, and (c) product for phenyldiazoaceteate decomposition starting from fcc-sitting procarbene carbon

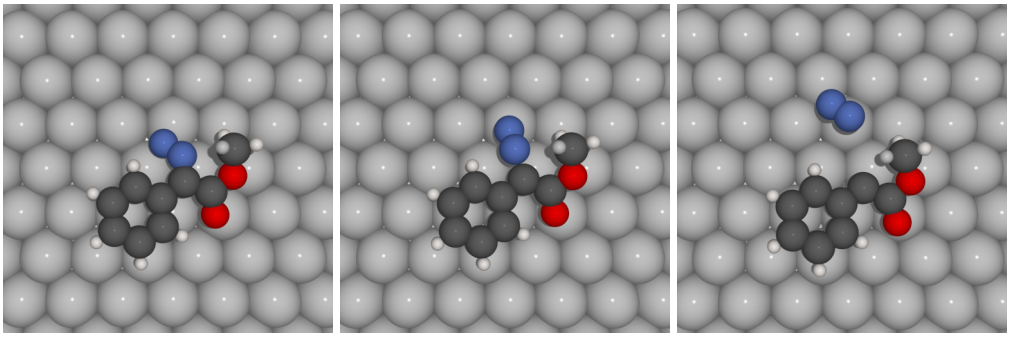

(a) (b) (c)

Figure 9.4: Optimized structures of (a) reactant, (b) transition state, and (c) product for phenyldiazoaceteate decomposition starting from hcp-sitting procarbene carbon

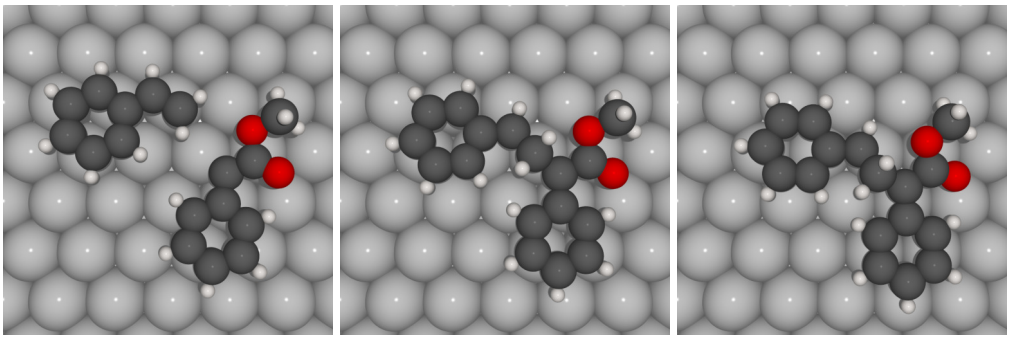

(a) (b) (c)

Figure 9.5: Optimized structures of (a) reactant, (b) transition state, and (c) intermediate for cyclopropanation step 1 followinng E1 mechanism

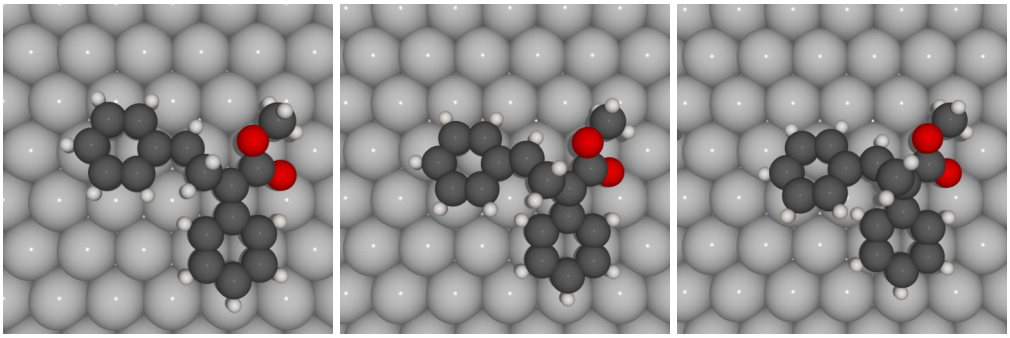

(a) (b) (c)

Figure 9.6: Optimized structures of (a) intermediate, (b) transition state, and (c) product for cyclopropanation step 2 followinng E1 mechanism

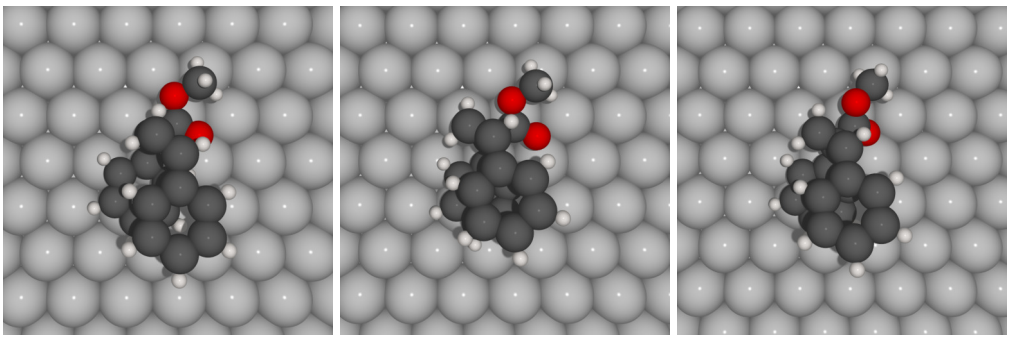

(a) (b) (c)

Figure 9.7: Optimized structures of (a) reactant, (b) transition state, and (c) product for cyclopropanation step followinng E2 mechanism

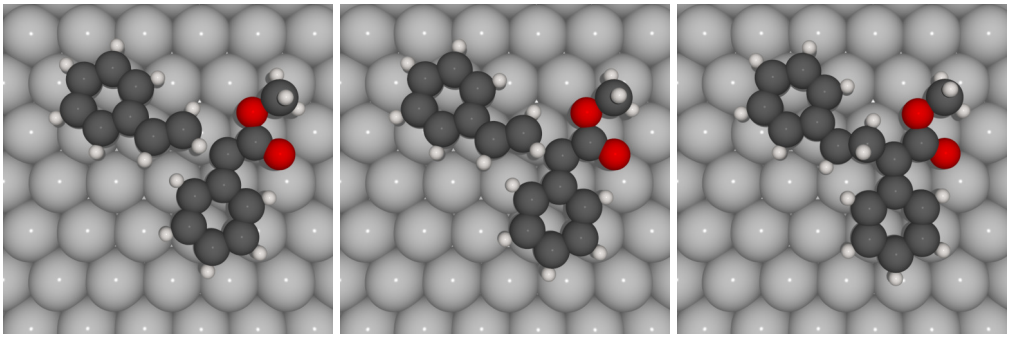

(a) (b) (c)

Figure 9.8: Optimized structures of (a) reactant, (b) transition state, and (c) intermediate for cyclopropanation step 1 followinng Z1 mechanism

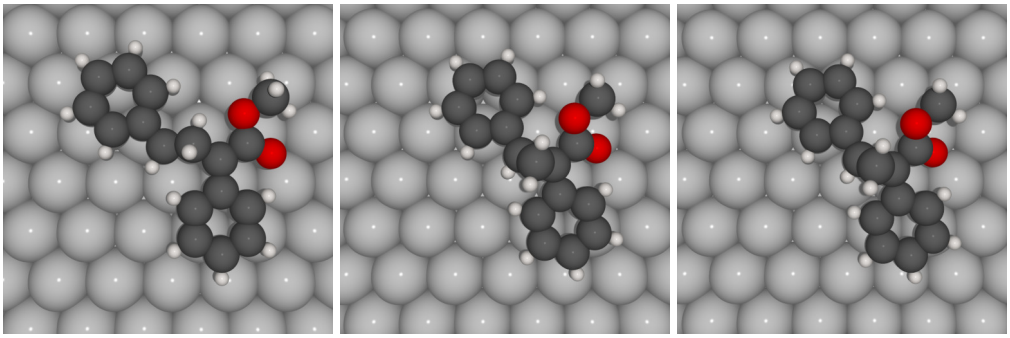

(a) (b) (c)

Figure 9.9: Optimized structures of (a) intermediate, (b) transition state, and (c) product for cyclopropanation step 2 followinng Z1 mechanism

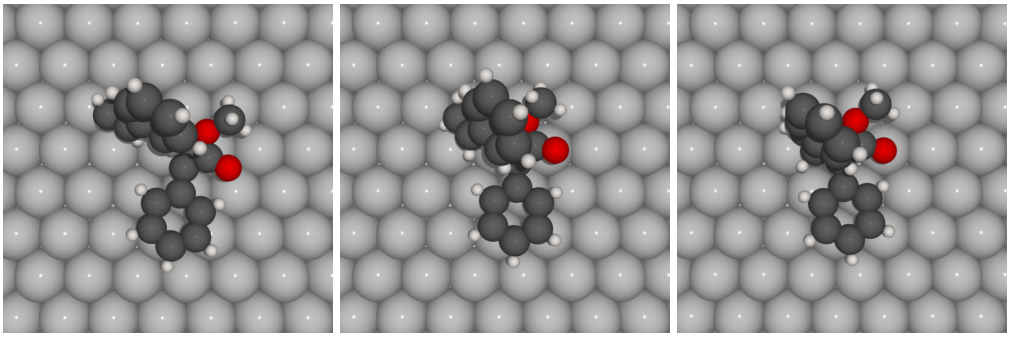

(a) (b) (c)

Figure 9.10: Optimized structures of (a) reactant, (b) transition state, and (c) intermediate for cyclopropanation step 1 followinng Z2 mechanism

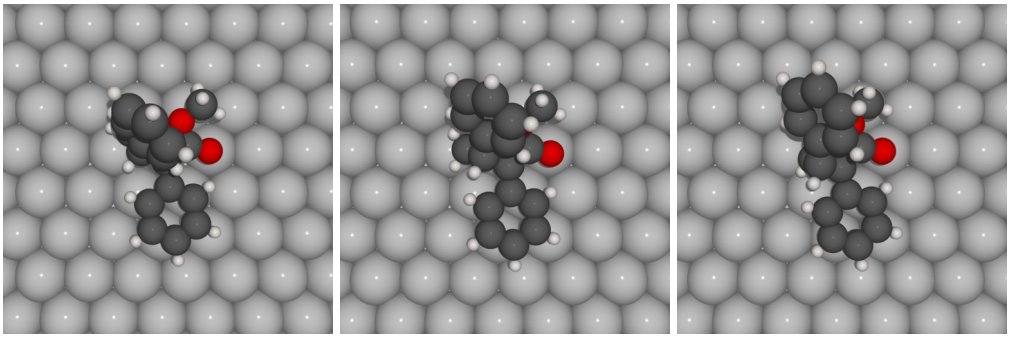

(a) (b) (c)

Figure 9.11: Optimized structures of (a) intermediate, (b) transition state, and (c) product for cyclopropanation step 2 followinng Z2 mechanism

Sandwich Slab Simulations

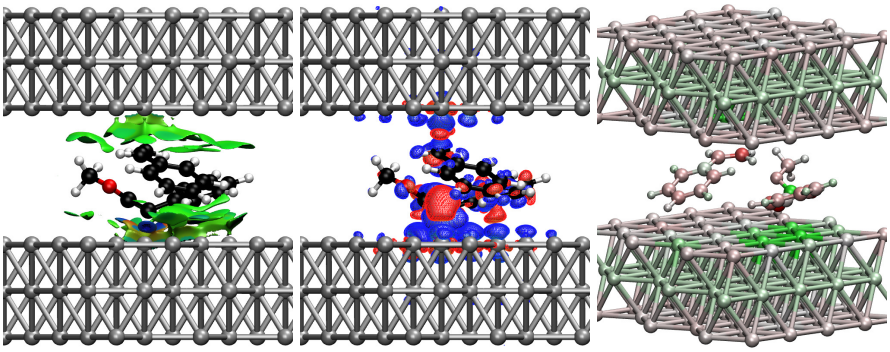

(a) (b) (c)

Figure 9.12: (a) Noncovalent interactions plot , (b) charge density difference, and (c) hirshfeld charges for optimized reactant along Path E1-D at 7.0 Åslab separation distance

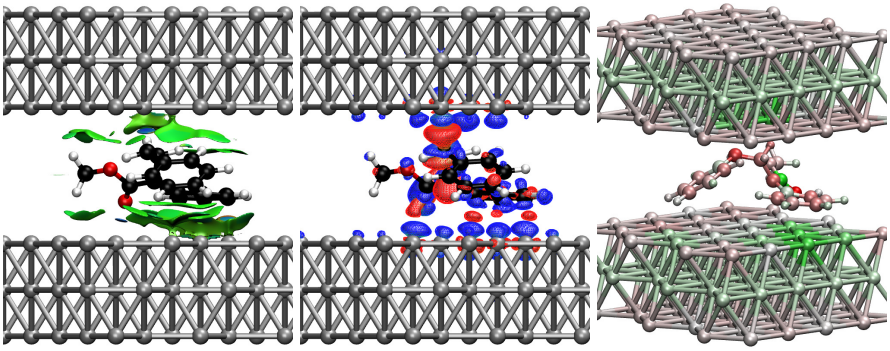

(a) (b) (c)

Figure 9.13: (a) Noncovalent interactions plot , (b) charge density difference, and (c) hirshfeld charges for optimized intermediate along Path E1-D at 7.0 Åslab separation distance

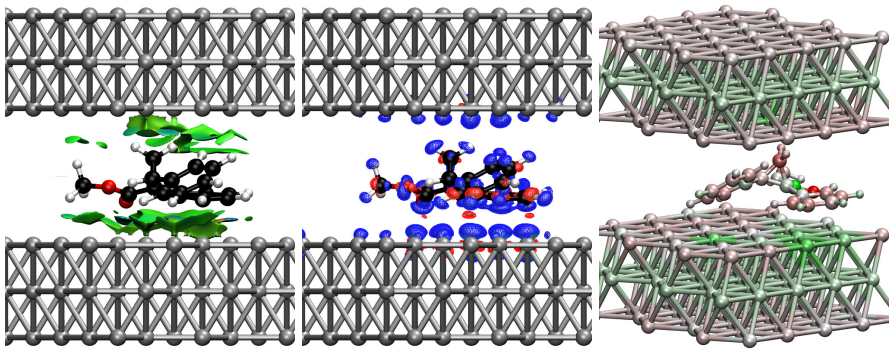

(a) (b) (c)

Figure 9.14: (a) Noncovalent interactions plot , (b) charge density difference, and (c) hirshfeld charges for optimized product along Path E1-D at 7.0 Åslab separation distance

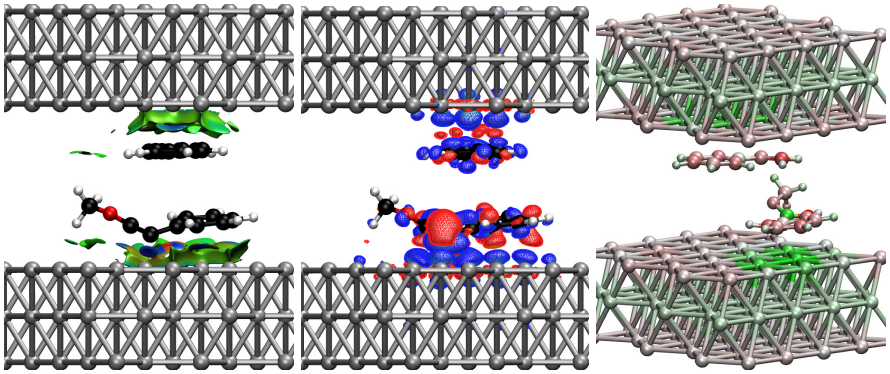

(a) (b) (c)

Figure 9.15: (a) Noncovalent interactions plot , (b) charge density difference, and (c) hirshfeld charges for optimized reactant along Path E1-D at 8.5 Åslab separation distance

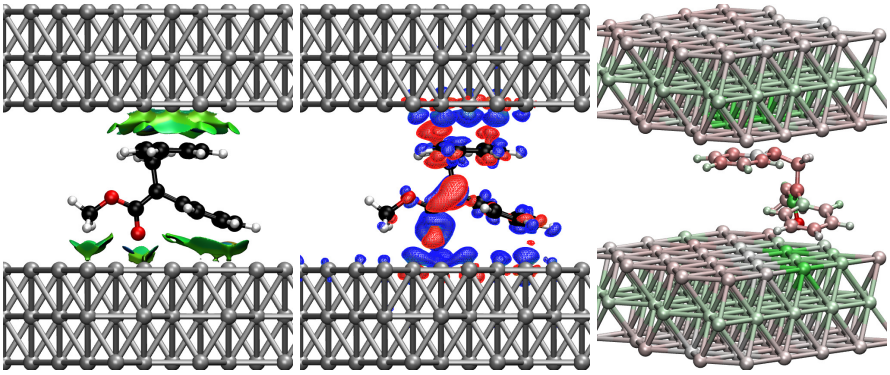

(a) (b) (c)

Figure 9.16: (a) Noncovalent interactions plot , (b) charge density difference, and (c) hirshfeld charges for optimized intermediate along Path E1-D at 8.5 Åslab separation distance

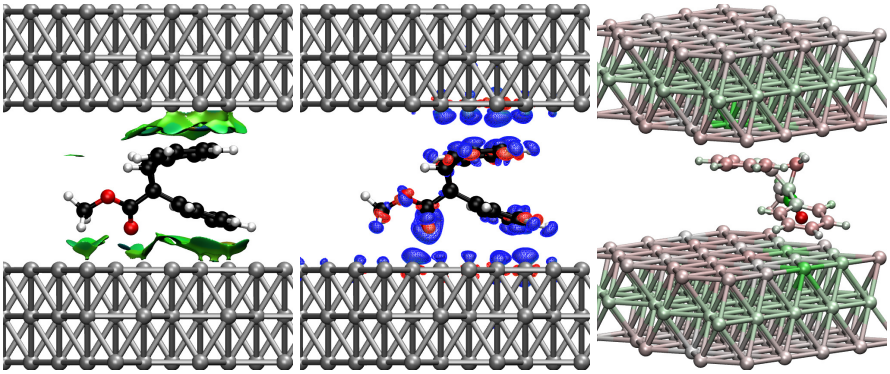

(a) (b) (c)

Figure 9.17: (a) Noncovalent interactions plot , (b) charge density difference, and (c) hirshfeld charges for optimized product along Path 1E1-D at 8.5 Åslab separation distance

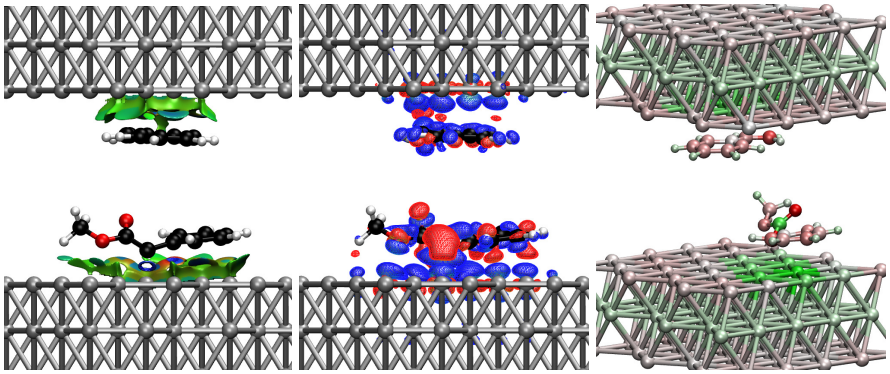

(a) (b) (c)

Figure 9.18: (a) Noncovalent interactions plot , (b) charge density difference, and (c) hirshfeld charges for optimized reactant along Path E1-D at 10.0 Åslab separation distance

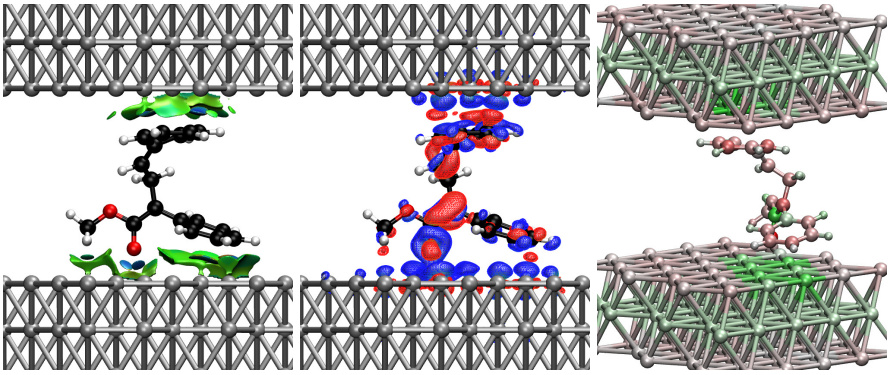

(a) (b) (c)

Figure 9.19: (a) Noncovalent interactions plot , (b) charge density difference, and (c) hirshfeld charges for optimized intermediate along Path E1-D at 10.0 Åslab separation distance

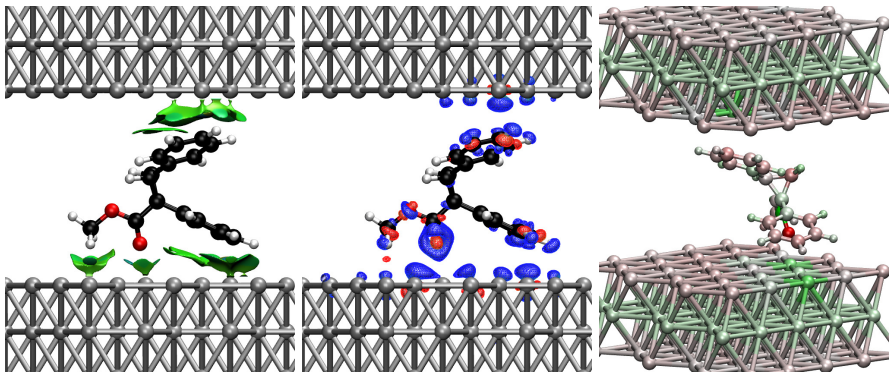

(a) (b) (c)

Figure 9.20: (a) Noncovalent interactions plot , (b) charge density difference, and (c) hirshfeld charges for optimized product along Path E1-D at 10.0 Åslab separation distance

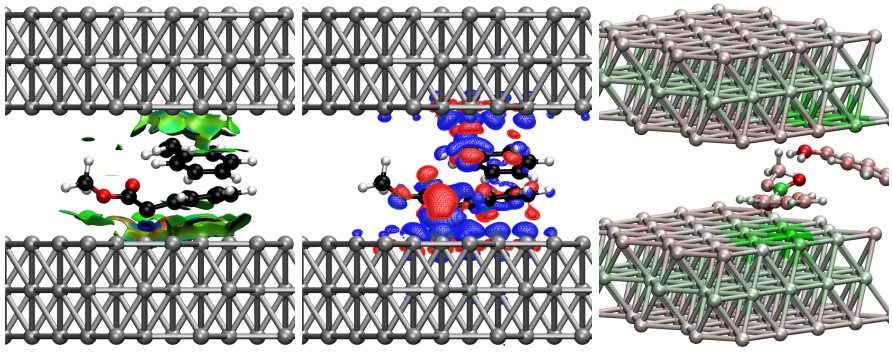

(a) (b) (c)

Figure 9.21: (a) Noncovalent interactions plot , (b) charge density difference, and (c) hirshfeld charges for optimized reactant along Path E2-D at 7.0 Åslab separation distance

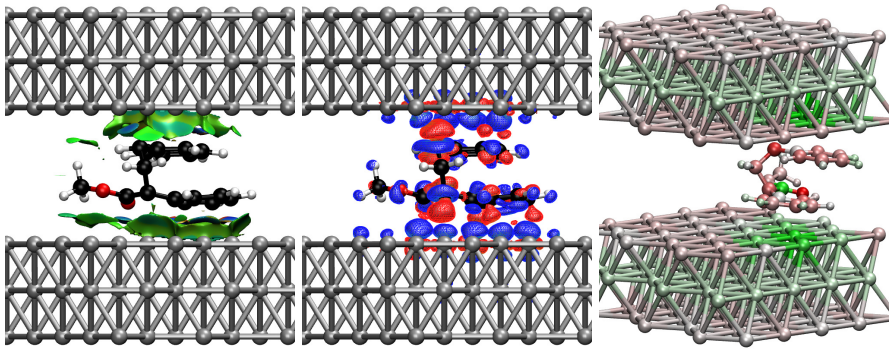

(a) (b) (c)

Figure 9.22: (a) Noncovalent interactions plot , (b) charge density difference, and (c) hirshfeld charges for optimized intermediate along Path E2-D at 7.0 Åslab separation distance

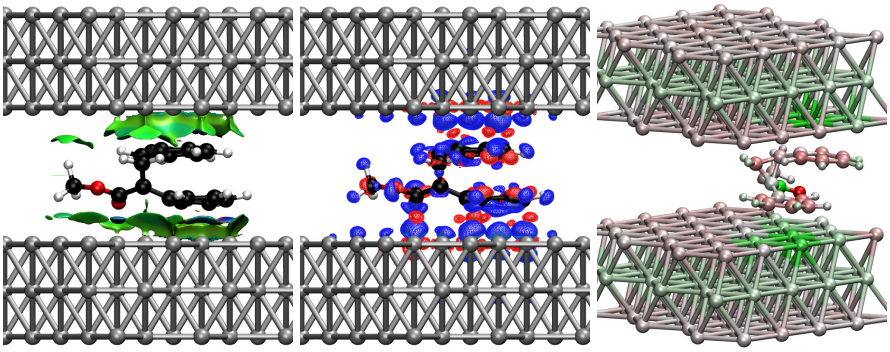

(a) (b) (c)

Figure 9.23: (a) Noncovalent interactions plot , (b) charge density difference, and (c) hirshfeld charges for optimized product along Path E2-D at 7.0 Åslab separation distance

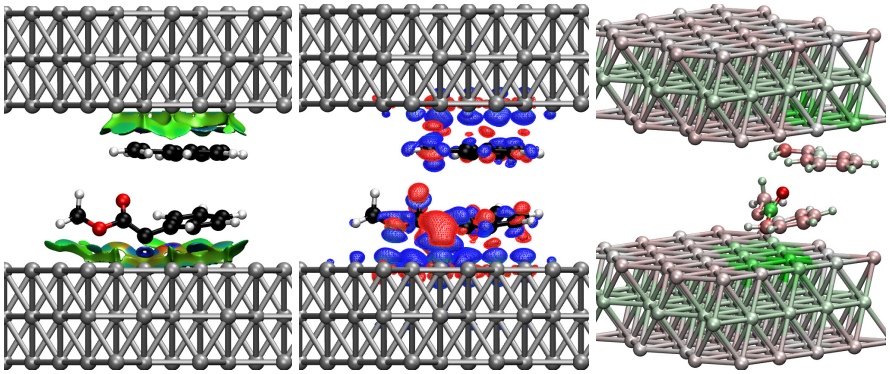

(a) (b) (c)

Figure 9.24: (a) Noncovalent interactions plot , (b) charge density difference, and (c) hirshfeld charges for optimized reactant along Path E2-D at 8.5 Åslab separation distance

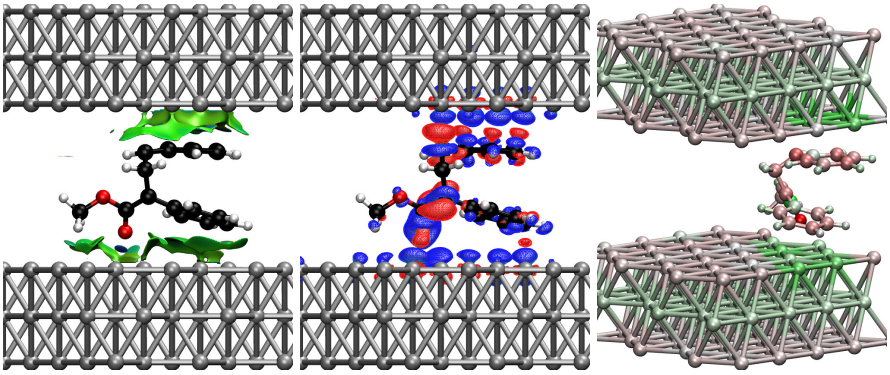

(a) (b) (c)

Figure 9.25: (a) Noncovalent interactions plot , (b) charge density difference, and (c) hirshfeld charges for optimized intermediate along Path E2-D at 8.5 Åslab separation distance

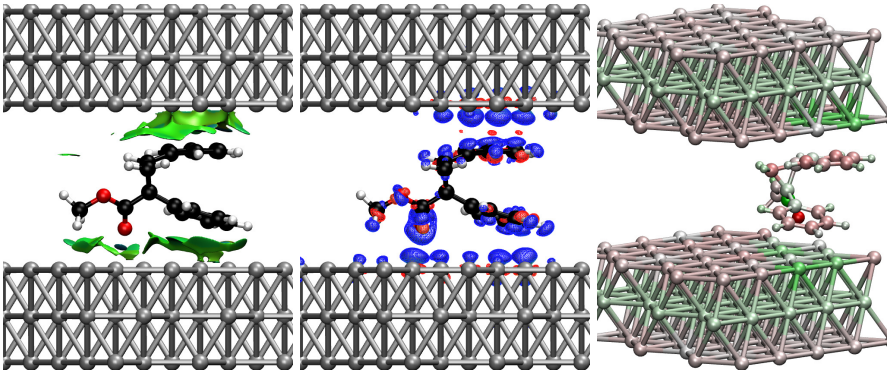

(a) (b) (c)

Figure 9.26: (a) Noncovalent interactions plot , (b) charge density difference, and (c) hirshfeld charges for optimized product along Path E2-D at 8.5 Åslab separation distance

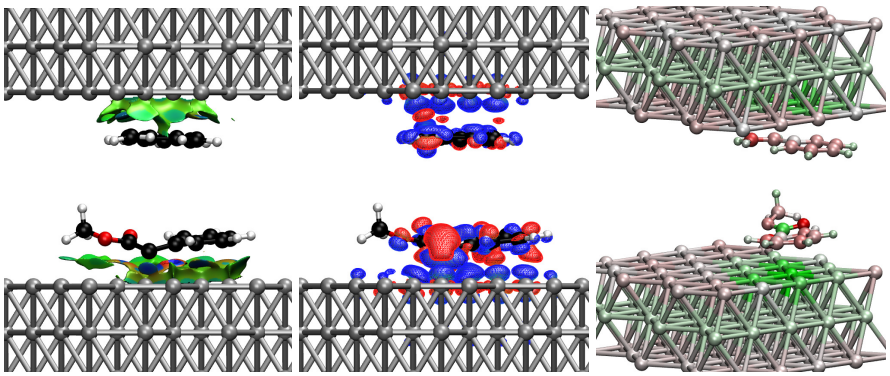

(a) (b) (c)

Figure 9.27: (a) Noncovalent interactions plot , (b) charge density difference, and (c) hirshfeld charges for optimized reactant along Path E2-D at 10.0 Åslab separation distance

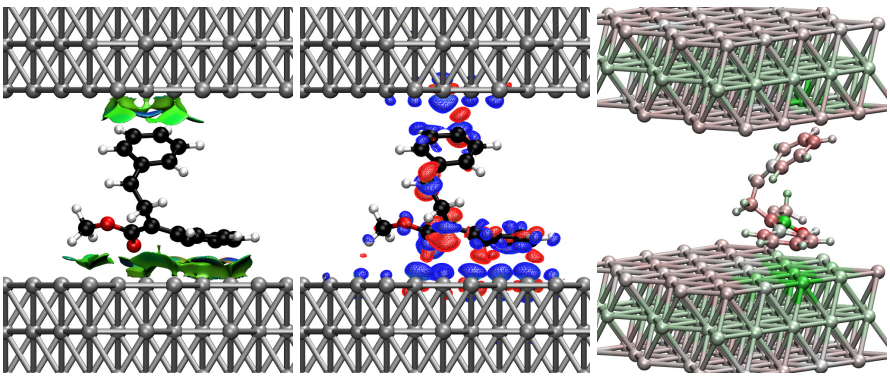

(a) (b) (c)

Figure 9.28: (a) Noncovalent interactions plot , (b) charge density difference, and (c) hirshfeld charges for optimized intermediate along Path E2-D at 10.0 Åslab separation distance

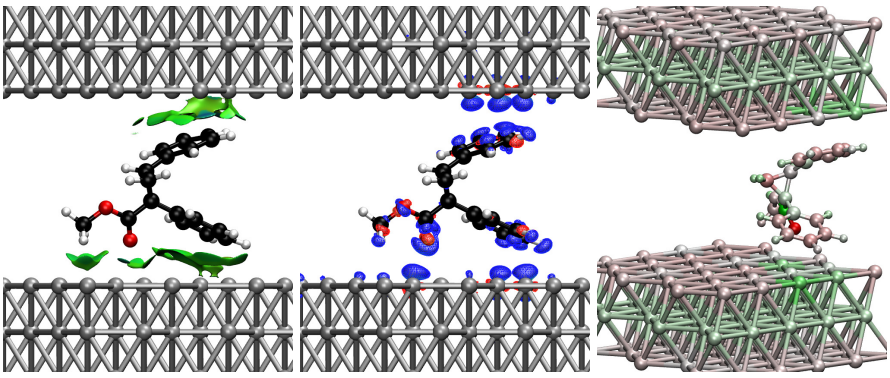

(a) (b) (c)

Figure 9.29: (a) Noncovalent interactions plot , (b) charge density difference, and (c) hirshfeld charges for optimized product along Path E2-D at 10.0 Åslab separation distance

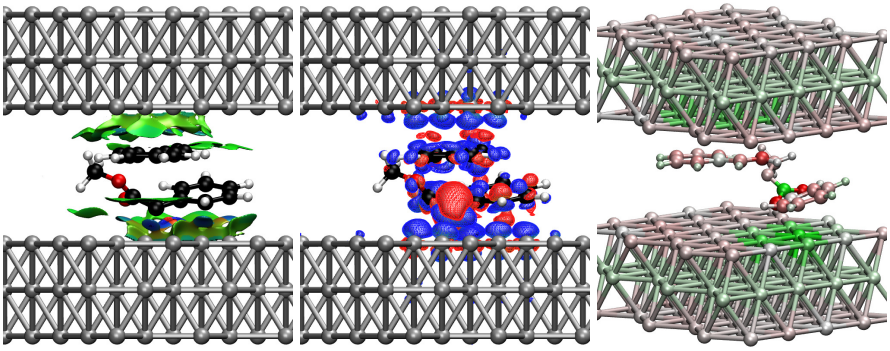

(a) (b) (c)

Figure 9.30: (a) Noncovalent interactions plot , (b) charge density difference, and (c) hirshfeld charges for optimized reactant along Path Z1-D at 7.0 Åslab separation distance

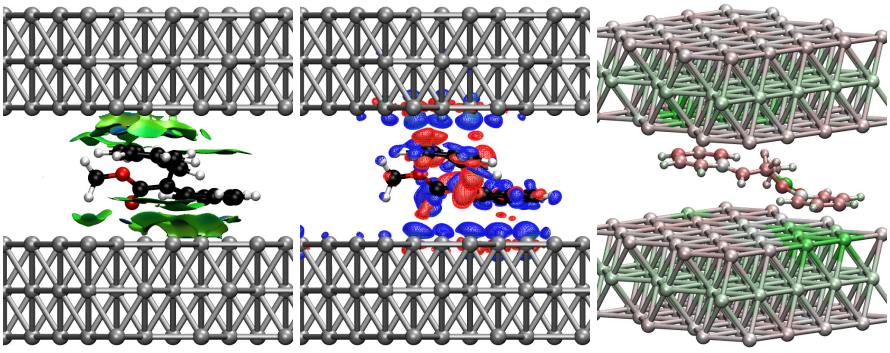

(a) (b) (c)

Figure 9.31: (a) Noncovalent interactions plot , (b) charge density difference, and (c) hirshfeld charges for optimized intermediate along Path Z1-D at 7.0 Åslab separation distance

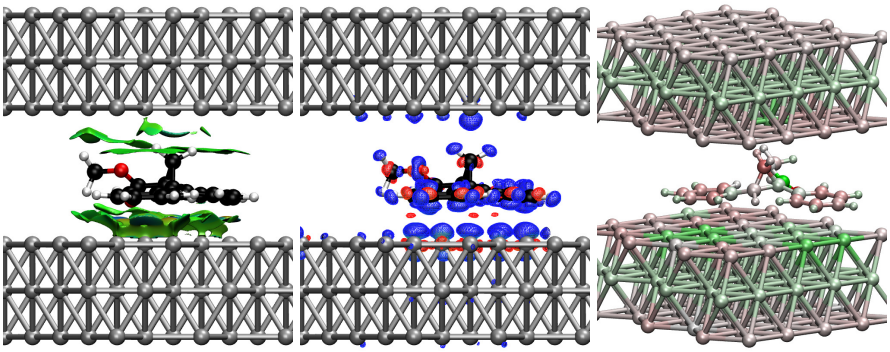

(a) (b) (c)

Figure 9.32: (a) Noncovalent interactions plot , (b) charge density difference, and (c) hirshfeld charges for optimized product along Path Z1-D at 7.0 Åslab separation distance

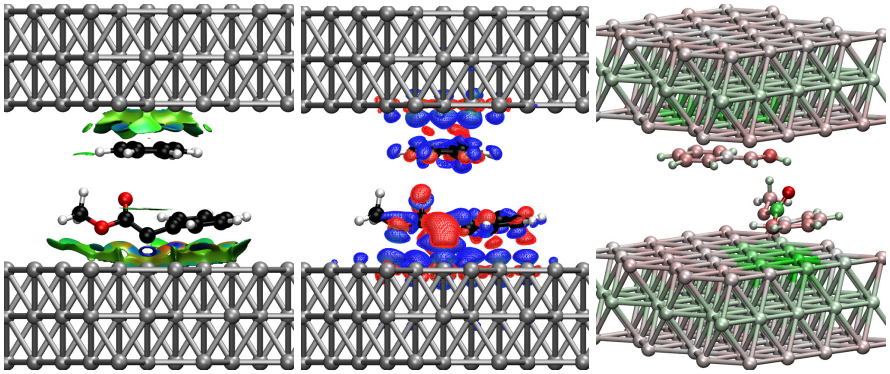

(a) (b) (c)

Figure 9.33: (a) Noncovalent interactions plot , (b) charge density difference, and (c) hirshfeld charges for optimized reactant along Path Z1-D at 8.5 Åslab separation distance

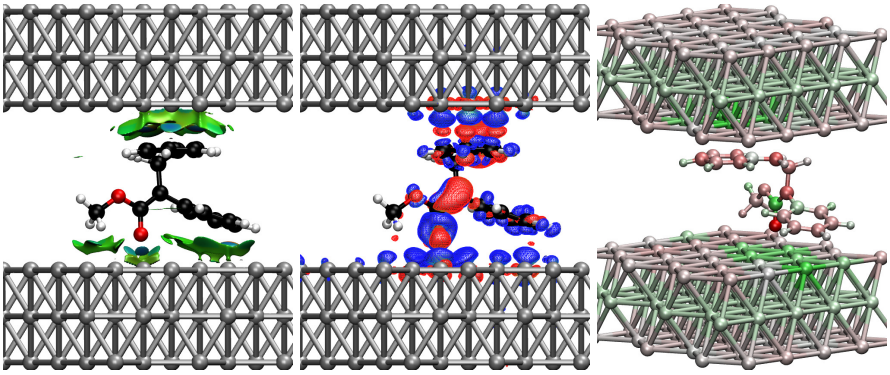

(a) (b) (c)

Figure 9.34: (a) Noncovalent interactions plot , (b) charge density difference, and (c) hirshfeld charges for optimized intermediate along Path Z1-D at 8.5 Åslab separation distance

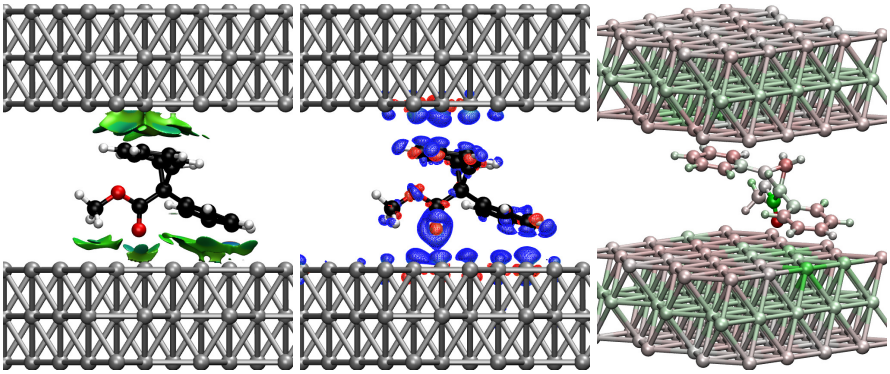

(a) (b) (c)

Figure 9.35: (a) Noncovalent interactions plot , (b) charge density difference, and (c) hirshfeld charges for optimized product along Path Z1-D at 8.5 Åslab separation distance

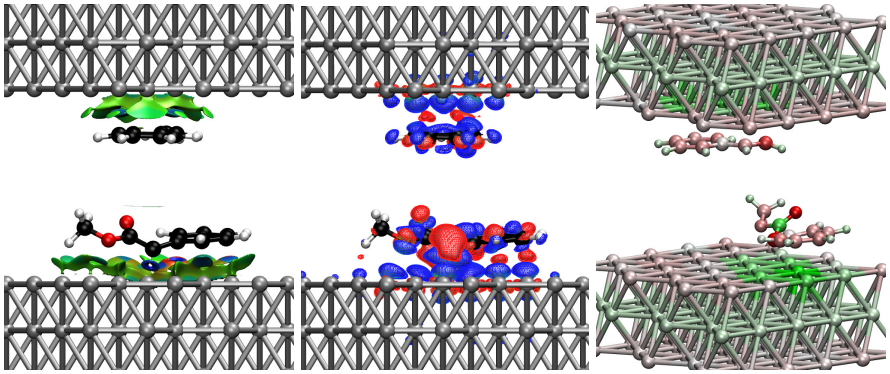

(a) (b) (c)

Figure 9.36: (a) Noncovalent interactions plot , (b) charge density difference, and (c) hirshfeld charges for optimized reactant along Path Z1-D at 10.0 Åslab separation distance

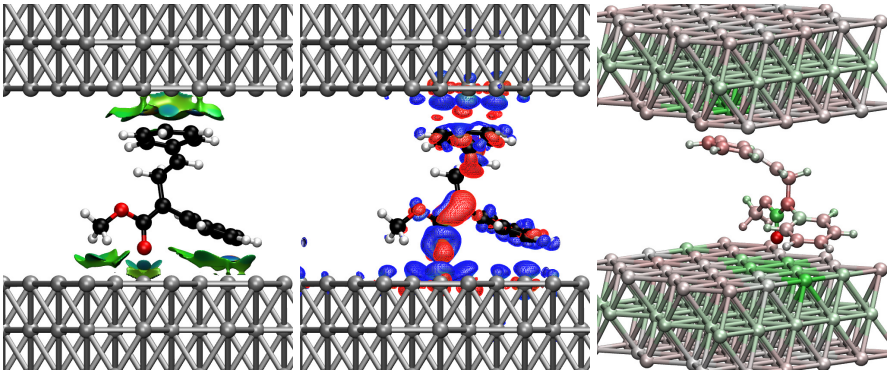

(a) (b) (c)

Figure 9.37: (a) Noncovalent interactions plot , (b) charge density difference, and (c) hirshfeld charges for optimized intermediate along Path Z1-D at 10.0 Åslab separation distance

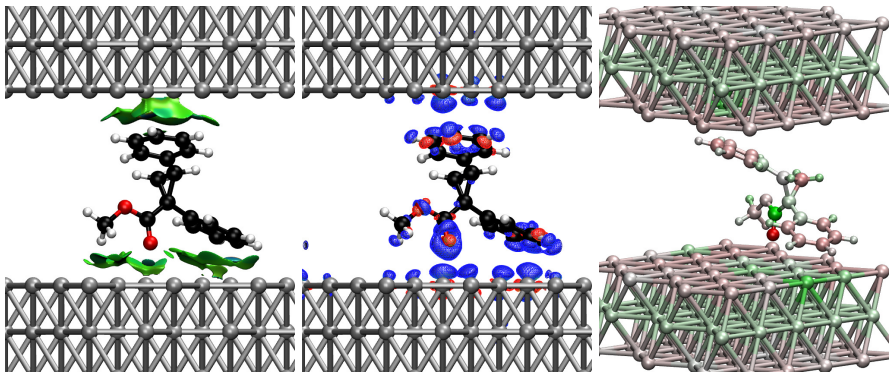

(a) (b) (c)

Figure 9.38: (a) Noncovalent interactions plot , (b) charge density difference, and (c) hirshfeld charges for optimized product along Path Z1-D at 10.0 Åslab separation distance

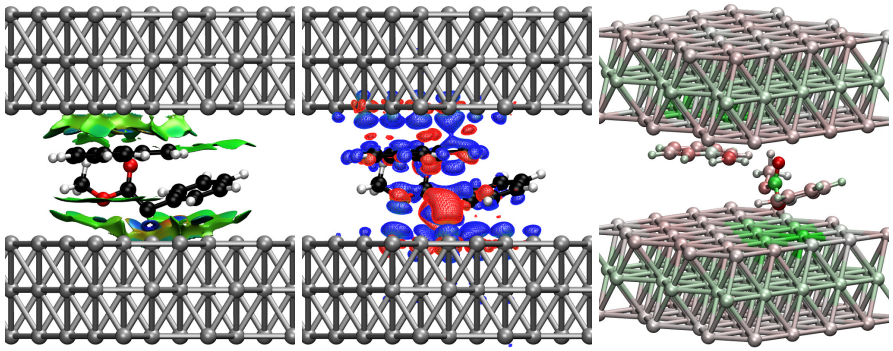

(a) (b) (c)

Figure 9.39: (a) Noncovalent interactions plot , (b) charge density difference, and (c) hirshfeld charges for optimized reactant along Path Z2-D at 7.0 Åslab separation distance

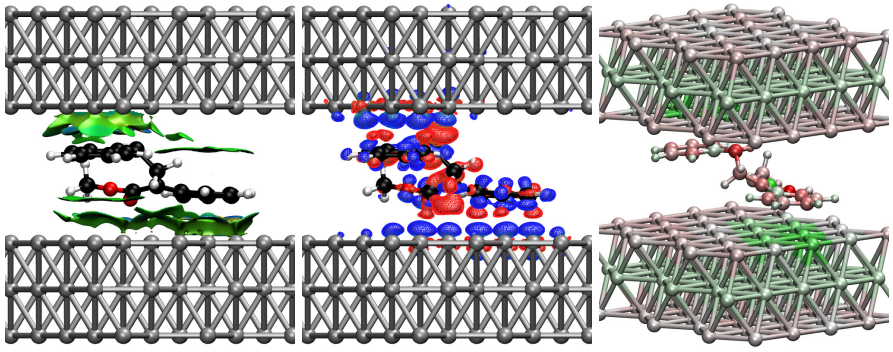

(a) (b) (c)

Figure 9.40: (a) Noncovalent interactions plot , (b) charge density difference, and (c) hirshfeld charges for optimized intermediate along Path Z2-D at 7.0 Åslab separation distance

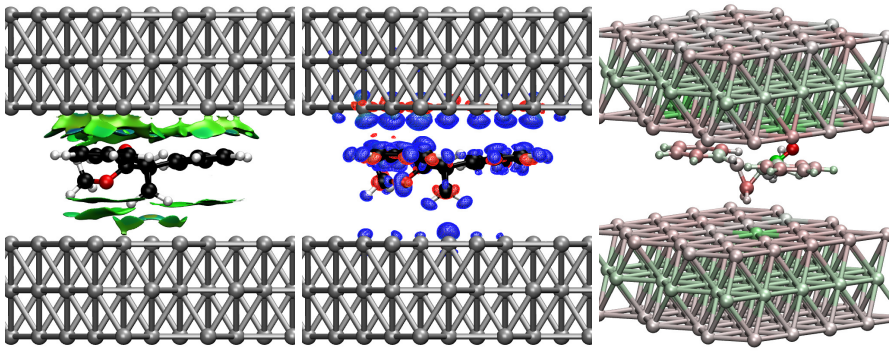

(a) (b) (c)

Figure 9.41: (a) Noncovalent interactions plot , (b) charge density difference, and (c) hirshfeld charges for optimized product along Path Z2-D at 7.0 Åslab separation distance

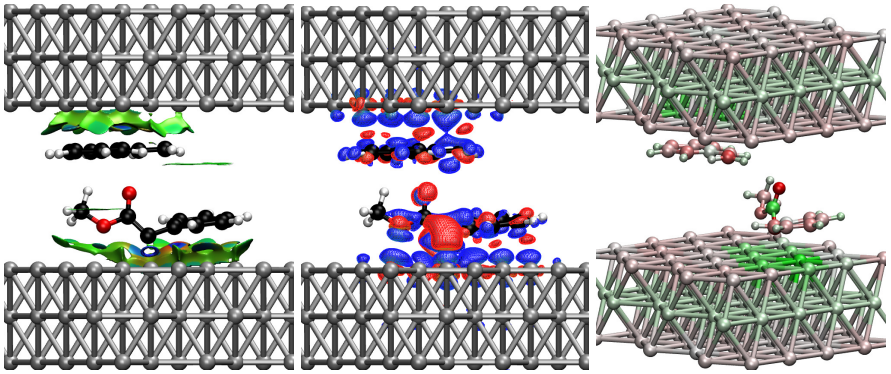

(a) (b) (c)

Figure 9.42: (a) Noncovalent interactions plot , (b) charge density difference, and (c) hirshfeld charges for optimized reactant along Path Z2-D at 8.5 Åslab separation distance

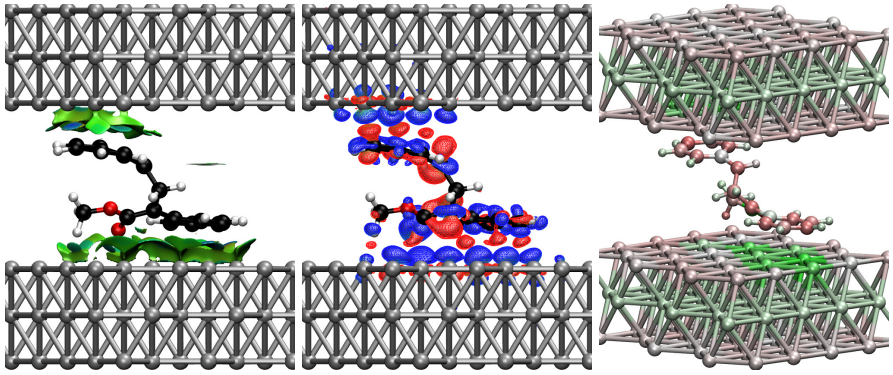

(a) (b) (c)

Figure 9.43: (a) Noncovalent interactions plot , (b) charge density difference, and (c) hirshfeld charges for optimized intermediate along Path Z2-D at 8.5 Åslab separation distance

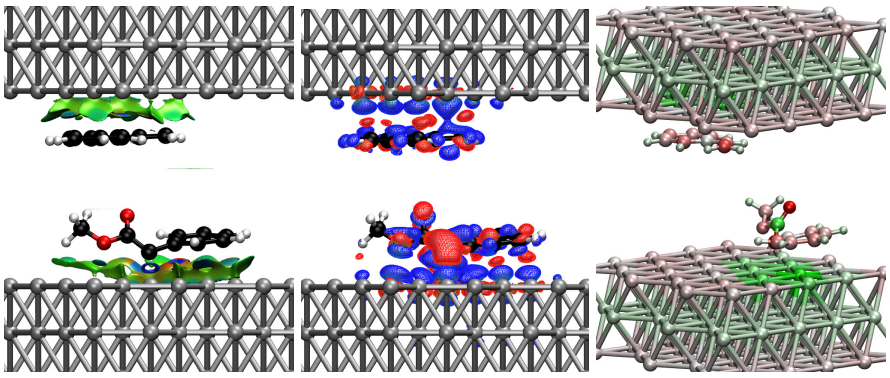

(a) (b) (c)

Figure 9.44: (a) Noncovalent interactions plot , (b) charge density difference, and (c) hirshfeld charges for optimized reactant along Path Z2-D at 10.0 Åslab separation distance

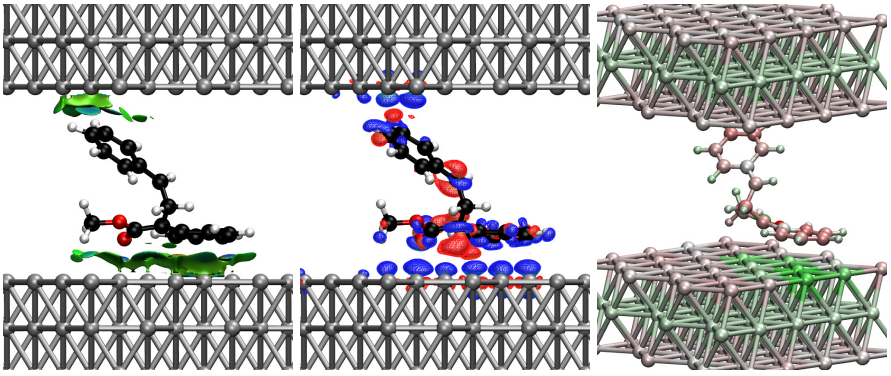

(a) (b) (c)

Figure 9.45: (a) Noncovalent interactions plot , (b) charge density difference, and (c) hirshfeld charges for optimized intermediate along Path Z2-D at 10.0 Åslab separation distance

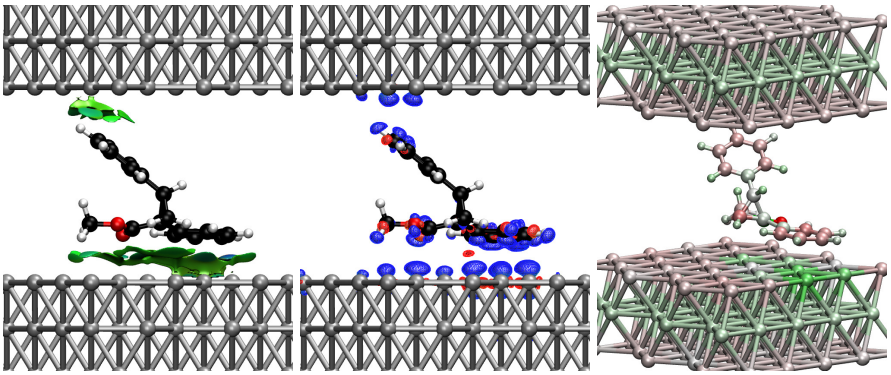

(a) (b) (c)

Figure 9.46: (a) Noncovalent interactions plot , (b) charge density difference, and (c) hirshfeld charges for optimized product along Path Z2-D at 10.0 Åslab separation distance

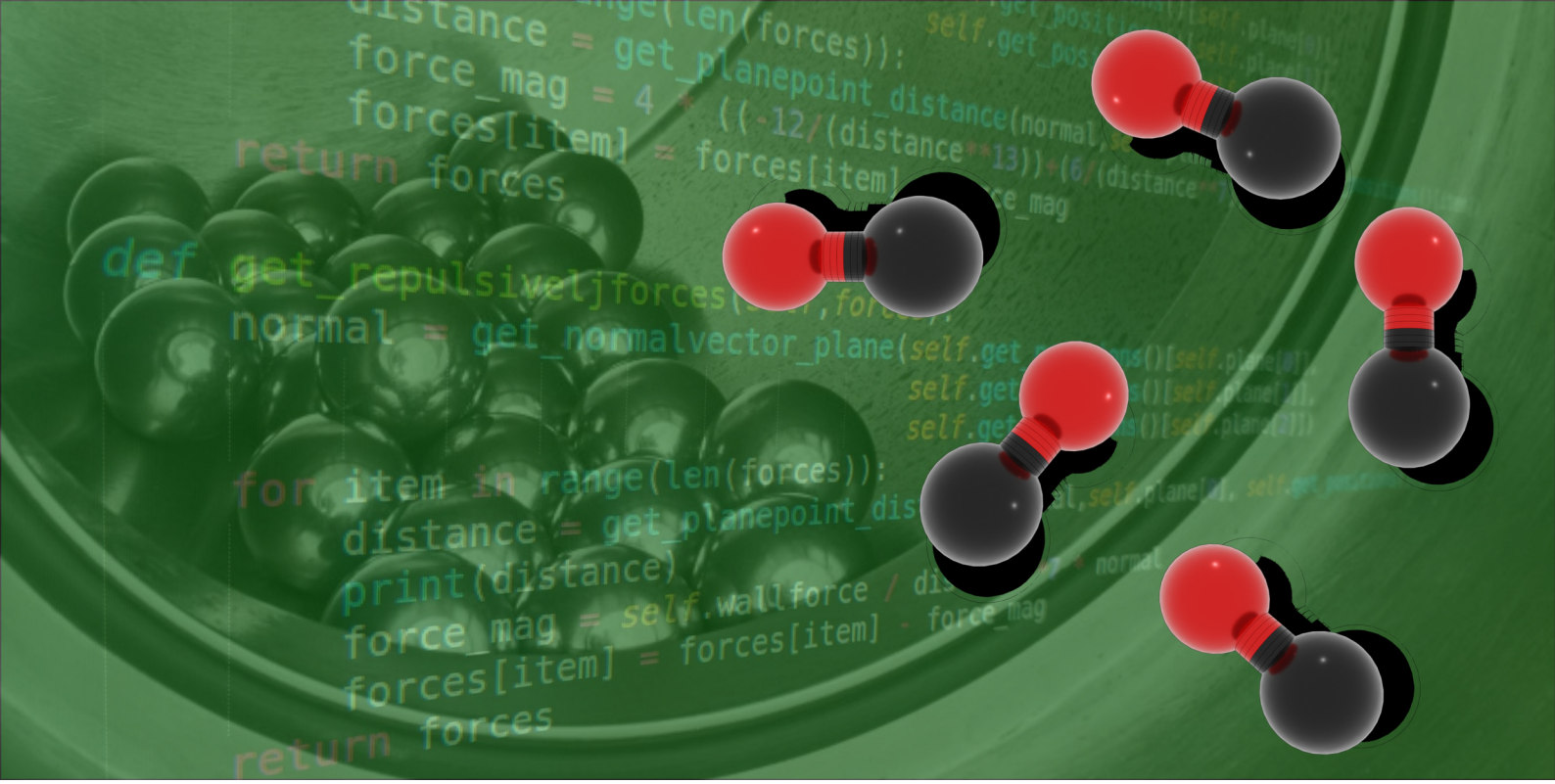

Optimized Structures CO dissociation

Relaxed Terrace Ru(0001) Surface

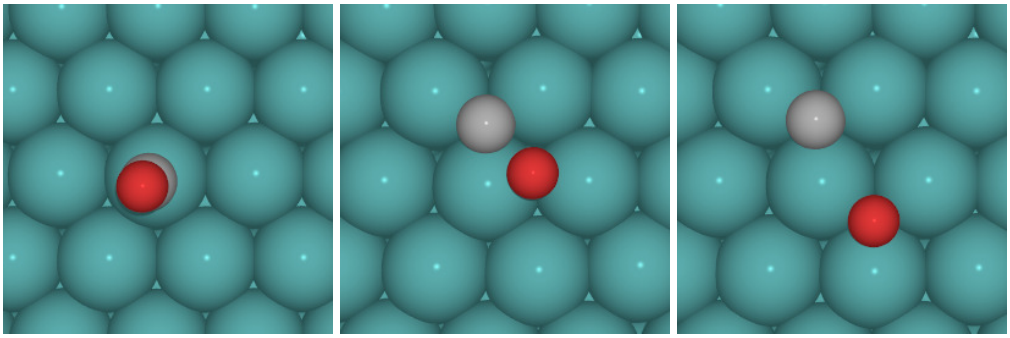

(a) (b) (c)

Figure 10.1: Optimized structures of (a) reactant (b) transition state and (c) product absorbed in relax terrace Ru(0001) surface for Path 1.

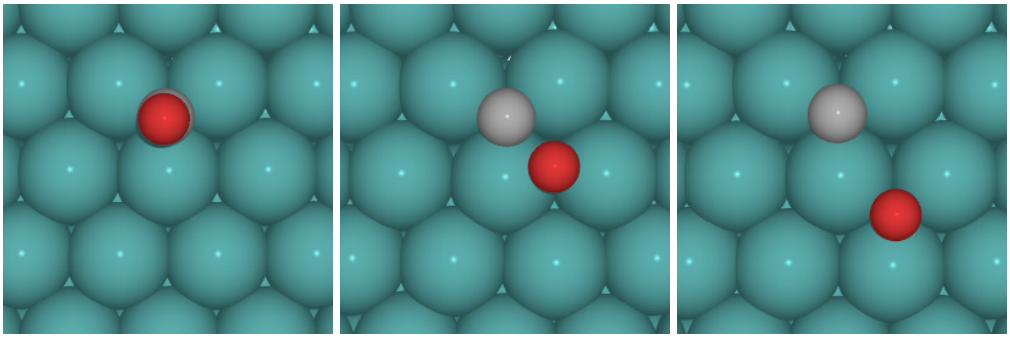

(a) (b) (c)

Figure 10.2: Optimized structures of (a) reactant (b) transition state and (c) product absorbed in relax terrace Ru(0001) surface for Path 2.

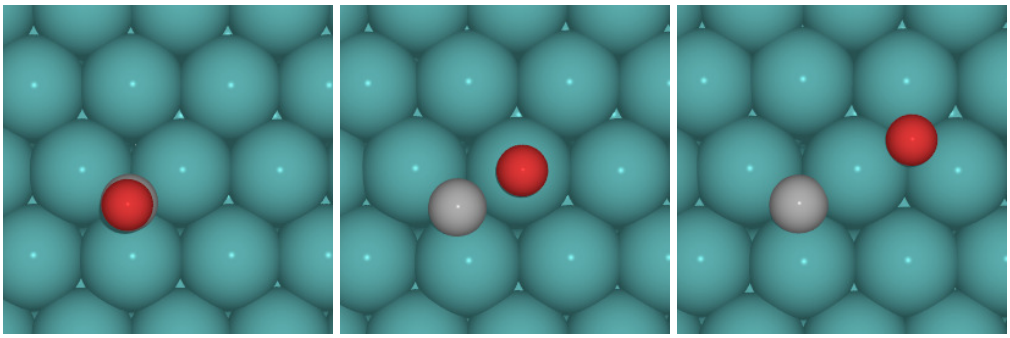

(a) (b) (c)

Figure 10.3: Optimized structures of (a) reactant (b) transition state and (c) product absorbed in relax terrace Ru(0001) surface for Path 3.

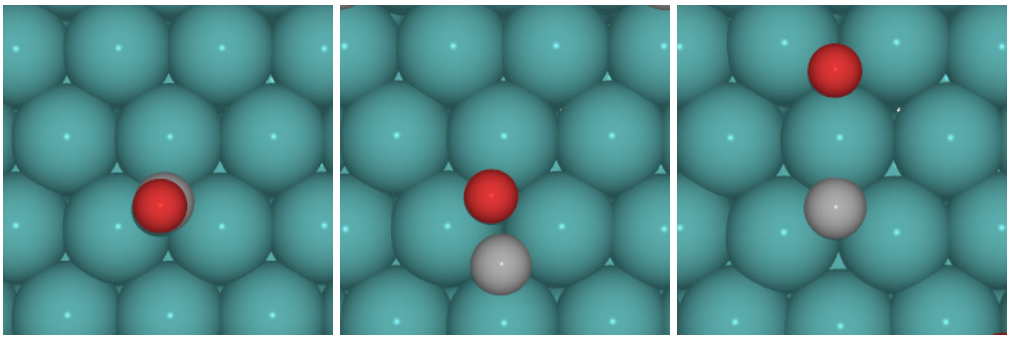

(a) (b) (c)

Figure 10.4: Optimized structures of (a) reactant (b) transition state and (c) product absorbed in relax terrace Ru(0001) surface for Path 4

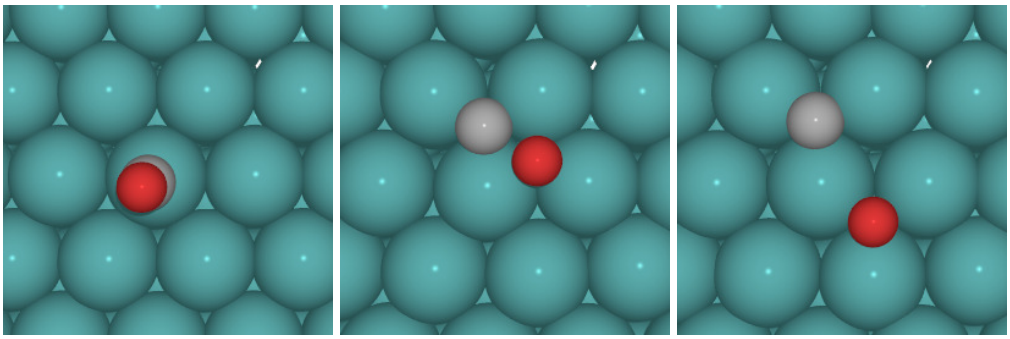

(a) (b) (c)

Figure 10.5: Optimized structures of (a) reactant (b) transition state and (c) product absorbed in relax terrace Ru(0001) surface for Path 1

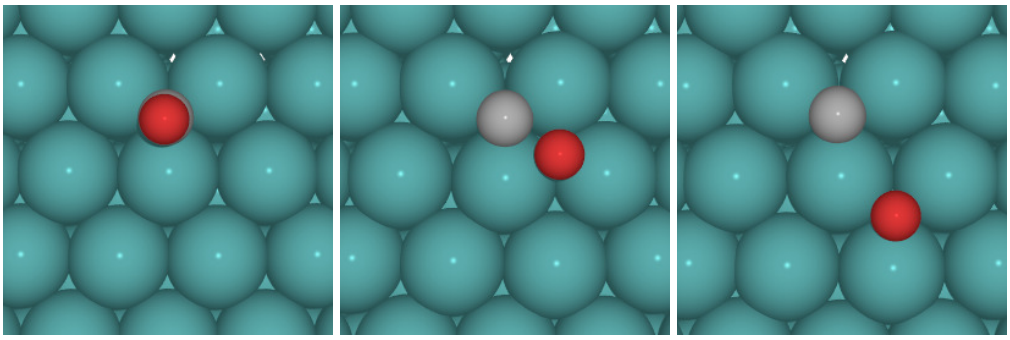

(a) (b) (c)

Figure 10.6: Optimized structures of (a) reactant (b) transition state and (c) product absorbed in relax terrace Ru(0001) surface for Path 2

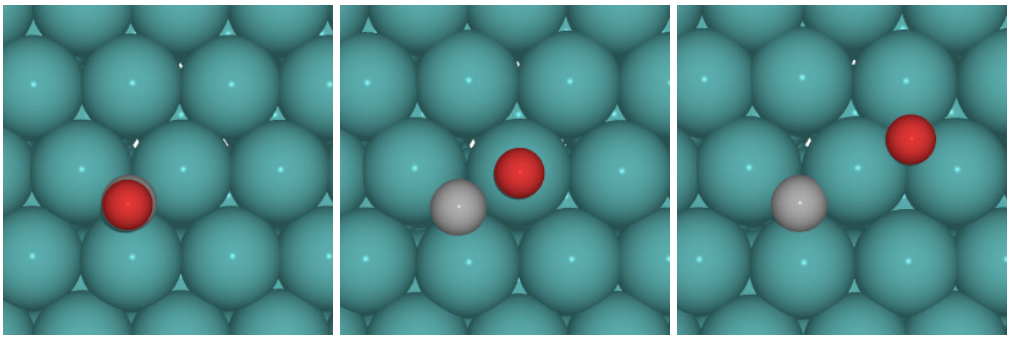

(a) (b) (c)

Figure 10.7: Optimized structures of (a) reactant (b) transition state and (c) product absorbed in relax terrace Ru(0001) surface for Path 3

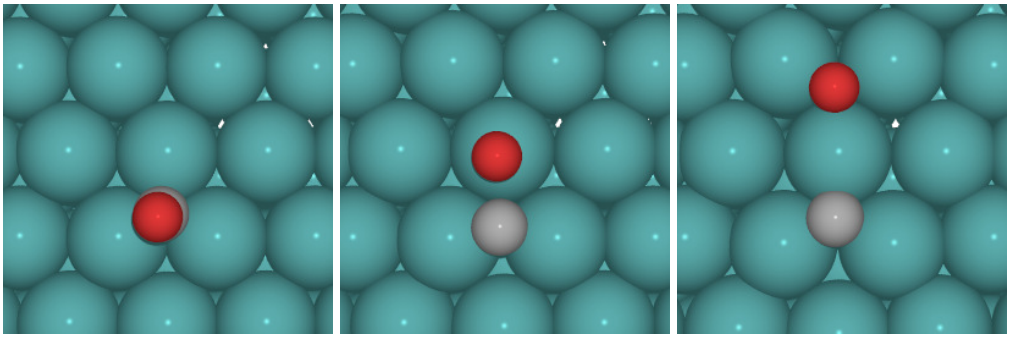

(a) (b) (c)

Figure 10.8: Optimized structures of (a) reactant (b) transition state and (c) product absorbed in relax terrace Ru(0001) surface for Path 4

Isotropic Compression on Terrace Ru(0001) Surface

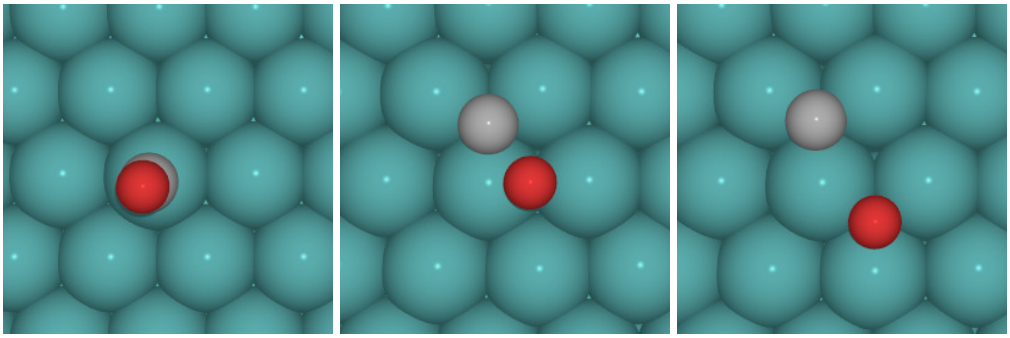

(a) (b) (c)

Figure 10.9: Optimized structures of (a) reactant (b) transition state and (c) product absorbed in relax terrace Ru(0001) surface for Path 1

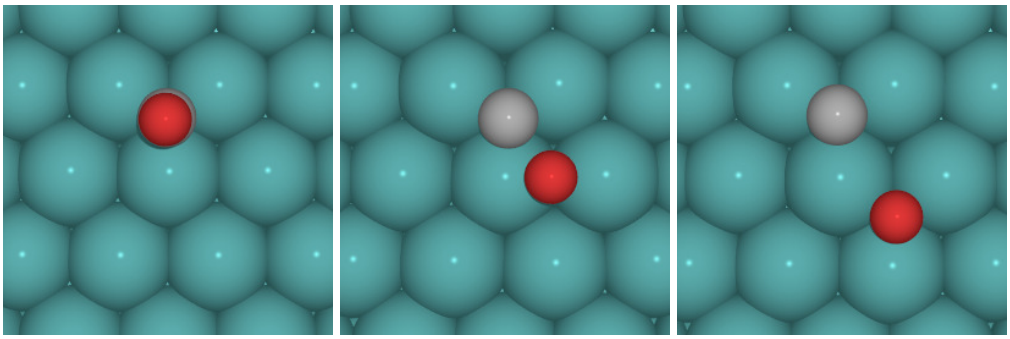

(a) (b) (c)

Figure 10.10: Optimized structures of (a) reactant (b) transition state and (c) product absorbed in relax terrace Ru(0001) surface for Path 2

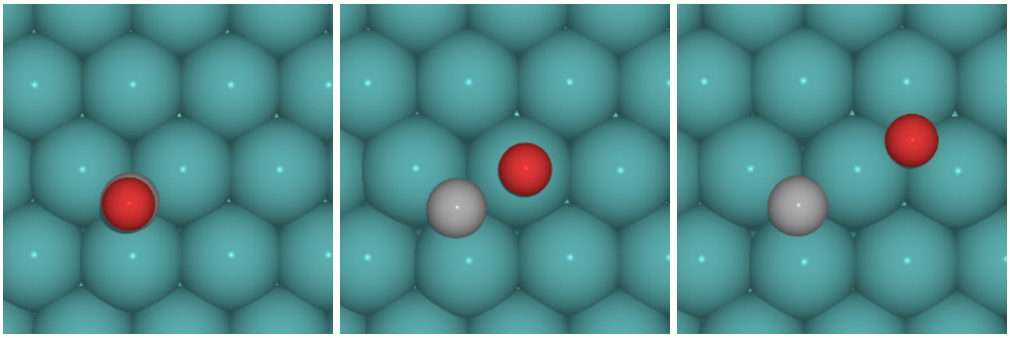

(a) (b) (c)

Figure 10.11: Optimized structures of (a) reactant (b) transition state and (c) product absorbed in relax terrace Ru(0001) surface for Path 3

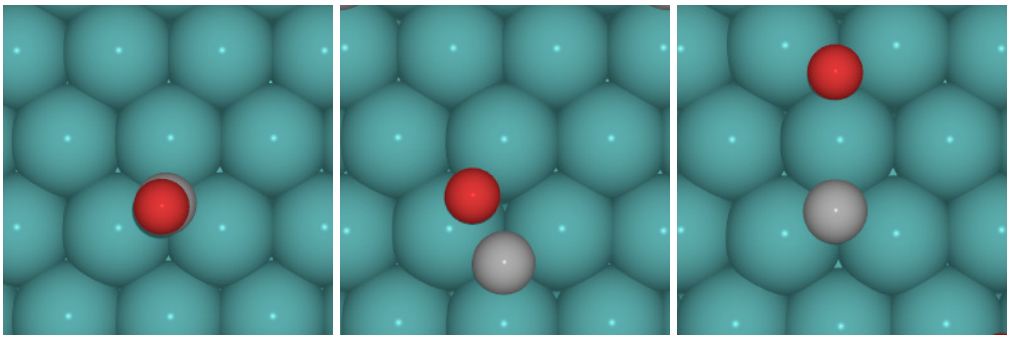

(a) (b) (c)

Figure 10.12: Optimized structures of (a) reactant (b) transition state and (c) product absorbed in relax terrace Ru(0001) surface for Path 4

Anisotropic Expansion on Terrace Ru(0001) Surface

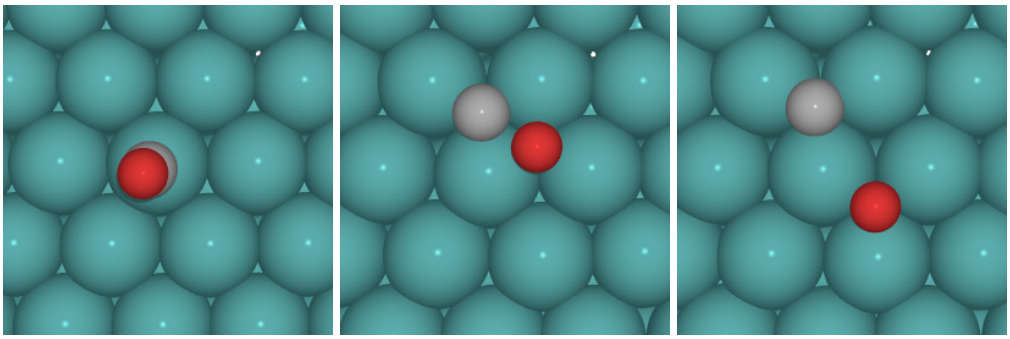

(a) (b) (c)

Figure 10.13: Optimized structures of (a) reactant (b) transition state and (c) product absorbed in relax terrace Ru(0001) surface for Path 1

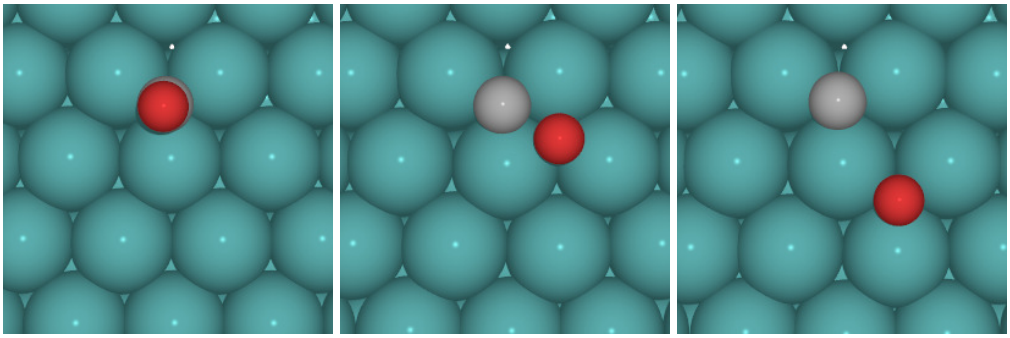

(a) (b) (c)

Figure 10.14: Optimized structures of (a) reactant (b) transition state and (c) product absorbed in relax terrace Ru(0001) surface for Path 2

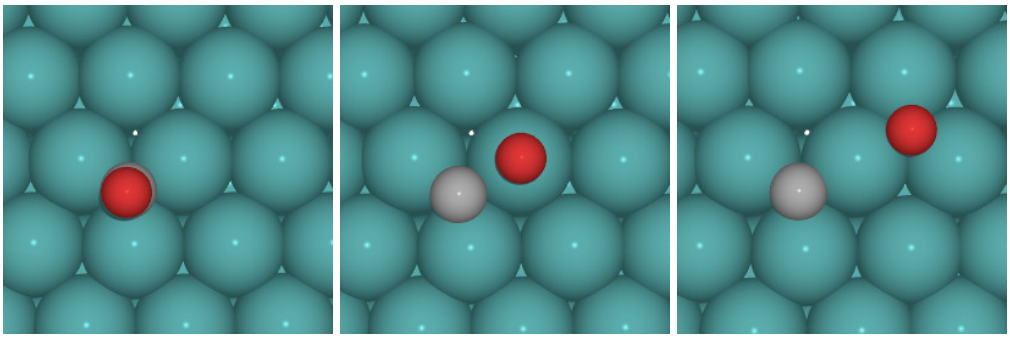

(a) (b) (c)

Figure 10.15: Optimized structures of (a) reactant (b) transition state and (c) product absorbed in relax terrace Ru(0001) surface for Path 3

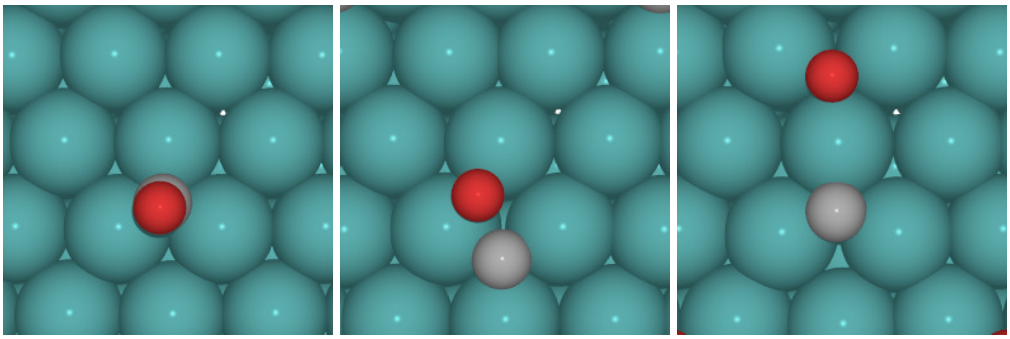

(a) (b) (c)

Figure 10.16: Optimized structures of (a) reactant (b) transition state and (c) product absorbed in relax terrace Ru(0001) surface for Path 4

Anisotropic Compression on Ru(0001) Surface

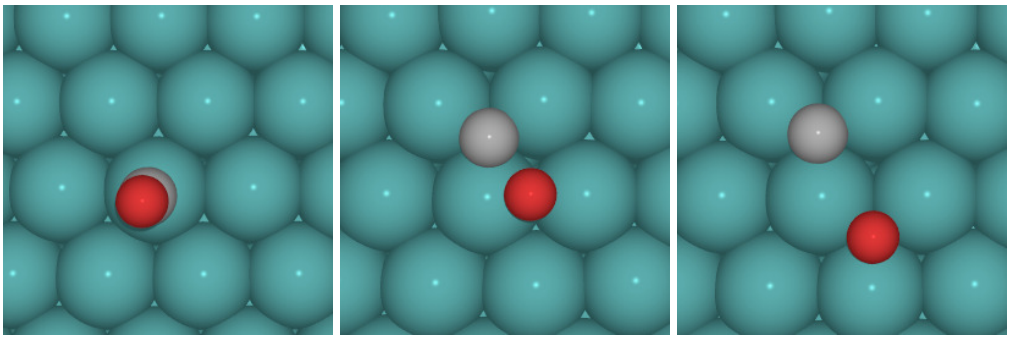

(a) (b) (c)

Figure 10.17: Optimized structures of (a) reactant (b) transition state and (c) product absorbed in relax terrace Ru(0001) surface for Path 1

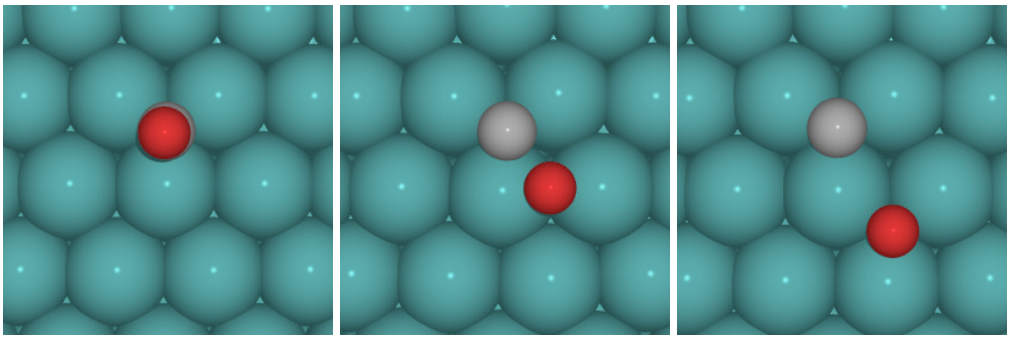

(a) (b) (c)

Figure 10.18: Optimized structures of (a) reactant (b) transition state and (c) product absorbed in relax terrace Ru(0001) surface for Path 2

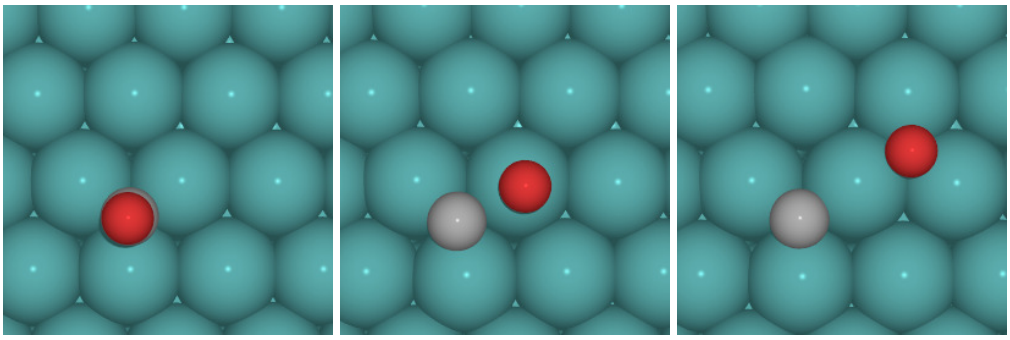

(a) (b) (c)

Figure 10.19: Optimized structures of (a) reactant (b) transition state and (c) product absorbed in relax terrace Ru(0001) surface for Path 3

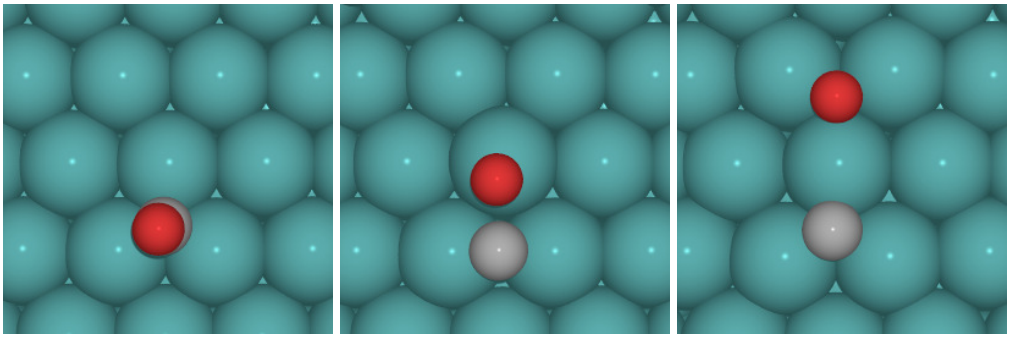

(a) (b) (c)

Figure 10.20: Optimized structures of (a) reactant (b) transition state and (c) product absorbed in relax terrace Ru(0001) surface for Path 4

Relaxed Stepped Ru(1015) Surface

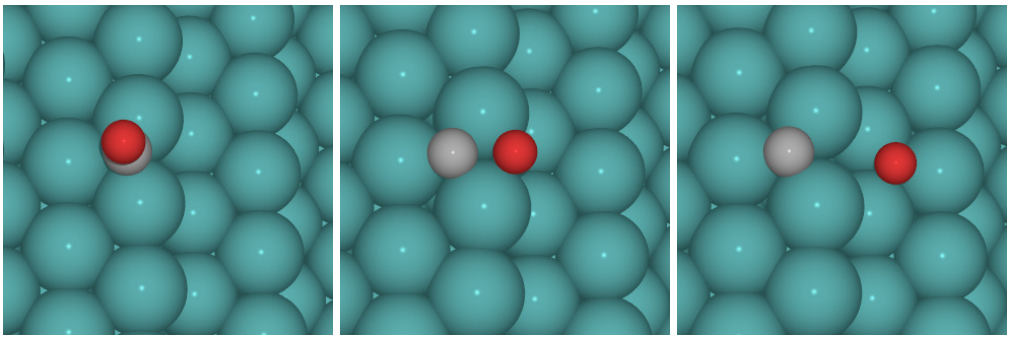

(a) (b) (c)

Figure 10.21: Optimized structures of (a) reactant (b) transition state and (c) product absorbed in relax stepped Ru(1015) surface for Path 1

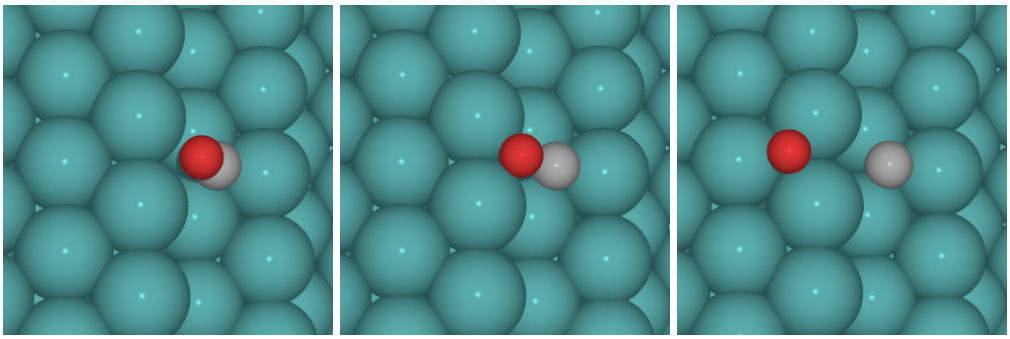

(a) (b) (c)

Figure 10.22: Optimized structures of (a) reactant (b) transition state and (c) product absorbed in relax stepped Ru(1015) surface for Path 2

Isotropic Exansion on Stepped Ru(1015) Surface

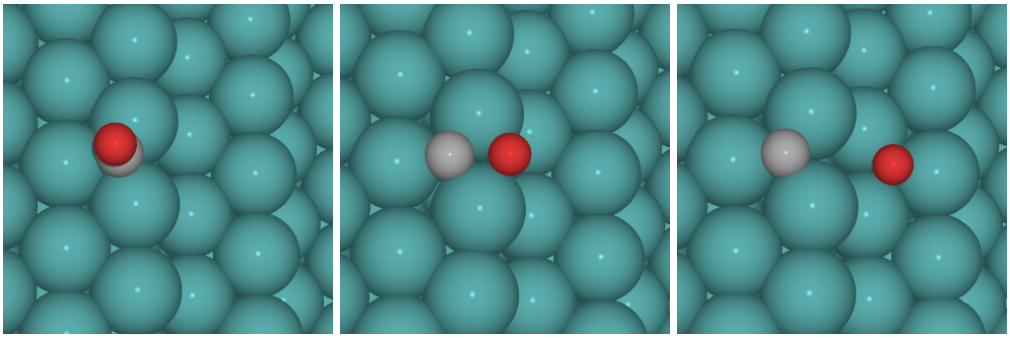

(a) (b) (c)

Figure 10.23: Optimized structures of (a) reactant (b) transition state and (c) product absorbed in relax stepped Ru(1015) surface for Path 1

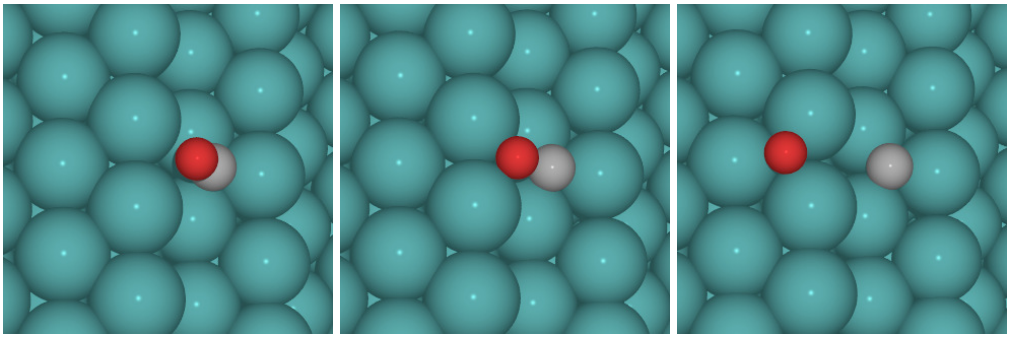

(a) (b) (c)

Figure 10.24: Optimized structures of (a) reactant (b) transition state and (c) product absorbed in relax stepped Ru(1015) surface for Path 2

Isotropic Compression on Stepped Ru(1015) Surface

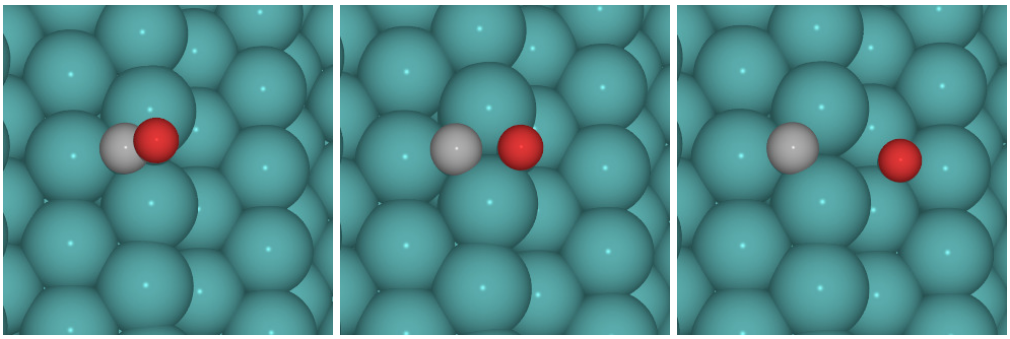

(a) (b) (c)

Figure 10.25: Optimized structures of (a) reactant (b) transition state and (c) product absorbed in relax stepped Ru(1015) surface for Path 1

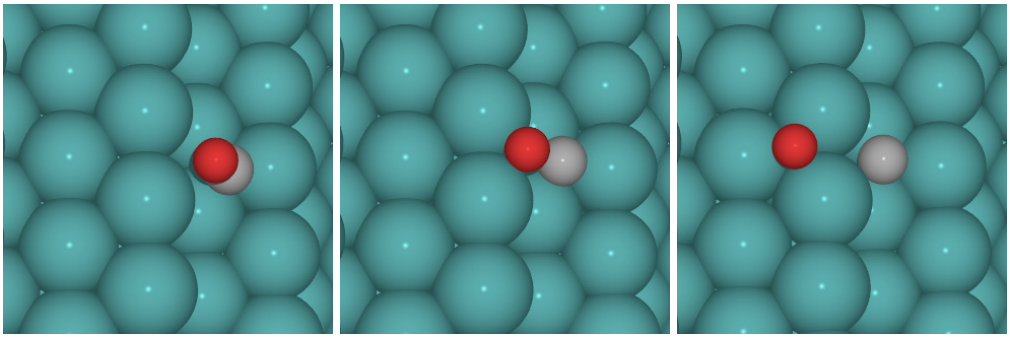

(a) (b) (c)

Figure 10.26: Optimized structures of (a) reactant (b) transition state and (c) product absorbed in relax stepped Ru(1015) surface for Path 2

Anisotropic Expansion in a of Stepped Ru(1015) Surface

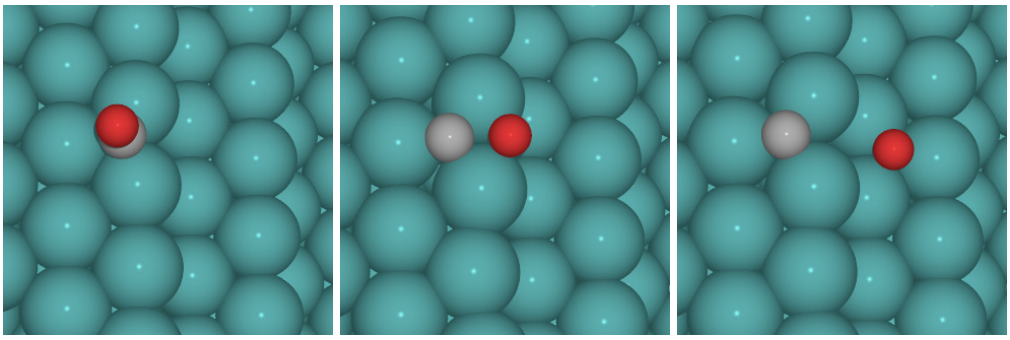

(a) (b) (c)

Figure 10.27: Optimized structures of (a) reactant (b) transition state and (c) product absorbed in relax stepped Ru(1015) surface for Path 1

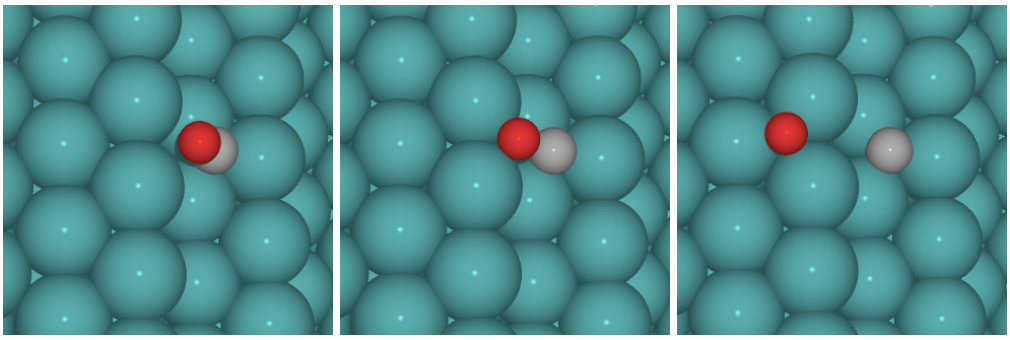

(a) (b) (c)

Figure 10.28: Optimized structures of (a) reactant (b) transition state and (c) product absorbed in relax stepped Ru(1015) surface for Path 2

Anisotropic Compression in a of Stepped Ru(1015) Surface

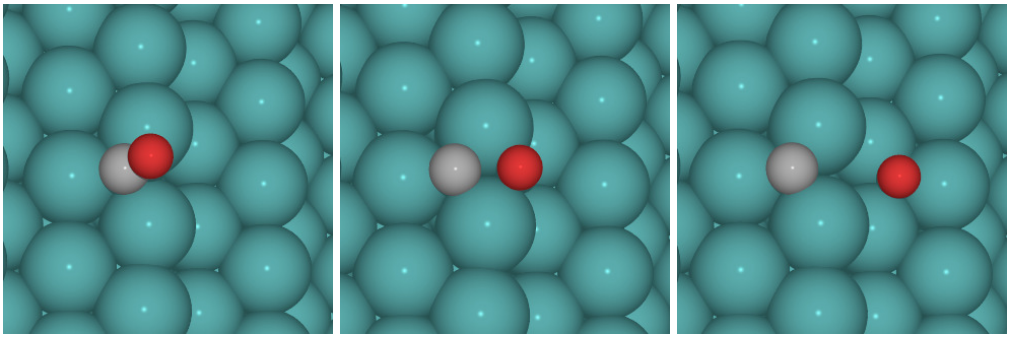

(a) (b) (c)

Figure 10.29: Optimized structures of (a) reactant (b) transition state and (c) product absorbed in relax stepped Ru(1015) surface for Path 1

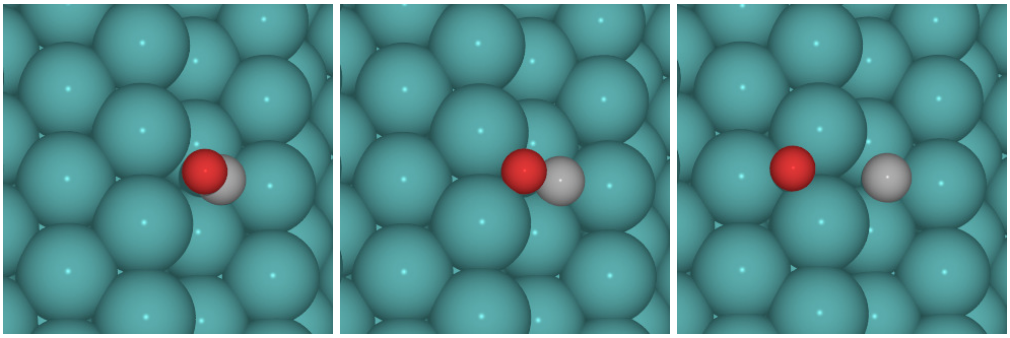

(a) (b) (c)

Figure 10.30: Optimized structures of (a) reactant (b) transition state and (c) product absorbed in relax stepped Ru(1015) surface for Path 2

Anisotropic Expansion in b of Stepped Ru(1015) Surface

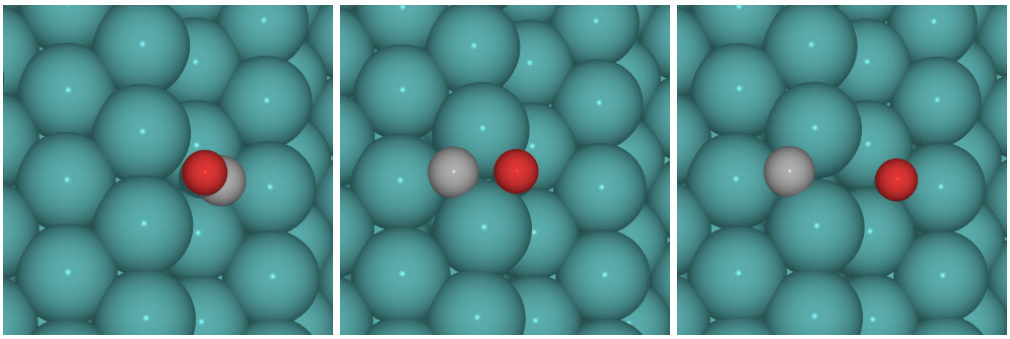

(a) (b) (c)

Figure 10.31: Optimized structures of (a) reactant (b) transition state and (c) product absorbed in relax stepped Ru(1015) surface for Path 1

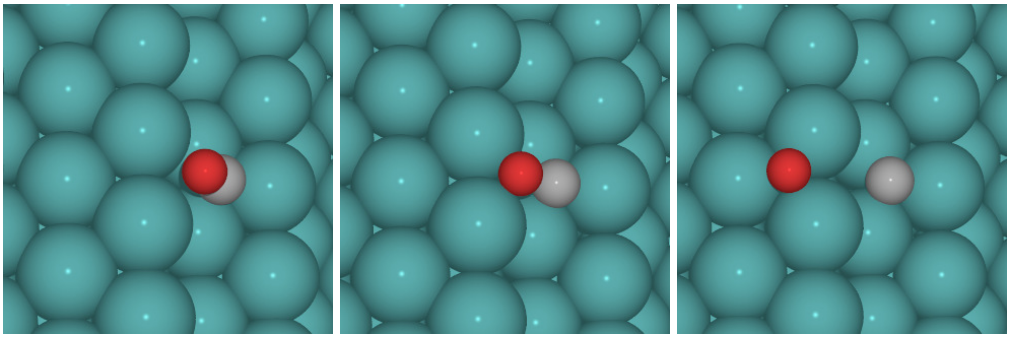

(a) (b) (c)

Figure 10.32: Optimized structures of (a) reactant (b) transition state and (c) product absorbed in relax stepped Ru(1015) surface for Path 2

Anisotropic Compression in b of Stepped Ru(1015) Surface

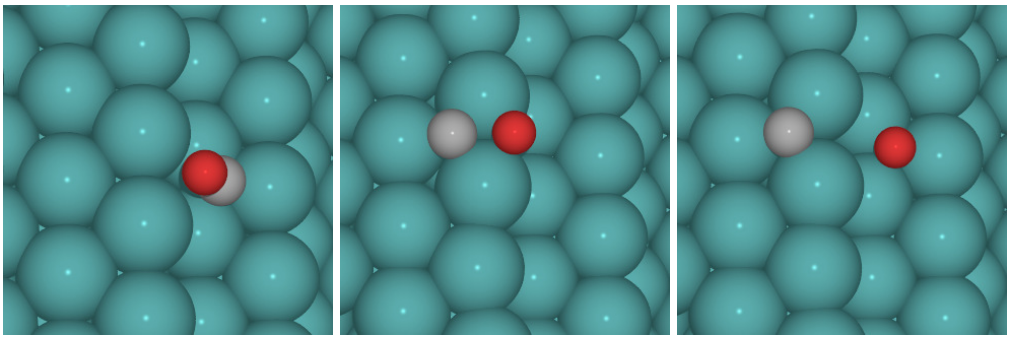

(a) (b) (c)

Figure 10.33: Optimized structures of (a) reactant (b) transition state and (c) product absorbed in relax stepped Ru(1015) surface for Path 1

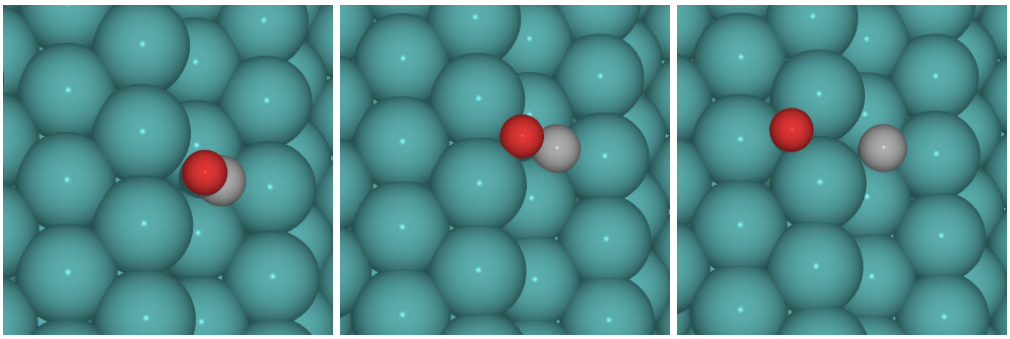

(a) (b) (c)

Figure 10.34: Optimized structures of (a) reactant (b) transition state and (c) product absorbed in relax stepped Ru(1015) surface for Path 2

Bader Charge Analysis

Terrace Ru(0001) Surface

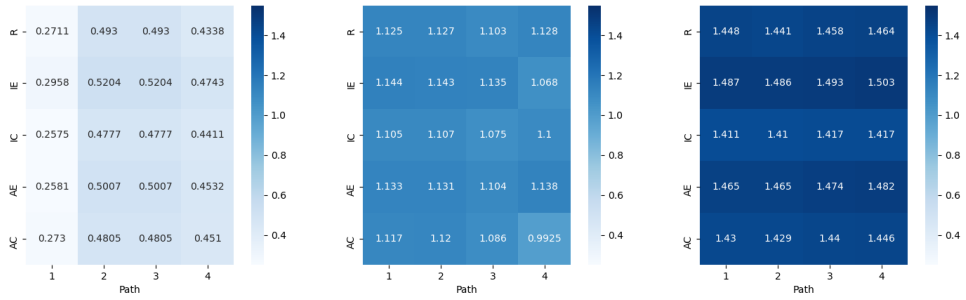

(a) (b) (c)

Figure 10.35: Bader Charges of terrace Ru(0001) Slab in (a) reactant (b) transition state and (c) product

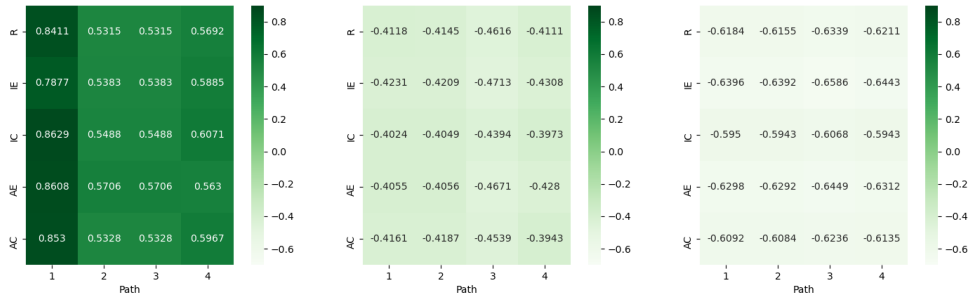

(a) (b) (c)

Figure 10.36: Bader Charges of C of (a) reactant (b) transition state and (c) product absorbed in terrace Ru(0001) surface

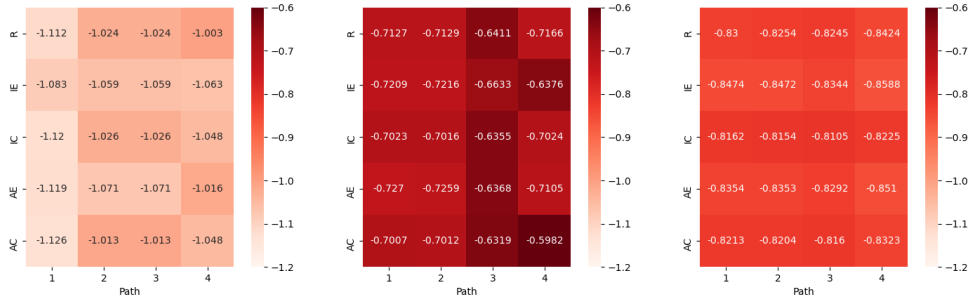

(a) (b) (c)

Figure 10.37: Bader Charges of O of (a) reactant (b) transition state and (c) product absorbed in terrace Ru(0001) surface

Stepped Ru(1015) Surface

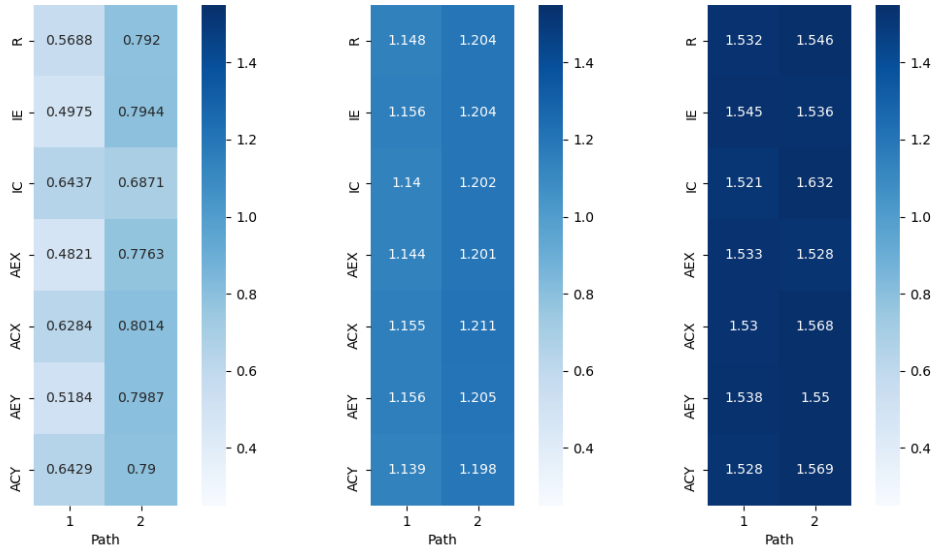

(a) (b) (c)

Figure 10.38: Bader Charges of stepped Ru(1015) Slab in (a) reactant (b) transition state and (c) product

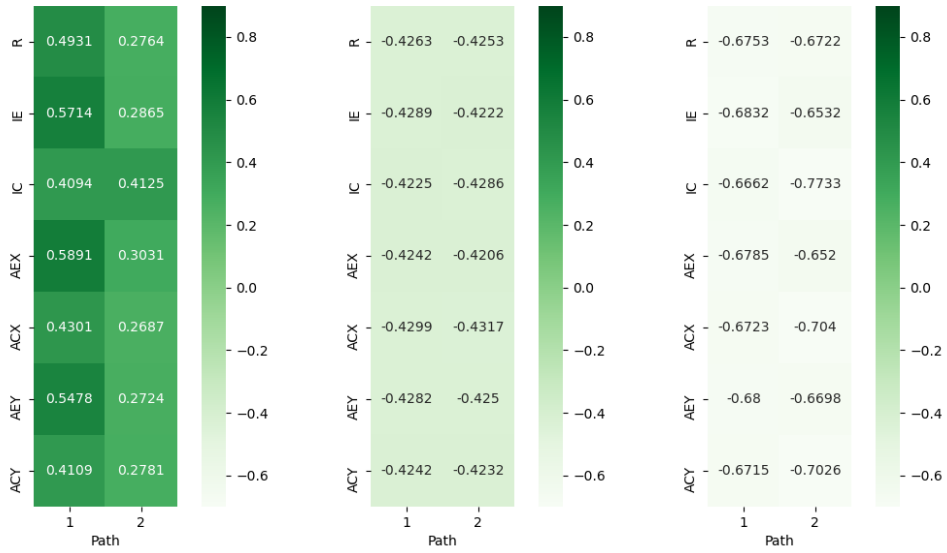

(a) (b) (c)

Figure 10.39: Bader Charges of C of (a) reactant (b) transition state and (c) product absorbed in stepped Ru(1015) surface

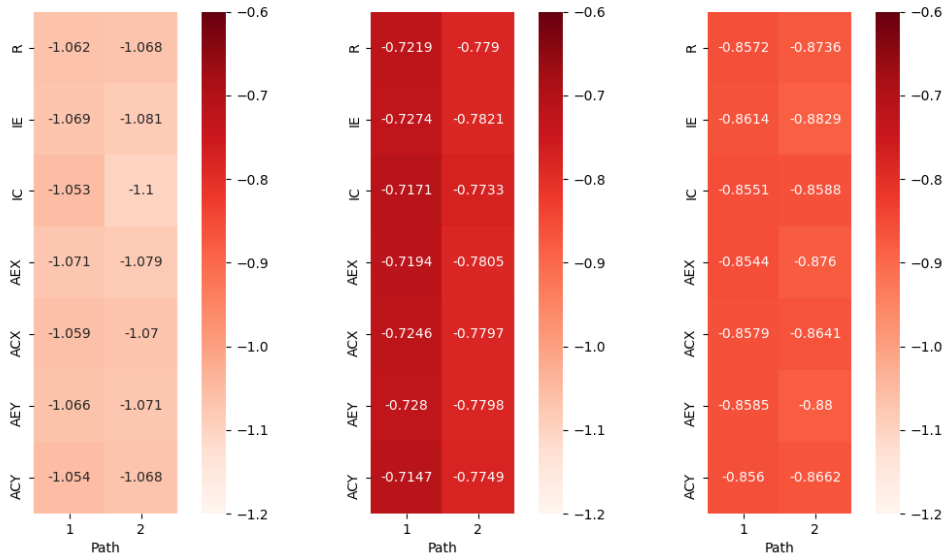

(a) (b) (c)

Figure 10.40: Bader Charges of O of (a) reactant (b) transition state and (c) product absorbed in stepped Ru(1015) surface

Charge Density Difference Maps

Relaxed Terrace Ru(0001) Surface

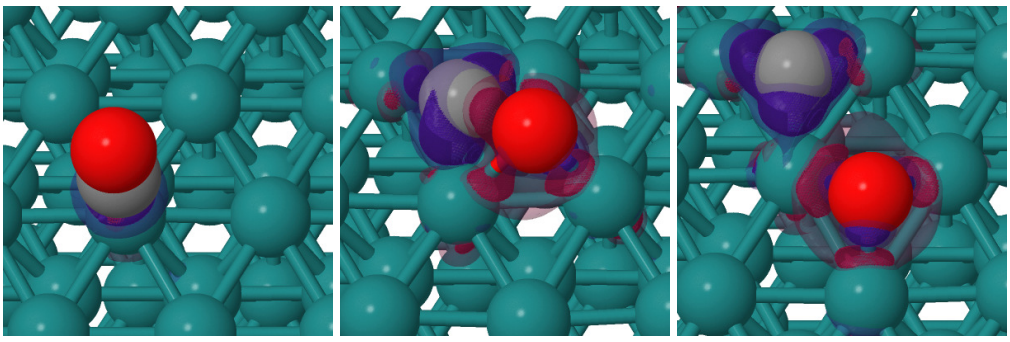

(a) (b) (c)

Figure 10.41: of (a) reactant (b) transition state and (c) product absorbed in relax terrace Ru(0001) surface for Path 1

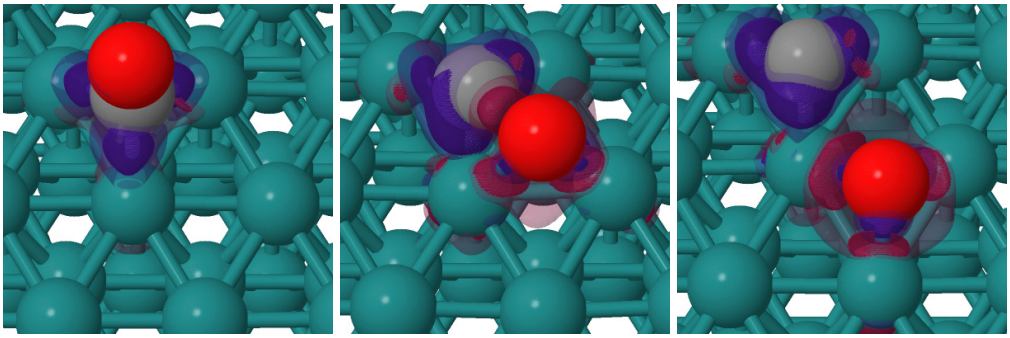

(a) (b) (c)

Figure 10.42: Charge Density Difference Maps of (a) reactant (b) transition state and (c) product absorbed in relax terrace Ru(0001) surface for Path 2

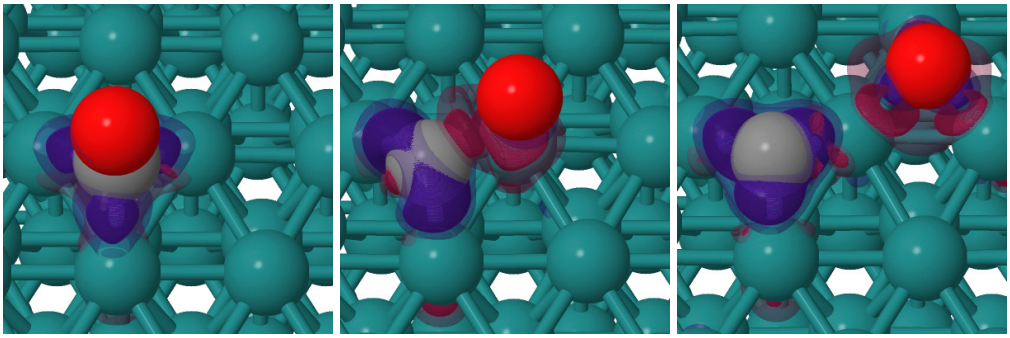

(a) (b) (c)

Figure 10.43: Charge Density Difference Maps of (a) reactant (b) transition state and (c) product absorbed in relax terrace Ru(0001) surface for Path 3

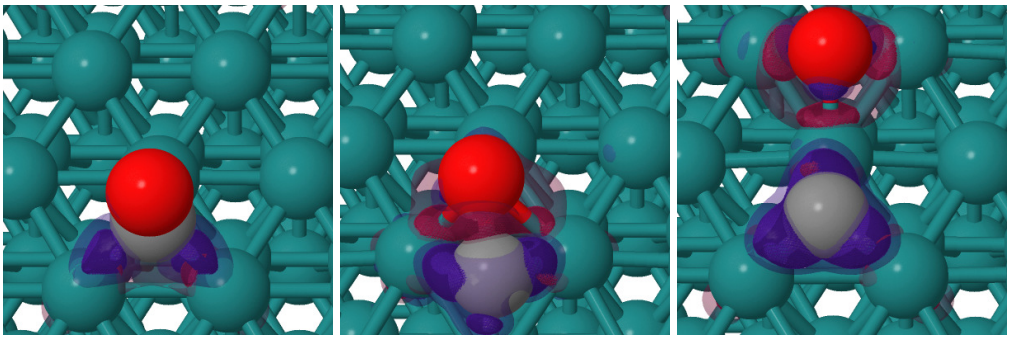

(a) (b) (c)

Figure 10.44: Charge Density Difference Maps of (a) reactant (b) transition state and (c) product absorbed in relax terrace Ru(0001) surface for Path 4

Isotropic Expansion on Terrace Ru(0001) Surface

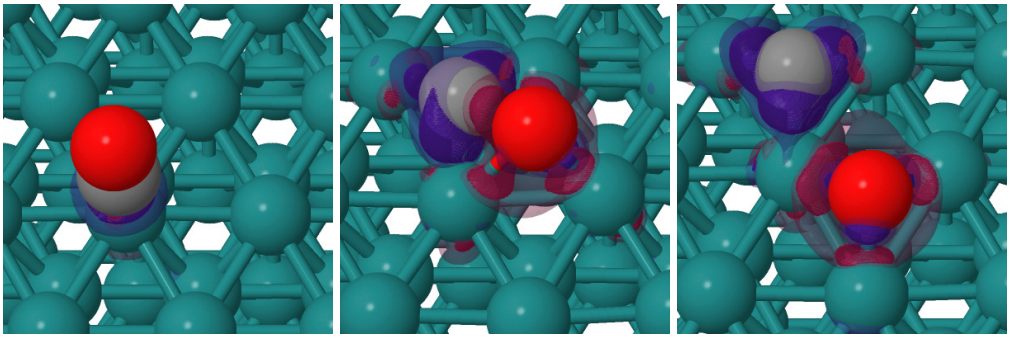

(a) (b) (c)

Figure 10.45: Charge Density Difference Maps of (a) reactant (b) transition state and (c) product absorbed in relax terrace Ru(0001) surface for Path 1

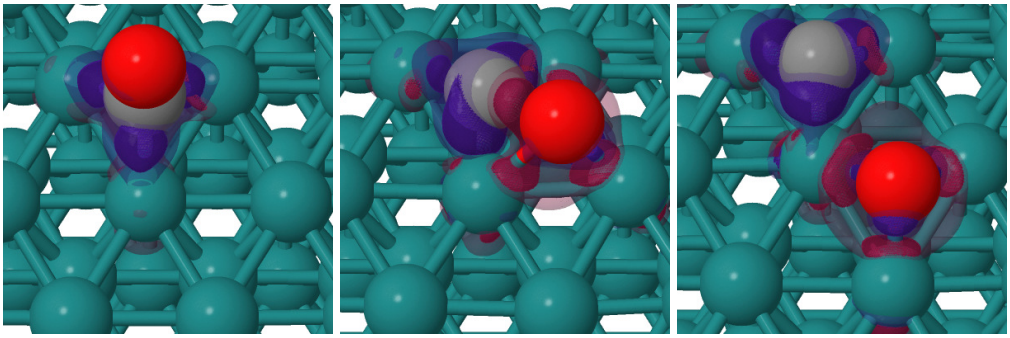

(a) (b) (c)

Figure 10.46: Charge Density Difference Maps of (a) reactant (b) transition state and (c) product absorbed in relax terrace Ru(0001) surface for Path 2

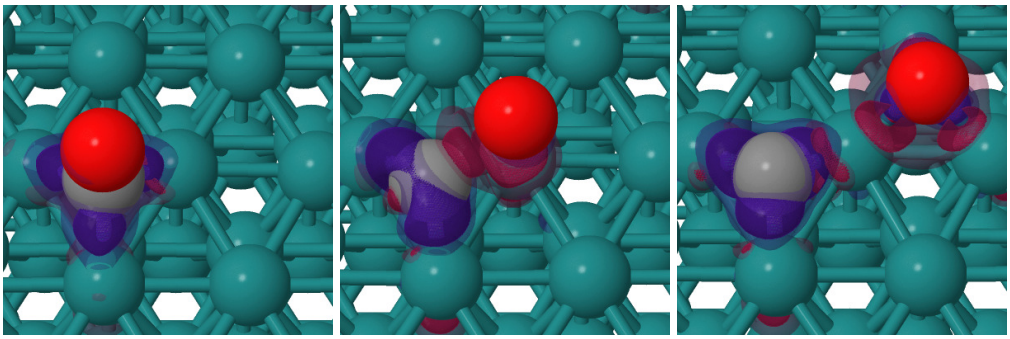

(a) (b) (c)

Figure 10.47: Charge Density Difference Maps of (a) reactant (b) transition state and (c) product absorbed in relax terrace Ru(0001) surface for Path 3

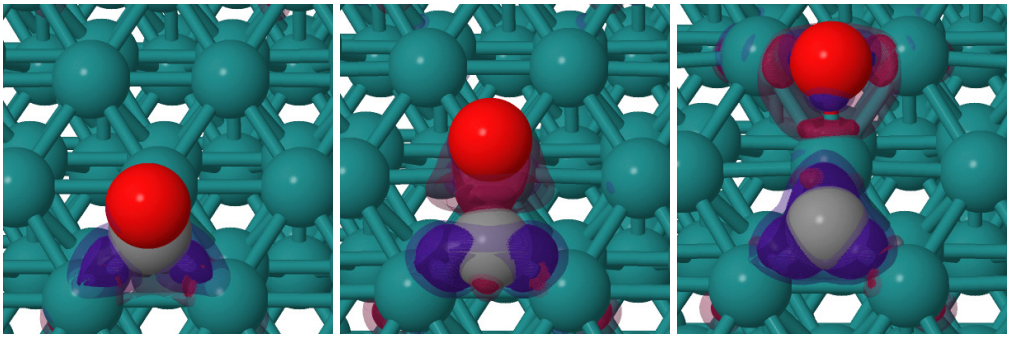

(a) (b) (c)

Figure 10.48: Charge Density Difference Maps of (a) reactant (b) transition state and (c) product absorbed in relax terrace Ru(0001) surface for Path 4

Isotropic Compression on Terrace Ru(0001) Surface

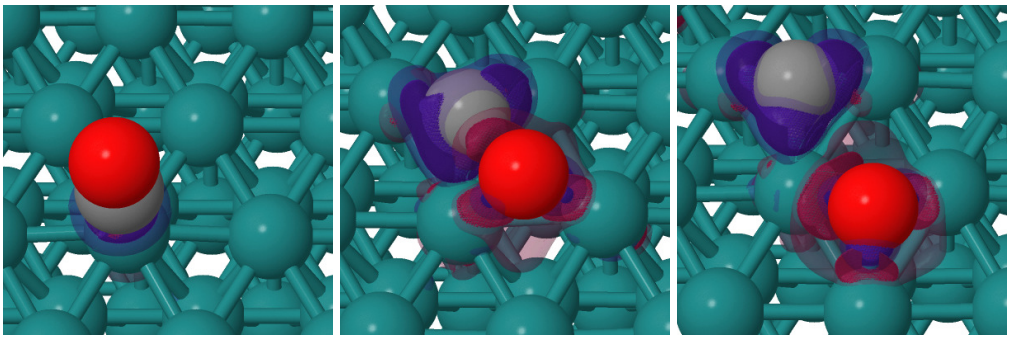

(a) (b) (c)

Figure 10.49: Charge Density Difference Maps of (a) reactant (b) transition state and (c) product absorbed in relax terrace Ru(0001) surface for Path 1

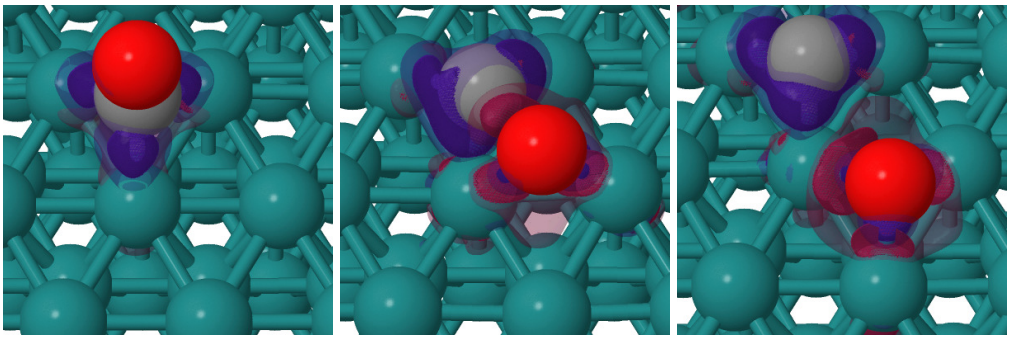

(a) (b) (c)

Figure 10.50: Charge Density Difference Maps of (a) reactant (b) transition state and (c) product absorbed in relax terrace Ru(0001) surface for Path 2

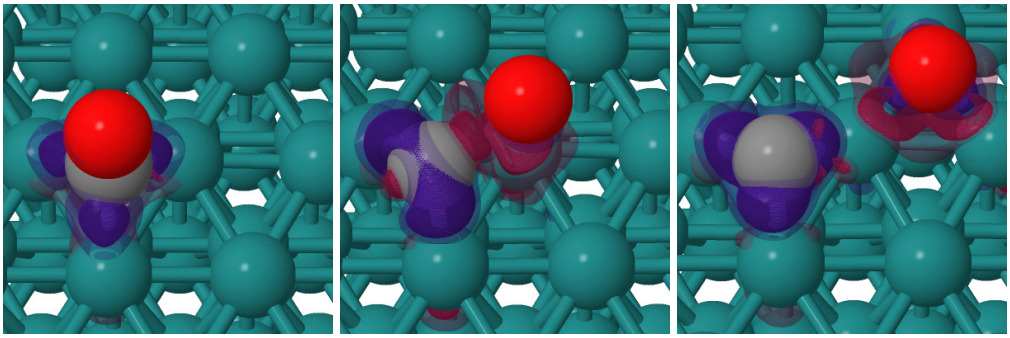

(a) (b) (c)

Figure 10.51: Charge Density Difference Maps of (a) reactant (b) transition state and (c) product absorbed in relax terrace Ru(0001) surface for Path 3

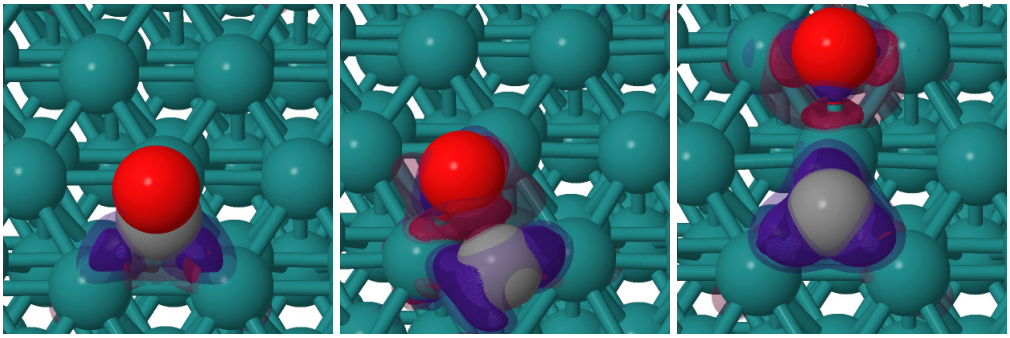

(a) (b) (c)

Figure 10.52: Charge Density Difference Maps of (a) reactant (b) transition state and (c) product absorbed in relax terrace Ru(0001) surface for Path 4

Anisotropic Expansion on Terrace Ru(0001) Surface

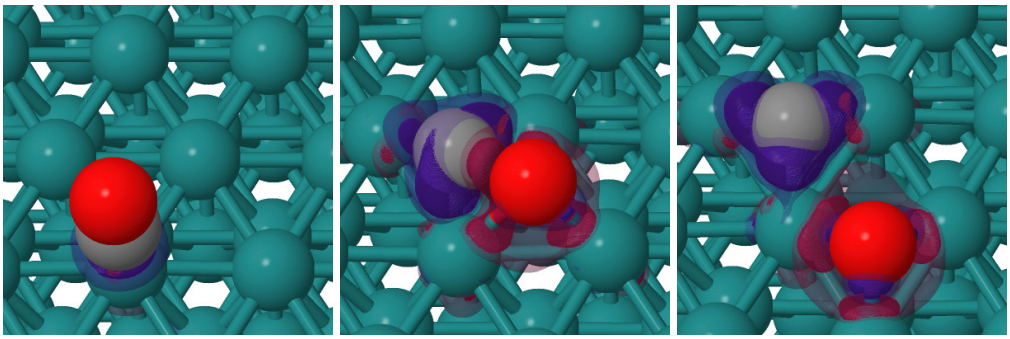

(a) (b) (c)

Figure 10.53: Charge Density Difference Maps of (a) reactant (b) transition state and (c) product absorbed in relax terrace Ru(0001) surface for Path 1

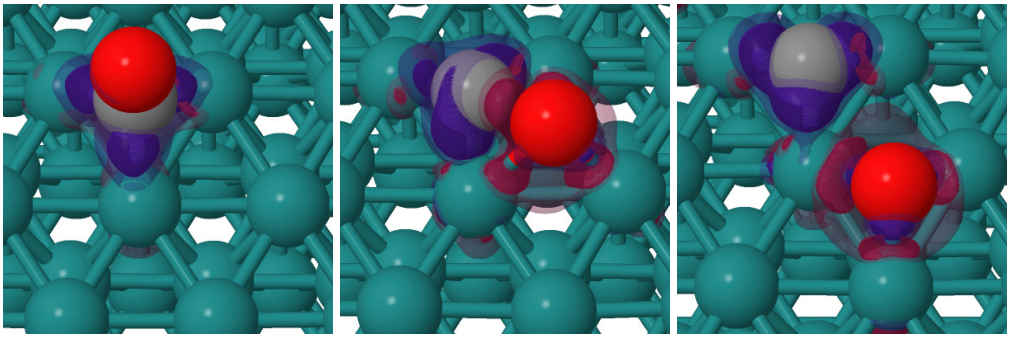

(a) (b) (c)

Figure 10.54: Charge Density Difference Maps of (a) reactant (b) transition state and (c) product absorbed in relax terrace Ru(0001) surface for Path 2

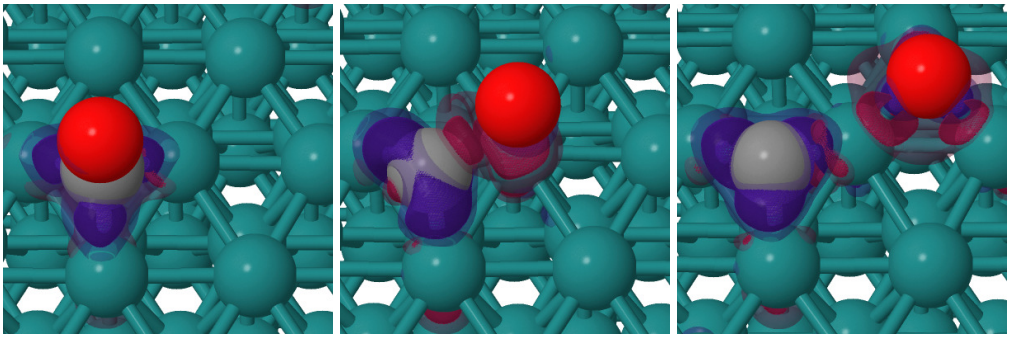

(a) (b) (c)

Figure 10.55: Charge Density Difference Maps of (a) reactant (b) transition state and (c) product absorbed in relax terrace Ru(0001) surface for Path 3

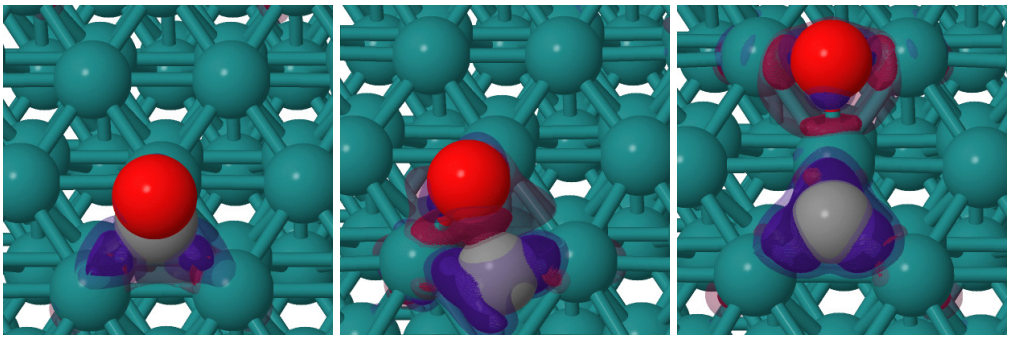

(a) (b) (c)

Figure 10.56: Charge Density Difference Maps of (a) reactant (b) transition state and (c) product absorbed in relax terrace Ru(0001) surface for Path 4

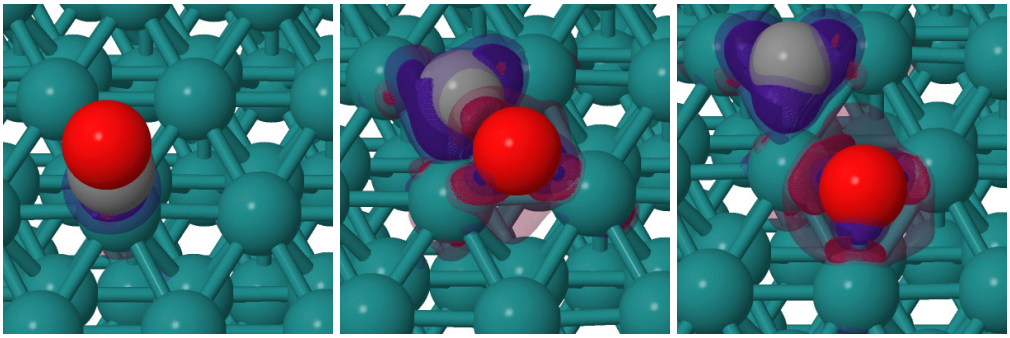

(a) (b) (c)

Figure 10.57: Charge Density Difference Maps of (a) reactant (b) transition state and (c) product absorbed in relax terrace Ru(0001) surface for Path 1

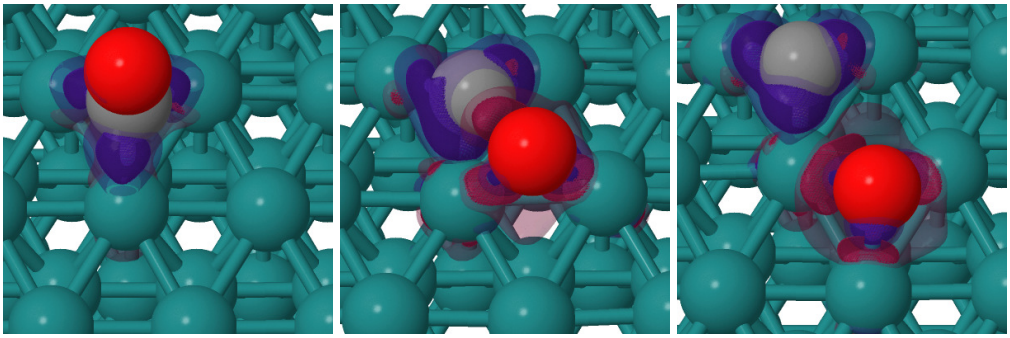

(a) (b) (c)

Figure 10.58: Charge Density Difference Maps of (a) reactant (b) transition state and (c) product absorbed in relax terrace Ru(0001) surface for Path 2

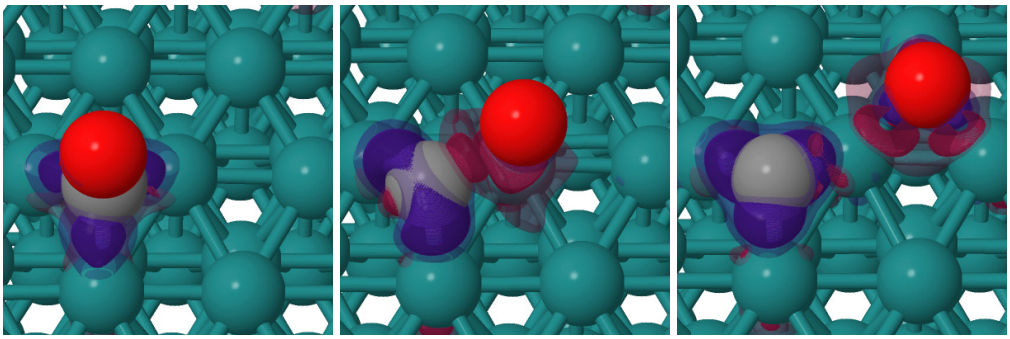

(a) (b) (c)

Figure 10.59: Charge Density Difference Maps of (a) reactant (b) transition state and (c) product absorbed in relax terrace Ru(0001) surface for Path 3

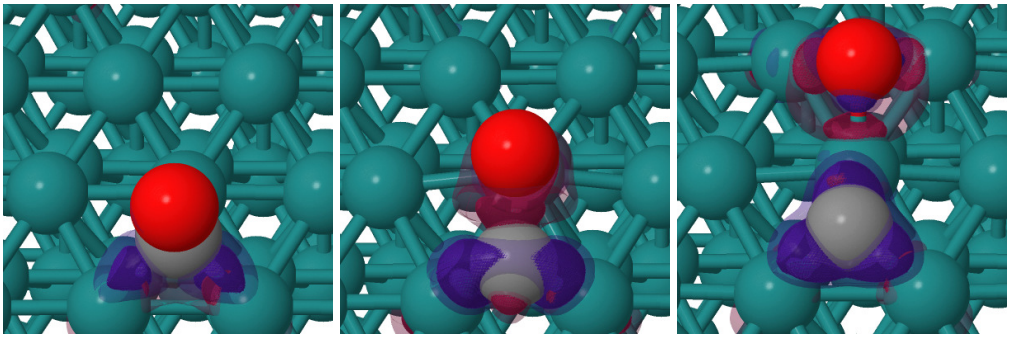

(a) (b) (c)

Figure 10.60: Charge Density Difference Maps of (a) reactant (b) transition state and (c) product absorbed in relax terrace Ru(0001) surface for Path 4

Relaxed Stepped Ru(1015) Surface

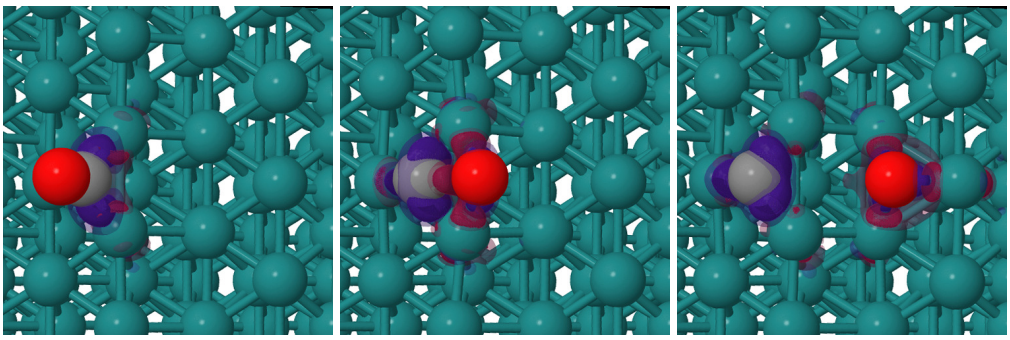

(a) (b) (c)

Figure 10.61: Charge Density Difference Maps of (a) reactant (b) transition state and (c) product absorbed in relax stepped Ru(1015) surface for Path 1

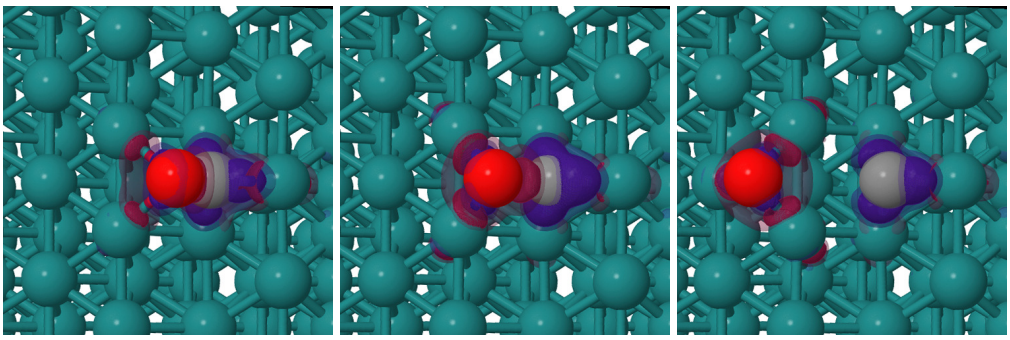

(a) (b) (c)

Figure 10.62: Charge Density Difference Maps of (a) reactant (b) transition state and (c) product absorbed in relax stepped Ru(1015) surface for Path 2

Isotropic Expansion on Stepped Ru(1015) Surface

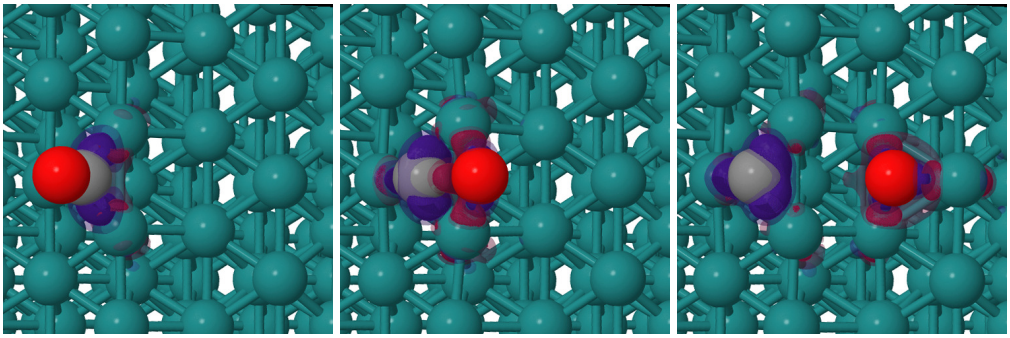

(a) (b) (c)

Figure 10.63: Charge Density Difference Maps of (a) reactant (b) transition state and (c) product absorbed in relax stepped Ru(1015) surface for Path 1

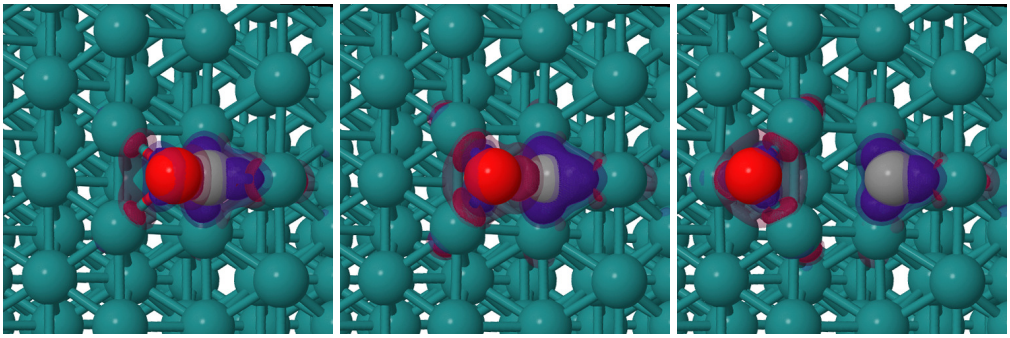

(a) (b) (c)

Figure 10.64: Charge Density Difference Maps of (a) reactant (b) transition state and (c) product absorbed in relax stepped Ru(1015) surface for Path 2

Isotropic Compression on Stepped Ru(1015) Surface

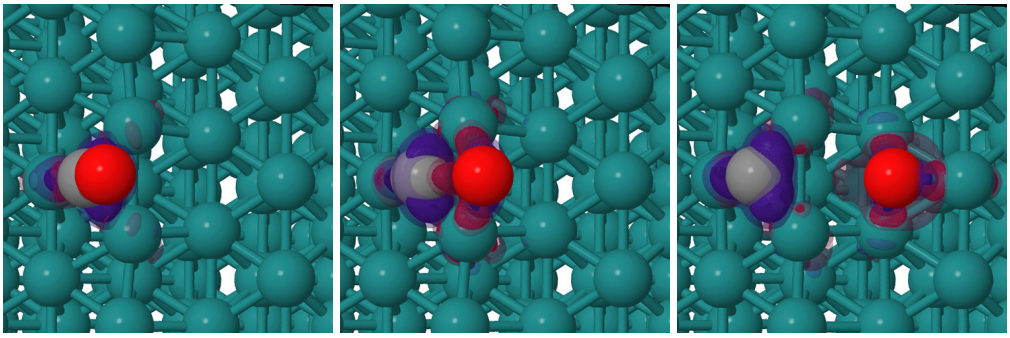

(a) (b) (c)

Figure 10.65: Charge Density Difference Maps of (a) reactant (b) transition state and (c) product absorbed in relax stepped Ru(1015) surface for Path 1

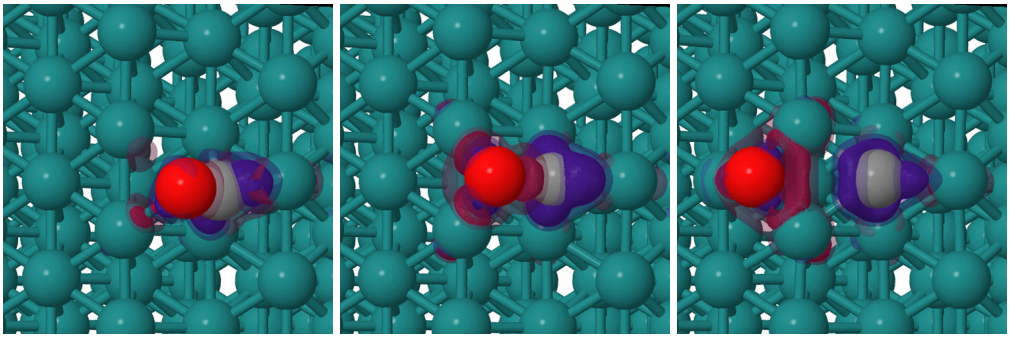

(a) (b) (c)

Figure 10.66: Charge Density Difference Maps of (a) reactant (b) transition state and (c) product absorbed in relax stepped Ru(1015) surface for Path 2

Anisotropic Expansion in a on Stepped Ru(1015) Surface

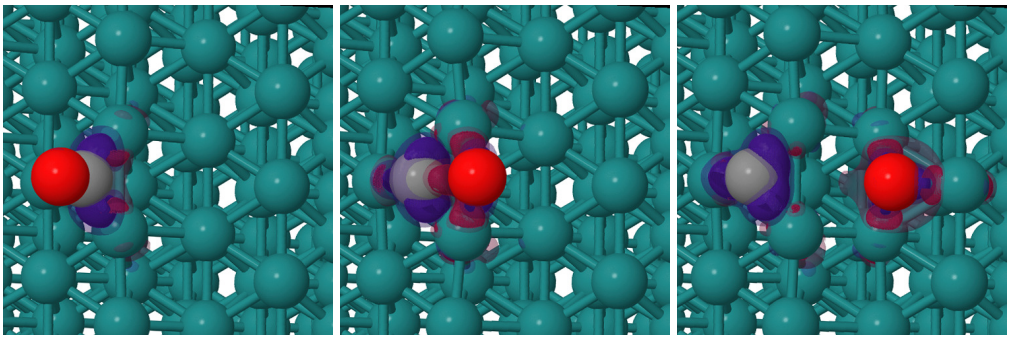

(a) (b) (c)

Figure 10.67: Charge Density Difference Maps of (a) reactant (b) transition state and (c) product absorbed in relax stepped Ru(1015) surface for Path 1

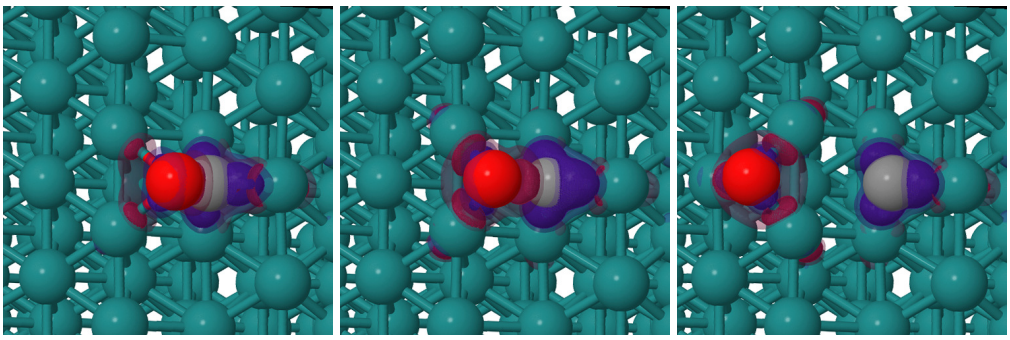

(a) (b) (c)

Figure 10.68: Charge Density Difference Maps of (a) reactant (b) transition state and (c) product absorbed in relax stepped Ru(1015) surface for Path 2

Anisotropic Compression in a Stepped Ru(1015) Surface

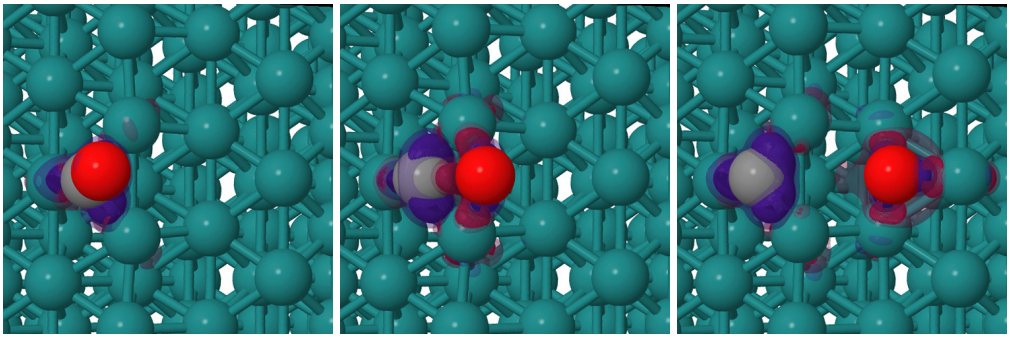

(a) (b) (c)

Figure 10.69: Charge Density Difference Maps of (a) reactant (b) transition state and (c) product absorbed in relax stepped Ru(1015) surface for Path 1

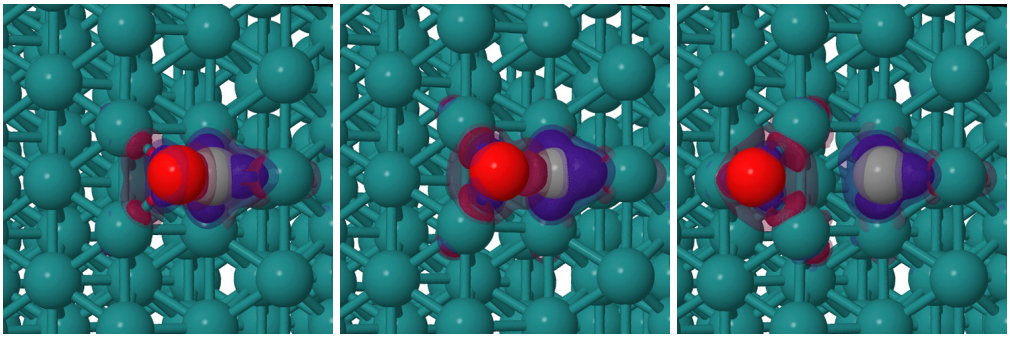

(a) (b) (c)

Figure 10.70: Charge Density Difference Maps of (a) reactant (b) transition state and (c) product absorbed in relax stepped Ru(1015) surface for Path 2

Anisotropic Expansion in b on Stepped Ru(1015) Surface

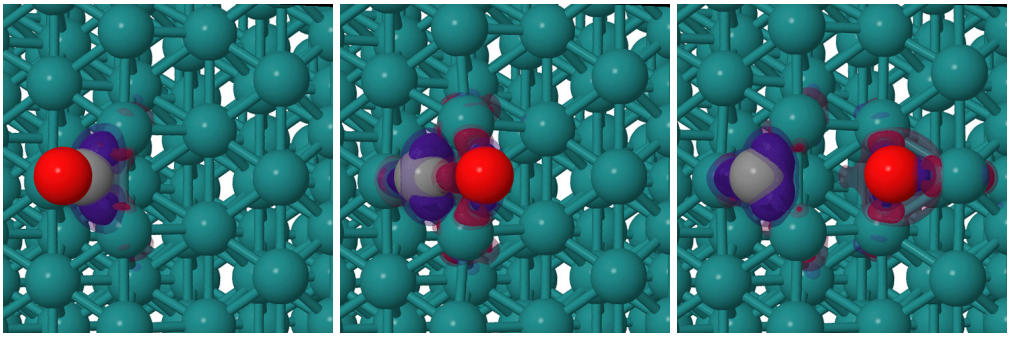

(a) (b) (c)

Figure 10.71: Charge Density Difference Maps of (a) reactant (b) transition state and (c) product absorbed in relax stepped Ru(1015) surface for Path 1

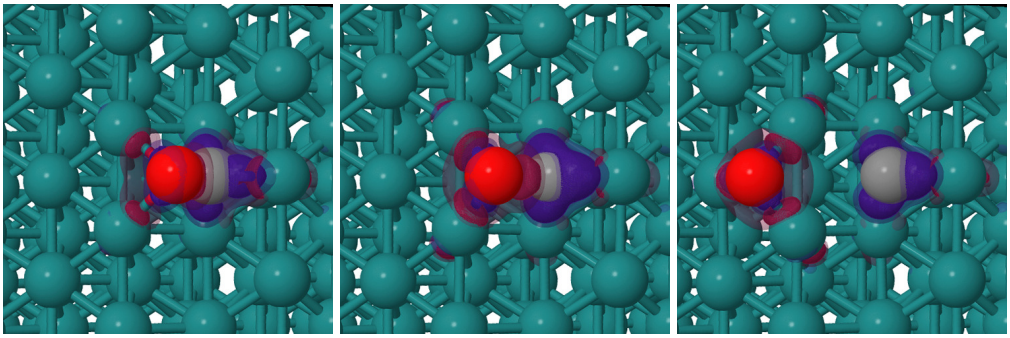

(a) (b) (c)

Figure 10.72: Charge Density Difference Maps of (a) reactant (b) transition state and (c) product absorbed in relax stepped Ru(1015) surface for Path 2

Anisotropic Compression in b Stepped Ru(1015) Surface

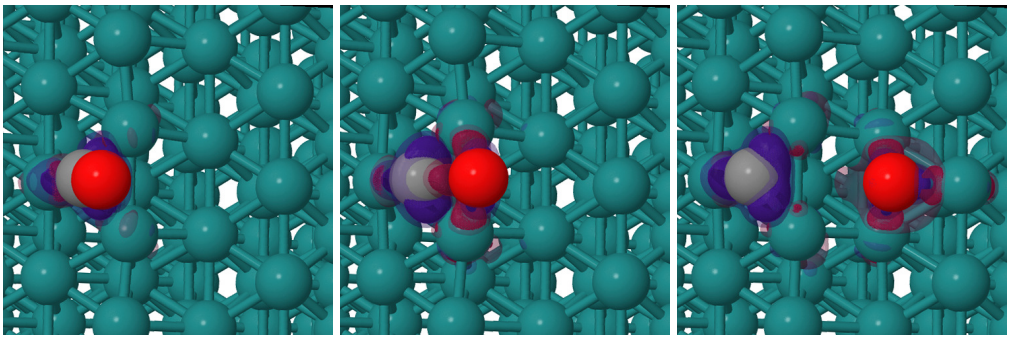

(a) (b) (c)

Figure 10.73: Charge Density Difference Maps of (a) reactant (b) transition state and (c) product absorbed in relax stepped Ru(1015) surface for Path 1

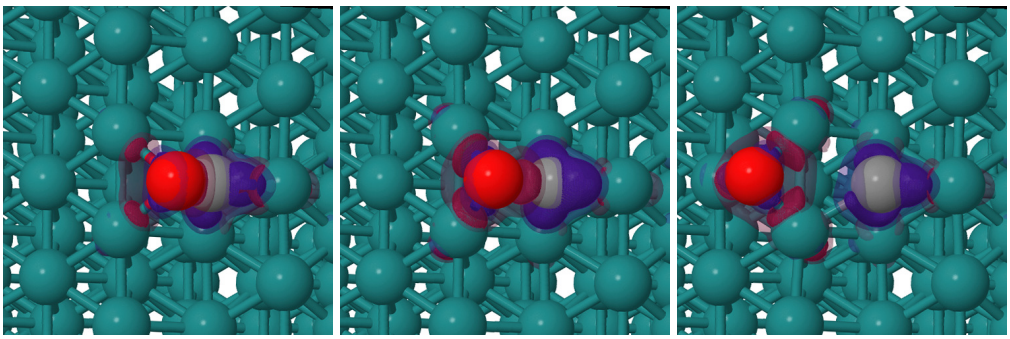

(a) (b) (c)

Figure 10.74: Charge Density Difference Maps of (a) reactant (b) transition state and (c) product absorbed in relax stepped Ru(1015) surface for Path 2

Projected Density of States (PDOS) and Integrated PDOS

Relaxed Terrace Ru(0001) Surface

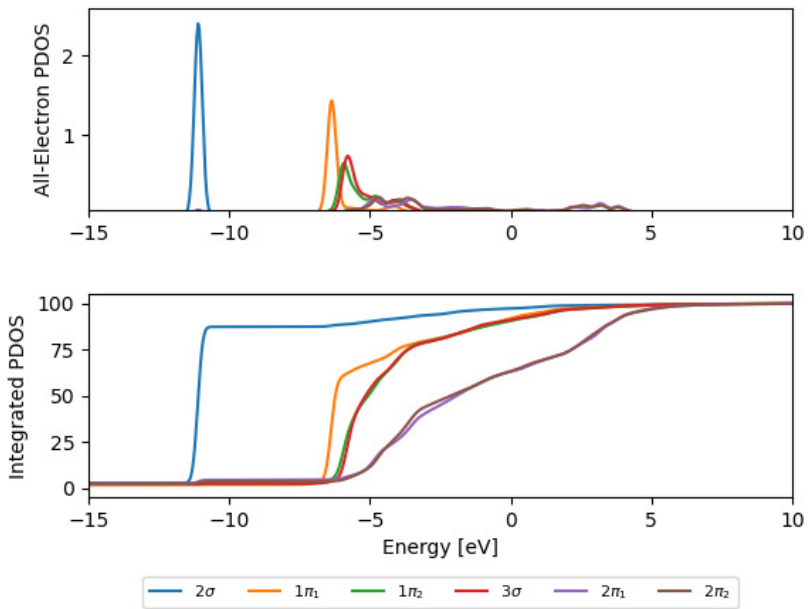

Figure 10.75: Projected Density of States (PDOS) and Integrated PDOS of reactant absorbed in relax terrace Ru(0001) surface for Path 1

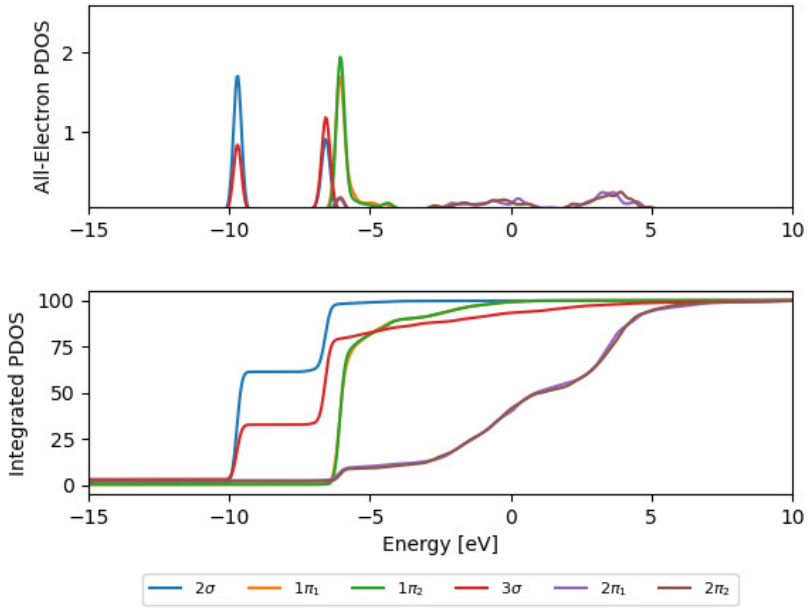

Figure 10.76: Projected Density of States (PDOS) and Integrated PDOS of reactant absorbed in relax terrace Ru(0001) surface for Path 2

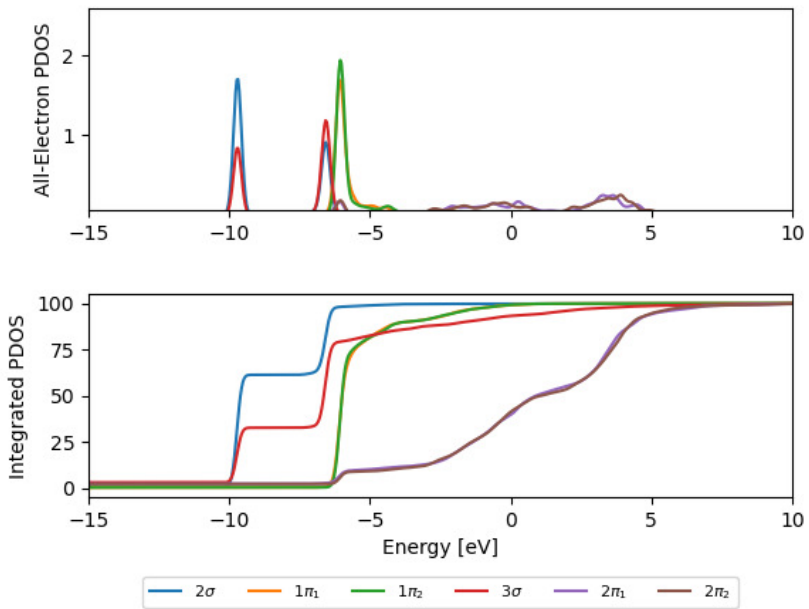

Figure 10.77: Projected Density of States (PDOS) and Integrated PDOS of reactant absorbed in relax terrace Ru(0001) surface for Path 3

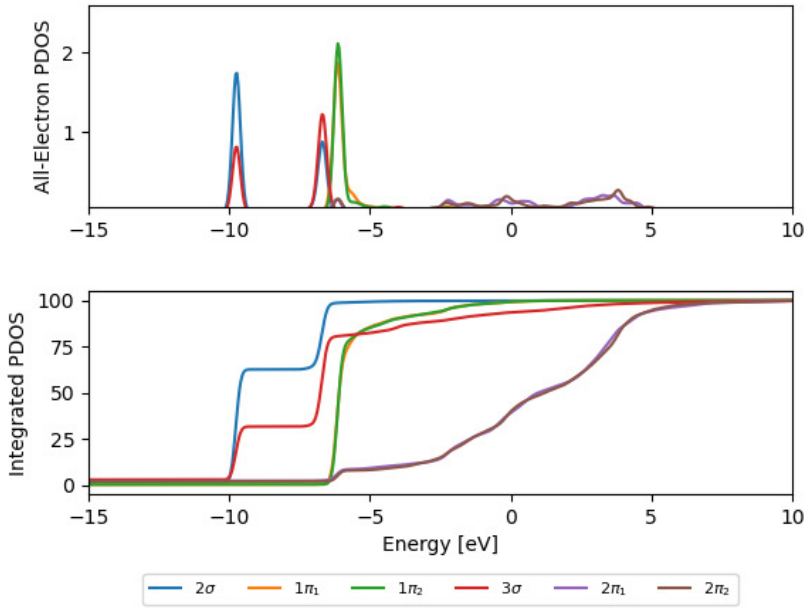

Figure 10.78: Projected Density of States (PDOS) and Integrated PDOS of reactant absorbed in relax terrace Ru(0001) surface for Path 4

Isotropic Expansion on Terrace Ru(0001) Surface

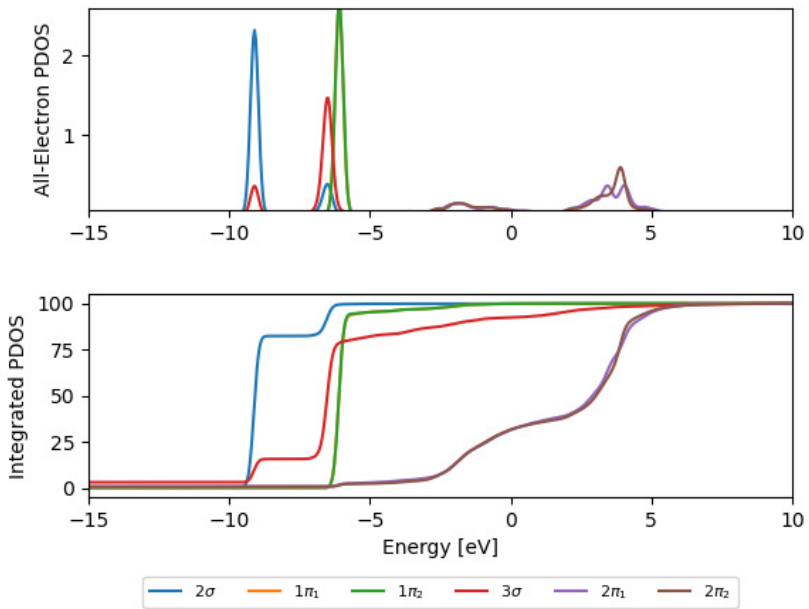

Figure 10.79: Projected Density of States (PDOS) and Integrated PDOS of reactant absorbed in relax terrace Ru(0001) surface for Path 1

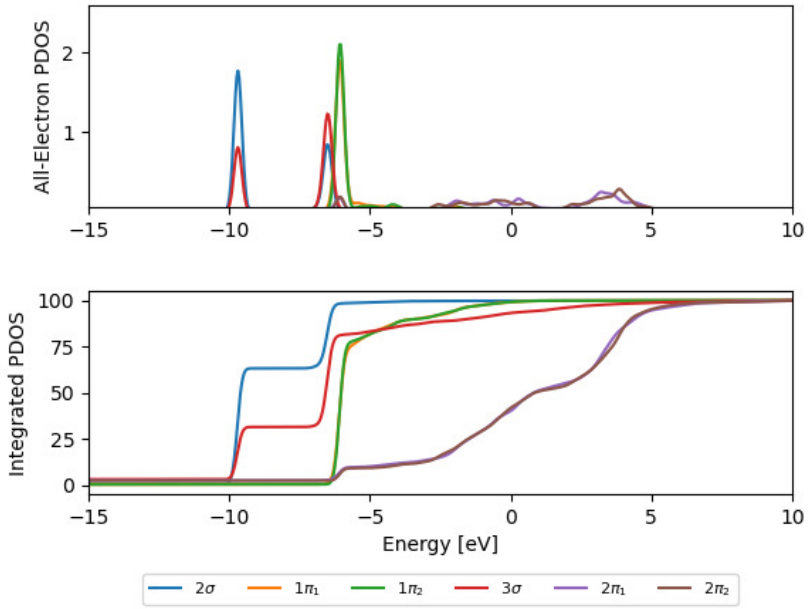

Figure 10.80: Projected Density of States (PDOS) and Integrated PDOS of reactant absorbed in relax terrace Ru(0001) surface for Path 2

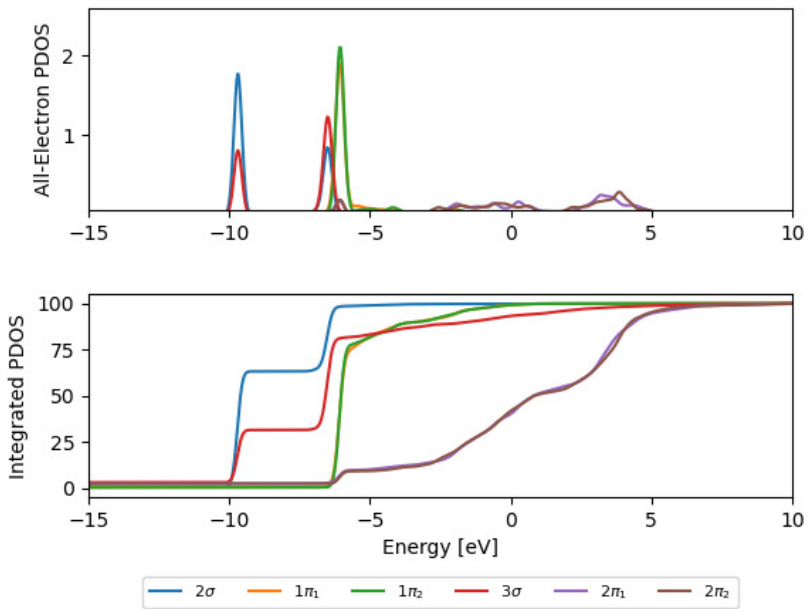

Figure 10.81: Projected Density of States (PDOS) and Integrated PDOS of reactant absorbed in relax terrace Ru(0001) surface for Path 3

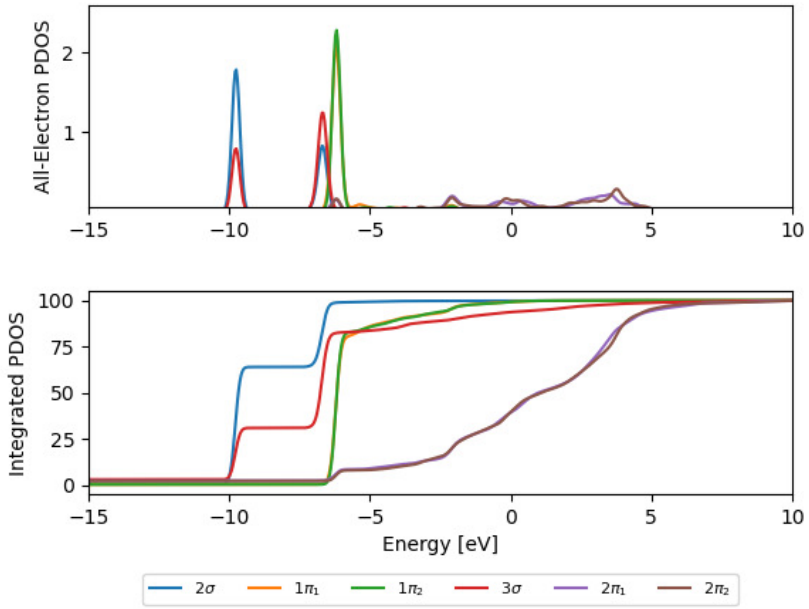

Figure 10.82: Projected Density of States (PDOS) and Integrated PDOS of reactant absorbed in relax terrace Ru(0001) surface for Path 4

Isotropic Compression on Terrace Ru(0001) Surface

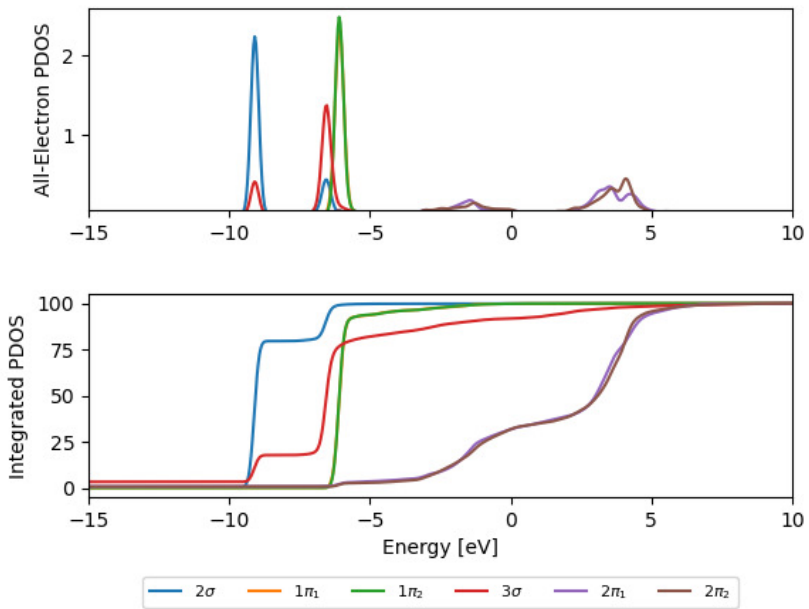

Figure 10.83: Projected Density of States (PDOS) and Integrated PDOS of reactant absorbed in relax terrace Ru(0001) surface for Path 1

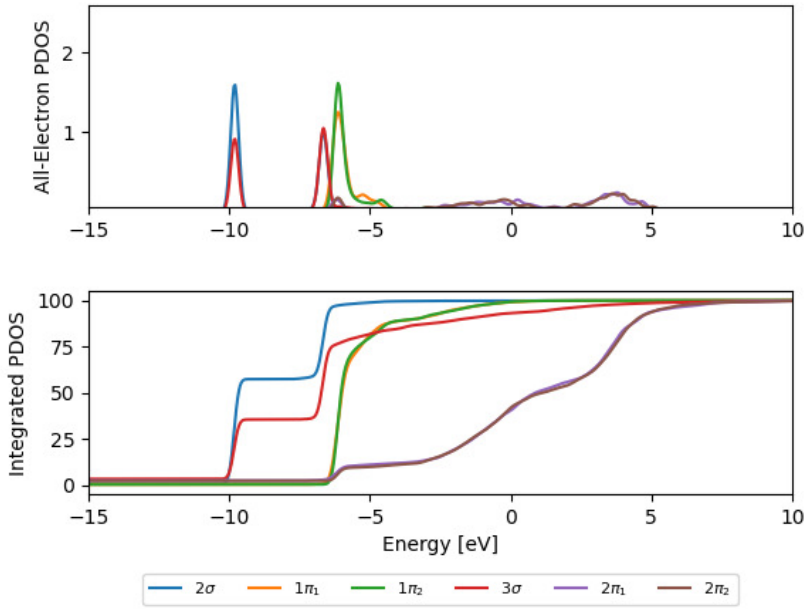

Figure 10.84: Projected Density of States (PDOS) and Integrated PDOS of reactant absorbed in relax terrace Ru(0001) surface for Path 2

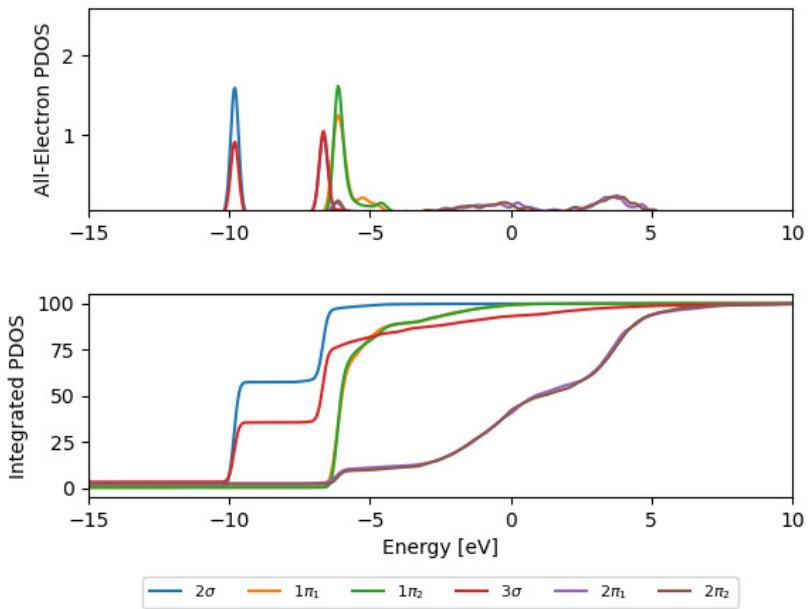

Figure 10.85: Projected Density of States (PDOS) and Integrated PDOS of reactant absorbed in relax terrace Ru(0001) surface for Path 3

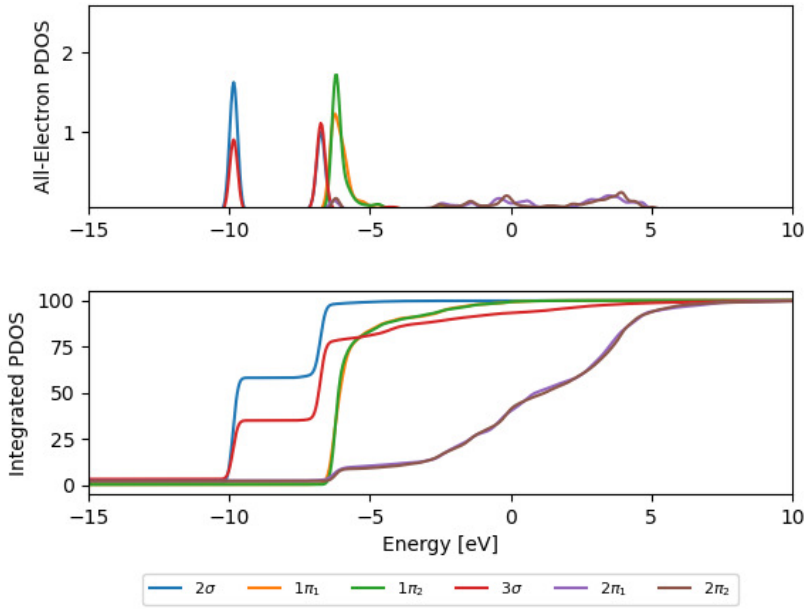

Figure 10.86: Projected Density of States (PDOS) and Integrated PDOS of reactant absorbed in relax terrace Ru(0001) surface for Path 4

Anisotropic Expansion on Terrace Ru(0001) Surface

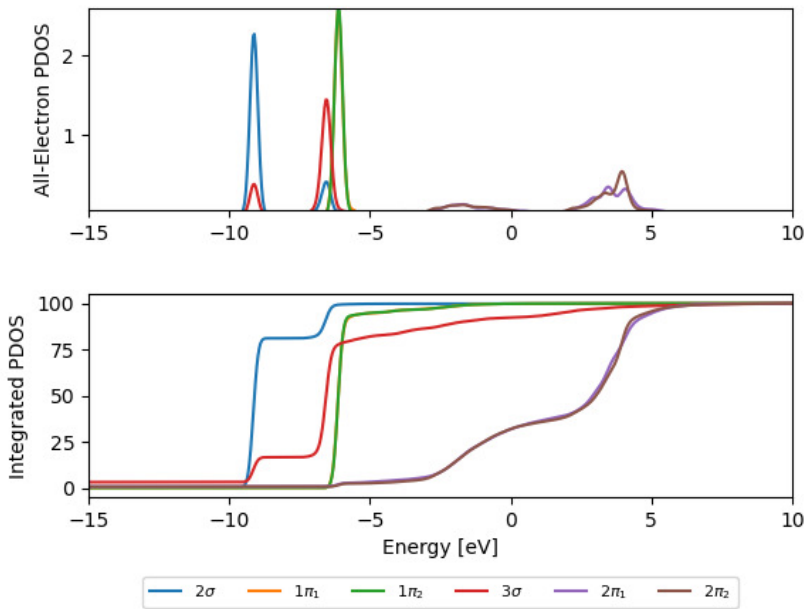

Figure 10.87: Projected Density of States (PDOS) and Integrated PDOS of reactant absorbed in relax terrace Ru(0001) surface for Path 1

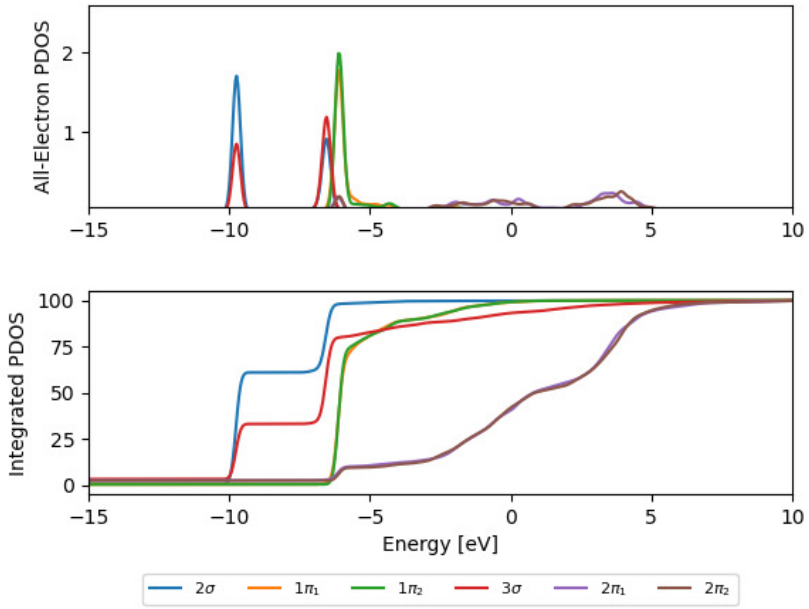

Figure 10.88: Projected Density of States (PDOS) and Integrated PDOS of reactant absorbed in relax terrace Ru(0001) surface for Path 2

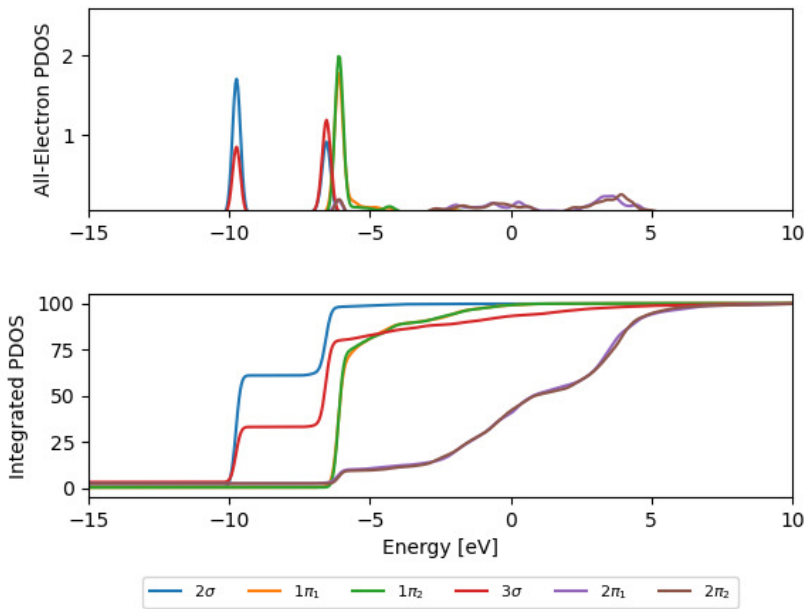

Figure 10.89: Projected Density of States (PDOS) and Integrated PDOS of reactant absorbed in relax terrace Ru(0001) surface for Path 3

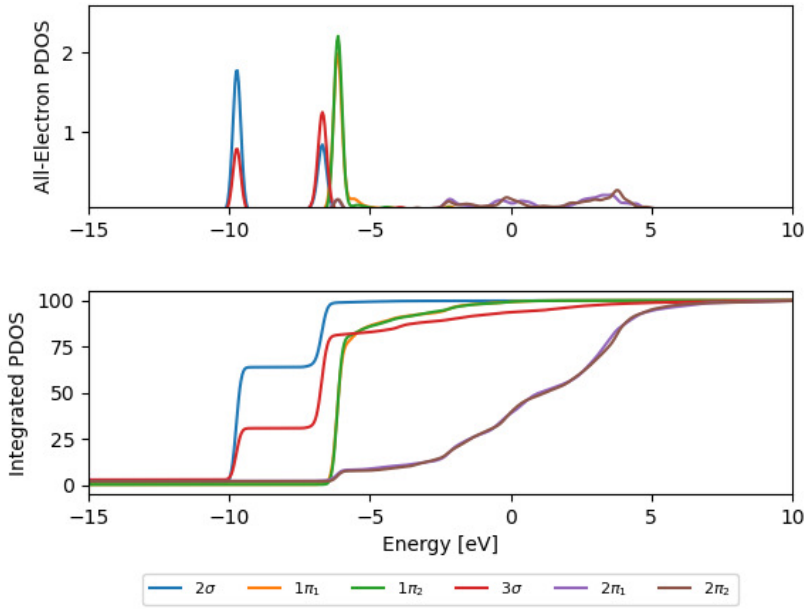

Figure 10.90: Projected Density of States (PDOS) and Integrated PDOS of reactant absorbed in relax terrace Ru(0001) surface for Path 4

Anisotropic Compression on Ru(0001) Surface

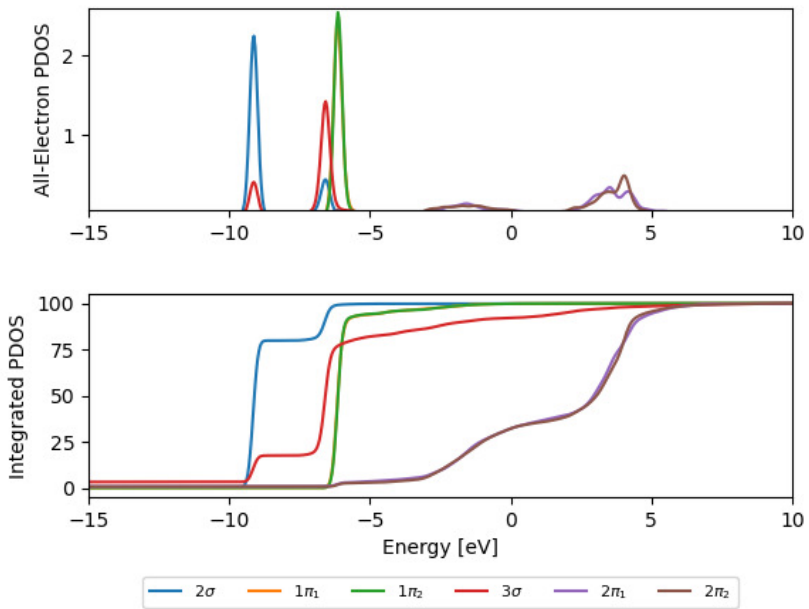

Figure 10.91: Projected Density of States (PDOS) and Integrated PDOS of reactant absorbed in relax terrace Ru(0001) surface for Path 1

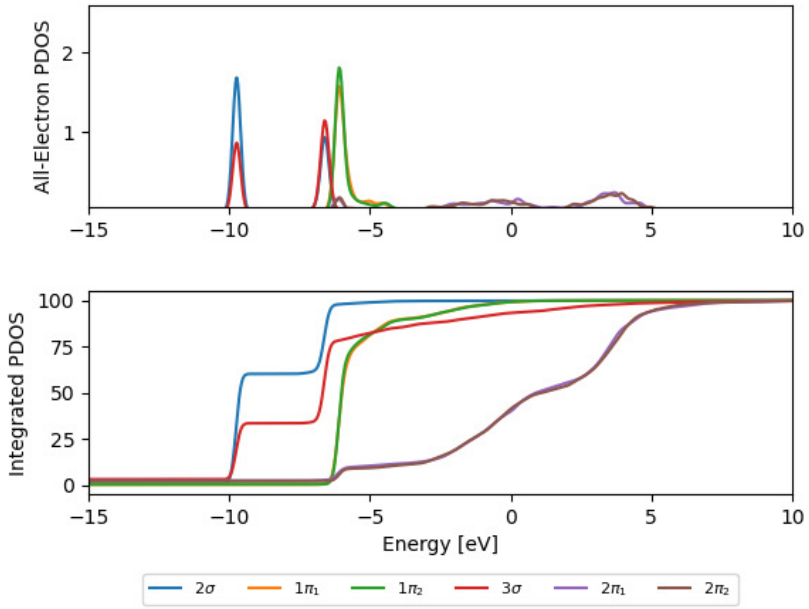

Figure 10.92: Projected Density of States (PDOS) and Integrated PDOS of reactant absorbed in relax terrace Ru(0001) surface for Path 2

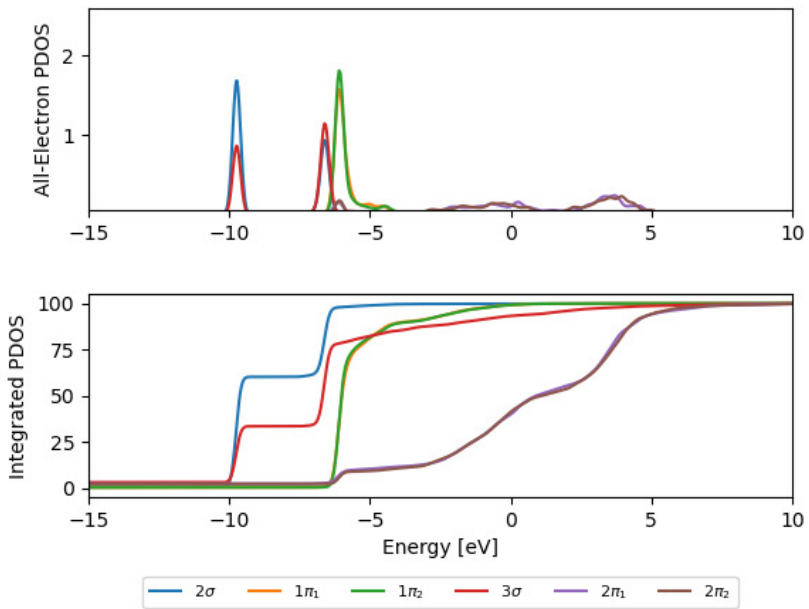

Figure 10.93: Projected Density of States (PDOS) and Integrated PDOS of reactant absorbed in relax terrace Ru(0001) surface for Path 3

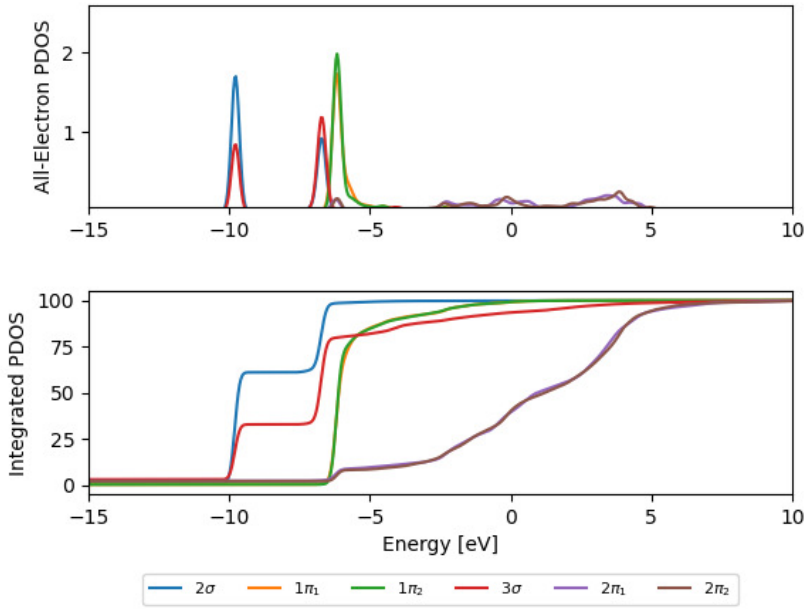

Figure 10.94: Projected Density of States (PDOS) and Integrated PDOS of reactant absorbed in relax terrace Ru(0001) surface for Path 4

Relaxed Stepped Ru(1015) Surface

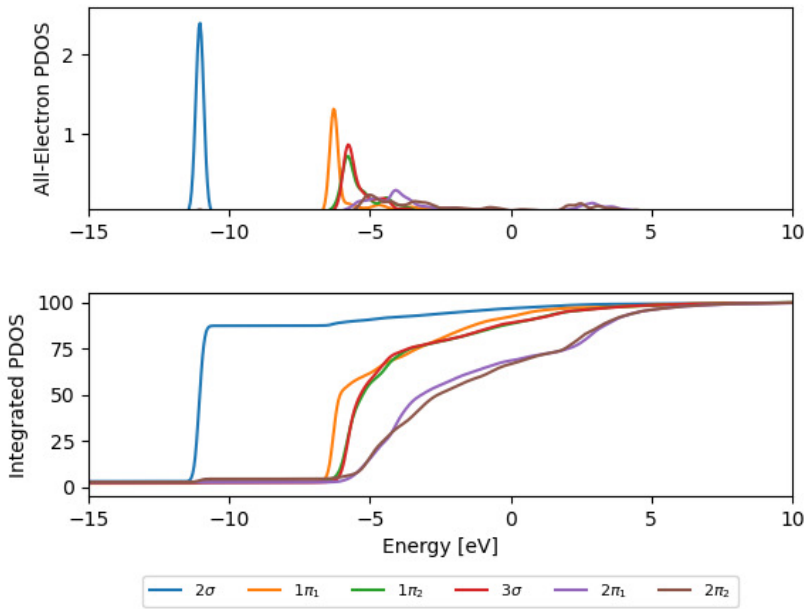

Figure 10.95: Projected Density of States (PDOS) and Integrated PDOS of reactant absorbed in relax stepped Ru(1015) surface for Path 1

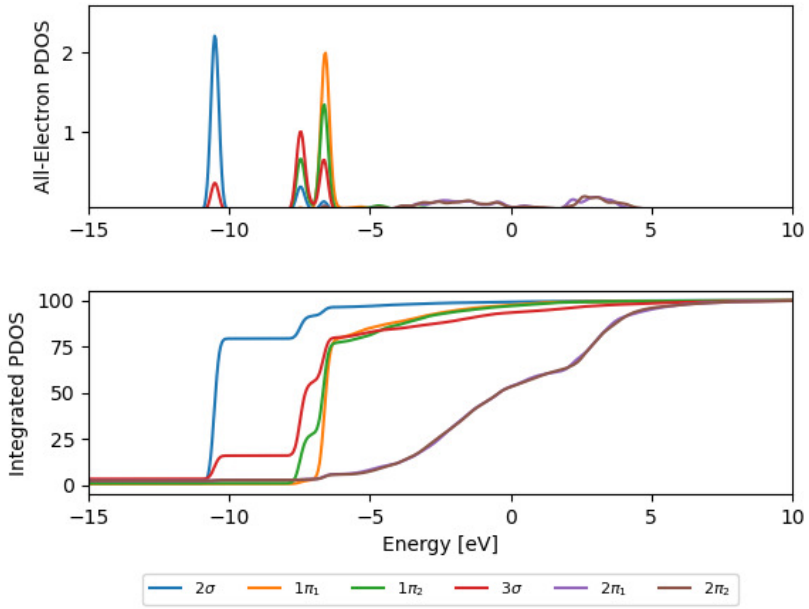

Figure 10.96: Projected Density of States (PDOS) and Integrated PDOS of reactant absorbed in relax stepped Ru(1015) surface for Path 2

Isotropic Expansion on Stepped Ru(1015) Surface

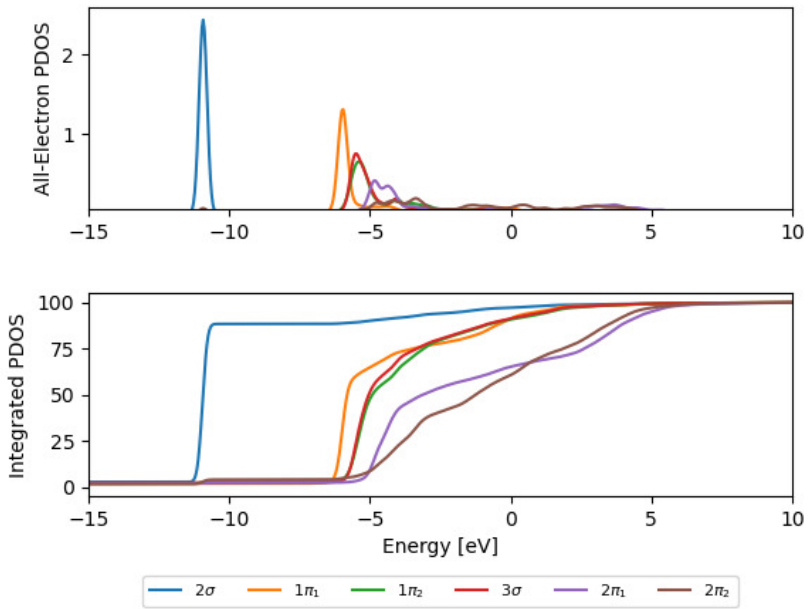

Figure 10.97: Projected Density of States (PDOS) and Integrated PDOS of reactant absorbed in relax stepped Ru(1015) surface for Path 1

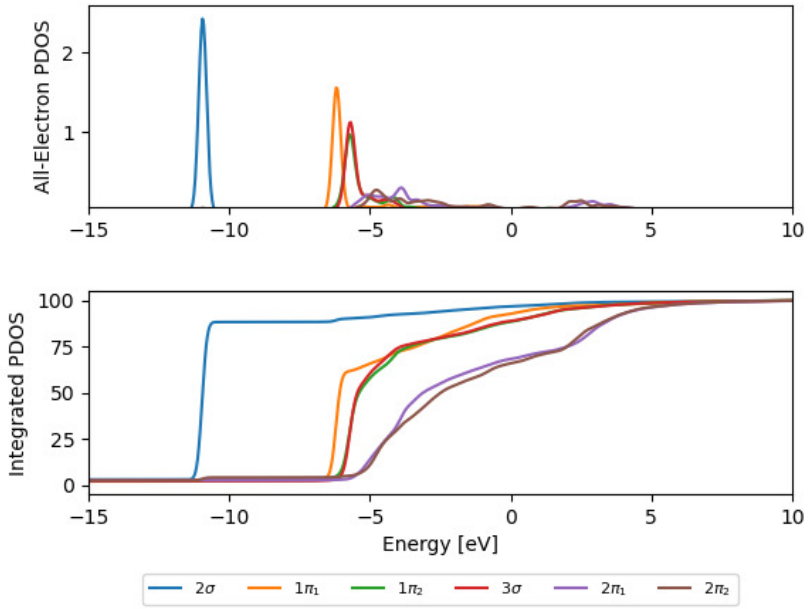

Figure 10.98: Projected Density of States (PDOS) and Integrated PDOS of reactant absorbed in relax stepped Ru(1015) surface for Path 2

Isotropic Compression on Stepped Ru(1015) Surface

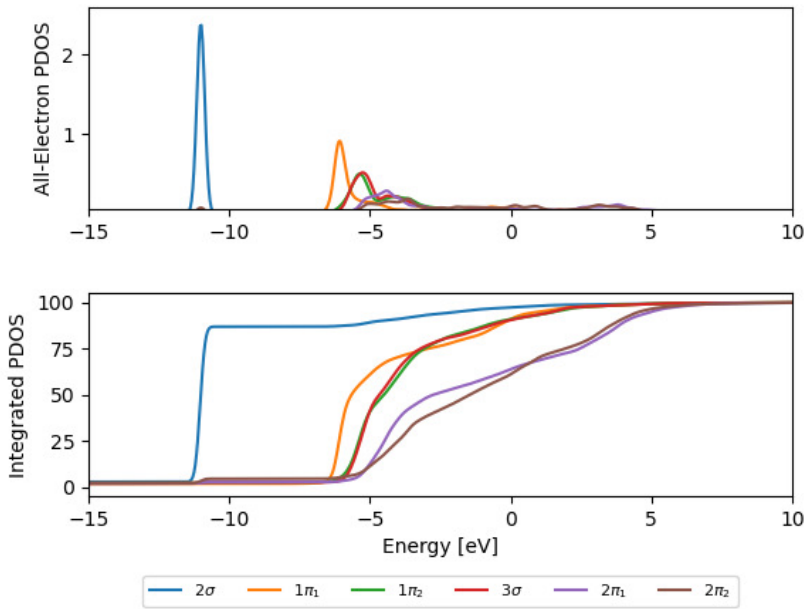

Figure 10.99: Projected Density of States (PDOS) and Integrated PDOS of reactant absorbed in relax stepped Ru(1015) surface for Path 1

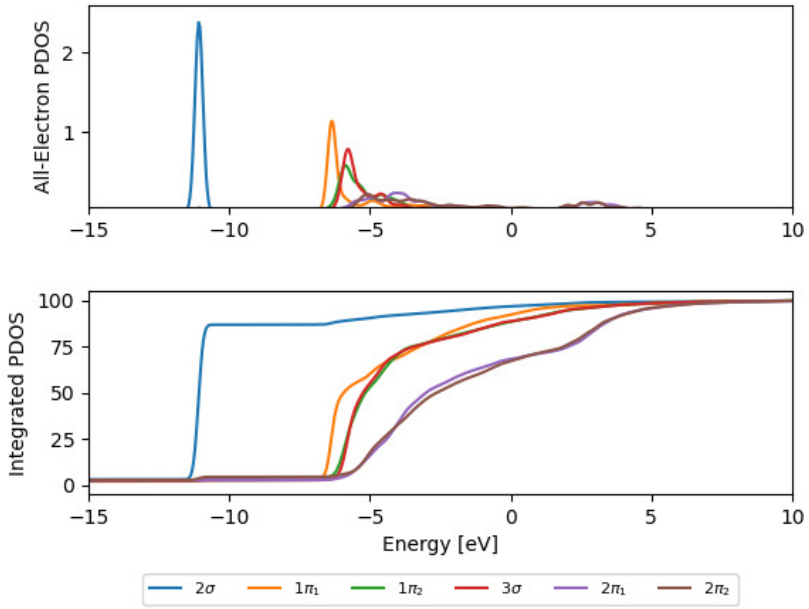

Figure 10.100: Projected Density of States (PDOS) and Integrated PDOS of reactant absorbed in relax stepped Ru(1015) surface for Path 2

Anisotropic Expansion in a on Stepped Ru(1015) Surface

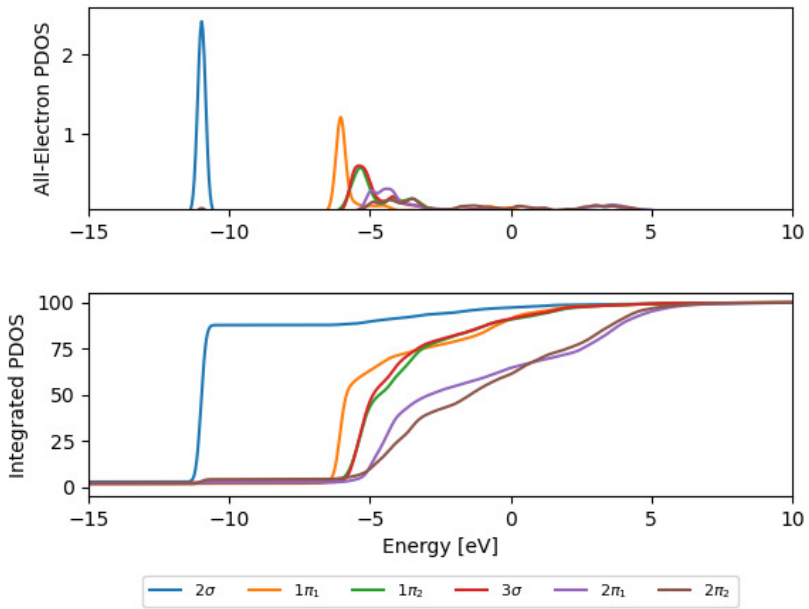

Figure 10.101: Projected Density of States (PDOS) and Integrated PDOS of reactant absorbed in relax stepped Ru(1015) surface for Path 1

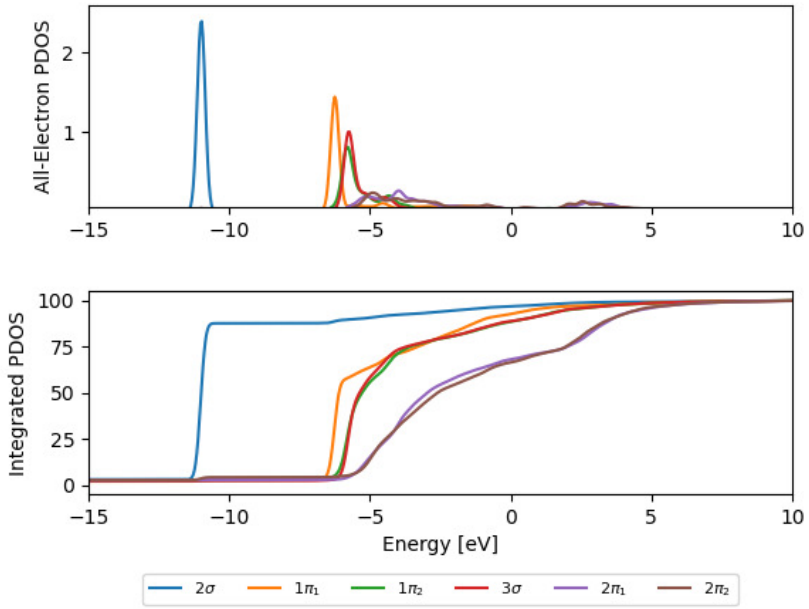

Figure 10.102: Projected Density of States (PDOS) and Integrated PDOS of reactant absorbed in relax stepped Ru(1015) surface for Path 2

Anisotropic Compression in a Stepped Ru(1015) Surface

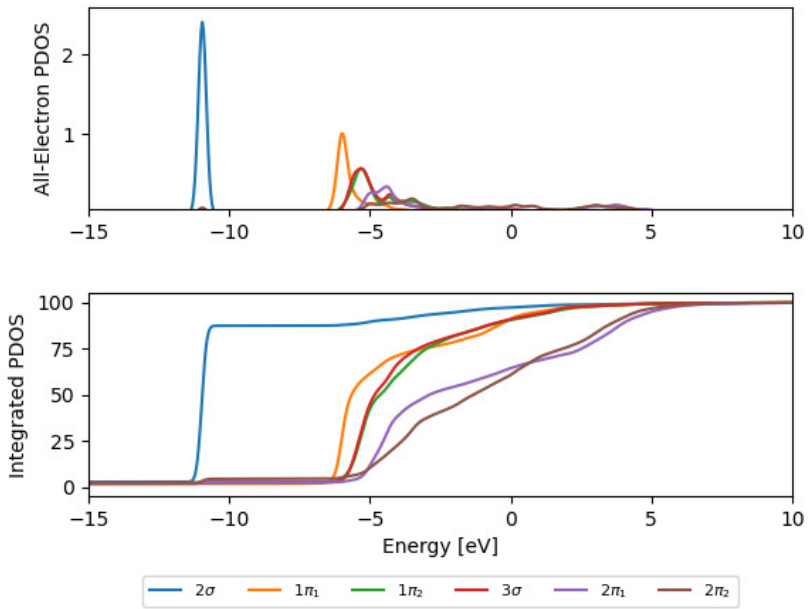

Figure 10.103: Projected Density of States (PDOS) and Integrated PDOS of reactant absorbed in relax stepped Ru(1015) surface for Path 1

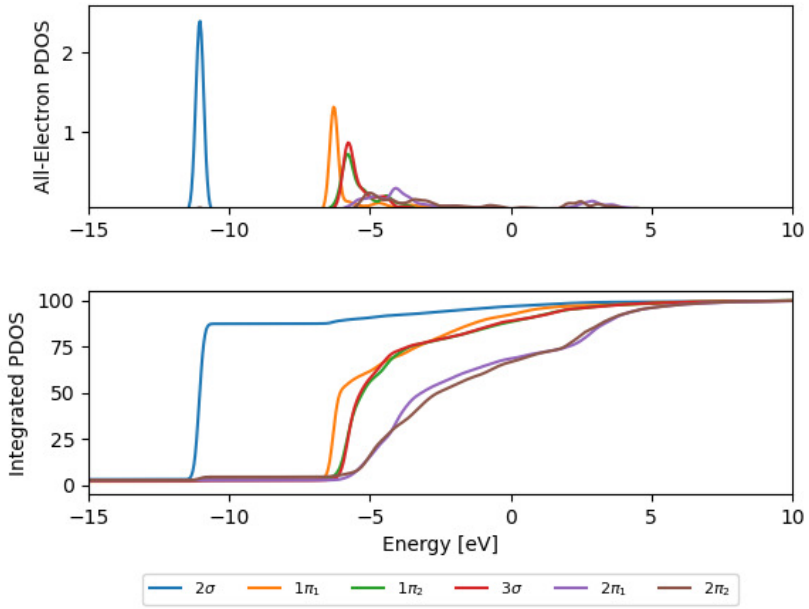

Figure 10.104: Projected Density of States (PDOS) and Integrated PDOS of reactant absorbed in relax stepped Ru(1015) surface for Path 2

Anisotropic Expansion in b on Stepped Ru(1015) Surface

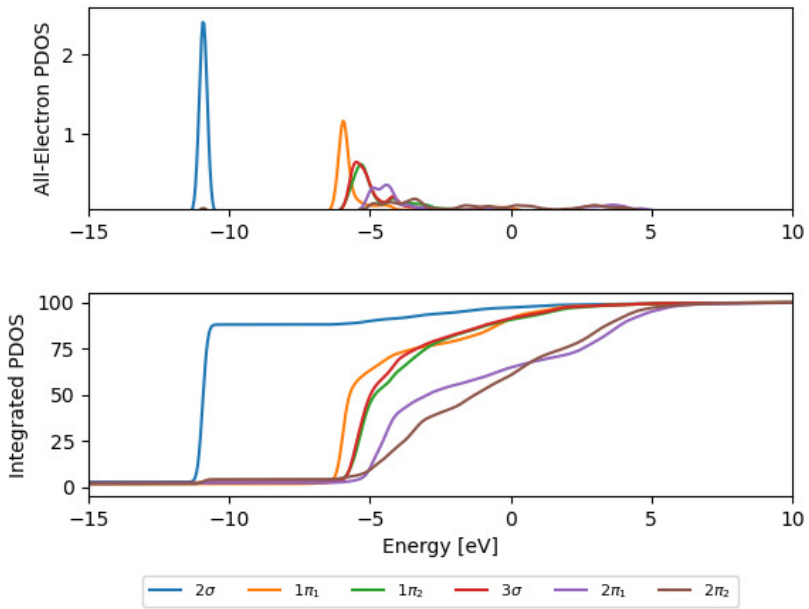

Figure 10.105: Projected Density of States (PDOS) and Integrated PDOS of reactant absorbed in relax stepped Ru(1015) surface for Path 1

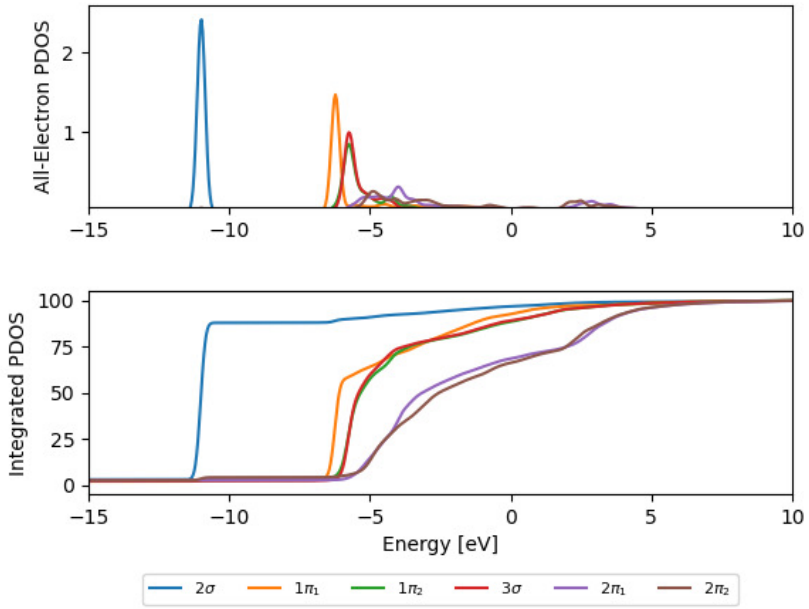

Figure 10.106: Projected Density of States (PDOS) and Integrated PDOS of reactant absorbed in relax stepped Ru(1015) surface for Path 2

Anisotropic Compression in b Stepped Ru(1015) Surface

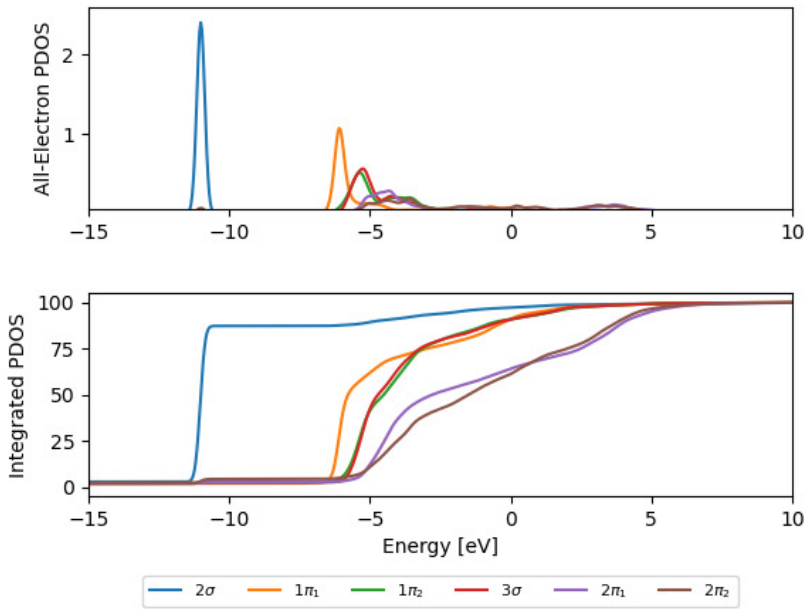

Figure 10.107: Projected Density of States (PDOS) and Integrated PDOS of reactant absorbed in relax stepped Ru(1015) surface for Path 1

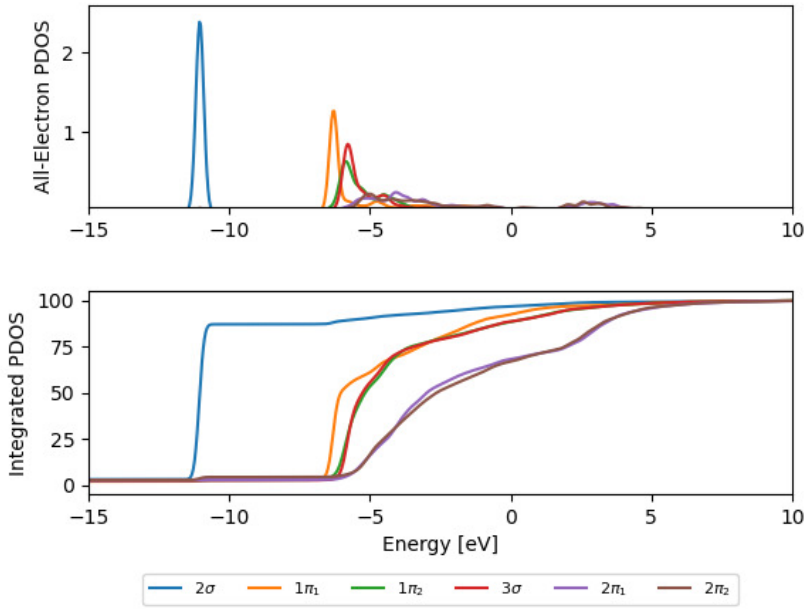

Figure 10.108: Projected Density of States (PDOS) and Integrated PDOS of reactant absorbed in relax stepped Ru(1015) surface for Path 2

NEB Pathways

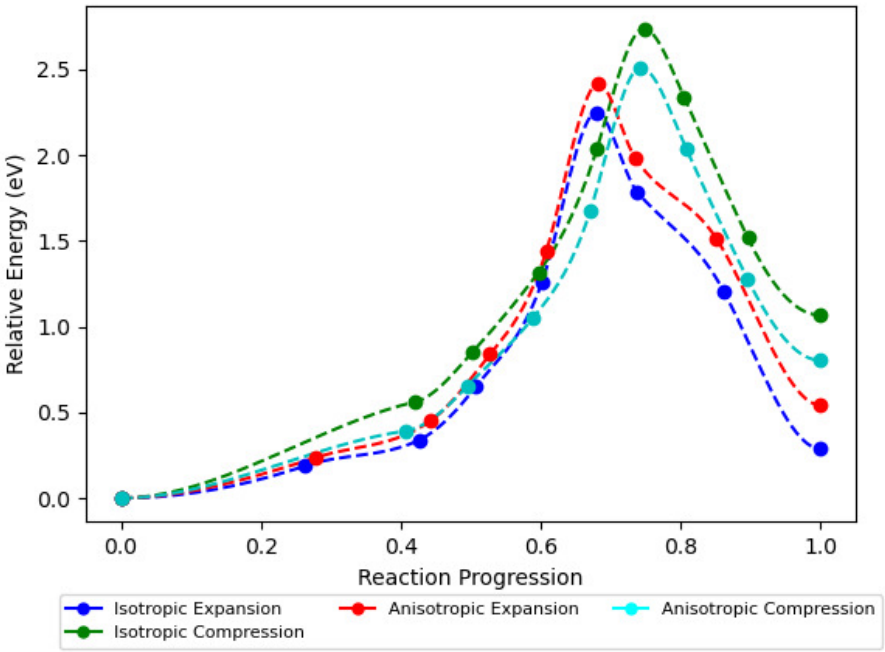

Figure 10.109: NEB Pathways for Path 1 in Terrace Ru(0001) Surface

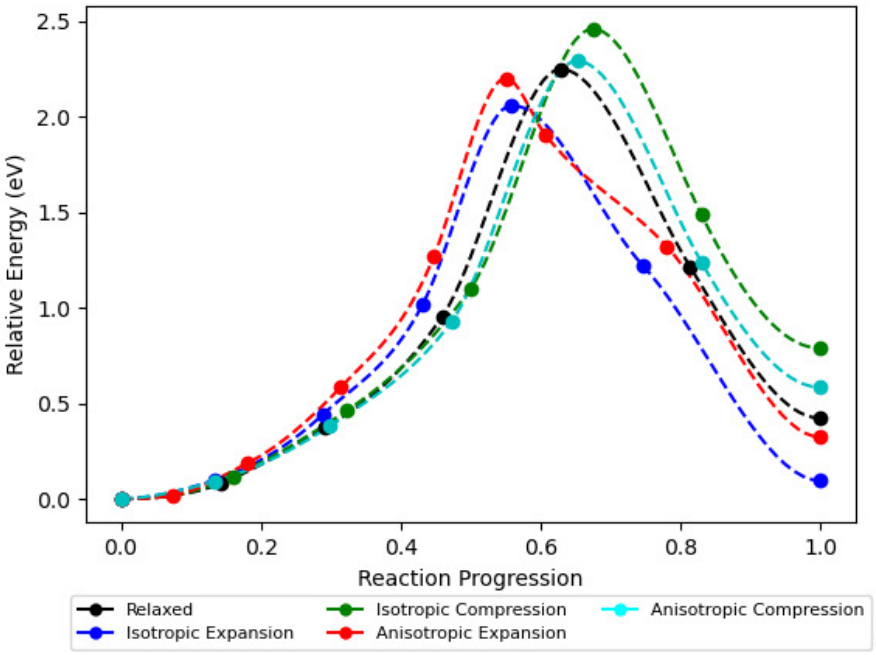

Figure 10.110: NEB Pathways for Path 2 in Terrace Ru(0001) Surface

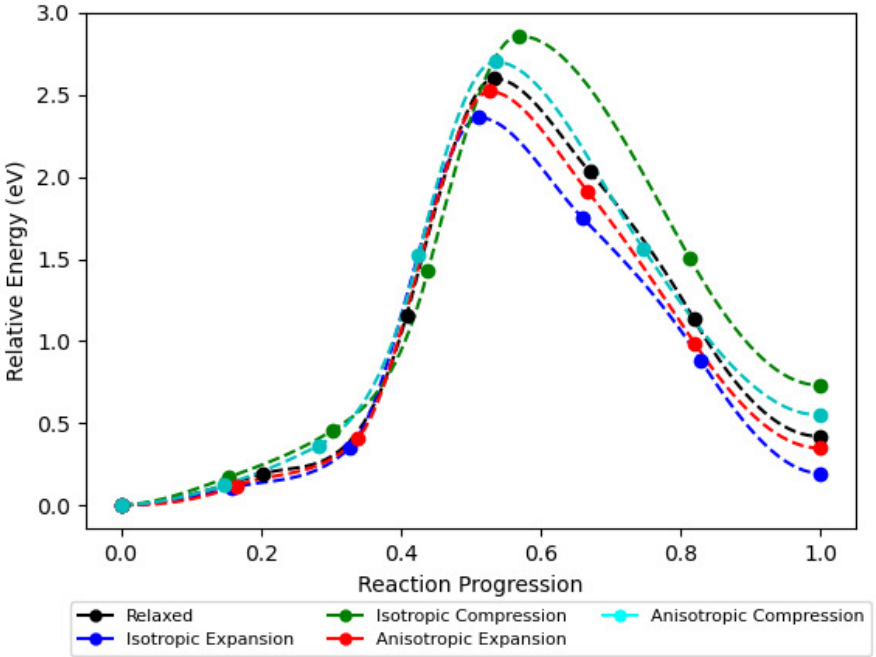

Figure 10.111: NEB Pathways for Path 3 in Terrace Ru(0001) Surface

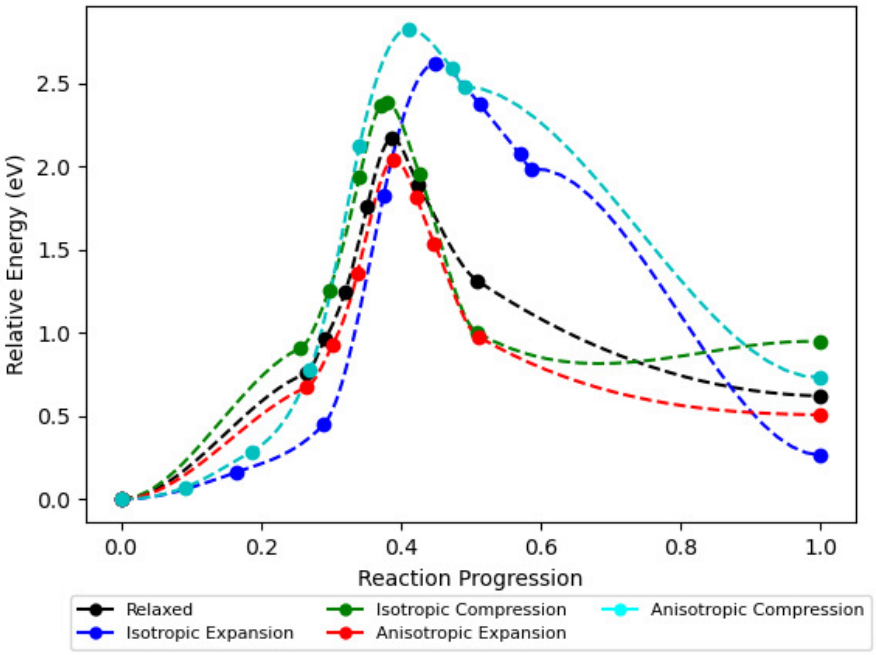

Figure 10.112: NEB Pathways for Path 4 in Terrace Ru(0001) Surface

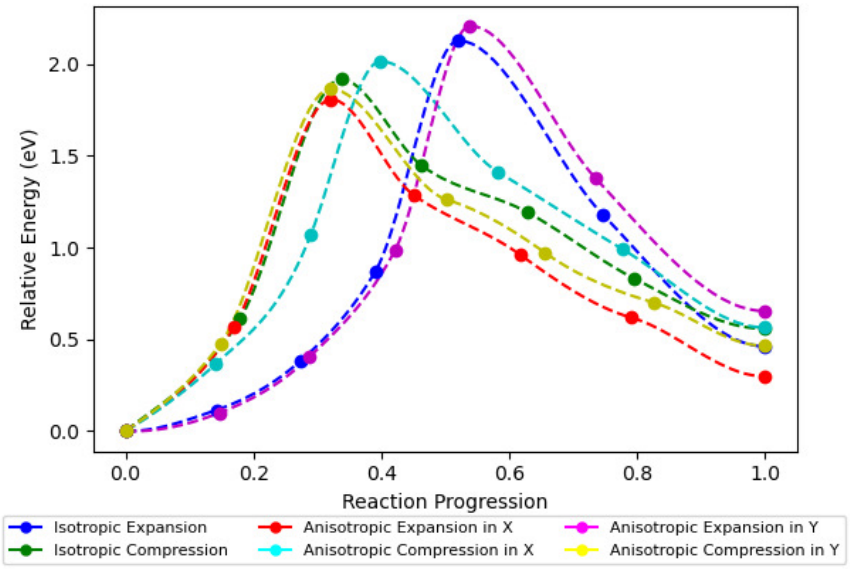

Figure 10.113: NEB Pathways for Path 1 in Stepped Ru(1015) Surface

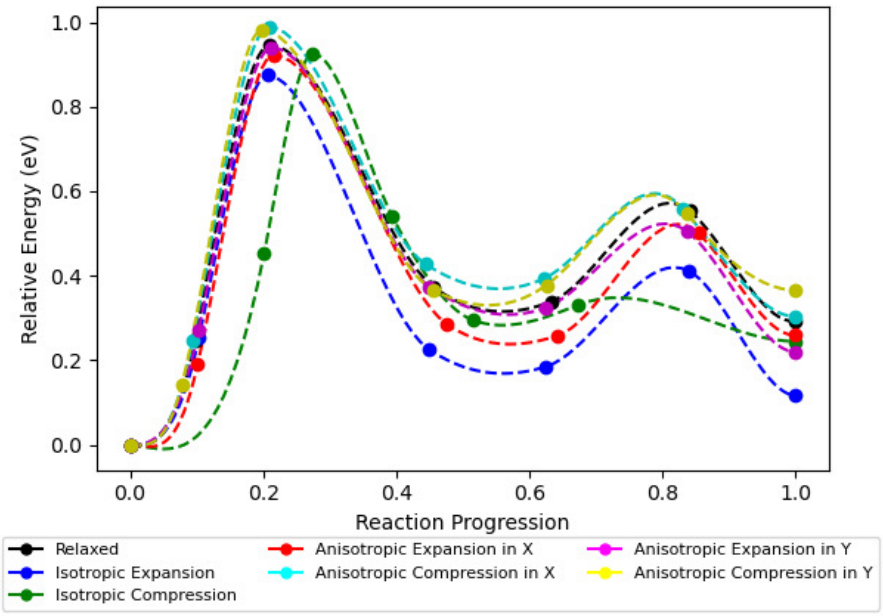

Figure 10.114: NEB Pathways for Path 2 in Stepped Ru(1015) Surface

Curriculum Vitae

DANJO DE CHAVEZ

PhD Candidate, Chemical Sciences and Engineering
Molecular Chemistry and Engineering Specialization

@ dechavezdanjo@gmail.com +8180-9328-8349 Sapporo, Hokkaido, Japan 001-0019

WORK EXPERIENCE

Instructor 1

Institute of Chemistry, University of the Philippines Diliman

June 2012 - April 2016 Quezon City, Philippines

- Biochemistry Laboratories Coordinator
- Instructor, Advanced Integrated Chemistry Laboratory, Biochemistry Laboratory, Organic Chemistry Laboratory

RESEARCH PROJECTS

Theoretical Studies on Mechanocatalytic Systems

Hokkaido University

Ongoing

I use Gaussian09, Siesta, GPAW, and self written codes (Python, Fortran) to study mechanical perturbation in chemical reactions by applying artificial push, pull and shear force on specific atoms during geometry optimizations and dynamics.

Role of Vicinal H bonding Groups to Organic Acid Catalyzed Glucan Hydrolysis

Hokkaido University

2018-2019

I investigate effects of hydrogen bonding moeities of acid catalysts for glucan hydrolysis DFT binding Metadynamics.

Structure-Based Pharmacophore Generation and Virtual Screening of Possible Inhibitors of Homology Modeled Plasmodium falciparum Signal Peptide Peptidase

University of the Philippines Manila

2011-2012

Using Discovery Studio, I did homology modelling followed by molecular docking to screen compound data bases and de novo evolution of hit compounds to find possible drug leads.

EDUCATION

Ph.D. in Chemical Sciences and Engineering

Hokkaido University

September 2018 - September 2021 Sapporo, Hokkaido, Japan

M.Sc. in Chemical Sciences and Engineering

Hokkaido University

September 2016 - September 2018 Sapporo, Hokkaido, Japan

B.S. in Biochemistry

University of the Philippines Manila

June 2008 - April 2012 Manila, Philippines

RESEARCH INTERESTS

- Biomolecular Simulations and Informatics
- Computational and Theoretical Chemistry
- Data Mining and Machine Learning

TECHNICAL SKILLS

Programming Languages

Python	●●●●○
R	●●●○○
FORTRAN	●●●○○
C++	●●●○○
Bash	●●●●○

Chemical Softwares

- Gaussian
- Siesta
- ORCA
- DC-DFTBK
- GROMACS
- NAMD
- AMBER
- Discovery Studio

STRENGTHS

- Hard-working
- Research
- Programming
- Critical Thinking
- Problem Solving
- Teamwork
- Resiliency

LANGUAGES

English	●●●●●
Tagalog	●●●●●
Japanese	●●●○○

WORKSHOP AND SPECIALIZATIONS

Python 3 Programming Specialization

University of Michigan

May 2020 | Coursera

- Python Basics
- Python Functions, Files, and Dictionaries
- Data Collection and Processing with Python
- Python Classes and Inheritance
- Python Project: pillow, tesseract, and opencv

TensorFlow in Practice Specialization

deeplearning.ai

February 2020 | Coursera

- Introduction to TensorFlow for Artificial Intelligence, Machine Learning, and Deep Learning
- Convolutional Neural Networks in TensorFlow
- Natural Language Processing in TensorFlow
- Sequences, Time Series and Prediction

Open Source Software Development, Linux and Git Specialization

The Linux Foundation

January 2019 | Coursera

- Open Source Software Development Methods
- Linux for Developers
- Linux Tools for Developers
- Using Git for Distributed Development

5th Asian Computational Materials Design Workshop (ACMD)

Material Simulations and Design

2012 | Manila, Philippines

Introduction to Computational Chemistry and Application

First Principles Calculations and Monte Carlo Simulations

2012 | Quezon City, Philippines

SCHOLARSHIPS AND RECOGNITION

Japanese Government (Monbukagakusho) Scholarship

Hokkaido University

April 2016 - September 2021 | Sapporo, Hokkaido, Japan

- Doctor of Philosophy Program
- Master's Degree Program
- Research Studentship

Best Undergraduate Research (Candidate)

BSc in Biochemistry, Department of Physical Sciences and Mathematics, University of the Philippines

April 2012 | Manila, Philippines

ORGANIZATIONS

Hokkaido University Association of Filipino Students

April 2016 - Present

Integrated Chemists of the Philippines

September 2012 – Present

Philippine Association of Chemistry Students

2009 – 2012

UP Biochemistry Society

2009 – 2012

VOLUNTEER WORK

Project Kapnayan

Institute of Chemistry, University of the Philippines

2012-2016

Project Kapnayan is the official extension arm of the Institute of Chemistry promoting chemistry to high school students.

UP Pahinungod

University of the Philippines

2013-2015

Pahinungod is the official extension social civic arm of the University of the Philippines.

UP Learning Resource Center Tutor

University of the Philippines

2010-2012 | Manila, Philippines

Peer tutor for Chemistry, Physics and Mathematics

REFERENCES

Prof. Jun-ya Hasegawa
Hokkaido University
hasegawa@cat.hokudai.ac.jp

Prof. Akira Nakayama
The University of Tokyo
nakayama@chemsys.t.u-tokyo.ac.jp

Prof. Junie Billones
University of the Philippines
jbbillones@up.edu.ph

CONFERENCE PRESENTATIONS

Electronic Structure Understanding of the Mechanically Induced Selectivity in Acid Catalyzed Chitin Hydrolysis

9th Asia-Pacific Association of Theoretical and Computational Chemists

September 30- October 3, 2019 | Sydney, Australia

Mechanochemical Selective Activation in Competing Chitin Hydrolysis Reactions

99th Spring Meeting of the Chemical Society of Japan 日本化学会第99春季年会

March 16-19, 2019 | Kobe, Japan

Electronic Structure Origin of Mechanochemically Activated Chitin Depolymerization

4th National Symposium on Material Chemistry 合物化学研究推第4回国内シンポジウム

October 29-30, 2018 | Kyushu, Japan

Theoretical Insights in Mechanochemical Selective Chitin Hydrolysis

Pre-conference of TOCAT8 and the 5th International Symposium of Institute for Catalysis)

August 3-4, 2018 | Hokkaido, Japan

Theoretical Analysis of Mechanically Induced Selective Hydrolysis of Chitin

16th International Congress of Quantum Chemistry (16-ICQC)

June 18-23, 2018 | Menton, France

Theoretical study for selective mechanochemical activation in chitin hydrolysis

Symposium on Nanomaterials for Environmental Purification and Energy Conversion

February 20-21, 2018 | Hokkaido, Japan

Activation Energy and Pulling Direction Relation in Mechanochemical Activation

北大理化学研究会：践理化学の最前

October 18 - 20, 2017 | Hokkaido, Japan

Directional Dependence of Ea Changes in Mechanochemical Activation

Car-Parinello Molecular Dynamics Workshop 2017

October 18 - 20, 2017 | Tsukuba, Japan

Structure-Based Pharmacophore Generation and Virtual Screening of Possible Inhibitors of Homology Modeled Plasmodium falciparum Signal Peptide Peptidase

Philippine Chemistry Congress

April 9 – 11, 2014 | Camarines Sur, Philippines

RESEARCH PUBLICATIONS

Mechanical Pushing Induced Selective Cyclopropanation Reaction in Ag(111) surface

***D. P. De Chavez*, and J. Hasegawa**

2021 In Preparation

Higher CO decomposition activity of Internally-Strained Ru(0001) and Ru(1015) Surfaces

***D. P. De Chavez*, and J. Hasegawa**

2021 In Preparation

On the Electronic Structure Origin of Mechanically Induced Selectivity in Acid Catalyzed Chitin Hydrolysis

***D. P. De Chavez*, H. Kobayashi, A. Fukuoka, J. Hasegawa**

2020 Journal of Physical Chemistry A (Cover)

DOI:10.1021/acs.jpca.0c09030

Adsorption Mediated Tandem Acid Catalyzed Cellulose Hydrolysis by Ortho-substituted Benzoic Acids

***D. P. De Chavez*, M. Gao, H. Kobayashi, A. Fukuoka, J. Hasegawa**

2019 Molecular Catalysis

DOI: 10.1016/j.mcat.2019.110459

Index

Index

L

M

N

O

P

R

S

T